Imperial College of Science, Technology and Medicine

Royal School of Mines

Department of Earth Science and Engineering

The Development of a Performance Assessment Methodology for CO_2 Storage Sites using Dynamic Pressure and Surface Deformation Data

by

Jorge de la Torre Guzman

A thesis submitted for the degree of
Doctor of Philosophy of Imperial College London
January 2016

Abstract

A basic requirement for safe geological storage of CO_2 is the ability and integrity of the storage complex to contain the CO_2. However, the storage formation and the caprock may contain fractures and/or faults that could provide a permeable conduit for CO_2 migration out of the prime storage formation. Furthermore, CO_2 injection may induce or reactivate fracture networks and faults providing a pathway for CO_2 leakage. Recent experience from large scale industrial CO_2 storage projects have shown that the geomechanical response of structural features to CO_2 injection is a critical parameter controlling the injection performance. The monitoring of the geomechanical response using InSAR surface deformation, injection pressure data and seismic data have provided valuable insight into CO_2 injection and storage performance. There is, however, a need for greater integration between monitored data and numerical modelling techniques used to assess performance in order to establish the conformity of the actual behaviour of the injected CO_2 with the modelled behaviour.

Research presented in this thesis developed an integrated performance assessment methodology for CO_2 storage sites, which incorporates satellite (InSAR) monitoring data, time-lapse seismic monitoring data, bottom hole pressure (BHP) data, inverse modelling, and coupled flow-geomechanical simulations using the ensemble Kalman filter (EnKF). The developed methodology has been applied to the In Salah CO_2 storage field dataset in order to demonstrate its application and usefulness for the performance assessment of CO_2 storage sites. First, an inversion scheme using Weiner filters based on a numerical geomechanical model was developed and used to invert InSAR surface deformation for reservoir pressure change. A forward coupled flow-geomechanical modelling study in conjunction with an InSAR and time-lapse

seismic analysis was then performed. This lead to an improved understanding of the flow and pressure behaviour at one of the injection wells. Finally, an integrated approach combining inverse and forward modelling using the EnKF was developed and applied. The EnKF tool developed provides a framework for the updating of flow and geomechanical model parameters through the joint assimilation of bottom hole pressure and InSAR data.

DEDICATED TO MY PARENTS

Affirmation

The work submitted in this thesis is my own, and has not been submitted previously for any other degree. The following publications and presentations have resulted from this work:

De La Torre Guzman, J., Shi, J.Q., Durucan, S., and Korre, A. InSAR monitoring leads to an improved understanding of flow and pressure behaviour during CO_2 injection at In Salah. Fourth EAGE CO_2 Geological Storage Workshop. 22^{nd}-24^{th} April, 2014, Stavanger, Norway, doi:10.3997/2214-4609.20140088.

De La Torre Guzman, J., Shi, J.Q., Durucan, S., and Korre, A., 2015. InSAR monitoring leads to an improved understanding of flow and pressure behaviour during CO_2 injection at In Salah. *First Break*. (accepted)

De La Torre Guzman, J., Shi, J.Q., Durucan, S., and Korre, A. Coupled Flow-Geomechanical Performance Assessment of CO_2 Storage Sites using the Ensemble Kalman Filter, Presented at the International Conference on Greenhouse Gas Technologies (GHGT12), 6^{th}-9^{th} October, 2014, Austin, Texas, *Energy Procedia*. 63(0), pp. 3475-3482, doi:10.1016/j.egypro.2014.11. 376.

Copyright Declaration

The copyright of this thesis rests with the author and is made available under a Creative Commons Non-Commercial No Derivatives licence. Researchers are free to copy, distribute or transmit the thesis on the condition that they attribute it, that they do not use it for commercial purposes and that they do not alter, transform or build upon it. For any reuse or redistribution, researchers must make clear to others the licence terms of this work.

Acknowledgements

First of all, I would like to thank my supervisors Professor Sevket Durucan, Professor Anna Korre and Professor Helmut Jakubowicz and for the support they have provided me over the years and for giving me the opportunity to conduct this research.

I wish to thank the In Salah JIP (BP, Statoil, Sonatrach) for allowing the use of the In Salah data and Michael Nickel from Schlumberger Stavanger Research Norway for providing the time-lapse seismic data used in this research. Also acknowledged is the data support received from the EU funded CO2ReMoVe project (Grant No 518350) in the early years of my research.

Thanks to CONACyT for providing part funding and giving me the opportunity to study abroad and the Minerals, Energy and Environmental Engineering Research Group (MERG) for providing part funding towards my PhD research.

Thanks to my colleagues and friends from the Minerals, Energy and Environmental Engineering Research Group who have accompanied and supported me through these years: Dr. Ji-Quan Shi, Dr. Rajesh Govindan, Dr. James Smith, Dr. Masoud Babaei, Dr. Amer Syed, Indranil Pan, Guangyao Si, Saba Manzoor, Tareq Al-Ansari and Nondas Andrianopoulos.

I also want to thank my friends Alejandro Elizondo Perea, Zeenia Mistry, Jose Santos Perez, Bisma Suleman, Akela Silverton, Renan Villareal, Thilo Wrona, Benoit Massart and Jacob Longridge for all the good times over the years.

Finally, I would like to thank my parents and my family for their support and constant encouragement.

Table of Contents

ABSTRACT ..... **I**

AFFIRMATION ..... **IV**

COPYRIGHT DECLARATION ..... **IV**

ACKNOWLEDGEMENTS ..... **V**

TABLE OF CONTENTS ..... **VI**

LIST OF FIGURES ..... **XII**

LIST OF TABLES ..... **XVII**

NOMECLATURE ..... **XVIII**

CHAPTER 1 INTRODUCTION AND OBJECTIVES **1**

1.1 THE MOTIVATION FOR CARBON CAPTURE AND STORAGE 1

1.2 CARBON CAPTURE AND STORAGE OVERVIEW 2

1.2.1 Unmineable coal seams *3*

1.2.2 Depleted hydrocarbon fields *3*

1.2.3 Saline aquifers *4*

1.2.4 Storage mechanisms *4*

1.3 CO_2 STORAGE SITE PERFORMANCE ASSESSMENT 5

1.4 RESEARCH OBJECTIVES 8

1.5 RESEARCH METHODOLOGY AND THE THESIS OUTLINE 9

CHAPTER 2 BACKGROUND AND LITERATURE REVIEW 11

2.1 PRINCIPLES OF GEOMECHANICS 12

2.1.1 Stress in the earth's crust 12

2.1.2 Measuring in situ stress 14

2.1.3 Local stress fields 16

2.1.4 Rock Deformation 17

2.1.5 Strength properties of rocks 18

2.1.6 Shear Failure 19

2.1.7 Tensile Failure 19

2.2 FAULTS, FRACTURES AND FLUID FLOW 20

2.2.1 Fluid flow through a planar fracture 21

2.2.2 Fracture growth 22

2.2.3 Critically stressed faults/fractures 22

2.3 THE GEOMECHANICS OF CO_2 STORAGE IN DEEP SEDIMENTARY FORMATIONS 23

2.3.1 Key geomechanical processes 23

2.3.2 Reservoir inflation and alteration of flow properties 25

2.3.3 Caprock sealing performance 26

2.3.4 Injection-induced seismicity 26

2.3.5 Wellbore failure and casing damage 27

2.4 COUPLED FLOW-GEOMECHANICAL MODELS FOR CO_2 STORAGE 27

2.5 MONITORING GEOMECHANICAL DEFORMATION AT CO_2 STORAGE SITES 29

2.5.1 Geodetic methods 29

2.5.2 Time-lapse seismic reflection surveys 30

2.5.3 Microseismic monitoring 32

2.6 ALTERNATIVE MONITORING TECHNIQUES 32

2.6.1 Gravity Surveying 32

2.6.2 Well-based Monitoring 33

2.7 MEGATONNE-SCALE CO_2 STORAGE SITES 33

2.7.1 Sleipner 33

2.7.2 Weyburn 34

2.7.3 Snøhvit 35

2.7.4 In Salah 35

2.8 SUMMARY AND DISCUSSION 37

CHAPTER 3 METHODOLOGY AND THEORY 39

3.1 COUPLED FLOW-GEOMECHANICAL MODELLING 40
3.1.1 ECLIPSE E300 reservoir simulator 40
3.1.2 Geomechanical Simulators 41
3.1.3 Coupling of fluid-flow and geomechanics 42
3.1.4 Coupled flow-geomechanical modelling workflow 43
3.1.5 Building a reservoir geomechanical model 44
3.2 INVERTING FOR RESERVOIR PRESSURE CHANGE USING GEOMECHANICAL DEFORMATION 46
3.2.1 Problem formulation 46
3.2.2 The Weiner filter formulation 47
3.2.3 Reservoir pressure change inversion workflow 49
3.3 THE ENKF APPROACH 51
3.3.1 Introduction 51
3.3.2 The Kalman filter 52
3.3.3 The Ensemble Kalman Filter 53
3.3.4 Geostatistical Methods 55
3.3.5 EnKF workflow 58
3.4 SUMMARY AND DISCUSSIONS 60

CHAPTER 4 THE IN SALAH CO_2 STORAGE PROJECT 62
4.1 THE IN SALAH PROJECT 62
4.2 IN SALAH GEOLOGICAL SETTING 63
4.2.1 History of the In Salah Field 66
4.3 MONITORING AT IN SALAH 68
4.4 MONITORING AT WELL KB-5 69
4.5 BOTTOM HOLE PRESSURE MONITORING 69
4.6 INSAR MONITORING AT IN SALAH 69
4.7 SEISMIC SURVEYS 71
4.8 MICROSEISMIC MONITORING 72
4.9 HYPOTHESES FOR THE GEOMECHANICAL BEHAVIOUR OF THE RESERVOIR AND CAPROCK SYSTEM 73
4.10 EVIDENCE FOR RESERVOIR-ONLY PRESSURISATION 73
4.11 EVIDENCE FOR PRE-EXISTING FRACTURES 77
4.11.1 Discrete Fracture Network Modelling 78
4.12 EVIDENCE FOR FAULT LEAKAGE 79

4.13 EVIDENCE FOR HYDRO-FRACTURING 80
4.14 SUMMARY AND DISCUSSIONS 84

CHAPTER 5 RESERVOIR PRESSURE CHANGE INVERSION 88
5.1 REVIEW OF INVERSE MODELLING USING OVERBURDEN DEFORMATION DATA 88
5.1.1 Analytical Approach 88
5.1.2 Semi-Analytical Approach 89
5.1.3 Numerical Approach 90
5.1.4 Deterministic vs. Stochastic Inversion 91
5.2 GREEN'S FUNCTIONS VS. TRANSFER FUNCTIONS 91
5.2.1 Linear Filters 91
5.2.2 Green's Function and Transfer Function Comparison 92
5.3 A GREEN'S FUNCTION FORMULATION 94
5.4 RESOLUTION 97
5.4.1 Geometrical Setup 98
5.4.2 Resolution Test 99
5.4.3 Multi-Component Resolution Test 100
5.4.4 Dipping Reservoir Resolution Test 101
5.5 REGULARISATION 102
5.5.1 The L_2 Norm 102
5.6 IMPACT OF MATERIAL PROPERTIES 103
5.6.1 Linear poroelastic halfspace 103
5.7 APPLICATION TO THE IN SALAH CO_2 STORAGE SITE 104
5.7.1 Inversion Setup 104
5.7.2 Geomechanical Model 105
5.7.3 Synthetic Pressure Source Design 106
5.7.4 Transfer function computation 107
5.7.5 Results 109
5.8 SUMMARY AND DISCUSSIONS 111

CHAPTER 6 COUPLED FLOW-GEOMECHANICAL SIMULATION OF CO_2 INJECTION AT THE IN SALAH STORAGE SITE 114
6.1 PREVIOUS MODEL MISMATCH AT INJECTION WELL KB-503 115
6.2 MODELLING APPROACH 116
6.3 ANALYSIS OF INSAR SURFACE UPLIFT AT IN SALAH 117
6.3.1 CO_2 injection rates and cumulative injection 117
6.3.2 Understanding the deformation pattern 117

6.3.3 InSAR Multi-point analysis 119
6.3.4 Hydraulic stimulation timing and geometry 120
6.4 INSIGHT FROM TIME-LAPSE SEISMIC 121
6.4.1 Geomechanical basis for time-lapse seismic time-shifts 121
6.4.2 The R Factor 122
6.4.3 The U Factor 123
6.4.4 Offset dependence 123
6.4.5 Time-Strain 123
6.4.6 Data quality and repeatability 124
6.4.7 Processing 125
6.4.8 Time-lapse Seismic Interpretation 127
6.4.9 Mapping the fault/fracture zone 128
6.5 NUMERICAL MODELLING 129
6.5.1 Model Description 129
6.5.2 Flow properties 130
6.5.3 Stress Regime and Geomechanical properties 130
6.5.4 Fault/Fracture zone transmissibility 131
6.5.5 Modelling Time Frame 132
6.6 RESULTS 133
6.6.1 History Matching and Sensitivity Analysis 133
6.6.2 BHP History Match 135
6.6.3 InSAR History Match 136
6.6.4 Comparison with other injection wells 137
6.7 SUMMARY AND DISCUSSIONS 138

CHAPTER 7 COUPLED FLOW-GEOMECHANICAL PERFORMANCE ASSESSMENT USING THE ENSEMBLE KALMAN FILTER 141
7.1 ENKF MODELLING IMPLEMENTATION 142
7.2 THE ENKF SETUP 143
7.2.1 Ensemble definition 143
7.2.2 Geostatistical simulation of flow properties 143
7.2.3 Incorporating prior knowledge from InSAR 147
7.2.4 Geomechanical properties 148
7.2.5 Observations 148
7.3 RESULTS 149
7.3.1 Scenario 1 - No Geomechanical Uncertainty 149

7.3.2 Scenario 2 - Geomechanical Uncertainty *153*
7.3.3 Scenario 3 - Lateral Variations in Geomechanical Uncertainty *158*
7.4 LIMITATIONS OF THE ENKF 165
7.5 SUMMARY AND DISCUSSIONS 166

CHAPTER 8 CONCLUSIONS 168
8.1 CONTRIBUTIONS TO KNOWLEDGE 168
8.1.1 Reservoir pressure change inversion *168*
8.1.2 Understanding flow and pressure behaviour from CO_2 injection *169*
8.1.3 Integrated Approach using the Ensemble Kalman Filter *169*
8.1.4 Main Conclusions and Learnings *170*
8.2 RECOMMENDATIONS FOR FUTURE RESEARCH 172
8.2.1 Two-way coupling between fluid flow and geomechanics *173*
8.2.2 Coupling with a seismic simulator *173*
8.2.3 Fracture Modelling *174*
8.2.4 Closed loop reservoir management *175*

APPENDICES 176
A.1 DISPLACEMENT FIELD AROUND A NUCLEUS OF STRAIN 176
A.1.1 Introduction *176*
A.1.2 Displacements *176*
B.1 ENKF 2D EXAMPLE 178
B.1.1 Model Description *178*
B.1.2 Case 1 ..... *179*
B.1.3 Case 2 ..... *181*
B.1.4 Case 3 ..... *183*
B.1.5 Case 4 ..... *185*
B.1.6 Case 5 ..... *185*
B.1.7 Comparison *187*

REFERENCES 191

List of Figures

Figure 1.1: The different kinds of geological formations suitable for CO_2 storage (IPCC, 2005). 2

Figure 1.2: Schematic of the evolution of CO_2 trapping mechanisms over time (IPCC, 2005). .. 5

Figure 1.3: Potential geomechanical deformation monitoring options for CO_2 storage sites. Adapted from Verdon *et al.* (2013). 7

Figure 2.1: Anderson's (1951) classification scheme for relative stress magnitudes in normal, strike-slip and reverse fault regions. 13

Figure 2.2: Directions of maximum horizontal stress from a compilation of stress sources taken in North America from the world stress map data base (http://world-stress-map.org). 15

Figure 2.3: (a) A micro-crack under a remote compressive stress , $\sigma 3$ (b) The tip region of the micro-crack where stress concentration is greatest. Modified from Pollard and Atilla (1988). 16

Figure 2.4: The three modes of fractures: mode I is an extensional opening fracture, mode II is a sliding fracture and mode III is a shearing fracture. 17

Figure 2.5: A plot of axial strain vs. axial stress for different confining stress. The failure stress is shown for failure mode changes from brittle failure to ductile failure. 18

Figure 2.6: Shear failure mechanism under compressive stress. 19

Figure 2.7: Tensile failure of a rock under tensile stress. 20

Figure 2.8: Geomechanical processes and key technical issues associated with geological CO_2 storage (Rutqvist, 2012). 24

Figure 2.9: Time-lapse seismic images of the Sleipner CO_2 plume. NS inline through the plume (top); plan view of total reflection amplitude in the plume (bottom). Modified from Chadwick *et al.* (2010). 31

Figure 2.10: Average field pressure over the history of the Weyburn field (After Verdon *et al.*, 2013). 34

Figure 2.11: Forward coupled flow-geomechanical numerical modelling of CO_2 injection including a vertical fracture zone reproduces observed surface uplift (After Rutqvist *et al.*, 2011). 36

Figure 3.1: Diagram showing the one-way coupling scheme between ECLIPSE E300 and FLAC^{3D}. 44

Figure 3.2: Workflow explaining the calculation and use of Weiner filters to estimate reservoir pressure changes from overburden deformation. 50

Figure 3.2: Idealised variogram plot. 56

Figure 3.3: Workflow for assessing coupled flow-geomechanical performance monitoring for CO_2 storage sites. 59

Figure 4.1: Geographic location of the In Salah field (Adapted from Mathieson *et al.,* 2010). . 64

Figure 4.2: Krechba stratigraphic log (Courtesy of In Salah Gas Joint Industry Project). 65

Figure 4.3: Structural geological setting for the In Salah area (After Ringrose *et al.*, 2011). 65

Figure 4.4: Schematic cross section at the Krechba injection site (After Mathieson *et al.*, 2010). 66

Figure 4.5: Krechba field map showing the location of the three CO_2 injection wells KB-501, KB-502 and KB-503 and the production wells. The black line indicates the gas-water contact (After Mathieson *et al.*, 2010). 66

Figure 4.6: Daily injection rates and cumulative CO_2 injected at well KB-501. 67

Figure 4.7: Daily injection rates and cumulative CO_2 injected at well KB-502. 67

Figure 4.8: Daily injection rates and cumulative CO_2 injection at well KB-503. 67

Figure 4.9: Monitoring technologies under consideration at the In Salah site (After Mathieson *et al.*, 2010). 68

Figure 4.10: Janurary 20, 2012 Surface deformation detected over the CO_2 injection and production wells using PSInSAR (Courtesy of the In Salah Gas Joint Industry Project). 70

Figure 4.11: Updated fault interpretation from 2009 3D seismic survey (After Ringrose *et al.*, 2011). 71

Figure 4.12: Time-lapse seismic time-shifts (red) superimposed on the InSAR surface uplift (blue) at injection wells KB-502 and KB-503 (Courtesy of M. Nickel, Schlumberger Stavanger Research, Norway). 72

Figure 4.13: Logarithm of permeability estimates at the reservoir interval at injection well KB-502 (After Vasco *et al.*, 2008). 74

Figure 4.14: Proposed mechanism to explain double-lobe deformation (After White *et al.*, 2014). 75

Figure 4.15: The spatial distribution of aperture change over the vertical fault/fracture model at KB-502 from the inversion of surface uplift data (Vasco *et al.*, 2010). 75

Figure 4.16: Fault interpretation at the reservoir interval (C10.2). The solid lines correspond to the fault interpretation from the 2009 seismic survey. The dashed line is a fault interpreted in the 1997 survey but not visible in the higher quality 2009 survey (After White *et al.*, 2014). 80

Figure 4.17: Estimated minimum horizontal stress profile. Red circle indicates the interpolated fracture pressure at the top reservoir (After Shi *et al.*, 2012). 81

Figure 4.18: Leak-off test (LOT), formation integrity test (FIT), and step-rate test (SRT) data compiled from injection and production wells (After White *et al.*, 2014). 82

Figure 5.1: Geometry for nucleus of strain model modified from (Hodgson *et al.*, 2007). 97

Figure 5.2: Pressure pulse and reservoir geometry used in the resolution test. 98

Figure 5.3: Geometrical setup for the resolution test. 98

Figure 5.4: Resolution test for different depths. (A) 0 m (B) 2,250 m (C) 2,500 m (D) 2,750 m. The true pressure source solution. 99

Figure 5.5: Resolution test using multi-component observations. (a) Inversion using Z component, (b) X component, (c) Y component, (de) XYZ component of surface deformation and (e) the true pressure source solution. 100

Figure 5.6: Geometric configuration for a dipping reservoir (a) observations located at the surface, (b) observations are located 200 m above the reservoir. 101

Figure 5.7: Resolution test for a dipping reservoir for two configurations. (a) Observations located at the surface, (b) Observations are located 200 m above the reservoir and parallel to the reservoir dip. 101

Figure 5.8: Plan view of geomechanical model with lateral dimensions. 105

Figure 5.9: Synthetic source used to simulate the system's impulse-response. The source consists of a 10 bar peak that decays exponentially. 106

Figure 5.10: Pressure source location for injection wells KB-501, KB-502 and KB-503. 107

Figure 5.11: Simulated deformation for injection well KB-501. 107

Figure 5.12: Simulated surface deformation for injection well KB-502. 108

Figure 5.13: Simulated surface deformation for injection well KB-503. 108

Figure 5.14: InSAR data upscaled to model resolution, (a) February 26, 2005, (b) March 18, 2006, (c) December 23, 2006 (d) January 12, 2008, (e) December 27, 2008, (f) May 16, 2009, (g) February 20, 2010, (h) May 6, 2010. 109

Figure 5.15: Reservoir pressure change inversion using InSAR deformation data, (a) February 26, 2005, (b) March 18, 2006, (c) December 23, 2006 (d) January 12, 2008, (e) December 27, 2008, (f) May 16, 2009, (g) February 20, 2010, (h) May 6, 2010... 110

Figure 6.1: (a) Previous history match of the CO_2 injection pressure at KB-501. (b) InSAR surface uplift time series (Courtesy of the In Salah Gas Joint Industry Project) and the previous model predictions. The two curves (with different offsets) correspond to two marked locations (centre and the toe) along the borehole (after Shi *et al.*, 2013). 115

Figure 6.2: (a) Previous history match of the CO_2 injection pressure at KB-503. (b) InSAR surface uplift time series (Courtesy of the In Salah Gas Joint Industry Project) and the previous model predictions. The two curves (with different offsets) correspond to two marked locations (centre and the toe) along the borehole (after Shi *et al.*, 2013). 116

Figure 6.3: CO_2 injection rate and cumulative injected CO_2 at injection well KB-503. 117

Figure 6.4: InSAR surface uplift at KB503. (a) Single uplift lobe suggesting well pressurisation (February 2005); (b) South-East uplift lobe elongation suggesting pressure propagation along a fault/fracture zone (September 2005). (Courtesy of the In Salah Gas Joint Industry Project). 118

Figure 6.5: Location of five different points at injection well KB-503 for the InSAR surface uplift time series analysis (Courtesy of the In Salah Gas Joint Industry Project). . 119

Figure 6.6: InSAR surface uplift at five different locations. 120

Figure 6.7: Histogram of the time-lapse signal to noise ratio (SNR) extracted along the Hercynian unconformity (Courtesy of M. Nickel, Schlumberger Stavanger Research, Norway). 126

Figure 6.8: Histogram of the time-lapse signal to noise ratio (SNR) extracted along the Hercynian Unconformity after cross-equalisation (Courtesy of M. Nickel, Schlumberger Stavanger Research, Norway). 126

Figure 6.9: A preliminary analysis of the time-lapse seismic time-shifts between 1997 and 2009 for illustrative purposes (Courtesy of M. Nickel, Schlumberger Stavanger Research, Norway). 128

Figure 6.10: (a) Flow and geomechanical model domain (b) Overburden layers (c) Reservoir layers. 129

Figure 6.11: Sensitivity analysis for the Young's modulus of the lower caprock. 134

Figure 6.12: Sensitivity analysis for the fault/fracture zone transmissibility. 135

Figure 6.13: (a) Improved history matching of the CO_2 injection pressure at KB-503; (b) Modelled fracture/fault zone with dynamic transmissibility. 136

Figure 6.14: InSAR surface uplift time series at the centre of the well and the model predictions at KB-503. 137

Figure 7.1: Seismic derived porosity surface for top reservoir. 144

Figure 7.2: Seismic derived porosity surface using a 5% porosity cut-off value. 145

Figure 7.3: Porosity variogram. 145

Figure 7.4: Permeability variogram. 145

Figure 7.5: Geostatistical simulation of horizontal permeability. 146

Figure 7.6: Geostatistical simulation of porosity. 147

Figure 7.7: InSAR surface uplift map showing preferential flow directions (white arrows). The preferential flow direction is marked by X and the minor flow direction is marked by Y. 148

Figure 7.8: Match to estimated BHP data from the initial ensemble and from the updated ensemble using BHP data assimilation for the injection wells KB-501, KB-502 and KB-503. 150

Figure 7.9: Updated ensemble transmissibility for well KB-502. 151

Figure 7.10: Updated ensemble permeability multipliers in the x- and y- direction for injection wells KB-501 and KB-503 151

Figure 7.11: Surface deformation predictions from the initial ensemble and from the updated ensemble using BHP data assimilation for injection wells KB-501, KB-502 and KB-503. 152

Figure 7.12: Match to estimated BHP data from the updated ensemble using BHP data assimilation and joint BHP and surface deformation data for injection wells KB-501, KB-502 and KB-503. 154

Figure 7.13: Match to estimated InSAR surface deformation data from the updated ensemble using BHP data assimilation and joint BHP and surface deformation data for injection wells KB-501 and KB-503. 155

Figure 7.14: Updated flow and geomechanical parameters using BHP data assimilation and joint BHP and surface deformation data. 156

Figure 7.15: Young's modulus prior (red) and posterior (blue) probility density function for the lower caprock. 157

Figure 7.16: Match to estimated BHP data from the initial ensemble and the updated ensemble using BHP data assimilation and joint BHP and surface deformation data for injection wells KB-501, KB-502 and KB-503. 159

Figure 7.17: Match to estimated InSAR surface deformation data using the initial ensemble and the updated ensemble using BHP data assimilation and joint BHP and surface deformation data for injection wells KB-501, KB-502 and KB-503.. 160

Figure 7.18: Updated flow and geomechanical parameters using BHP data assimilation and joint BHP and surface deformation data. 161

Figure 7.19: Zone 1 Young's modulus prior (red) and posterior (blue) probility density function for the lower caprock. 163

Figure 7.20: Zone 2 Young's modulus prior (red) and posterior (blue) probability density function for the lower caprock. 163

Figure B.1: 2D CO_2 storage site conceptual model. 179

Figure B.2: Case 1: Data assimilation for BHP. 180

Figure B.3: Case 1: Data assimilation for surface deformation. 181

Figure B.4: Case 2: Data assimilation for BHP. 182

Figure B.5: Case 2: Data assimilation for surface deformation. 183

Figure B.6: Case 3: Data assimilation for BHP. 184

Figure B.7: Case 3: Data assimilation for surface deformation. 185

Figure B.8: Case 5: Data assimilation for BHP. 186

Figure B.9: Case 5: Data assimilation for surface deformation. 187

Figure B.10: Permeability pdf for Case 1. 188

Figure B.11: Permeability pdf for Case 2. 188

Figure B.12: Permeability pdf for Case 3. 189

Figure B.13: Permeability pdf for Case 4. 189

Figure B.14: Permeability pdf for Case 5. 189

Figure B.15: Young's Modulus pdf for Case 5. 190

List of Tables

Table 4.1: Fault/Fracture properties derived by Vasco *et al.* (2010) 76

Table 5.1: Geomechanical model rock elastic properties 106

Table 6.1: Flow properties (based on data by the In Salah JIP) ..... .129

Table 6.2: Gas-water relative permeabilities and capillary pressures used in the reservoir simulations..... .130

Table 6.3: Geomechanical model rock elastic properties 131

Nomeclature

Geomechanical

U_i	Displacement
σ_{ij}	Stress tensor
ε_{ij}	Stress tensor
μ	Shear modulus
ν	Poisson's ratio
E	Young's modulus
K	Bulk modulus
ρ	Density
α	Biot's coefficient
C_m	Uniaxial compaction coefficient
Δp	Change in reservoir pressure
S_0	Shear strength
T_0	Tensile strength

Geophysical

t	Two-way seismic travel time
R	Factor relating change in velocity to change in vertical strain
V_p and v	Seismic P-wave velocity
U	Factor relating change in velocity to change in stress
$\mathbf{G}$	Green's function relating reservoir changes to overburden deformation

$\boldsymbol{f}$	Weiner filter

Fluid Flow

ϕ	Porosity
k	Permeability
$k_{r\alpha}$	Relative Permeability
$\mathbf{J}_{\alpha}^{i}$	Diffusive Flux
D_{α}^{i}	Diffusion coefficient
Q	Volumetric Flow
η	Fluid viscosity
k_b	Effective permeability
k_m	Matrix permeability
k_f	Fracture permeability
n_f	Number of conductive fractures
w	Fracture aperture
S_{α}	Saturation

Ensemble Kalman Filter

$y_{k,i}$	State vector
Ψ_k	Ensemble of augmented state vectors
d_j	Observational data vector
K_e	Kalman gain
N_e	Ensemble size
H	Measurement operator
C_D	Data covariance matrix
$C_{\Psi,\mathrm{e}}$	Ensemble covariance matrix
L_e	Square root of ensemble covariance matrix

Geostatistics

γ	Variogram function
C_0	Nugget

C_1	Sill

Abbreviations

4D	Multiple 3D seismic surveys taken at different times
BHP	Bottom Hole Pressure
BHT	Bottom Hole Temperature
InSAR	Interferometric Synthetic Aperture Radar
EnKF	Ensemble Kalman Filter
SGS	Sequential Gaussian Simulation
LOT	Leak-off test
FIT	Formation integrity test
SRT	Step rate test
EMW	Equivalent mud weight
SG	Specific gravity
SNR	Signal to noise ratio
CSEM	Controlled Source Electromagnetic
FMI	Formation Micro Imager
UBI	Ultrasonic Borehole Imager
DFN	Discrete Fracture network
HPHT	High Pressure High Temperature
JIP	Joint Industry Project

Chapter 1 Introduction and Objectives

1.1 *The motivation for carbon capture and storage*

A growing concern that the ongoing increase in atmospheric concentrations of the greenhouse gas carbon dioxide (CO_2) is contributing to global climate change has led to a search for technologies to reduce CO_2 emissions. This observed increase over the last two centuries has been driven almost entirely by anthropogenic emissions associated with combustion of fossil fuels. Stabilising atmospheric CO_2 concentrations caused by anthropogenic emissions constitutes a great challenge for the 21st century which will require vast reductions in CO_2 emissions. The largest increases in CO_2 emissions in the upcoming decades will come from developing countries due to their rapid urbanisation and industrialisation. The huge energy demand this generates is at present met by its majority with coal, which is abundant, cheap and geopolitically secure. Petroleum fuels used for transportation, gas and biomass power stations also make significant contributions to CO_2 emissions with energy intensive industries: cement, oil refineries, iron and steel, gas processing, chemicals, and pulp and paper representing large sources of CO_2 emissions. This scenario is likely to persist as countries put economic development and the raising of living standards ahead of climate change concerns. If the increase in CO_2 emissions is to be prevented, the emitted CO_2 must be stored somewhere other than the

atmosphere. For this purpose, CO_2 carbon capture and storage (CCS) has been proposed as a promising technology to reduce CO_2 emissions produced by the combustion of fossil fuels (IPCC, 2005).

1.2 *Carbon capture and storage overview*

The concept of carbon capture and storage involves the capture of CO_2 produced from fossil fuel combustion and the subsequent storage of the captured CO_2 somewhere other than the atmosphere. The captured CO_2 would be injected into a suitable deep geological formation having the following characteristics (Bachu, 2008):

- Capacity or sufficient pore space to accept the intended volume of CO_2.
- Sufficient permeability to take in CO_2 at the rate that is supplied by the CO_2 emmiter(s).
- Overlain by very low permeability formations to prevent the migration and leakage of the injected buoyant CO_2 from the storage formation to shallow potable groundwater or the surface.

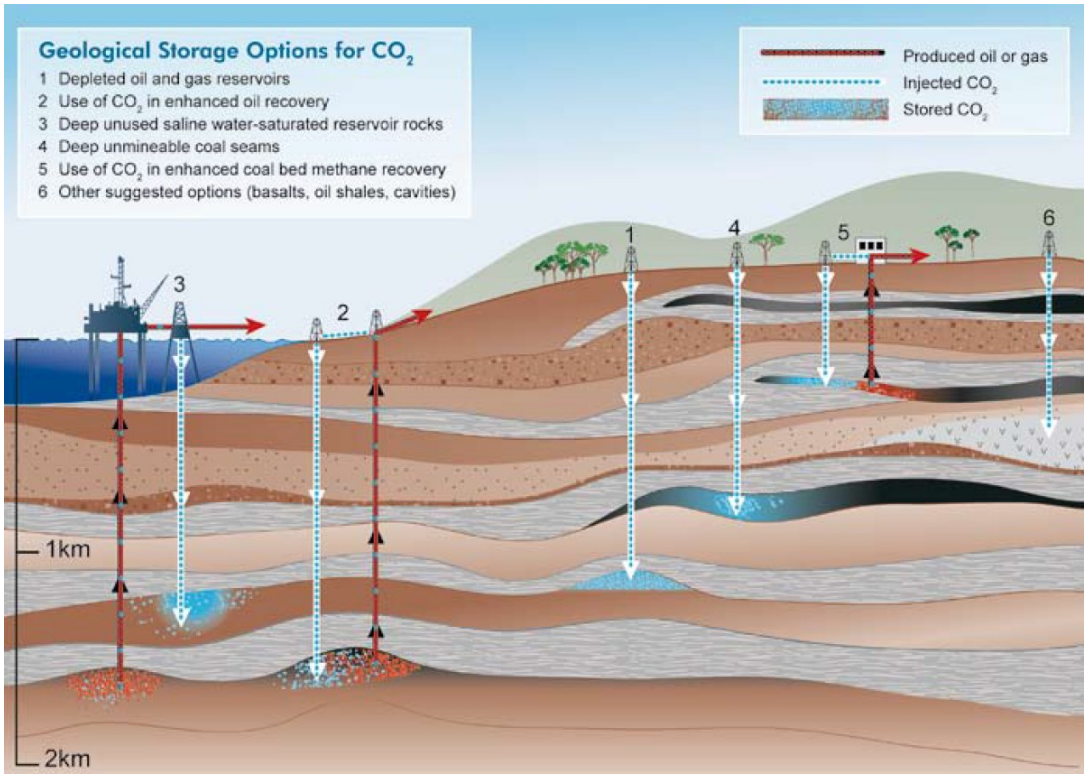


Figure 1.1: The different kinds of geological formations suitable for CO_2 storage (IPCC, 2005).

These characteristics can be found in deep sedimentary formations: depleted oil and gas reservoirs, saline aquifers and deep unmineable coal seams (Bachu, 2008; Benson and Cole, 2008; Bickle, 2009). Figure 1.1 shows the different kinds of geological formations suitable for geological storage of CO_2.

1.2.1 Unmineable coal seams

Unmineable coal seams contain some porosity in the form of fractures and micropores, usually filled with methane created during the heating of the organic matter that constitutes the coal. CO_2 has a greater affinity for coal than methane. The injection of CO_2 would result in the adsorption of CO_2 and the production of methane. An example of successful CO_2 injection into coal seams is the Allison and Tiffany projects in the San Juan Basin, USA (Reeves 2001; Reeves *et al.*, 2003). Although the production of methane offers an economic incentive for CO_2 storage, the storage volumes available in coal seams are not large enough to play a significant role on a global scale.

1.2.2 Depleted hydrocarbon fields

Depleted hydrocarbon fields are prime candidates for CO_2 storage sites. It is a common reservoir engineering practice to inject fluids into the reservoir as hydrocarbons are produced. This is usually done to maintain the reservoir pore pressure, prevent surface subsidence or increase hydrocarbon production. The injected fluids include brine and CO_2. As a result the oil and gas industry already has the expertise and technology needed for CO_2 storage in depleted hydrocarbon reservoirs. CO_2 has been injected into the subsurface for more than 25 years as part of enhanced oil recovery (EOR) operations. Further advantages of CO_2 storage in such reservoirs is that they have been well characterised and much of the infrastructure needed for CO_2 injection is already in place. An economic benefit is that the increased production of hydrocarbons through CO_2 injection may potentially offset some of the storage costs. However, hydrocarbon fields also present some problems such as potential leakage at abandoned wells. The Weyburn project is an example of CO_2 storage as part of an enhanced oil recovery (EOR) operation

(Verdon *et al.*, 2010b). The In Salah CO_2 storage site (Mathieson *et al.*, 2010) where CO_2 is removed from the producing gas stream and reinjected into the aquifer leg will be discussed at length in this thesis.

1.2.3 Saline aquifers

Injection of CO_2 into saline aquifers represents the largest volumes of storage available. Due to their vast size and common occurrence, the storage capacity of saline aquifers is estimated to be up to 10 times greater than depleted oil and gas fields (IPCC, 2005). However, unlike depleted oil and gas fields, saline aquifers are often poorly characterised. Guaranteeing storage security is more challenging and extensive work is required to characterise the storage complex prior to subsurface CO_2 storage. The best known example of CO_2 storage in a saline aquifer is the Sleipner field in Norway (Chadwick *et al.*, 2010).

1.2.4 Storage mechanisms

CO_2 is injected through an injection well into the storage reservoir. For a depth below 800 m the CO_2 would be within the pressure and the temperature range to be a supercritical fluid. In a supercritical state the CO_2 will exhibit both gas-like and liquid-like properties. It can move through the pore space like a gas but can dissolve materials like a liquid.

CO_2 can be stored in deep sedimentary formations through a variety of physical and chemical trapping mechanisms (Gunter *et al*., 2004; Bachu, 2008; Benson and Cole, 2008). During and immediately after CO_2 injection, physical trapping is the dominant trapping mechanism. At this stage when most of the CO_2 exists as a buoyant separate phase a competent caprock is required to keep the CO_2 within the injection formation. This is referred to as structural or stratigraphic trapping. Progressively, CO_2 becomes trapped as residual saturation and larger amounts of CO_2 dissolve into the brine. The latter is referred to as solubility trapping. At longer time scales, geochemical reactions with the rock matrix results in mineral trapping.

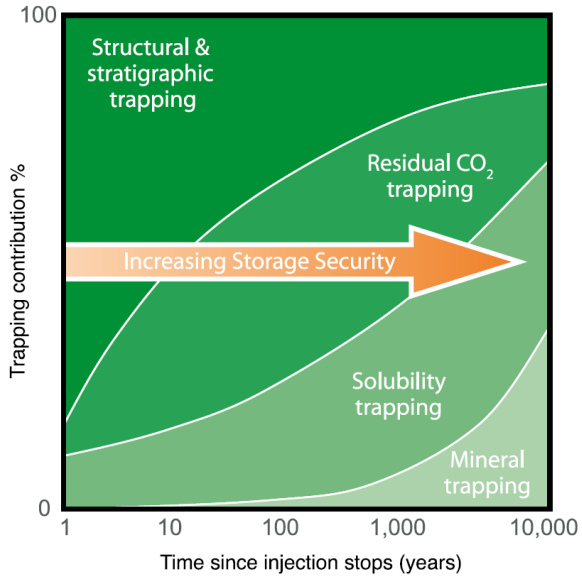


Figure 1.2: Schematic of the evolution of CO_2 trapping mechanisms over time (IPCC, 2005).

Storage security will increase with time after the end of injection. CO_2 changes from a fluid driven upward by buoyancy to a fluid that is trapped as residual saturation or dissolved into the brine. When CO_2 dissolves into brine, the density of the brine increases and is therefore pulled downward by gravity. Furthermore, mineral trapping would produce a very stable form of trapped CO_2. Figure 1.2 shows the evolution of the dominant CO_2 trapping mechanisms over time. Efficient CO_2 injection design may also lead to higher storage efficiency. Qi *et al.* (2009), for example, have proposed an injection strategy where CO_2 and brine are injected together followed by brine injection alone rendering most of the CO_2 immobile.

1.3 *CO_2 storage site performance assessment*

Geological storage of CO_2 in saline aquifers from large stationary sources (e.g. coal-fired power plants) would generate large plumes in the subsurface, with linear dimensions in the order of 10 km or more. One of the key requirements in storage site selection is the ability and integrity of the storage complex to contain the CO_2. However, the selected storage formation and the caprock may be heterogeneous and discontinuous, and is likely to contain imperfections, such as fracture zones and/or faults, that could provide permeable conduits for CO_2 migration out of the prime storage formation. Furthermore, increases in reservoir pressure in response to CO_2 injection would induce mechanical stresses and deformation in and around the

injection reservoir. Moreover, there is also a potential to induce seismicity on nearby faults. If reservoir pressure increase becomes too large, the induced stresses may cause irreversible mechanical changes, creating new fractures or reactivating pre-existing ones. Such changes could open new flow paths from the reservoir into the lower caprock formation(s), and therefore compromise the storage integrity of the reservoir.

In order for CO_2 storage to have a significant impact in reducing anthropogenic CO_2 emissions, the CO_2 must be safely stored over considerable timescales (10^4-10^5 years). Major CCS pilot projects and ongoing commercial projects to date, including In Salah in Algeria, Sleipner and Snøhvit in Norway, Weyburn in Canada, Ketzin in Germany and Otway in Australia have demonstrated that geological storage of CO_2 in deep sedimentary formations is technologically feasible (Michael *et al.*, 2010). However, if CCS is to be implemented on full scale power plants (such as the Saskpower Boundary Dam project in Canada (Stephenne, 2013)) with the aim of emission reduction of atmospheric CO_2 more than a billion metric tons must be stored annually (Benson and Cole, 2008). At this scale a major challenge is in our understanding of the whole system behaviour and the development of models that predict, with confidence, the evolution of the CO_2 storage system. The experience and knowledge gained from large scale industrial CO_2 storage projects have shown that fluid behaviour and the geomechanical response of the CO_2 storage formation and surrounding structures are some of the critical parameters that will determine the overall system performance. In this respect, the key issues in CO_2 storage system performance are: the structural response of fractures and faults in the reservoir, the seal and the geosphere, extending to the surface.

Geomechancial models are routinely used in industries like mining to predict stress changes in the subsurface. A key development has been the coupling of fluid flow effects within a reservoir with geomechanical models. The use of coupled flow-geomechanical models in the hydrocarbon industry is relatively recent and has been applied to show how pore pressure reduction may result in reservoir compaction and surface subsidence. Coupled flow-geomechanical models can compute the effects of CO_2 injection induced pressure changes on deformation. In a two-way coupling approach the effects of deformation on fluid flow via porosity and permeability can also be estimated.

Prior to CO_2 injection, simulation studies will be conducted to predict CO_2 behaviour. Knowledge of the behaviour of the injected CO_2 is necessary to verify containment. The CO_2 behaviour can then be confirmed by monitoring methods. In order to benchmark coupled flow-geomechanical models, monitoring methods must be employed to validate the models. A range of monitoring techniques has been proposed for use at CO_2 storage sites depending on cost, monitoring requirements and site location. Among the variety of technologies available to monitor the geomechanical changes associated with CO_2 injection are InSAR monitoring, tilt-metres, bottom hole pressure monitoring, controlled-source seismic monitoring and micro-seismic monitoring. Figure 1.3 shows some of the potential options for monitoring geomechanical changes at CO_2 storage sites.

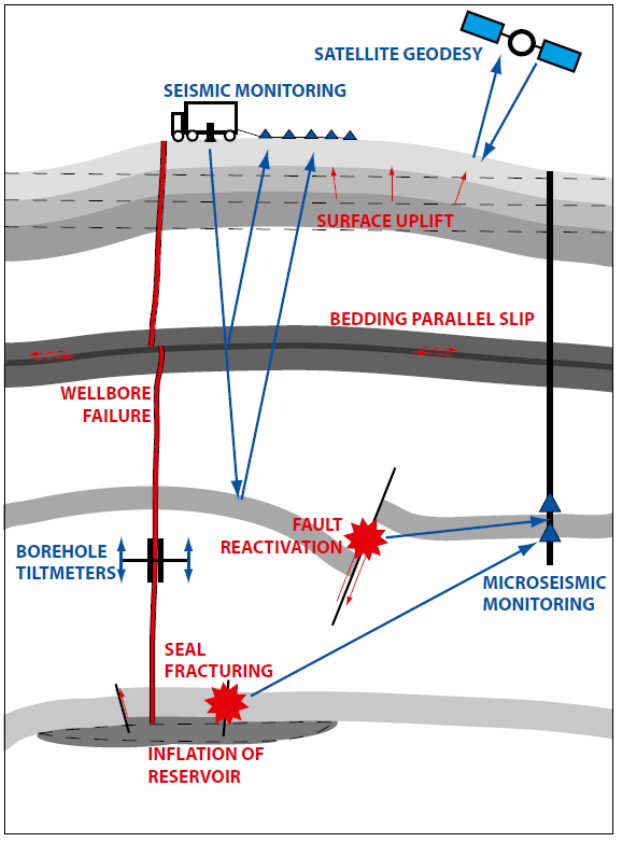


Figure 1.3: Potential geomechanical deformation monitoring options for CO_2 storage sites. (Adapted from Verdon *et al.*, 2013).

InSAR has proven to be a cost-effective method for monitoring surface deformation at some CO_2 storage sites. At the In Salah CO_2 storage site, surface uplift has been detected at all three CO_2 injection wells using InSAR data. Together with seismic

data and injection pressure data, the InSAR data has been used to gain valuable insight into the CO_2 storage site performance.

1.4 *Research objectives*

Given our current modelling and monitoring capabilities, a fundamental scientific question concerning CO_2 storage can then be asked:

> *Can model predictions be linked to field observations to ensure that the modelled behaviour matches the actual behaviour?*

The consideration of this fundamental research question forms the focus of this thesis.

Attempts to date use forward coupled flow-geomechanical modelling to replicate field observations without using the field observations themselves to infer the model properties during CO_2 injection. The model properties are subject to large uncertainties whereas field observations can be measured relatively precisely. There is significant opportunity for developing methodologies for improvement in the integration between coupled flow-geomechanical models and observables such as flowing bottom hole pressure and surface deformation. The E.U. CO_2 Storage Directive (2009) requires that "the conformity of the actual behaviour of the CO_2 with the modelled behaviour" is demonstrated before a storage site can be decomissioned. It is therefore crucial that the methodologies be tested on real CO_2 storage sites. Developing an integrated methodology for CO_2 storage site performance assessment and validating it on a field site has been the concern of the present study.

Although some progress has been made in the analysis and interpretation of satellite monitored surface deformation and injection well pressure data towards the understanding of the behaviour of CO_2 storage formations subjected to injection pressure, the major limitation of the existing methodologies is that they deal with restricted compartments of the system, model the processes that operate at different scales in a decoupled manner, and suffer from lack of integration between monitored data and detailed reservoir characterisation and coupled flow-geomechanical modelling. For example, Rutqvist *et al.* (2010) and Rinaldi and Rutqvist (2013) have simply tried to replicate surface deformation values in their coupled flow-

geomechanical model rather than using the monitored InSAR data to constrain their subsurface simulation models and infer the dynamic properties of the reservoir parameters during injection. Ramirez and Foxall (2014) carried out inversions of InSAR data using a homogeneous model to assess pressure perturbations but do not make use of the available numerical geomechanical models than include subsurface variations in geomechanical and flow properties.

The main objective of this PhD research is:

- to develop an integrated CO_2 storage site performance assessment methodology which incorporates satellite (InSAR) monitoring data, flowing bottom hole pressure, time-lapse seismic monitoring data, inverse modelling and coupled reservoir flow and geomechanical simulations, and
- to validate the developed methodology by applying it to a real CO_2 storage site.

1.5 *Research methodology and the thesis outline*

The basic method to model the evolution of a CO_2 storage complex is with a coupled flow-geomechanical model. The models are used to make predictions and manage and optimise well pressures to ensure that the CO_2 remains in the main storage formation. Observations available at a CO_2 storage site are crucial as they allow the models to be calibrated.

An inverse approach may be taken to derive model parameters from available observations. A forward approach consists in defining the parameters from prior knowledge for a simulation and comparing the model predictions with the available observations. An integrated approach would couple forward and inverse modelling and update the model parameters every time an observation is available.

In summary, the sequence of tasks in the methodology development is:

Inverse Approach: Use deformation observations to map reservoir pressure change by inverting the data using a numerical geomechanical model that permits variations in geomechanical properties.

Forward Approach: Coupled flow-geomechanical modelling using insight from bottom hole pressure, InSAR data and time-lapse seismic to improve the understanding of the flow and pressure behaviour during CO_2 injection.

Integrated Approach: Define an initial set of coupled flow-geomechanical models that capture the uncertainty in the model parameters. Run forward simulations and compare model predictions with observations. An update of the model parameters is made based on the difference between predicted values and observed values using the ensemble Kalman filter (EnKF).

The developed methodology is tested on the In Salah CO_2 storage site.

The remainder of this thesis consists of seven chapters.

Chapter 2 presents an overview of the geomechanics relevant to geological storage of CO_2 and a review of current modelling tools and monitoring methods. A review of the geomechanical behaviour of several megatonne CO_2 storage deployments to date is also included.

Chapter 3 reviews the theory and describes the methodology that will be employed for the coupled flow-geomechanical performance monitoring of CO_2 storage sites. Three workflows are presented: (1) A coupling scheme for flow and geomechanical modelling. (2) An inversion scheme for reservoir pressure change inversion. (3) The EnKF adaptation to coupled flow-geomechanical modelling.

Chapter 4 introduces the In Salah CO_2 storage site, the data sources available and summarises previous work.

Chapter 5 presents the application of a reservoir pressure change inversion scheme using InSAR surface deformation data from the In Salah CO_2 storage site.

Chapter 6 presents the application of forward coupled flow-geomechanical modelling using insight from InSAR, bottom hole pressure and time-lapse seismic to simulate CO_2 injection at the In Salah site.

Chapter 7 builds on previous chapters and presents the application of the integrated approach using the EnKF to estimate the parameters controlling the performance of a CO_2 storage site through the joint assimilation of surface deformation and bottom hole pressure observations. The In Salah case study data set is used to validate the methodology.

Chapter 8 presents the conclusions of this thesis. In addition, recommendations are made for further development of the methodology presented in this thesis.

Chapter 2 Background and Literature Review

This chapter presents a general review of the geomechanics associated with geological CO_2 storage in deep sedimentary formations. The role of geomechanics has become more widely recognised given its impact on the long-term integrity of a CO_2 storage complex. The geomechanical aspects of geological CO_2 storage, including reservoir stress-strain, well integrity, microseismicity, fault reactivation and caprock sealing performance are reviewed. The joint use of flow-geomechanical modelling tools and monitoring of geomechanical observables at CO_2 storage field deployments, which have been used to detect subsurface geomechanical changes, is described..

The chapter also provides a brief review of the geomechanical response of several industrial scale CO_2 storage field deployments with specific reference to the monitoring methods implemented at these sites.. Lessons learned from these CO_2 storage field deployments are particularly important for the verification of CO_2 storage site performance. The importance of ground truthing CO_2 storage models with field observations is emphasised and the methodology to be developed within this research for the performance assessment of CO_2 storage sites presented.

2.1 *Principles of Geomechanics*

2.1.1 Stress in the earth's crust

Compressive stresses are encountered everywhere at depth in the earth. The stress magnitudes inside the earth are a function of depth, pore pressure and active geological processes. The state of stress can be fully described using the three principal stress magnitudes σ_1, σ_2 and σ_3 and their relative orientations. σ_1, σ_2 and σ_3 are the principal, intermediate and minimum principal stresses, respectively.

A major source of stress is the weight of the overlying rocks at a given depth. One principal stress is generally normal to the earth's surface and the other two principal stresses act in an approximately horizontal plane. This is generally true in the upper crust range where CO_2 storage operations will take place (Zoback, 1992). Assuming this is the case, the principle stress magnitudes are σ_V, the vertical stress; σ_{Hmax}, the maximum horizontal stress; and σ_{hmin}, the minimum horizontal stress. The magnitude of σ_V is equivalent to the integration of rock densities ρ from the surface to the depth of interest, z:

$$\boldsymbol{\sigma_V = \int_0^z \rho(z) g dz} \tag{2.1}$$

where g is the gravitational force (Zoback, 2010). The Poisson effect states that as the overburden rocks vertically compress the underlying rock body, it has a tendency to strain laterally. Since the rock body is horizontally constrained this results in horizontal stress components. Under unpressurised uniaxial strain conditions the horizontal stress components can be expressed as

$$\boldsymbol{\sigma_{Hmax} = \sigma_{hmin} = \rho g z \frac{\nu}{(1-\nu)}} \tag{2.2}$$

where ν is Poisson's ratio, the ratio between transverse and longitudinal strain. Stresses may also arise from geological processes that act at a variety of different spatial and temporal scales such as current plate tectonic activity, uplift, erosion or residual stresses from past tectonic events. Variations in rock stiffness may lead to changes in the horizontal stresses. Thermal changes may lead to the contraction or expansion of a rock body. If the rock body is constrained this will also lead to stress changes. The stress state at a given point is the result of the superposition of the

variety of forces at play resulting in significant stress heterogeneity and stress anisotropy inside the earth (Amadei and Stephansson, 1997).

In addition to the largely compressive stresses acting on a rock, there is a pressure due to the fluids within the pore space of the rock. The pore pressure acts isotropically within the pore space and can be seen to act as a tensile stress. The concept of effective stress (Terzaghi, 1923) can therefore be defined as the principal stress minus the pore pressure where α is the effective stress coefficient.

$$\boldsymbol{\sigma_1' = \sigma_1 - \alpha P, \quad \sigma_2' = \sigma_2 - \alpha P, \quad \sigma_3' = \sigma_3 - \alpha P} \tag{2.3}$$

In this formulation, the principle stresses are reckoned positive if compressive. The value of the pore pressure at depth is usually described in relation to hydrostatic pressure. Hydrostatic pressure is the pressure associated with a column of water from the surface to the depth of interest. The hydrostatic pore pressure can be estimated with equation 2.4:

$$\boldsymbol{P_{\text{hydro}} \equiv \int_0^z \rho_w(z) g dz \approx \rho_w g z} \tag{2.4}$$

where ρ_w is the water density. In sedimentary basins, abnormal pore pressures are encountered that are greater or less than the hydrostatic pressure at depth due to a variety of natural mechanisms (Swarbrick and Osborne, 1998). The upper limit for the pore pressure is the overburden stress σ_{v}.

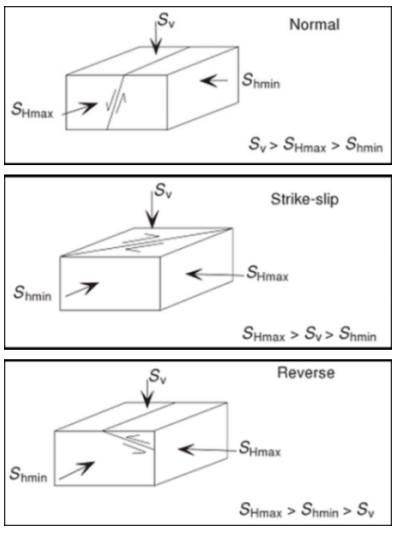


Figure 2.1: Anderson's (1951) classification scheme for relative stress magnitudes in normal, strike-slip and reverse fault regions.

Anderson (1951) developed a classification scheme for the relative macroscopic stress magnitudes inside the earth based on the style of faulting that they would produce. In a normal stress regime the vertical stress σ_v is the maximum principal stress. In a strike-slip regime σ_v is the intermediate principle stress and in a reverse regime σ_v is the least principle stress. Figure 2.1 illustrates the classification scheme for the relative stress magnitudes and the associated faulting style. The principal stresses however are not always vertical and horizontal. The principal stresses can be rotated nearby faults, highly fractured zones, structural pinchouts and complex topography. Sedimentary basins around the world which have the highest potential for CO_2 storage are found in normal, strike-slip and reverse faulting environments.

2.1.2 Measuring *in situ* stress

The *in situ* macroscopic stress field has been shown to be coherent at a regional level. Compilations of stress measurements have been made over the years in many areas of the world using a variety of techniques which can constrain both the magnitude and the orientation of the principle stresses inside the earth (Zoback, 2010). Figure 2.2 shows a compilation of stress indicators from different sources showing the coherent nature of the macroscopic stress field.

It is usually the case that the overburden is a principal stress. The magnitude of σ_V can be estimated from the integration of density logs using equation 2.1.

Wellbore breakouts are an effective technique for determining stress orientations from wells as they are normally encountered in oil and gas wells drilled around the world. Wellbore breakouts can occur as a result of either compressive or tensile stress concentrations around the wellbore. The minimum principal stress can be estimated from mini-fracs and leak-off tests (LOT) (Bell, 2003). In the case of a vertically drilled well where σ_V is a principal stress, borehole breakouts form at the azimuth of the minimal horizontal compressive stress (Zoback *et al.*, 1985). Breakouts occur when the strength of the rock is exceeded by the hoop stress around the borehole causing that portion to fail in compression. Image logs are able to detect these fractures from which the horizontal stress directions can be inferred. The assessment of different types of compressive and tensile borehole failure modes using logging-while-drilling tools are described by Rezmer-Cooper *et al*. (2006).

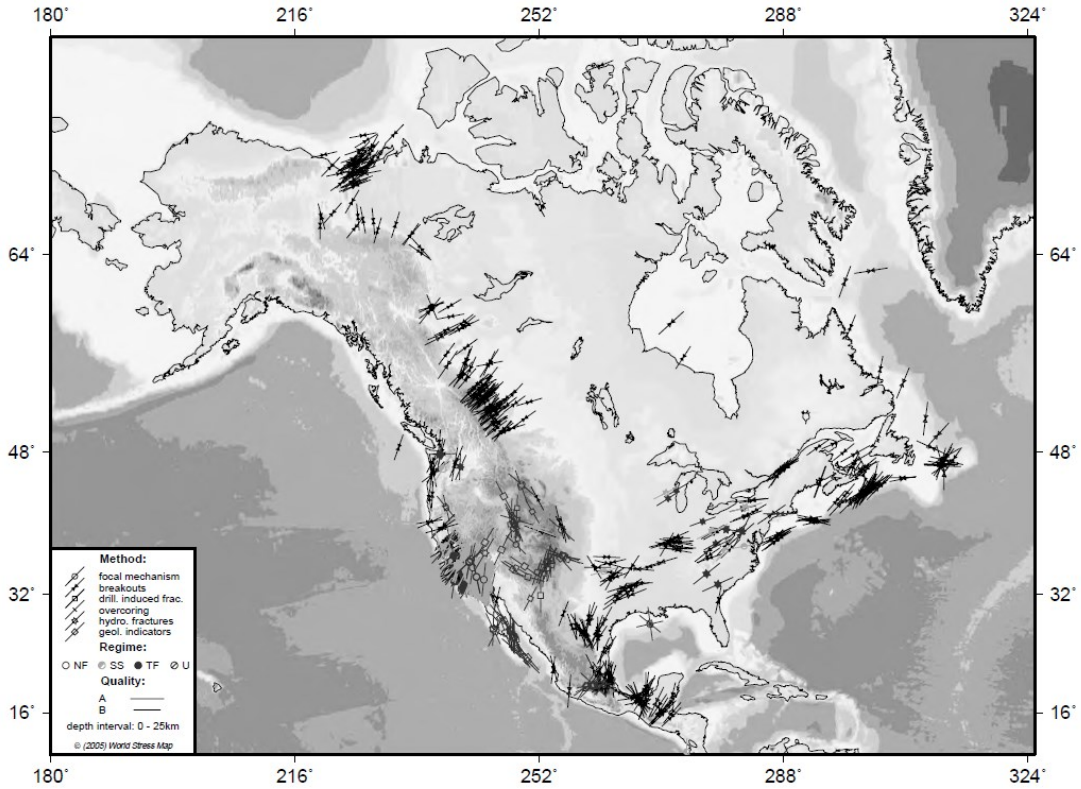


Figure 2.2: Directions of maximum horizontal stress from a compilation of stress sources taken in North America from the world stress map data base (http://world-stress-map.org).

Another form of wellbore failure that can be used to understand the state of stress is drilling induced tensile fractures (Moos and Zoback, 1990). Tensile failures around the wellbore form at the azimuth of the greatest horizontal compressive stress.

Overcoring is a borehole relief method that isolates a rock sample from the stress field in the rock mass and monitors its re-equilibrium deformation response. Overcoring requires knowledge of the rocks Young's modulus and Poisson's ratio to estimate the state of stress (Reinecker *et al.*, 2008).

Earthquake focal mechanisms are also routinely used to extract information about the large scale stress field (Barth *et al.*, 2008). The normal, strike-slip and reverse faulting stress regimes described previously each have a specific pattern of seismic radiation resulting from slip on a fault. The style of faulting in turn defines the relative magnitudes of σ_{v}, σ_{Hmax} and σ_{hmin}.

Geological features can also be used as an indicator of *in situ* stress such as fault slip data and the orientation of igneous dikes (Nakamura, 1977). Pore pressure can be

measured directly or estimated from seismic data or geophysical logs (Huffman and Bowers, 2002). There are clearly a number of practical methods that allow the assessment of the *in-situ* stress field.

2.1.3 Local stress fields

In the previous section, the macroscopic stress field was defined using the principal stresses. It is important to consider the local stress field. If rocks were homogeneous then the macroscopic and local stress fields would be identical. Rocks however are heterogenous and contain flaws leading to perturbations in the local stress field. Sedimentary rock layers for example are formed under many different types of depositional environments at different geological times resulting in a wide range of rock properties. Joints are by far the most common type of geological structure. They are defined as fractures or cracks inside the rock along which there has been little or no transverse displacement. Consider the microcrack shown in Figure 2.3.

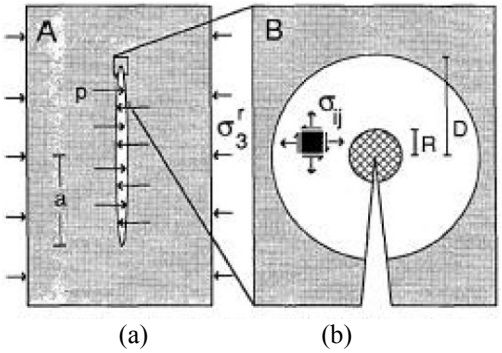


Figure 2.3: (a) A micro-crack under a remote compressive stress , σ_3 (b) The tip region of the micro-crack where stress concentration is greatest (Modified from Pollard and Atilla,1988).

The propagation of a joint is controlled by the stress field near the joint tip. The local stress field is heterogeneous with a small region of high stress concentration at the tip which decreases as one over the square root of the distance from the tip. Criteria for joint propagation have been described using three stress intensity factors (K_I, K_{II}, K_{III}) to describe the different fracturing modes (I, II and III) (Pollard and Atilla, 1988).

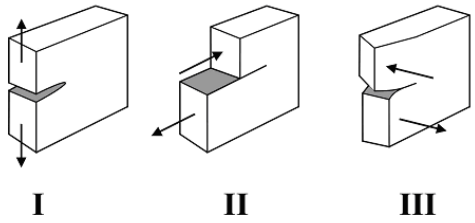


Figure 2.4: The three modes of fractures: mode I is an extensional opening fracture, mode II is a sliding fracture and mode III is a shearing fracture.

The stress intensity factor is a function of the pressure inside the fracture, the fracture geometry and the macroscopic stress. This formulation breaks down in the core region near the tip where inelastic deformation occurs. Figure 2.4 displays the different modes of displacement. Mode I involves displacement perpendicular to the crack surface. Mode II and Mode III are shearing displacements parallel to the crack surface.

2.1.4 Rock Deformation

Rock deformation is governed by constitutive laws. A constituve law describes the deformation of a rock in response to stress. A linearly elastic material for example is one in which stress and strain are linearly related. The compression of the rock matrix may initially display elastic behaviour. When the applied stress is removed the rock returns to its original state. Young's modulus E and Poisson's ratio ν are the most commonly used elastic properties in geomechanics to describe linear elastic behaviour. Young's modulus E is the ratio of applied axial stress and resulting axial strain in a uniaxial compression test.

$$\boldsymbol{E = \frac{\sigma_z}{\varepsilon_z}} \tag{2.5}$$

Poisson's ratio is defined as the ratio between vertical strain and the radial strain during the same test.

$$\boldsymbol{\nu = -\frac{\varepsilon_x}{\varepsilon_z}} \tag{2.6}$$

Other moduli such as Lame's first parameter λ, the shear modulus G, the bulk modulus K and its inverse compressibility $1/K$ are also in use. Knowledge of any two of the moduli allows the computation of the others (Jaeger *et al.*, 2007).

Past a critical stress at which a rock is said to yield, stress changes will cause permanent strain to the rock matrix. Past this critical stress the rock may display plastic behaviour or violently fail. The manner in which a rock deforms will depend on the confining stress. At a larger confining stress, the yield stress of the rock increases. Figure 2.5 displays a diagram illustrating the transition from brittle to ductile behaviour in a rock specimen as the confining stress increases. In the context of geological CO_2 storage it is rocks in the upper crust that are of interest. At this depth range, relatively low temperatures and low confining stresses are encountered so rocks are expected to behave in a brittle manner. The plastic regime is relatively small and the rock will be in the elastic regime before abrupt failure.

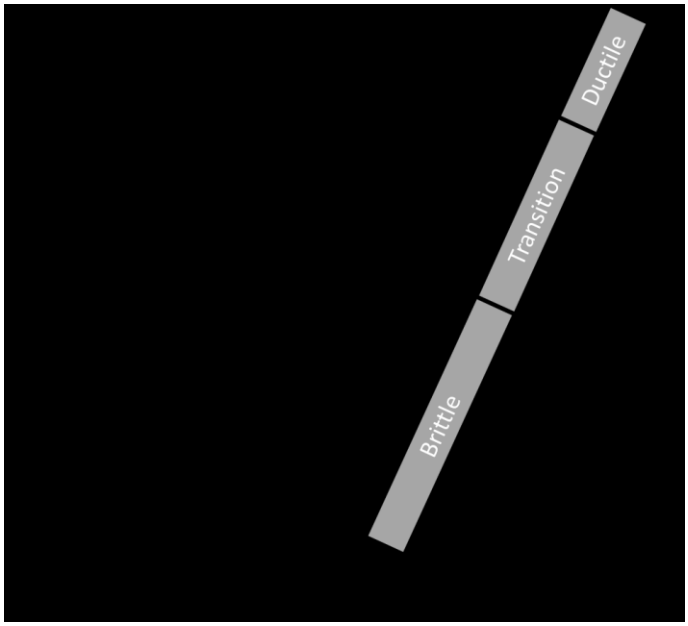


Figure 2.5: A plot of axial strain vs. axial stress for different confining stress. The failure stress is shown for failure mode changes from brittle failure to ductile failure.

2.1.5 Strength properties of rocks

The failure of a rock is a complex process that involves microscopic cracks and frictional sliding on grain boundaries eventually forming macroscopic discontinuities in the rock.The basic ideas behind rock strength and failure are intuitive to understand. Rock failure occurs when the stresses acting on the rock mass exceed its

strength. In this section, two basic types of failure are described: tensile and shear failure.

2.1.6 Shear Failure

The strength of a rock will depend on how it is confined. As the level of confining stress increases, the failure mode changes from brittle failure to ductile failure. For a brittle rock, failure results in the abrupt loss of its strength when a shear fault forms. In more ductile materials failure is characterised by a more gradual weakening of the rock resulting in inelastic deformation at lower stresses.

The Mohr-Coulomb failure criterion is commonly used to determine whether the rock at a given stress state at depth will be in a state of elastic deformation or close to shear failure. The Mohr-Coulomb failure criterion can be written as:

$$|\boldsymbol{\tau}| = \boldsymbol{S_0} + \boldsymbol{\mu\sigma'} \tag{2.7}$$

In this form, the Mohr-Coulomb failure criteria describes the shear stress τ acting parallel to the plane at which failure occurs. The shear stress must overcome the sum of the inherent shear strength of the rock S_0 and the product of the coefficient of internal friction μ with the normal stress σ' acting perpendicular to the failure plane.

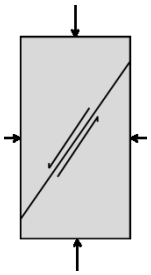


Figure 2.6: Shear failure mechanism under compressive stress.

2.1.7 Tensile Failure

When injecting fluids into rocks, the pore pressure will increase and the effective compressive stress will decrease. A sufficient rise in pore pressure can cause the minimum effective stress to go into tension. This condition is referred to as tensile failure. In this failure mode, fractures develop with its normal parallel to the tensile stress. For intact rock, the stress at which tensile failure occurs is referred to as the

tensile strength T_0 of the rock. If a rock sample contains a fluid at pressure P and is compressed externally, then the condition at which tensile strength will occur can be written as

$$\boldsymbol{P - \sigma_3 \geq T_0} \tag{2.8}$$

Pre-existing fractures can also go into tensile failure. Tensile failure will occur if the pressure inside the fracture exceeds the prevailing minimum horizontal stress.

$$\boldsymbol{P > \sigma_3} \tag{2.9}$$

Tensile failure that occurs when the fluid pressure exceeds the local least principal stress is referred to as hydraulic fracturing.

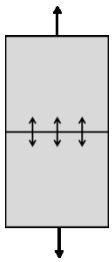


Figure 2.7: Tensile failure of a rock under tensile stress.

Equation 2.8 represents the general criterion for tensile splitting of the material and equation 2.9 respresents the criterion for the re-opening of pre-existing fractures.

2.2 *Faults, fractures and fluid flow*

Faults and fractures are ubiquitous inside the earth. They are found in essentially all rocks at depth and can have a profound impact on fluid transport (Nelson, 2001). In Section 2.3.1 the relationship between fluid flow and an idealised planar fracture is presented. The different stages in fracture growth are discussed in Section 2.3.2 and Section 2.3.3 describes how it is critically stressed faults and fractures that tend to contribute to fluid flow.

2.2.1 Fluid flow through a planar fracture

A parallel plate approximation for fluid flow through a planar facture is given by the following equation:

$$\boldsymbol{Q = \frac{b^3}{12\eta}\nabla P} \tag{2.10}$$

where Q is the volumetric flow rate, ∇P is the pressure gradient, η is the fluid viscosity and b is the separation between plates. The interplay between the fracture properties, stress and fluid pressure can be better understood for an elliptical crack of length L and elliptical cross section. The maximum value of the fracture aperture at its midpoint is given by

$$\boldsymbol{b_{\max} = \frac{2(P_f - \sigma_3)L(1-\nu^2)}{E}} \tag{2.11}$$

where P_f is the fluid pressure in the fracture, ν is Poisson's ratio and E isYoung's Modulus. The flow rate is then given by

$$\boldsymbol{Q = \frac{\pi}{8\eta}\left(\frac{b_{\max}}{2}\right)^3 \nabla P} \tag{2.12}$$

which can be expressed as

$$\boldsymbol{Q = \frac{\pi}{8\eta}\left[\frac{L(1-\nu^2)(P_f - \sigma_3)}{E}\right]^3 \nabla P} \tag{2.13}$$

The flow rate through a fracture in response to a pressure gradient is proportional to the cube of the difference between the fluid pressure inside the fracture and the least principal stress normal to it. This is an example of Mode I failure where the displacements are perpendicular to the fracture plane. When the fluid pressure acting to open the fracture exceeds the least principal stress acting to close it, the fracture would be expected to propagate, after which the fracture is expected to close and the pressure to drop. Fractures in nature however do not have a perfectly smooth surface. A finite aperture would remain even after the fracture is closed.

2.2.2 Fracture growth

The pressure required to extend the fracture can be divided into three parts (Fjaer *et al.*, 2008):

- Pressure required to keep the fracture open towards the minimum stress.
- Pressure required to flow fluid through the fracture.
- Pressure required to overcome the resistance of the fracture tip and create new fracture volume.

Fracture orientation, growth and confinement are well understood for theoretical cases while drilling (Hossain *et al.*, 2000). In practice however the resulting fracture patterns can be very difficult to predict. Induced fractures can interact with existing fractures and contrasts in *in situ* stresses.

2.2.3 Critically stressed faults/fractures

Faults which are planar discontinuities with an appreciable amount of shear deformation can also enchance flow. They have experienced Modes II and III of failure with displacements acting to shear the fault wall. In well cemented rocks shearing will cause breciation along the fault surface and also damage the adjacent rocks to the bed-plane. The resulting fragmentation and grain breakage allows the faults to maintain its permeability.

Fractures and faults of variable orientations may have been created over the deformational episodes throughout the geological history of a rock formation. Studies suggest that many of these faults and fractures may be inactive in the present stress regime and it is rather a subset of these that are most likely to contribute to reservoir permeability (Bond *et al.*, 2013). It has been observed from field examples (Dholakia *et al.*, 1998) that faults and fractures that are favourably oriented for slip under the current *in situ* stress regime have a tendency to provide permeable conduits for fluid flow (Barton et al., 1995; Wiprut and Zoback, 2002). These are commonly referred to as critically stressed faults or fractures. While these observations are valid close to surface, at larger depths this rule of thumb does not always hold as the fractures are more likely to be closed and unstable fractures may lead to permeability loss.

2.3 *The Geomechanics of CO_2 storage in deep sedimentary formations*

2.3.1 Key geomechanical processes

The key geomechanical processes and technical issues associated with geological CO_2 storage are presented in Figure 2.8. Injection of CO_2 into the reservoir formation is achieved by raising the pressure of the CO_2 in the wellbore to a value above the entry pressure of the formation material. The injection well may penetrate the reservoir formation vertically or horizontally. The top figure illustrates how the CO_2 plume is surpassed in extent by the area of actual pressure changes. If the reservoir formation contains open fractures, then the pressure inside these fractures will also increase. The pressure increase during CO_2 injection is fundamentally due to an increase in the total fluid content in a confined space. A significant factor controlling the build up of pressure is the permeability of the storage formation. The rate at which the pressure increase is transmitted is strongly dependent on the permeability. If the permeability is high the pressure change would transmit relatively quickly throughout the storage formation as the injected CO_2 can easily flow away from the injection well. However, at low permeabilities, pressure would build up around the injection well. The CO_2 can no longer flow away with the same ease.

A temperature difference would also arise between the cold CO_2 and the storage formation. The strong temperature dependence of CO_2 density may affect the pressure profile at the injection well (Pruess, 2005). Pressure changes are wide spread with significant changes propagating several km away from the injection well. Temperature changes, on the other hand, are limited in extent to the immediate surroundings of the injection well.

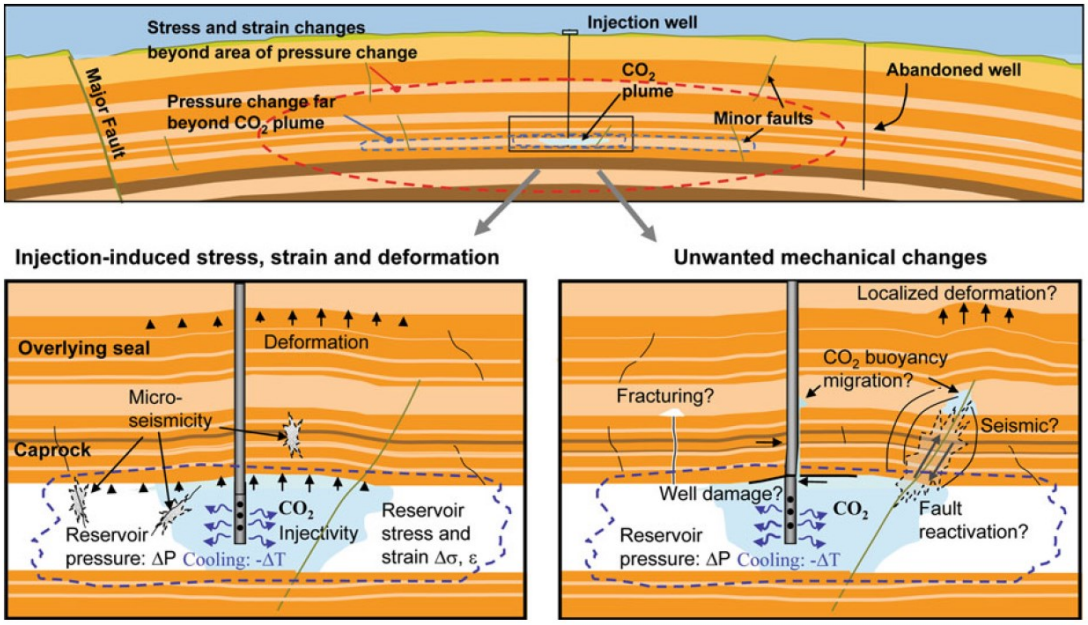


Figure 2.8: Geomechanical processes and key technical issues associated with geological CO_2 storage. Adapted from Rutqvist (2012).

The compressibility of the rock, pore fluid and CO_2 are an additional constraint to the build up of pressure. If the compressibilities are significant then a rise in pressure would lead to an increase in the volume available for the injected CO_2 to flow into and would therefore reduce the pressure increase.

The overall pressure change of a CO_2 storage complex is dependent on the following:

- Injection rate/volume
- Permeability
- Storage volume
- Compressibility (CO_2, storage reservoir fluid and storage reservoir rock)

Changes in reservoir pressure and temperature will result in stress and strain changes in and around the injection zone. In this sense, pressure and temperature are analogous. This in turn may induce several types of geomechanical responses such as detectable ground surface deformation and micro-seismic events. Moreover, the injection-induced fluid pressure could potentially result in noticeable changes in injectivity and permeability. There are also concerns that the overpressure needed to inject CO_2 into saline aquifers my displace brine either vertically or laterally, posing a threat to shallower groundwater aquifers.

If the reservoir pressure becomes sufficiently high, the induced stresses may cause irreversible mechanical changes, creating new fractures or reactivating pre-existing ones. Such changes could open new flow paths from the reservoir into the low-permeability caprock formations, and therefore compromise the integrity of the CO_2 storage complex. Furthermore, the reactivation of a fault could potentially result in a noticeable (felt) seismic event that could impact the integrity of the CO_2 storage complex and the overall public perception of carbon capture and storage.

For a CO_2 storage project to be approved, a risk assessment will be required to show that the CO_2 will remain safely stored underground within acceptable limits. CO_2 leakage is undesirable as it would negate the benefit of storing CO_2. Moreover, it is potentially detrimental to drinking water supplies, marine life, plant life, human health etc. Considering the aforementioned geomechanical issues associated with geological CO_2 storage, geomechanics will play a key role in determining the suitability of the injection-site. CO_2 leakage risk assessment however is not limited to geomechanical processes but also includes, for example, the risk of CO_2 leakage via leaky wells and faults to shallow potable-ground water aquifers.

2.3.2 Reservoir inflation and alteration of flow properties

The flow properties of a CO_2 storage reservoir can be influenced by CO_2 injection induced pore pressure increase and reservoir inflation. Laboratory experiments (Armitage *et al.*, 2011) with the In Salah CO_2 storage site rocks have shown the permeability variations across a range of effective pressures. Moreover, enhanced CO_2 paths may be created by the opening of pre-existing fracture networks or the creation of new ones. Accurate fluid-flow and geomechanical simulations are necessary to predict the resulting subsurface CO_2 distribution. Although enhanced permeability due to CO_2 injection at the reservoir level is not a direct leakage risk, it would impact model accuracy (Verdon *et al.*, 2013). For example, a permeability increase can reduce the time it takes for CO_2 to reach a spill point, therefore also reducing the potential amount of CO_2 that can be stored. At the In Salah site, for example, Bissell *et al.* (2011) and Shi *et al.* (2012) have shown that CO_2 flow is influenced by the opening and closing of fractures.

2.3.3 Caprock sealing performance

In the case of CO_2 injection into a depleted oil and gas reservoir, the ability to contain buoyant fluids has been proven. For CO_2 storage into saline aquifers, the overall sealing properties of the overlying caprock may not be well known or may not be well characterised. The selected storage formation may be heterogeneous and discontinuous and is likely to contain imperfections such as fracture zones and/or faults. Experience from industrial underground gas storage into aquifers is analogous to CO_2 storage. The majority of reported instances from gas leaks from such sites have been related to the effectiveness of the caprock seal (Evans, 2009). A caprock capillary entry pressure in excess of any pressure due to the CO_2 injection process would provide an effective capillary seal against the upward migration of CO_2. Laboratory tests investigating the capillary entry pressure for CO_2/brine systems suggests an over-pressure of a few MPa due to CO_2 injection may suffice to break the capillary barrier (Carles *et al.*, 2010). For water-bearing shales and marls typical values capillary entry pressure are around 7 MPa (Warren, 2007). For example, at the Sleipner CO_2 storage site, the thin shale layers within the storage reservoir, previously thought to be impermeable, were found to be permeable at places. It has been noted that overpressure in the overburden provides a very efficient barrier against CO_2 leakage.

Furthermore, the reservoir rock may fracture under CO_2 injection and the created fracture may increase the connectivity of permeable interbeds and propagate to the top seal creating a leakage path for buoyant CO_2 to escape (Orlic, 2009). If the stress changes are sufficient, then shear or tensile geomechanical failure may occur creating new faults/fractures or opening pre-existing closed faults/fractures (Hawkes *et al.*, 2005). At the In Salah storage site, for example, the presence of fractures and faults in the reservoir lead to early CO_2 breakthrough at one of the appraisal wells (now fully decomissioned) (Mathieson *et al.*, 2010).

2.3.4 Injection-induced seismicity

Injection-induced seismic events result from the release of stored energy triggered by the increase in fluid pressure from injection. Seismicity associated with underground injection is a well-documented phenomena (Nicol *et al.*, 2011). The rates and maximum magnitudes of induced earthquakes generally increase with rising

reservoir pressure, total fluid volumes and injection/extraction rates. The expected risks associated with induced seismicity are therefore expected to be higher for commercial megatonne CO_2 storage operations than for kiloton pilot projects due to the magnitude and extent of the pressure disturbance associated with large scale CO_2 operations. A key issue is the triggering of seismic events could impact the public perception of CO_2 storage (Zoback and Gorelick, 2012).

2.3.5 Wellbore failure and casing damage

Abandoned wells from oil and gas exploration and production have been identified as potential leakage paths and are considered one of the greatest risks for large scale CO_2 storage. Geomechanical processes such as changes in reservoir stress and deformation can impact well integrity during CO_2 injection, in particular the hydraulic aperture of rock-cement and well casing-cement interfaces considered to be the most likely pathways for potential CO_2 leakage around abandoned wells (Bachu and Bennion, 2009).

2.4 *Coupled flow-geomechanical models for CO_2 storage*

The existing fluid flow-geomechanical models for analysing the various geomechanical issues associated with CO_2 storage can be broadly categorised into three different groups: simple analytical models, semi-analytical models and numerical models. Simple analytical models have been developed by using basic concepts of uniaxial poro-elasticity (Hawkes *et al.*, 2005). Semi-analytical models implement analytical solutions accompanied by numerical integration procedures to find the stress change distribution throughout the field. These models are usually developed using the assumption of a poro-elastic material behaviour for the reservoir and the surrounding rocks (Segall, 1985). They are also usually constrained by simplified reservoir geometries and fluid-flow assumptions and therefore require a small number of input parameters. Both analytical and semi-analytical flow-geomechanical models have been used for a quick first order analysis of CO_2 injection site suitability (Chiaramonte *et al.*, 2008; Mathias *et al.*, 2009; Soltanzadeh and Hawkes, 2009). The developed models can be used as a guide for site selection and to evaluate the potential for injection induced fault/fracture reactivation and seismic events. Estimates of sustainable fluid pressures that will not induce

fracturing or enhance fault permeability are required. Bjørnarå *et al.* (2014) developed simplified models for the fast evaluation of injectivity and flow-geomechanical coupling in CO_2 storage. These models are generally suitable at the injection site-selection stage when the shortage of data may lead to the use of a less complicated model.

In order to consider more complicated characteristics such as a realistic subsurface geometry, contrasts in material properties and discontinuities such as faults, the use of numerical models is essential. A number of coupled fluid-flow and geomechanical numerical models have been developed in recent years as the main tool to analyse the various geomechanical issues associated with CO_2 storage. Generic synthetic coupled fluid flow-geomechanical numerical studies of CO_2 injection into hypothetical brine aquifers indicated that geomechanics would play a central role should CO_2 storage be developed at a large scale (Rutqvist, 2002; Rutqvist *et al.*, 2008; Streit and Hillis, 2004). These studies concluded that the greatest risk of rock failure would occur in the lower part of the caprock with shear reactivation being the more likely primary failure mode. Rutqvist (2012) has reviewed various examples of coupled fluid flow-geomechanical simulators applied to the study of CO_2 storage. These include ECLIPSE-VISAGE (Ouellet *et al.*, 2011), TOUGH-FLAC (Rutqvist *et al.*, 2011), STARS (Bissell *et al.*, 2011), and DYNAFLOW (Preisig and Prévost, 2011) among others. Although coupled flow-geomechanical numerical modelling is a powerful tool for understanding the dynamics of a CO_2 storage site and investigating particular phenomena (e.g. surface uplift, induced fracturing, fault reactivation), an adequate characterisation of the CO_2 storage complex, site-specific geomechanical properties and *in situ* stress field are necessary to produce accurate models. These models require calibration to *in situ* data before they can be used as a predictive tool. They require a constituve model defining the relation between the stress and strain for a given rock formation. The simplest of these being linear elasticity, where it is assumed that the stress and strain are linearly related and deformation is completely reversible once the applied stresses are removed. Linear poro-elasticity includes the effects of fluid-filled pores on deformation (Rice and Cleary, 1976). More complex constitutive models include non-linear effects, such as post-yield deformation. Examples of geomechanical characterisations for CO_2 storage sites include the Teapot Dome, Wyoming (Chiaramonte, 2008), the Otway

Basin (Vidal-Gilbert *et al.*, 2010) and the Dogger Carbonate, Paris Basin (Vidal-Gilbert *et al.*, 2009). Cappa and Rutqvist (2011) for example model the coupled deformation and permeability evolution due to fault reactivation from underground CO_2 injection. Konstantinovskaya *et al.* (2014) used 2D coupled flow-geomechanical modelling of the St. Lawrence Lowlands basin to evaluate the potential for shear failure along pre-existing normal faults as well as tensile failure in the caprock units. Moreover, geomechanical-geochemical interactions may need to be included to assess the long-term changes in the reservoir and caprock due to CO_2 exposure. The geomechanical impact of progressive rock dissolution due to CO_2 exposure will need to be assessed (Wojtacki *et al.*, 2014). Although modelling the geomechanical processes associated with CO_2 injection will play an important part in assessing the short and long-term performance of the site, it is the active CO_2 injection period that is of greatest interest. A large storage reservoir may experience an initial build up of pressure during the injection period but given enough time the pressure will eventually dissipate and the overall pressure change in the storage formation will be negligible. For a smaller storage reservoir the build up of pressure may remain significant after long time periods.

2.5 *Monitoring geomechanical deformation at CO_2 storage sites*

Historically the monitoring of geomechanical deformation due to injection or production of subsurface fluids has remained something of a niche activity in the hydrocarbon industry. The monitoring technologies available to characterise the injection induced deformation are described in the following sections.

2.5.1 Geodetic methods

Depending on the magnitude of the pore pressure increase due to CO_2 injection, the subsurface structure (surface topography, geometry of subsurface layers and location and orientation of faults) and the distribution of material properties in the reservoir and surrounding sediments, deformation at the reservoir level may be transferred all the way to the surface resulting in detectable surface displacement. Geodetic techniques can be used to measure this displacement and can provide the basis for cost effective long-term reservoir surveillance (Vasco and Ferretti, 2005; Vasco *et al.*, 2000). Satellite-based Interferometric Synthetic Aperture Radar (InSAR) has

been particularly successful in detecting surface displacements with millimetric precision in a wide range of settings but is most effective in a bare, rocky setting. A synthetic aperture radar system consists of a moving antenna assembled on a satellite that sends electromagnetic waves towards the ground surface and records the back-scattered signal. The received signals are recorded into a regular grid according to the azimuth location of the satellite and the range, the distance between the target and the sensor. The radar data is then focused and made coherent. Interferometric processing can be used to estimate the distance variations between successive acquisitions (Rocca *et al.*, 2013).

Tilt-metres, leveling surveys and global positioning system (GPS) measurements also provide centimetre to millimetre accuracy. At sea regular bathymetry surveys can be used to monitor seafloor deformation.

Geodetic measurements typically consist of a map of displacements at the surface. Geophysical inversion techniques can be used to infer flow within the reservoir and other parameters of interest (Vasco *et al.*, 2010). They also serve as the calibration for forward coupled fluid flow-geomechanical numerical modelling. An example of successful InSAR monitoring is provided by the InSalah CO_2 storage site. Surface uplift extending several kilometres laterally was detected at all three CO_2 injection wells. Given the high spatial and temporal resolution of the InSAR data it has been possible to detect injection-induced responses at depth.

2.5.2 Time-lapse seismic reflection surveys

Seismic surveys generate seismic waves, which travel downwards and are reflected where there are significant changes in acoustic impedance. Time-lapse seismic reflection surveys have been proven as a monitoring technology and have traditionally been used to image changes in fluid saturation at the reservoir level (Calvert, 2005). It may be possible to distinguish the CO_2 trapping mechanism from the time-lapse seismic response of the reservoir (Cairns *et al.*, 2012).

The CO_2 storage site at Sleipner in the Norwegian North Sea provides an excellent demonstration of time-lapse seismic methods for CO_2 plume monitoring (Figure 2.9) (Chadwick *et al.*, 2010). Time-lapse seismic amplitude changes have also been used to monitor the CO_2 plume at the Ketzin site, Germany (Lüth, 2011). At the Weyburn site seismic amplitude and travel-time differences have been used to outline the CO_2

plume in the subsurface (White, 2013a) and to estimate the amount of CO_2 in various regions in the subsurface (White, 2013b).

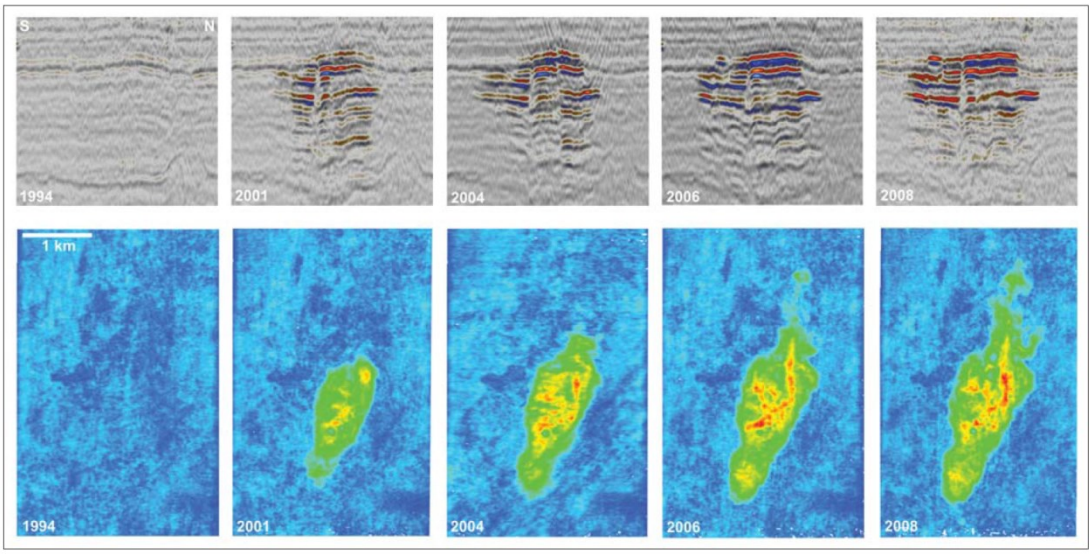


Figure 2.9: Time-lapse seismic images of the Sleipner CO_2 plume. NS inline through the plume (top); plan view of total reflection amplitude in the plume (bottom). Modified from Chadwick *et al.* (2010).

CO_2 substitution of the initial brine or oil in place usually creates a significant acoustic impedance contrast at the top of the reservoir. Furthermore, it would also create a time delay for seismic waves passing through the reservoir.

At the Snøhvit field, located in the Barents Sea, time-lapse seismic data has been used to discriminate between CO_2 pressure and saturation effects (Grude *et al.*, 2013). A continuous pressure-build up terminating against a fault 1-2 kilometres away from the CO_2 injection well was estimated.

Pressure changes due to injection/withdrawal of fluids create changes in the stress and strain fields of the rock material both inside and outside the reservoir. Seismic waves propagating through these rocks have different travel-times before and after fluid injection/withdrawal due to the combined effect of changes in layer thicknesses and seismic velocity induced by the changes in the stress and strain fields (Hatchell and Bourne, 2005). The accumulation of the travel-time differences are referred to as time-lapse seismic time-shifts. In the oil and gas industry, time-lapse seismic time-shift measurements have found many applications in support of reservoir management decisions. They have been used as a calibration tool for the geomechanical model such as for detection of reservoir compartmentalisation by sealing faults (Staples *et al.*, 2007), fault transmissibility assessment (De Gennaro *et*

al., 2008) and horizontal anisotropic permeability and fracture permeability assessment.

Herwanger and Horne (2009) have described how changes in anisotropic seismic wave velocities, measured via azimuthal variations in seismic attributes, can potentially reveal rotation of stress tensors during fluid injection/production.

2.5.3 Microseismic monitoring

The need to monitor hydraulic fracturing of tight and shale gas reservoirs has resulted in an increase in the use of micro-seismic monitoring. These advances can be readily applied to monitoring CO_2 injection (Verdon *et al.*, 2010a). Microseismic events are a manifestation of injection-induced stress changes and geomechanical deformation. Fault movement and fluid movement across faults can potentially generate microseismicity (Angus *et al.*, 2010). An array of geophones at the surface or down a bore-hole can be used to record the seismic energy from the micro-seismic events. Event magnitude and location can be estimated from the recorded events. Shear-wave splitting in micro-seismic data can also be used for estimating fracture parameters (Verdon and Kendall, 2011). Accurate location of micro-seismic events can reveal clustering along an active fault surface. Microseismic monitoring was the principal method chosen to monitor geomechanical deformation at the Weyburn site.

2.6 *Alternative Monitoring Techniques*

2.6.1 Gravity Surveying

Time-lapse gravitational methods are utilised to detect density changes in the subsurface. Injected CO_2 will displace denser formation water, causing a gravity change above the plume. Repeat gravity surveys have been conducted over the Sleipner field (Nooner *et al.*, 2007). The data was used to estimate the CO_2 density and was combined with temperature measurements to determine the CO_2 density distribution within the plume (Alnes *et al.*, 2008). The CO_2 plume geometry was constrained from time-lapse seismic data.

2.6.2 Well-based Monitoring

Well-based monitoring can provide detailed information about CO_2 saturation and migration near the well. Cross-well monitoring requires wells located relatively close to each other. At the Nagoka CO_2 storage pilot site in Japan, well-based monitoring has been the framework to assess the migration of stored CO_2. Onishi *et al.* (2009) conducted a time-lapse crosswell seismic tomography. Experimental work has shown that injected CO_2 leads to a reduction in seismic velocity (Shi *et al.*, 2007). The reduced velocity in the tomography was used to detect the CO_2 movement. Sato *et al.* (2011) combined continuous well-based monitoring of pressure, temperature, *in situ* fluid sampling, time-lapse well logging and time-lapse crosswell seismic tomography to assess CO_2 movement at different scales.

At the Ketzin CO_2 injection pilot, three boreholes have been designed for time-lapse controlled source electromagnetic (CSEM) imaging. CO_2 injection in a saline reservoir is expected to strongly modify the electrical current paths due to an increase in electrical resistivity (Girard *et al.*, 2011). The strong modifications of the electric field amplitude at Ketzin have been used to constrain the extent of the moving CO_2 plume.

2.7 *Megatonne-scale CO_2 storage sites*

Ultimately, the strength of the geomechanical response will be determined by the pressure increase induced by CO_2 injection which is likely to be a function of the volume of CO_2 injected. It is therefore highly instructive to look at commercial-scale sites where CO_2 is stored at rates approaching or greater than 1 megatonne of CO_2 per year. In this section, the observed geomechanical behaviour at four megatonne-scale CO_2 storage sites is reviewed: Sleipner, Weyburn, Snøhvit and In Salah.

2.7.1 Sleipner

At Sleipner, CO_2 is injected into the Utsira Sand saline aquifer at a rate of ~1 Mt/year since 1996. The Utsira formation is a very large saline aquifer with a thickness in the order of 200-300 metres. It has an average porosity of 35-40% and permeabilities above 1 Darcy. Although there is no downhole pressure monitoring at Sleipner, Chadwick *et al.* (2012) used time-lapse seismic to estimate pressure changes less than 0.1 MPa suggesting lateral wide hydraulic connectivity and

geomechanical deformation unlikely. The pressure changes are negligible given the easy flow of CO_2 through the reservoir due to a very large storage volume, high permeability and very few barriers to flow.

It is noted that bottom hole pressure is not measured directly but derived from well head pressure measurements and subject to uncertainties. Eiken *et al.* (2011) have suggested that down-hole measurements of pressure and temperature should be prioritised in future CO_2 storage projects.

2.7.2 Weyburn

The Weyburn field in Canada is a mature oilfield that has been under production for more than 50 years. CO_2 injection began in 2000 for the purpose of enhanced oil recovery storing over 30 megatonnes of CO_2 by the end of field operation. The ongoing enhanced oil recovery has served to mitigate the pressure increase due to CO_2 injection. Initial conditions were hydrostatic with pore-pressures at 15 MPa. Unsupported oil production reduced pore pressure to 6-7 MPa. Water injection subsequently returned the pore pressure to initial conditions and when CO_2 injection operations started the pressure increased to 20 MPa. Figure 2.10 summarises the complex pressure history at Weyburn. Given the long history of the field combined with pore-pressure variations due to oil-production, water-injection and CO_2 injection, complex deformation patterns have been observed. Verdon *et al.* (2011) located micro-seismic activity in the overburden above the production wells and not around the injection wells as expected in the SE of the field. Using forward geomechanical modelling they concluded that the micro-seismic events in the overburden were not caused by hydraulic connectivity between the reservoir and the caprock but by stress transfer to the overburden.

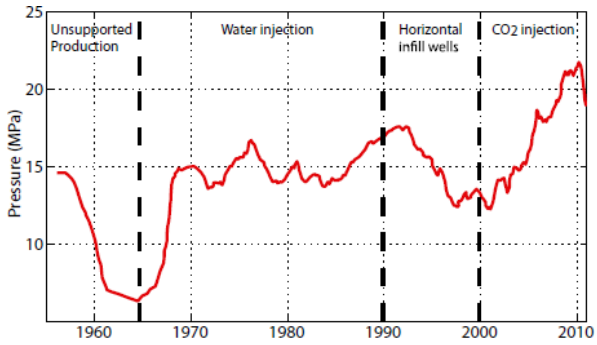


Figure 2.10: Average field pressure over the history of the Weyburn field (After Verdon *et al.*, 2013).

2.7.3 Snøhvit

At the Snøhvit field in the Barents Sea approximately 2 megatonnes of CO_2 have been injected since 2008. The CO_2 is injected into a relatively low permeability and low porosity sandstone reservoir. Down-hole pressures and temperatures were measured 800 m above the reservoir. The early injection starts and stops have shown a series of pressure build ups and fall offs with a clear trend in pressure increase. A time lapse seismic survey revealed amplitude anomalies over a spatial extent too large to be due to CO_2 saturation. The anomaly has been interpreted as dominated by the pressure induced response with an estimated pressure build up of 4-5 MPa away from the well (Grude *et al.*, 2013). Chiaramonte *et al.* (2015) concluded that is unlikely that the pressure reached the values necessary for hydraulic fracturing of the caprock or reactivation of major bounding faults. In 2011, the storage was moved from the Tubåen formation to the Stø formation, and CO_2 is currently stored in the reservoir from which it is produced.

2.7.4 In Salah

At the In Salah storage site in Algeria, CO_2 is stripped from the producing gas stream and re-injected into the aquifer leg of a relatively thin, low permeability formation. Over the injection period from August 2004 to June 2011 approximately 3.8 million metric tonnes of CO_2 have been separated from the extracted natural gas from the In Salah gas fields and re-injected into the aquifer leg. It is considered representative of the saline aquifers that might be used for large scale CO_2 storage in the U.S Midwest, China and Northwestern Europe (Wright *et al.*, 2009). There is little apparent pressure communication between the producing and injecting parts of the reservoir. Pressure communication would serve to moderate the pressure increase during CO_2 injection. Pore pressure at the injection wells have been modelled to increase from ~180 bar to ~300 bar while reducing ~10 bar at the producing wells. Given the substantial rise in injection pressure and site-specific geomechanical conditions, detectable surface deformation has been observed at all three injection wells using InSAR.

The InSAR data has proven very valuable to understand the geomechanical response of the reservoir and the overburden to injection. A bilobate uplift pattern above one the injection wells has attracted much research interest. This has been interpreted to

be caused by the development or reactivation of a fault/fracture zone. Inverse modelling (Vasco *et al.*, 2008) from InSAR data and forward coupled flow-geomechanical modelling (Rutqvist *et al.*, 2010; Morris *et al.*, 2011; Bissell *et al.*, 2011) of the surface uplift have been used to gain valuable insight into behaviour of the CO_2 storage site.

Figure 2.11 shows how the coupled flow-geomechanical modelling of a vertical fracture zone reproduces a bilobate surface uplift pattern. It is important to note that the *in situ* stress, the geomechanical properties and their distributions are subject to uncertainties. Current estimates indicate that the fault/fracture zone does not extend further than 100-200 metres (Rinaldi and Rutqvist, 2013). It remains well within the 950 m thick sealing caprock formation and does not pose a risk to the integrity of the CO_2 storage system.

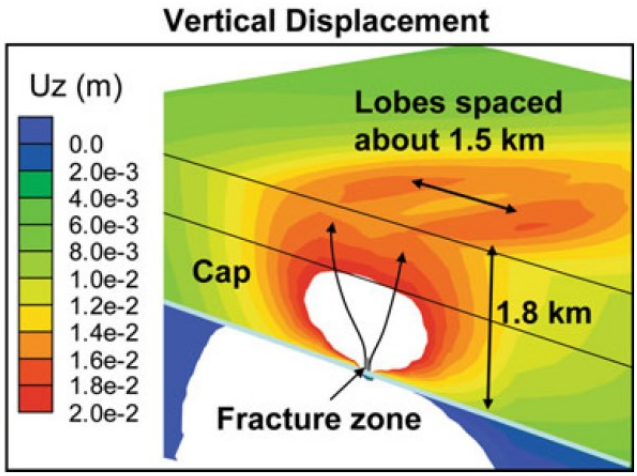


Figure 2.11: Forward coupled flow-geomechanical numerical modelling of CO_2 injection including a vertical fracture zone reproduces observed surface uplift (After Rutqvist *et al.*, 2011).

The combination of monitoring of the geomechanical response and coupled flow-geomechanical analyses has led to preventative changes in the injection parameters (reducing the injection pressure).

From a geomechanical perspective, In Salah remains the most important CO_2 storage field deployment to date. In Chapter 4 the In Salah CO_2 storage site, monitoring data sources and coupled flow-geomechanical studies will be described in greater detail. The application of the developed methodology will then be presented in the remainder of the thesis.

2.8 Summary and Discussion

In this chapter, the importance of the geomechanical processes associated with geological CO_2 storage has been reviewed alongside the main modelling tools and techniques available for the monitoring and understanding of such processes. Simple flow-geomechanical models have proven useful in the site-selection stage when little data is available. However, numerical coupled flow-geomechanical models are a requirement to model all the relevant phenomena. Once CO_2 injection starts, monitoring methods must be employed and CO_2 storage models need to be groundtruthed with field observations. Without field observations there can be no way to determine which models will provide accurate predictions of the fate of the injected CO_2. Linking available observations to our models needs to be advanced in order to conform the actual behaviour of the injected CO_2 to the modelled behaviour.

The importance of characterising both flow and geomechancial properties before CO_2 injection starts has been shown at the mega-tonne CO_2 storage field deployments. Each site has responded differently to CO_2 injection. At Sleipner, where the target storage formation is a thick, high permeability sandstone formation, pressure increases during injection have been minimal leading to very little geomechanical deformation being created. At Weyburn, the ongoing enhanced oil recovery serves to mitigate the pressure increase from CO_2 injection. Intuitively, micro-seismic events were expected to occur overlying the injection wells where the pressure change is expected to be greatest. However, given the complex pressure history of the field, micro-seismic events have been identified to cluster near the producing wells. At Snøhvit a pressure build up away from the well has been estimated from time-lapse seismic data. At In Salah, CO_2 is injected into a thin, tight sandstone formation. This in turn has led to substantial geomechanical deformation. The surface has been uplifted by 2 cm and a hydrofracture appears to have been created or re-activated extending from the reservoir to the overburden. However, the caprock sequence at In Salah consists of a 950 m sequence of mudstones, so the stimulation of fractures into the lower caprock does not pose a risk to storage security.

If the storage complex has storage volume and permeability characteristics that are likely to favour substantial pore pressure increases, it is important to monitor geomechanical deformation. Monitoring and coupled flow-geomechanical modelling

will be particularly important at sites where *in situ* conditions may lead to significant pore-pressure increases during CO_2 injection.

A variety of monitoring methods have been deployed to monitor geomechanical deformation. Micro-seismic monitoring has proven to be an effective tool at the Weyburn field, time-lapse seismic monitoring at Sleipner and InSAR monitoring at In Salah.

The focus of the remainder of this thesis will be on developing an integrated methodology for CO_2 storage site performance assessment that incorporates InSAR monitoring data, time-lapse seismic monitoring data, bottom hole pressure data and coupled fluid-flow geomechanical modelling with a focus on understanding the dynamic behaviour of a CO_2 storage complex in response to changes in the CO_2 injection pressure. The methodology will then be applied on the In Salah field data set.

Chapter 3 Methodology and Theory

This chapter reviews the theory and presents a methodology developed for the coupled flow-geomechanical performance assessment of CO_2 storage sites. The methodology is divided into three parts – a forward, inverse and fully integrated approach. A forward modelling approach is proposed for the coupling of a flow and a geomechanical simulator by which the behaviour of a CO_2 storage complex can be modelled over time. An inverse methodology is developed by using geomechanical simulations to derive a set of transfer functions allowing geomechanical observables like surface deformation to be used to estimate the reservoir pressure change due to CO_2 injection. Finally, a fully integrated approach using the ensemble Kalman filter (EnKF) is proposed. Observables such as bottom-hole pressure and surface deformation can be assimilated by the EnKF and used to update the flow-geomechanical model parameters and can reduce the uncertainty in the parameters controlling the overall performance of a CO_2 storage complex. The methodology proposed allows for all the modelling tools and different monitoring data sets to be integrated in a single platform for the performance assessment of a CO_2 storage site.

3.1 *Coupled flow-geomechanical modelling*

3.1.1 ECLIPSE E300 reservoir simulator

The compositional simulator ECLIPSE E300 (Schlumberger, 2010) is used to conduct the reservoir simulations. The CO2STORE option was activated to simulate injection and geological storage of CO_2 into the saline aquifer systems that were modelled. The estimates from the simulation are the molar mass of CO_2 that is dissolved, as well as the residually trapped and free CO_2 found in the gaseous state. For the simulations using the CO2STORE option, three phases are considered, a CO_2 rich phase, a H_2O rich phase and a solid phase. The mutual solubilities of CO_2 and H_2O are calculated to match experimental data for CO_2-H_2O systems under typical CO_2 storage conditions ranging between 12-100 °C and up to 600 bars. These are calculated following the procedure given by Spycher and Pruess (2005) based on fugacity equilibration between water and CO_2-phase. Water fugacity is obtained by Henry's law, while CO_2 fugacity is calculated using a modified Redlich-Kwong equation of state (Redlich and Kwong, 1949). The components that can be considered in the CO2STORE option are CO_2 and H_2O present in water and gas phases and the salts NaCl, $CaCl_2$ and $CaCO_3$ present in either aqueous or solid phase (Schlumberger, 2010).

The mathematical model for this simulator includes the extended Darcy law for multiphase flow of each phase (α)

$$\mathbf{v}_{\alpha} = -\boldsymbol{\rho}_{\alpha}\frac{\mathbf{K}\boldsymbol{k}_{r\alpha}}{\boldsymbol{\mu}_{\alpha}}(\boldsymbol{\nabla p}_{\alpha} - \boldsymbol{\rho}_{\alpha}\boldsymbol{g}\boldsymbol{\nabla z}) \tag{3.1}$$

and the mass conservation equation for each component (i) in present phases including the diffusive flux:

$$\frac{\boldsymbol{\partial}}{\boldsymbol{\partial t}}\left(\sum_{\alpha}\boldsymbol{\varphi S}_{\alpha}\boldsymbol{\rho}_{\alpha}\boldsymbol{x}_{\alpha}^{\boldsymbol{i}}\right) + \boldsymbol{\nabla}.\sum_{\alpha}(\boldsymbol{x}_{\alpha}^{\boldsymbol{i}}.\mathbf{v}_{\alpha} + \mathbf{J}_{\alpha}^{\boldsymbol{i}}) = \boldsymbol{q}^{\boldsymbol{i}} \tag{3.2}$$

where $\mathbf{v}_{\alpha}$, μ_{α}, $k_{r\alpha}$, p_{α} and ρ_{α} are respectively the velocity, viscosity, relative permeability, pressure and density of phase α (gaseous and aqueous brine phase) and **K** is the absolute permeability. In equation 3.2 for the mass conservation, φ is porosity of the porous medium, S_{α} is the saturation of phase α, x_{α}^{i} is the mass

fraction of component i in fluid phase α. Hence, $x_\alpha^i.\mathbf{v}_\alpha + \mathbf{J}_\alpha^i$ is the mass flux of component i, within fluid phase α, written as the sum of the advective (Darcy) and nonadvective (diffusive) mass fluxes. The diffusive flux of component i in phase α in a porous medium is computed using Fick's law as:

$$\mathbf{J}_\alpha^i = -\boldsymbol{\varphi S_\alpha \rho_\alpha D_\alpha^i I \nabla x_\alpha^i} \tag{3.3}$$

where, D_α^i is the normal diffusion coefficient of component i, within fluid phase α. In the CO2STORE option enabled simulations D_α^i is defined by the keywords DIFFCGAS and DIFFCWAT for each component in respectively gaseous and aqueous phases in ECLIPSE E300 (Schlumberger, 2010).

3.1.2 Geomechanical Simulators

The simulators FLAC^{3D} and VISAGE are used to conduct geomechanical simulations. FLAC^{3D} is an explicit finite difference program to study, numerically, the mechanical behaviour of a continuous three-dimensional medium as it reaches equilibrium (Itasca, 2012). VISAGE is a finite element program similarly used for the study of mechanical behaviour. The coupled flow and geomechanical modelling work described in Chapter 6 used VISAGE within Petrel Geomechanics since as no further model coupling was necessary. The implementation of ensemble Kalman Filter (EnKF) described in Chapter 7 was possible with the use of FLAC^{3D},given its greater flexibility to run an ensemble of geomechanical models and program the automated update of model parameters.

The governing equations of linear elasticity consist of the equation of motion and equilibrium, the constitutive laws, and the description of stress and strain (Jaeger *et al.*, 2007). The state of stress is characterised by the symmetric stress tensor $\boldsymbol{\sigma}$. In an infinitesimal time interval, a rock experiences an infinitesimal strain where the corresponding components of the strain tensor $\boldsymbol{\varepsilon}$ may be written as:

$$\boldsymbol{\varepsilon_{ij}} = \frac{\mathbf{1}}{\mathbf{2}}\left(\frac{\boldsymbol{\partial u_i}}{\boldsymbol{\partial X_j}} + \frac{\boldsymbol{\partial u_j}}{\boldsymbol{\partial X_i}}\right) \tag{3.4}$$

where $\mathbf{X}$ is the material coordinate and $\mathbf{u}$ is the displacement. Application of the continuum form of the momentum principle yields Cauchy's equations of motion:

$$\frac{\partial \sigma_{ij}}{\partial X_j} + \rho b_i = \rho \frac{\partial^2 u_i}{\partial t^2} \tag{3.5}$$

where **b** is the body force and ρ is the density. In the case of static equilibrium of the medium, the acceleration term is zero and reduces to the partial differential equations of equilibrium.

$$\frac{\partial \sigma_{ij}}{\partial X_j} + \rho b_i = 0 \tag{3.6}$$

The constitutive equations define the behaviour of the particular rock under consideration

$$\sigma_{ij} = \lambda \varepsilon_{kk} \delta_{ij} + 2\mu \varepsilon_{ij} \tag{3.7}$$

Where λ and μ are two Lame elastic constants and δ is the Kronecker delta. The two Lame elastic constants can be related to the Young's modulus E, and the Poisson's ratio ν as follows:

$$\mu = G = \frac{E}{2(1+\nu)} \tag{3.8}$$

and

$$\lambda = \frac{\nu E}{(1+\nu)(1-2\nu)} \tag{3.9}$$

If the material is homogeneous and isotropic, the elastic behaviour can be described by any combination of two parameters. Adding boundary conditions to the equations of motion, the constitutive equations and the definition of strain, the governing system of equations can be solved.

3.1.3 Coupling of fluid-flow and geomechanics

Various algorithms have been investigated and developed for coupling fluid flow and geomechanical simulators. These algorithms range from the tightest coupling of physics (fully coupled) (Grechka and Soutter, 2005) to loose coupling (one-way coupling) (Settari and Mouritis, 1998; Samier *et al.*, 2008). Samier *et al.* (2006)

provide a comparison between several coupling methods. Smart *et al.* (2003) and Ali *et al.* (2003) review the applications of coupled flow-geomechanical modelling from exploration to abandonment of petroleum reservoirs in the oil and gas industry.

Coupled flow-geomechanical modelling entails reservoir simulation, the modelling of fluid flow and pressure changes, while additionally solving the equations governing subsurface deformation and stress changes. The physics governing fluid flow and geomechanics are interrelated. Pore-pressure changes modelled in the fluid flow domain lead to stress changes in the geomechanical domain. The stress changes may in turn cause porosity and permeability changes in the fluid flow domain.

The interrelation between fluid flow and geomechanics can be described using the concept of effective stress. The effective stress σ'_{ij} acting on porous rocks is defined as follows (Terzaghi, 1923):

$$\boldsymbol{\sigma'_{ij} = \sigma_{ij} - \beta \delta_{ij} P} \tag{3.10}$$

where σ_{ij} is the stress applied by regional tectonic stresses and the overburden weight, β is the Biot-Willis coefficient, δ_{ij} is the Kroenecker delta, and P is the pore pressure.

3.1.4 Coupled flow-geomechanical modelling workflow

Two computer codes, ECLIPSE E300 and FLAC^{3D}, are linked and jointly executed for coupled flow-geomechanical analysis of flow and deformation in geological media. In a one way coupling approach information is transferred in one way only from the reservoir flow simulator to the geomechanical simulator.

Figure 3.1 presents a diagram showing the one-way coupling scheme between ECLIPSE E300 and FLAC^{3D}. For a geomechanical simulation the reservoir model is embedded into a larger geomechanical model with side burden and underburden added to minimize boundary effects. Once the reservoir model and geomechanical model are initialised, the pore pressure output from the ECLIPSE E300 simulation at a given time-step is transferred into FLAC^{3D}. For this purpose an external coupling module was developed to link both computer codes.

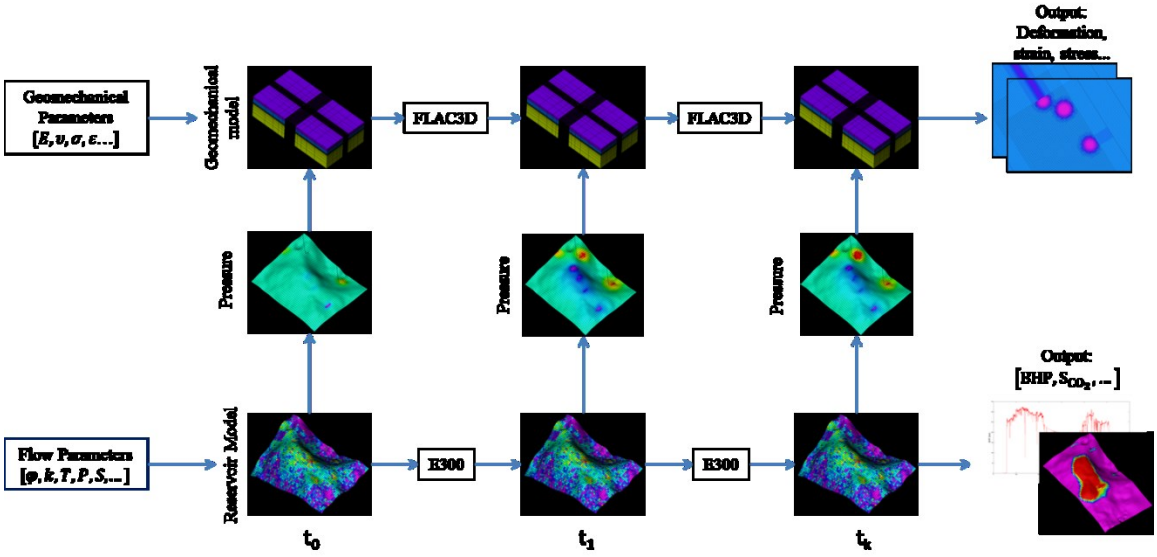


Figure 3.1: Diagram showing the one-way coupling scheme between ECLIPSE E300 and FLAC^{3D}.

The fluid-flow model domain is usually a subset of the geomechanics domain. The geomechanical model domain is extended up to the earth's surface and is further extended in the lateral directions and below the reservoir.

In this workflow the user designates a flow time-step and a separate geomechanical time step. The geomechanical time-step is defined as $\Delta t_1 = t_1 - t_0$. The flow simulator runs first and is likely to subdivide the Δt_1 time interval into multiple fluid flow time steps.

3.1.5 Building a reservoir geomechanical model

A reservoir geomechanical model synthesises the available data and knowledge about the interaction between (Herwanger and Koutsabeloulis, 2011):

- Spatial distribution of the elastic and strength properties of the subsurface material properties and the location and mechanical properties of faults
- Pore pressure
- Geometry and structure of the reservoir and overburden
- Tectonic stress and overburden stress

The first step in building a reservoir geomechanical model is defining the horizons that separate the different geological units. Typically, these would be interpreted

form seismic data (Brown, 2012). After dividing each geological unit into layers, the layers are subdivided into grid blocks.

The next step is determining the magnitude and spatial distribution of the elastic and strength properties. This is a central step in building a geomechanical model. Soft layers concentrate strain and stiffer layers concentrate stress. Strength properties determine whether rock failure will occur at a specified stress level.

The geomechanical properties commonly used are Young's Modulus E and Poisson's ratio ν. The elastic properties are usually measured either statically or dynamically. The static elastic moduli are determined from compressional testing on cores (Fjaer *et al.*, 2008). Dynamic moduli are determined from elastic wave velocities from ultra-sonic testing, well-log testing or seismic data. Seismic AVO inversions have also been used to infer elastic properties (Bachrach *et al.*, 2009). In practice the static elastic moduli are estimated from calibrated correlation functions using dynamic elastic moduli as input (Eissa and Kazi, 1988). In practice strength properties are typically derived from correlation functions between log-derived properties and strength properties. Here, only the elastic-brittle regime is considered. Given the larger extent of the geomechanical model compared to the reservoir model, characterising both the reservoir and overburden remains challenging. The availability of cores is typically limited to the reservoir interval and does not include the entire overburden.

The numerical solution of the stress equations requires the application of boundary conditions. In the geomechanical modelling domain the grid is of a limited spatial extent and the boundary conditions are applied at the outer faces of the model. Zero-displacement conditions are applied at the lateral and bottom boundaries. The top boundary is a free surface where movement is allowed. Alternatively, if stress data is available (Zoback, 2010), the stress boundary conditions can be defined.

3.2 *Inverting for reservoir pressure change using geomechanical deformation*

3.2.1 Problem formulation

CO_2 injection into a reservoir causes changes in reservoir stresses and strains that can propagate laterally along with the expanding fluid pressure front within the injection zone. The injection induced pressurisation of the reservoir leads to its vertical expansion which in turn leads to changes in the surrounding stress field. Depending on the geomechanical properties and the geometry of the subsurface, the vertical expansion of the reservoir may result in ground surface deformation that might be detectable using tilt meters and state-of-the-art satellite interferometry (InSAR) in addition to subsurface strain detectable using time-lapse seismic time-shifts.

Approaches to the geomechanical problem of relating overburden deformation to reservoir pressure changes can be divided into three categories: analytical, semi-analytical and numerical.

Analytical: Analytical solutions have been developed under the assumption of a homogeneous linear-poroelastic (HLP) whole or half-space and for simple reservoir geometries. Geertsma (1973) developed an analytical solution for a uniform thin disk-shaped reservoir in a HLP halfspace. Segall (1992) provided a more general analytic solution for calculating the displacements, strains and stresses for axisymmetric depletion patterns and reservoir geometries in a HLP halfspace, where the Geertsma (1973) thin disk-shaped model was recovered as a special case.

Semi-analytical: The analytic displacement solution for a nucleus of thermo-elastic strain (Mindlin and Cheng, 1950) in a half-space with a traction-free surface was adapted to poroelasticity by Geertsma (1966). The analytic nucleus of strain solution can be integrated over the reservoir region. A common approach is the superposition of nucleus of strain (point sources) in a HLP halfspace.

Numerical: For arbitrary geometries and distributions of geomechanical properties the problems needs to be analysed numerically mainly by using one of the following methods: Finite Elements, Boundary Elements, Finite Differences or the image source technique. These methods have been developed for forward modelling displacements due to reservoir fluid injection/production.

In principle any of these approaches can be used to solve the inverse problem of relating overburden deformation to reservoir pressure changes. However, the use of analytical solutions rarely represents realistic reservoir geometries or injection/production scenarios. The use of fully numerical schemes for an inversion process require the carrying out of a full field simulation for as many model cells to generate the associated Green's functions. The significant computational effort demanded for these inversion schemes has prevented their widespread use.

Successful inversion schemes that have been tested and applied have used a semi-analytical nucleus of strain approach to construct the Green's functions. Du and Olson (2001) developed a forward/inverse model using a Geertsma type solution and validated it using two synthetic examples. Hodgson *et al.* (2007) applied this approach on the Genesis field in the Gulf of Mexico using subsurface strain estimated from time lapse seismic to invert for reservoir pressure change. Garcia *et al.* (2010) presented a method for relating overburden strain to reservoir volumetric strain using transfer functions and applied it to the HP/HT (high pressure high temperature) Elgin field. This approach however requires a subsurface model and a geomechanical simulation to generate the transfer functions.

In the following section, a linear relationship between overburden deformation and reservoir pressure change using a transfer function method approach is presented. The method is adapted from Garcia *et al.* (2010) where it was used to understand reservoir compaction in a HP/HT field using time-lapse seismic observations. If a fully geomechanical numerical model is available the transfer function approach can capture the subsurface's structural and material complexity while still being computationally fast.

3.2.2 The Weiner filter formulation

A discrete linear inverse problem can be written as the following system of equations

$$\mathbf{Gm}=\mathbf{d} \tag{3.11}$$

Where **m** represents the set of physical parameters that characterise the model, **d** is a set of observed data and **G** is the function(s) that relates **m** and **d**.

The *forward problem* consists of predicting the values of the observable parameters **d** that would correspond to a given model **m**. The *inverse problem* is that of finding the model parameters **m** given the observable parameters **d**. A solution to the inverse problem can be found by finding the set **m** that produces the smallest misfit. A least-squares solution requires minimising the objective function $F(\mathbf{m})$ with respect to **m** where the objective function is given by

$$F(\mathbf{m}) = \|\mathbf{Gm} - \mathbf{d}\|_2^2 \tag{3.12}$$

There is a third problem known as the *system identification problem* which consists of determining **G** given **m** and **d**. The system identification problem can be described using linear filter theory by the convolution

$$\mathbf{d} = \mathbf{G} * \mathbf{m} \tag{3.13}$$

In order not to confuse **G** with the conventional Green's functions from here onwards it will be referred to as **f** since it is operating as a linear-filter. Reformulating the objective function for the system identification problem and assuming the impulse response **d** is known, it is now minimised with respect to **f**

$$F(\mathbf{f}) = \|\mathbf{f} * \mathbf{m} - \mathbf{d}\|_2^2 \tag{3.14}$$

The resulting filter **f** describes in a least-square sense the process under consideration. The advantage of this formulation is that it is possible to describe any linear process regardless of its complexity and is suited for solving both forward and inverse problems. A process known as Wiener deconvolution (Gonzalez, 1983) can be used to solve the inverse problem by using the inverse filter $\mathbf{f}^{-1}$, which has the following property

$$\mathbf{m} = \mathbf{f}^{-1} * \mathbf{d} \tag{3.15}$$

3.2.3 Reservoir pressure change inversion workflow

The relative ease with which ground surface deformation in addition to subsurface displacements can be measured can be used to track changes in reservoir pressure given a Green's function or any other type of transfer function.

In the context of the monitoring of a CO_2 storage site the observable parameters are the overburden displacements **u** and the model parameters are the changes in reservoir pressure $\Delta\mathbf{p}$. In order to estimate the transfer function **f**, knowledge of both **u** and $\Delta\mathbf{p}$ is required. Garcia and Macbeth (2013) have argued that in theory it is possible to estimate the earth's impulse response directly from a well test and monitored overburden deformation. In practice this is difficult as monitoring of overburden deformation is done after CO_2 injection has begun at the wells. As field data is unlikely to be available, a geomechanics simulator can be used to calculate the impulse response (Garcia and Macbeth, 2013; Garcia *et al.*, 2010). As any prior knowledge is included in the geomechanical model, the estimated transfer function will include all the available information. The process for the inversion scheme can be applied in the following manner:

1. Select an isolated CO_2 injection area and associated overburden deformation. The CO_2 injection area will be excited with a pressure pulse and the overburden deformation will be forward modelled using a geomechanical simulator.
2. Using the pressure pulse as the input and the modelled overburden deformation as the output, the system's transfer function f can be calculated via a Wiener filter.
3. Once the system's transfer function f is known it can be used for geomechanical forward modelling by convolving it with the pressure field from a reservoir flow simulation or the inverse f^{-1} can be used by convolving with observed overburden deformation to calculate the changes in reservoir pressure.

Figure 3.2 summarises the workflow for estimating reservoir pressure changes from overburden deformation estimates.

The system can be assumed to be elastic even though the reservoir may not behave in a linear elastic manner. The overburden materials are not expected to undergo

significant geomechanical changes and can therefore be expected to behave in a linear elastic manner regardless of how the reservoir and the immediate overburden deform (Vasco and Ferretti, 2005). Ultimately the following linear relationship between overburden deformation and reservoir pressure change can be assumed

$$u = f * \Delta p \tag{3.16}$$

where the inverse process is given by

$$\Delta p = f^{-1} * u \tag{3.17}$$

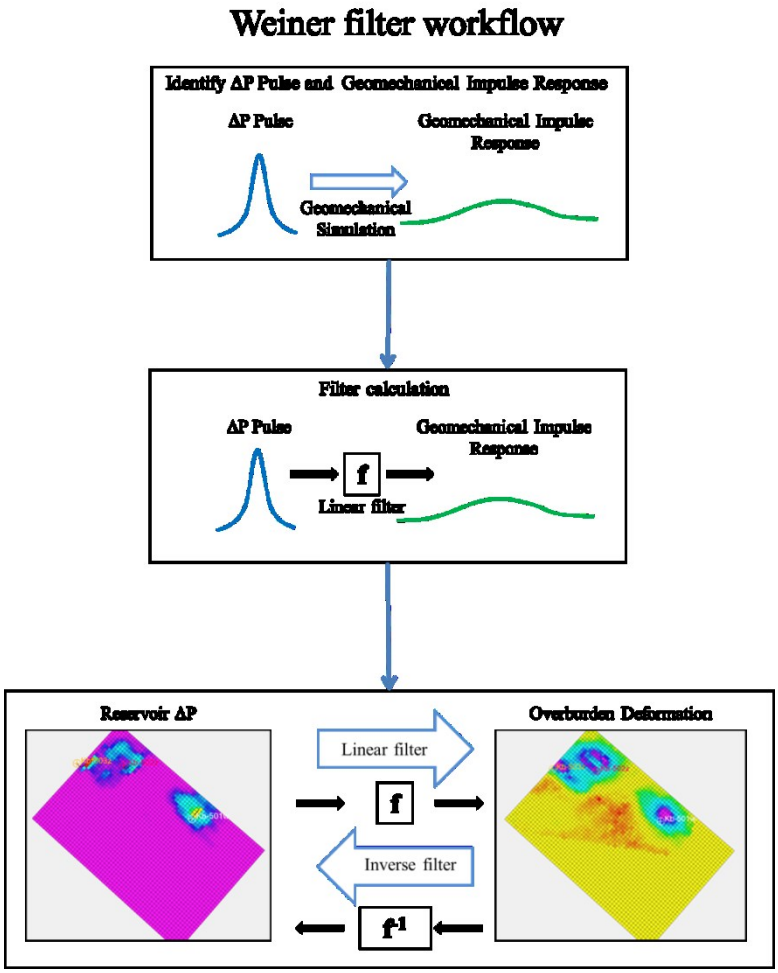


Figure 3.2: Workflow explaining the calculation and use of Weiner filters to estimate reservoir pressure changes from overburden deformation.

3.3 *The EnKF approach*

3.3.1 Introduction

The ensemble Kalman Filter (EnKF) was first introduced by Evensen (1994) for the purpose of handling large-scale nonlinear ocean models with much of its development in the field of weather prediction. The atmospheric models must take into account the available observations of variables such as atmospheric pressure and temperature for improved forecasting of the weather (Houtekamer *et al.*, 2005).

Some of the early applications of the EnKF to petroleum engineering began with Naevdal *et al.* (2005) using a simple 2D field model where only reservoir flow is simulated and permeability is updated. The model is continuously updated using production data. The updated models gave improved forecasts as more data was assimilated. Gu and Oliver (2005) performed a series of studies on a synthetic model where both permeability and porosity were estimated. The first demonstration of the use of the EnKF on a field case was presented by Skjervheim *et al.* (2007) using real time-lapse seismic data from a Northern Sea field. Field examples where production data is assimilated include the Zagor field in West Africa (Bianco *et al.*, 2007) and North Sea reservoirs (Haugen *et al.*, 2008; Evensen *et al.*, 2007).

Chang *et al.* (2010) tested the applicability of the EnKF to coupled flow-geomechanical phenomena due to fluid production and showed an improved performance of the EnKF by assimilating both surface subsidence and production data. In addition, Wilschut *et al.* (2011) have used the EnKF to assimilate surface subsidence and production data to estimate reservoir fault transmissibilities at the Roswinkel field. In the case study presented, they were not able to match both production data and surface subsidence such that they can be explained in a consistent way leading to a re-evaluation of the reservoir model concept itself.

Section 3.4.2 presents the Kalman filter on which the EnKF is based on. The EnKF is presented in Section 3.4.3. Section 3.4.5 describes the workflow for the methodology and how the EnKF is adapted to the coupled flow-geomechanical modelling of CO_2 storage sites.

3.3.2 The Kalman filter

The EnKF is based on the much simpler Kalman filter (Kalman, 1960). The Kalman filter is an efficient recursive filter that estimates the state of a linear dynamical system from a series of noisy measurements. It specifically addresses the problem of estimating the current state of the system that is described by a linear stochastic differential equation of the form (Oliver *et al.*, 2008):

$$\boldsymbol{x_k = A_k x_{k-1} + w_{k-1}} \tag{3.18}$$

where x_k is the current state of the system, x_{k-1} is the previous state of the system, A_k is the state transition model applied to the previous state and w_{k-1} is the process noise. The measurements $d_{obs,k}$ are related to the system state through a linear relationship

$$\boldsymbol{d_{obs,k} = G_k x_k + \epsilon_k} \tag{3.19}$$

where G_k is the observational model which maps the state of the system x_k into the observed space $d_{obs,k}$ and ϵ_k is the observation noise.The application of the Kalman filter method consists of two stages. The first stage is the forecast stage where given the estimate $\hat{x}_{k-1}$ at time t_{k-1}, the best estimate of x_k^f (before data assimilation) can be obtained directly from the linear dynamic relation

$$\boldsymbol{x_k^f = A_k \hat{x}_{k-1}} \tag{3.20}$$

where the f superscript denotes forecast. The covariance C_k^f is obtained from the following equation relating the covariance of two variables that are linearly related

$$\boldsymbol{C_k^f = A_k C_{k-1} A_k^T} \tag{3.21}$$

where the superscript T dennotes the transpose. The second stage is the analysis or data assimilation stage. The best estimate of $\hat{x}_k$ is obtained from

$$\hat{\boldsymbol{x}}_{\boldsymbol{k}} = \boldsymbol{x}_{\boldsymbol{k}}^{\boldsymbol{f}} + \boldsymbol{K}\left(\boldsymbol{d}_{\boldsymbol{obs,k}} - \boldsymbol{G}_{\boldsymbol{k}}\boldsymbol{x}_{\boldsymbol{k}}^{\boldsymbol{f}}\right) \tag{3.22}$$

where

$$\boldsymbol{K} = \boldsymbol{C}_{\boldsymbol{k}}^{\boldsymbol{f}}\boldsymbol{G}_{\boldsymbol{k}}^{\boldsymbol{T}}\left(\boldsymbol{G}_{\boldsymbol{k}}\boldsymbol{C}_{\boldsymbol{k}}^{\boldsymbol{f}}\boldsymbol{G}_{\boldsymbol{k}}^{\boldsymbol{T}} + \boldsymbol{C}_{\boldsymbol{D,k}}\right)^{-\mathbf{1}} \tag{3.23}$$

K is called the Kalman gain and $C_{D,k}$ is the covariance of the observation errors. The posterior covariance at time t_k after data assimilation is

$$\boldsymbol{C}_{\boldsymbol{k}} = \boldsymbol{C}_{\boldsymbol{k}}^{\boldsymbol{f}} - \boldsymbol{C}_{\boldsymbol{k}}^{\boldsymbol{f}}\boldsymbol{G}_{\boldsymbol{k}}^{\boldsymbol{T}}\left(\boldsymbol{C}_{\boldsymbol{D,k}} + \boldsymbol{G}_{\boldsymbol{k}}\boldsymbol{C}_{\boldsymbol{k}}^{\boldsymbol{f}}\boldsymbol{G}_{\boldsymbol{k}}^{\boldsymbol{T}}\right)^{-\mathbf{1}}\boldsymbol{G}_{\boldsymbol{k}}\boldsymbol{C}_{\boldsymbol{k}}^{\boldsymbol{f}} \tag{3.24}$$

The Kalman filter can be used to continuously update the model states as new observations are acquired. However, the posterior covariance must be computed for each model update. The Kalman filter is limited by the computational effort required to compute the covariance matrix in addition to the assumption of linearity of the model dynamics. For multi-phase reservoir flow applications such as oil and gas production and CO_2 storage this method is impractical. The Kalman filter however serves as the foundation for extensions of the method which deal with the problem of non-linear dynamics and the computation of the covariance matrix.

3.3.3 The Ensemble Kalman Filter

The EnKF method is a Monte Carlo implementation of the Kalman filter in which the mean of an ensemble of realisations provides the best estimator of the population mean and the ensemble members provide an empirical estimate of the probability density. It is a sequential data-assimilation method that updates both model parameters and system state variables as they become available. Like the Kalman filter, the EnKF consists of sequentially running a forecast step followed by an analysis step.

The first step in the implementation of the ensemble Kalman filter is to define an ensemble of N_e initial models consistent with any prior knowledge of the initial state. The ensemble of augmented state vectors at time t_k is denoted by Ψ_k:

$$\boldsymbol{\Psi_k} = \{\boldsymbol{y_{k,1}}, \boldsymbol{y_{k,2}}, \dots, \boldsymbol{y_{k,N_e}}\} \tag{3.25}$$

where N_e is the number of ensemble members. $y_{k,i}$ for $i = 1, \dots, N_e$ are state vectors. The augmented state vector Ψ_k contains all the parameters that define the state of the system. At time t_k the i state vector for the system is expressed as:

$$\boldsymbol{y_{k,i}} = \left[(\boldsymbol{x_{k,i}})^{\boldsymbol{T}}, \boldsymbol{g}(\boldsymbol{x_{k,i}})^{\boldsymbol{T}}\right]^{\boldsymbol{T}} \tag{3.26}$$

Where $x_{k,i}$ consists of the parameters for the system and $g(x_{k,i})$ is the simulated data from the model state $x_{k,i}$.

The next stage is the forecast step. The forecast step consists of a model prediction forward in time based on the solution of the governing equations:

Forecast step:

$$\boldsymbol{y^f_{k,i}} = \boldsymbol{f}(\boldsymbol{y_{k-1,i}}) \textbf{ for } \boldsymbol{i = 1, \dots, N_e} \tag{3.27}$$

where $f(\cdot)$ is the physical model considered. The superscript f indicates the forecast state or model prediction. This stage does not usually modify the model parameters but replaces the simulated data in the predicted augmented state vector Ψ_k for the appropriate time t_k.

The second stage is the data assimilation or analysis step in which both the model parameters and the state of the system are updated to honour the available observations:

Data Assimilation Analysis step:

$$y_j = y_j^f + K_e(d_j - Hy_j^f) \text{ for } j = 1, \dots, N_e \tag{3.28}$$

Where K_e is the ensemble Kalman gain and H is the measurement operator that extracts the simulated data from the state vector y_j^f.

$$\boldsymbol{H_k} = [\mathbf{0} \quad \boldsymbol{I}] \tag{3.29}$$

and d_j is a vector of observational data d_{obs} that has been perturbed with random errors ϵ_j from the same distribution as the measurement error:

$$\boldsymbol{d_j} = \boldsymbol{d_{obs}} + \boldsymbol{\epsilon_j}, \textbf{for } \boldsymbol{j} = \mathbf{1}, \dots, \boldsymbol{N_e} \tag{3.30}$$

The ensemble Kalman gain K_e is defined as follows:

$$\boldsymbol{K_e} = \boldsymbol{C_{\Psi,e}H^T}\left(\boldsymbol{HC_{\Psi,e}H^T} + \boldsymbol{C_D}\right)^{-1} \tag{3.31}$$

The covariance matrix of the state vectors $C_{\Psi,\mathrm{e}}$ at any time is approximated from the ensemble members using the standard statistical formula:

$$\boldsymbol{C_{\Psi,\mathrm{e}}} = \frac{\mathbf{1}}{\boldsymbol{N_e} - \mathbf{1}} \sum_{\boldsymbol{i,j=1}}^{\boldsymbol{N_e}} \left(\boldsymbol{y_i^f} - \boldsymbol{\bar{y}^f}\right)\left(\boldsymbol{y_i^f} - \boldsymbol{\bar{y}^f}\right)^{\boldsymbol{T}} \tag{3.32}$$

where the indices i and j refer to ensemble members. $\bar{y}^f$ is the mean of the N_e ensemble members at the current data assimilation step. The size of the covariance matrix $C_{\Psi,\mathrm{e}}$ is $N_y \times N_y$, where N_y is the size of each state vector. The square root of $C_{\Psi,\mathrm{e}}$ can be computed and stored for efficiency.

$$\boldsymbol{L_e} = \frac{\mathbf{1}}{\sqrt{\boldsymbol{N_e} - \mathbf{1}}}\left(\boldsymbol{\Psi} - \boldsymbol{\bar{y}^f}\right) \tag{3.33}$$

The computationally efficient form of the Kalman gain (Oliver *et al.*, 2008) is therefore

$$\boldsymbol{K_e} = \boldsymbol{L_e}(\boldsymbol{HL_e})^{\boldsymbol{T}}\left((\boldsymbol{HL_e})(\boldsymbol{HL_e})^{\boldsymbol{T}} + \boldsymbol{C_D}\right)^{-1} \tag{3.34}$$

3.3.4 Geostatistical Methods

Geostatistical methods deal with the science of estimation and simulation of spatial variables (Isaaks and Srivastava, 1989). It is based on the concept of a regionalised variable that presents both spatial distribution and variability. The properties of the

regionalised variables are captured in a spatial auto-correlation function called the variogram. The variogram is assumed to obey the properties of stationarity. The mean value is constant and the variance depends on the lag (spacing distance) between points. Both the mean and variance parameters are finite and computable. For a random variable Z this is expressed by the variogram function:

$$\boldsymbol{\gamma(h)} = \frac{\mathbf{1}}{\mathbf{2N(h)}} \sum_{\boldsymbol{i=1}}^{\boldsymbol{N(h)}} [\boldsymbol{Z(x_i)} - \boldsymbol{Z(x_i + h)}]^{\mathbf{2}} \tag{3.35}$$

where $\gamma(\boldsymbol{h})$ is the variogram function, $Z(\boldsymbol{x_i})$ and $Z(\boldsymbol{x_i + h})$ are pairs of values of the random variable at locations $\boldsymbol{x_i}$ and $\boldsymbol{x_i + h}$ separated by the separation (lag) vector $\boldsymbol{h}$. $N(\boldsymbol{h})$ is the number of pairs available for a specific lag.

An idealised variogram plot where the variagrom values are plotted against the separation distance between samples may be characterised by three main features. The first feature is the nugget C_0 defined as the intercept. Theoretically it would take on a zero value when $\boldsymbol{h} = 0$ but due to very short range variability and inherent inaccuracies in the analysis technique, the nugget takes on a positive value. In practical terms, the nugget represents the small-scale variability of the data. The second feature is the sill, C_1 which corresponds to the variogram value at the range a. In Figure 3.2, C_1 is the total sill which is the total variance contribution or the maximum variability between pairs of points. The third feature is the range, a, which is the distance at which the variogram function reaches a plateau. The plateau indicates that the samples are no longer spatially correlated.

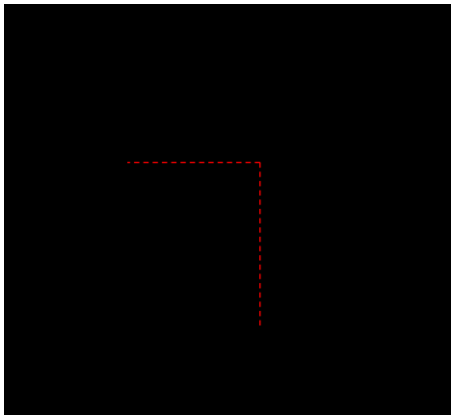


Figure 3.2: Idealised variogram plot.

For a sparsely sampled data set, geostatistical methods can be used to estimate the unknown values of data at unsampled locations for a better understanding of the phenomena under study with respect to its spatial location. Mathematically, this is an interpolation problem.

Before estimation can be performed, the experimental variogram must be fitted by a suitable model function. This could be done by using traditional least square fitting methods. Variogram models are then used to assign weights to samples in order to generate estimates with an associated variance at unsampled locations. In order to prevent the possibility of assigning negative weights, standard functions are used to fit to the variogram. Among the functions used to fit a model to the experimental variogram is the Gaussian function, which describes smoothly varying phenomena. For phenomena which are less continuous near the origin, as often is the case, the spherical and exponential functions are commonly used. A generalised Cauchy function may also be used. The variogram models may be nested where a number of spatial processes operate at different ranges. The total sill is the sum of the nugget plus the sills of each nested structure. Anisotropic models can also be fitted with the longer ranges in the preferential direction of continuity.

Kriging is an interpolation method that uses a moving window weighted-least squares estimator, which weights nearby samples according to weights determined from a variogram model, and so takes advantage of the spatial relationship between samples. Kriging involves solving a system of constrained linear equations by the method of Lagrange multipliers to determine the weights.

A feature of kriging is that it minimises the error variance at each estimation point to produce an unbiased best estimate.

An alternative approach is to use a simulation algorithm. A popular algorithm is Sequential Gaussian Simulation (SGS). Sequential simulation, unlike kriging, is based on producing multiple estimations which reasonably match the sample statistics, variogram model and sample data. The SGS makes the assumption that the data have a gaussian distribution. In practice when this is not the case, it can be achieved through a number of transformations. An anamorphosis function can be defined to fit the raw histogram of the sample data. The results can then be back transformed to the original space. The model variogram can be calculated from the transformed data.

The simulations are normally performed on a regular grid. A random path is defined which visits each of the remaining grid nodes once. In the conditional execution of the algorithm, SGS uses the real sample data and previously estimated samples to estimate the gaussian conditional cdf according to user specified neighborhood. A simulated value is then drawn from the distribution and added to the regular grid. The algorithm then repeats the process until the entire grid has been simulated. The simulated values can then be back transformed.

3.3.5 EnKF workflow

In this section the proposed EnKF workflow is described for the coupled flow-geomechanical modelling of a CO_2 storage site where the monitoring of BHP and surface deformation data are history-matched and used to update the flow and geomechanical parameters. In the context of a CO_2 storage site, a typical state vector for a multi-phase flow problem is:

$$\boldsymbol{x_{k,i}}^{T} = [\ln \boldsymbol{k}^{T}, \boldsymbol{\phi}^{T}, \boldsymbol{P}^{T}, \boldsymbol{S_w^T}, \boldsymbol{Tr}^{T}]_{k,i}^{T} \tag{3.36}$$

Where $\ln k$ is permeability, ϕ is porosity, P is pressure, S_w is saturation and Tr is transmissibility and the superscript T denotes the transpose. When geomechanical processes are considered, the state vector is extended to include the corresponding model parameters and state variables

$$\boldsymbol{x_{k,i}}^{T} = \begin{bmatrix} \ln \boldsymbol{k}^{T}, \boldsymbol{\phi}^{T}, \boldsymbol{E}^{T}, \boldsymbol{\nu}^{T}, \boldsymbol{P}^{T}, \boldsymbol{S_w^T}, \boldsymbol{Tr}^{T} \\ \boldsymbol{\sigma_{xx}^T}, \boldsymbol{\sigma_{yy}^T}, \boldsymbol{\sigma_{zz}^T}, \boldsymbol{\sigma_{xy}^T}, \boldsymbol{\sigma_{xz,}^T} \\ \boldsymbol{\sigma_{yz,}^T}, \boldsymbol{\varepsilon_{xx}^T}, \boldsymbol{\varepsilon_{yy}^T}, \boldsymbol{\varepsilon_{zz}^T}, \boldsymbol{\varepsilon_{xy}^T}, \\ \boldsymbol{\varepsilon_{xz}^T}, \boldsymbol{\varepsilon_{yz}^T}, \boldsymbol{u}^{T}, \boldsymbol{v}^{T}, \boldsymbol{w}^{T} \end{bmatrix}_{k,i}^{T} \tag{3.37}$$

where E indicates Young's modulus, ν indicates Poisson's ratio, σ indicates stresses, ε indicates strains and u, v, and w are displacements. The augmented state vector Ψ_k may include all available observations such as bottom hole pressure and surface displacements.

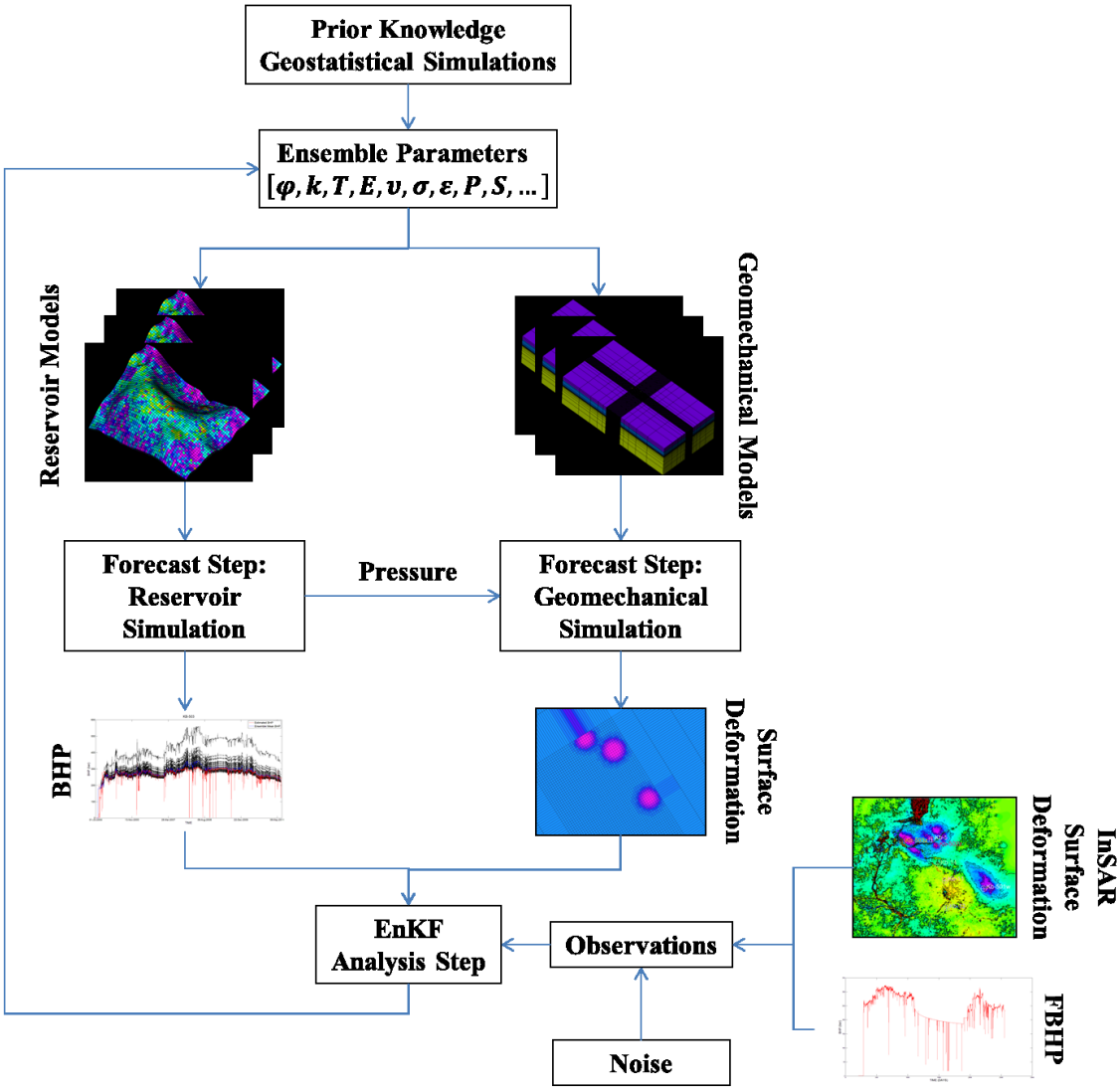


Figure 3.3: Workflow for assessing coupled flow-geomechanical performance monitoring for CO_2 storage sites.

Figure 3.3 shows a diagram describing the workflow for assessing the coupled flow-geomechanical performance of a CO_2 storage site. Constructing the initial ensemble is a crucial step. The initial ensemble contains information about the initial model parameters and their uncertainties. Geostatistical techniques are well established for representing heterogeneity and assessing uncertainty in flow parameters such as porosity and permeability (Deutsch, 2002). Geostatistical simulation algorithms provide a means of representing uncertainty in these properties by generating a large number of equi-probable realisations which honour any known characteristics through the use of hard or soft data usually in the form of core samples, well logs or seismic data. Geomechanical properties may also be derived from core samples, well logs and seismic data (Schön, 2004).

In the EnKF forecast step, the flow and geomechanical properties realisations can then be used as input for coupled flow-geomechanical simulation models as described in section 3.4.3 to assess the resulting uncertainty in outcomes such as bottom-hole pressure and surface deformation.

Observations such as bottom-hole pressure and InSAR surface deformation may be available for monitoring the CO_2 storage site. Adding measurement noise to the observations is also an important part for the methodology to work and will depend on the type of observation to be assimilated. Without the addition of measurement noise the system would be overly specified and have no solution.

The data assimilation or EnKF analysis step will then proceed to update the model parameters in a sequential manner as the observations become available.

3.4 *Summary and Discussions*

This chapter presented the methodologies and associated theory that will be used and further developed through implementation as described in the remainder of the thesis.

First, an external coupling module that has been developed to link the reservoir simulator ECLIPSE E300 with the geomechanical simulator FLAC^{3D} using a one-way coupling scheme was described. Using a forward approach, this will be the main modelling tool to analyse the coupled flow-geomechanical behaviour of CO_2 storage sites.Next, a method for inverting for reservoir pressure change from measured overburden deformation was described. The method is not limited to InSAR surface deformation but can also be used with other monitoring techniques such as time-lapse seismic time-strains.

The Chapter also reviewed the ensemble Kalman filter formulation, which was adapted to develop a methodology for coupled flow-geomechanical performance monitoring of CO_2 storage sites. This builds on the workflow, in which the ECLIPSE300-FLAC^{3D} coupling scheme remains the main modelling tool but is extended to include uncertainty in coupled flow-geomechanical parameters and data assimilation using the EnKF. The EnKF will be used to assimilate observations that may be available at CO_2 storage sites to update the parameters controlling the

performance of the CO_2 storage site. The remainder of the thesis will present the application of the developed methodology to the In Salah field data set.

Chapter 4 The In Salah CO_2 Storage Project

The In Salah CO_2 storage project is one of the largest carbon capture and storage projects to date. It has played a central role in demonstrating the feasibility of CO_2 storage in deep saline aquifers. The field experience at In Salah provides a valuable case study in managing large-scale CO_2 injections and highlights the importance of geomechanics and an integrated approach between modelling and monitoring to understand the field behaviour. Monitoring observations at In Salah suggest that the storage complex has experienced geomechanical changes at depth leading to interesting questions about the geomechancial behaviour of the system. Fault leakage, pre-existing fractures and induced hydraulic fractures have been proposed to explain the pressure, seismic, micro-seismic and surface deformation behaviour. Studies to date indicate that the overall storage complex has not been compromised and that the CO_2 is contained within the defined storage complex.

4.1 *The In Salah Project*

A major issue concerning carbon capture and storage is the lack of a sufficient number of field demonstrations. The four major operational fields where CO_2 is injected for the purpose of storage: BP's In Salah Field in Algeria, Statoil's Sleipner and Snøhvit sites in the North Sea and the Weyburn Field in central Canada, are intended to be used as experiments where theories and ideas can be tested using a

learn-as-you-go approach, in order to develop best practise principles and methodologies for future application to large scale CO_2 storage projects.

The In Salah industrial-scale CO_2 storage project in Algeria started operation in 2004 with CO_2 injection ending in 2011. CO_2 from several surrounding gas fields, which have a CO_2 content of 5-10%, is extracted from the produced gas to meet the sales gas-export specification of 0.3% CO_2 content (Mathieson *et al.*, 2010). In the past, normal industry practise for such gas production plants was to vent the separated CO_2 to the atmosphere. BP and its joint venture partners, Sonatrach and Statoil, invested in a project to dehydrate, compress, transport, and inject that CO_2 into the deep saline aquifer leg of the producing Krechba gas field. The In Salah joint venture obtained no commercial benefit from the CO_2 storage operation with its value solely derived from its role as an experimental and demonstration project to provide insights into geological CO_2 storage in deep saline formations. The In Salah joint industry project (JIP) was set up to monitor the CO_2 storage process. The monitoring technologies included a variety of geophysical, geochemical and production techniques which will be presented in detail in the following sections.

4.2 *In Salah geological setting*

The In Salah CO_2 storage site is situated in the central Algerian desert (Figure 4.1). The main CO_2 storage reservoir is the C10.2 formation, an anticline of 20-25 m thick Carboniferous sandstone at approximately 1,880 m depth. The main reservoir is overlain by the 20 m thick tight sandstone and siltstone C10.3 formation. These are in turn overlain by a 950 m thick formation of mudstone interbedded with thin dolomite and siltstone layers collectively referred to as the Visean mudstones (Figure 4.2). The C10 formations, together with the lower caprock (C20.1–C20.3) form the CO_2 storage complex at Krechba. The C20 units above the Hot Shale (C20.4) are referred to as the main caprock. The regional Hercynian unconformity separates the main caprock from the overlying Cretaceous sandstone deposits and the Pan-Saharan Aquifer, a key water source for the region. Figure 4.2 shows a stratrigraphic log of the In Salah site with the key geological horizons.



Figure 4.1: Geographic location of the In Salah field (Adapted from Mathieson *et al.,* 2010).

The reservoir anticline is estimated to have been formed in the Late Carboniferous to Early Permian during the Hercynian Orogeny under a NE-SW oriented principal compressive stress regime (Coward and Ries, 2003). Although the reservoir structure remained relatively un-faulted by the continued compression, some of the compression folds were breached by strike-slip faults. After the folding event, the faults experienced strike-slip movement. The Hercynian unconformity indicates substantial erosion, with up to 2 km of uplift, leading to stress relaxation and the formation of joints. The present-day stress regime is strike-slip with a NW-SE maximum horizontal stress direction. The complex structural history of the In Salah site is shown in Figure 4.3. A key feature of the interpreted structural geology is the presence of deep seated faults which in turn cause minor faults and associated fracture zones in the folding anticline where the CO_2 injection wells are located. Both folding and faulting relating fracturing can be inferred from the structural history.

Image log and core analysis have shown the presence of conductive fractures aligned with the present day stress field (Iding and Ringrose, 2010). The reservoir formation can be best described as a fracture-influenced, matrix dominated sandstone (Ringrose *et al.*, 2009).

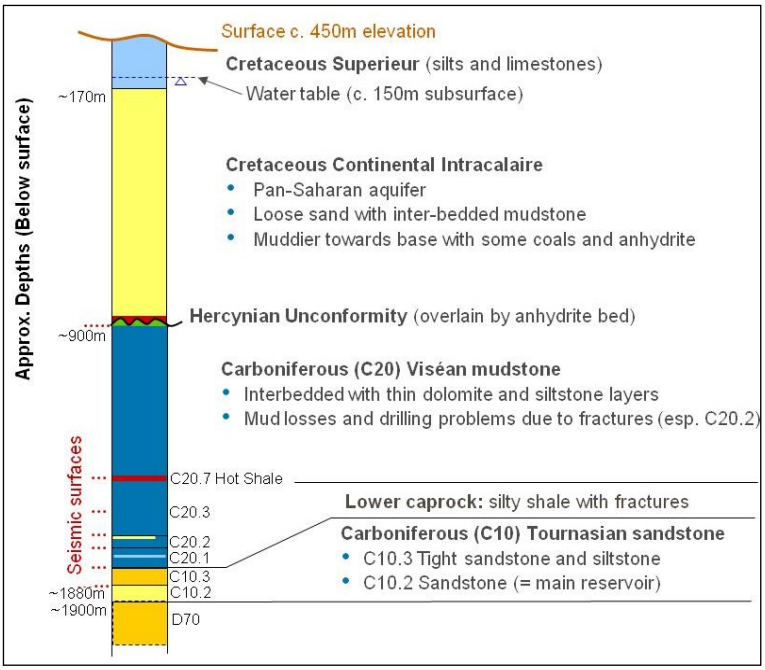


Figure 4.2: Krechba stratigraphic log (Courtesy of In Salah Gas Joint Industry Project).

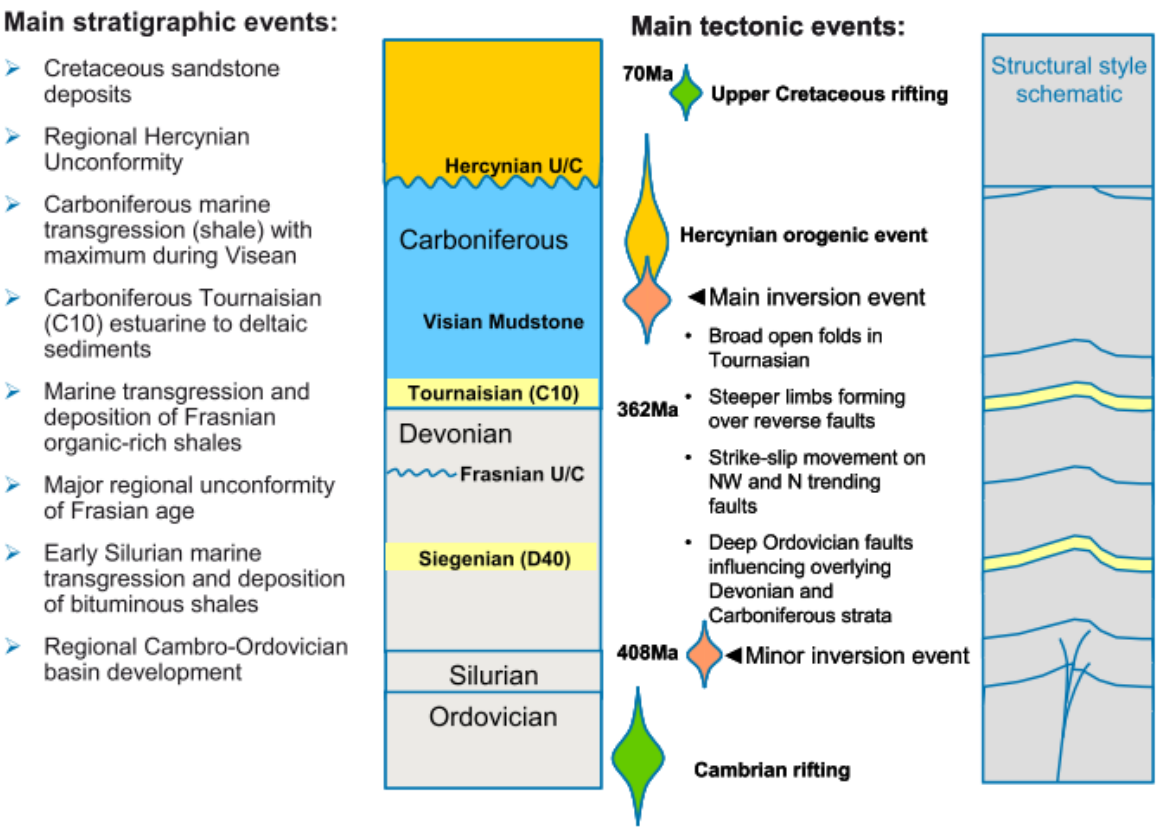


Figure 4.3: Structural geological setting for the In Salah area (After Ringrose *et al.*, 2011).

4.2.1 History of the In Salah Field

Over the injection period from August 2004 to June 2011 approximately 3.8 million metric tonnes of CO_2 have been separated from the extracted natural gas from the In Salah gas fields and re-injected into the aquifer leg of the Krechba field Carboniferous reservoir (Figure 4.4) through three horizontal injection wells KB-501, KB-502 and KB-503. The three state-of-art horizontal injection wells were drilled perpendicular to the maximum horizontal stress and the dominant fracture orientation in order to maximise the CO_2 injection capacity. The CO_2 injectors are long-reach wells that extend for several hundred metres across the reservoir formation. Figure 4.5 shows the location of the three CO_2 injection wells and the gas production wells.

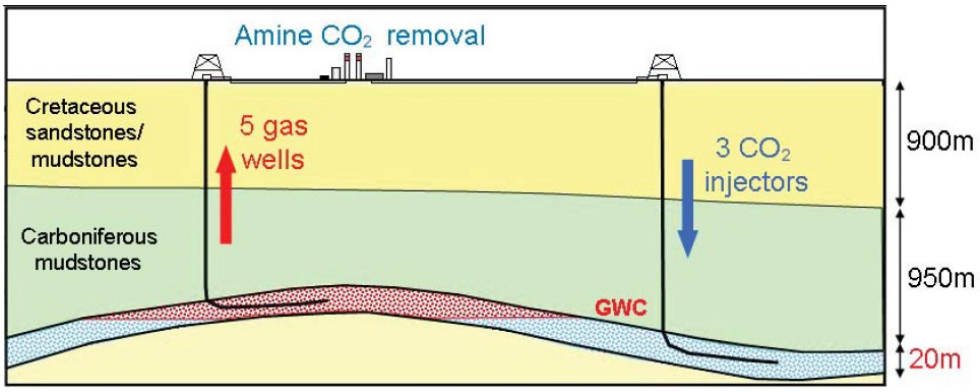


Figure 4.4: Schematic cross section at the Krechba injection site (After Mathieson *et al.*, 2010).

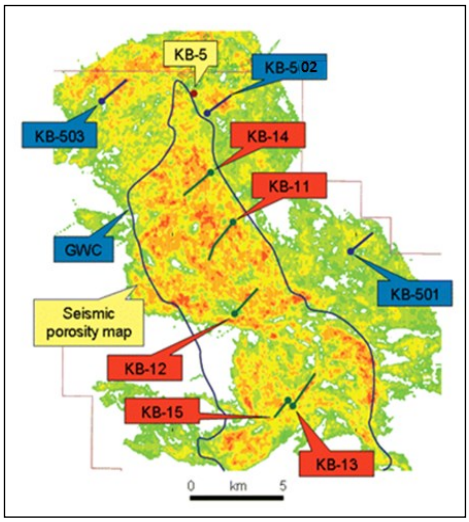


Figure 4.5: Krechba field map showing the location of the three CO_2 injection wells KB-501, KB-502 and KB-503 and the production wells. The black line indicates the gas-water contact (After Mathieson *et al.*, 2010).

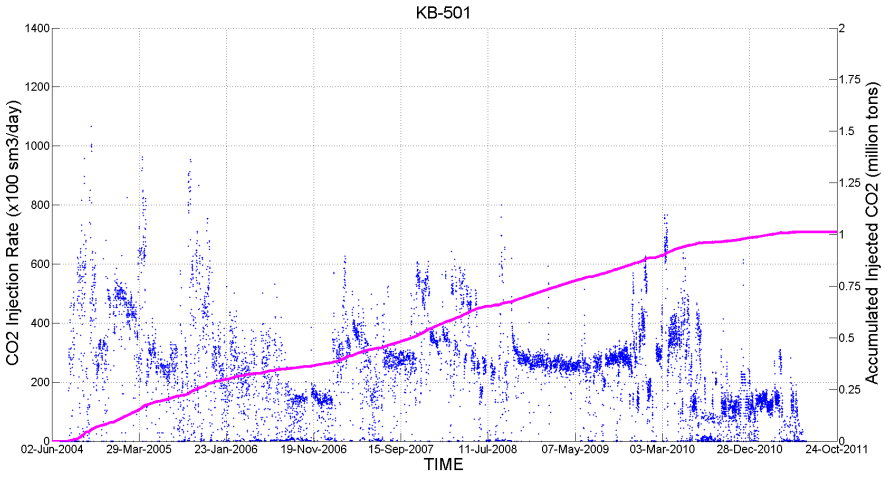


Figure 4.6: Daily injection rates and cumulative CO_2 injected at well KB-501.

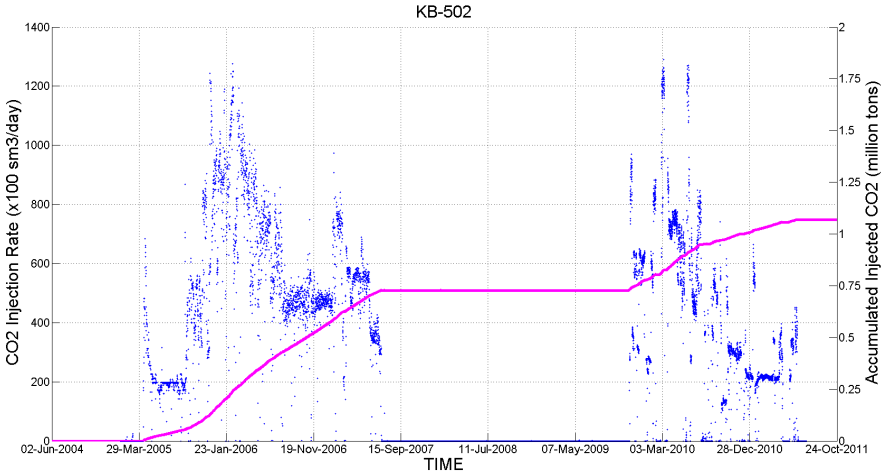


Figure 4.7: Daily injection rates and cumulative CO_2 injected at well KB-502.

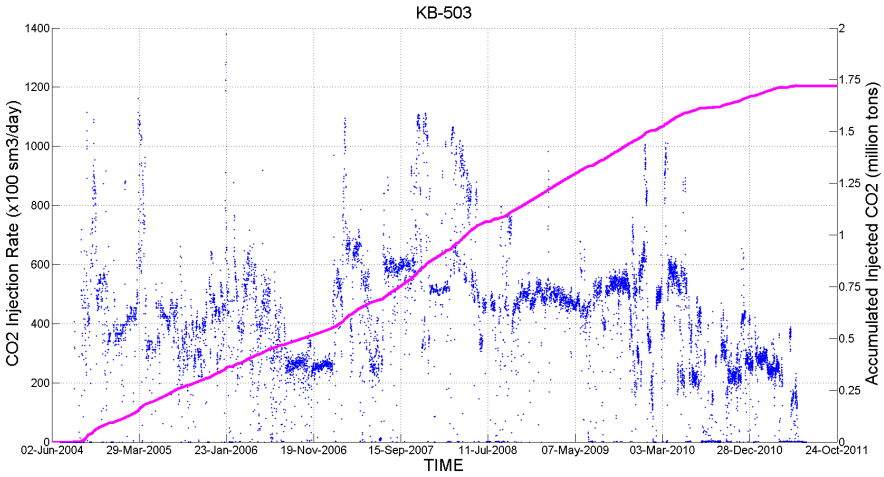


Figure 4.8: Daily injection rates and cumulative CO_2 injection at well KB-503.

The injection rate history and the cumulative amount of CO_2 stored at each of the injection wells are shown in Figures 4.6 to 4.8. At injection well KB-501 approximately one million metric tons of CO_2 have been stored. At well KB-502 approximately 1.1 million metric tons of CO_2 were stored and approximately 1.75 million metric tons of CO_2 were stored at well KB-503. CO_2 injector KB-502 was shut-in during the 2007-2009 period. The daily injection rates show a complex injection history with many fluctuations at all three injection wells.

4.3 *Monitoring at In Salah*

A range of monitoring techniques has been suggested for use at CO_2 storage sites. Determining the appropriate monitoring technique will depend on cost, monitoring requirements and site location. Seismic surveys for example are more expensive onshore than offshore. A cost analysis will be required to determine which monitoring technologies are most appropriate. Figure 4.9 shows the analysis performed at the In Salah site (Mathieson *et al.*, 2010).

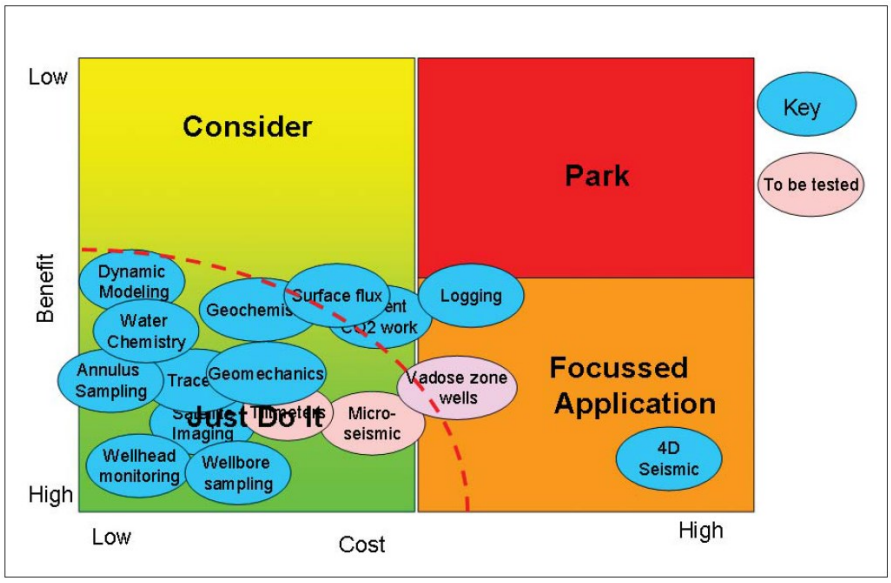


Figure 4.9: Monitoring technologies under consideration at the In Salah site (After Mathieson *et al.*, 2010).

Monitoring data includes geochemical, geophysical, geological and satellite data. Standard oil and gas industry geological characterisation data have been collected. This includes wireline and well logging suites, core sampling and seismic surveys. Geochemical monitoring data include surface and soil gas monitoring and down-hole gas measurements. Tracer chemicals are added to the injected CO_2 at each well in

order to distinguish it from natural CO_2. Should leakage be detected in can be traced to one of the injection wells. A downhole geophone detector has also been installed for the purpose of monitoring microseismic events. Even though time-lapse seismic surveys incur a high cost, they have been acquired given their high potential benefit. In particular the use of InSAR satellite monitoring has proven to be successful at detecting subtle ground deformation above the injection wells.

4.4 *Monitoring at well KB-5*

One of the first important insights into the CO_2 plume development at In Salah was acquired by monitoring CO_2 breakthrough at a suspended appraisal well (KB-5) (Ringrose *et al.*, 2009). Well KB-5 is located 1.5 km to the NW of injection well KB-502 (Figure 4.5). A breakthrough occurred sometime between two well-head inspections in August 2006 and June 2007. Perfluorocarbon tracers were injected into all three CO_2 injection wells on 1 June 2007. In March 2008 the KB-502 tracer was first detected confirming that the source of the breakthrough was the injected CO_2. This earlier than expected breakthrough detected at KB-5 suggested the existence of a highly permeable pathway connecting the two wells.

4.5 *Bottom hole pressure monitoring*

Bottom hole pressure (BHP) was not measured directly and all BHP estimates at all three CO_2 injection wells are estimated from well head pressure (WHP), flow rate, and temperature using a well model. Bissell *et al.* (2011) describe a well model used to convert WHP to BHP. There is uncertainty regarding the BHP conversion with discrepancies up to ~30 bar between the In Salah JIP model and that of Rinaldi and Rutqvist (2013) and Shi *et al.* (2012).

4.6 *InSAR monitoring at In Salah*

Surface deformation uplift has been observed extending laterally for several kilometres at all three CO_2 injection wells using Interferometric Synthetic Aperture Radar (InSAR) monitoring. InSAR can measure surface displacement at sub-mm accuracy and has a spatial resolution of a few tens of metres. InSAR measurements indicate uplift of approximately 2 cm after five years of injection. Figure 4.10 provides a snapshot of the measured deformation in January 20, 2012. The surface

uplift suggests preferential flow parallel to the direction of the present day maximum horizontal stress (NW-SE). Of particular interest is the deformation pattern around KB-502. Unlike the other two injection wells it displays an unusual, double-lobe pattern. A central trough is superimposed on the overall uplift pattern running perpendicular to the well but parallel to the estimated present-day maximum horizontal stress. This deformation pattern has been evaluated independently by three independent groups: Onuma and Ohkawa (2009), Vasco *et al.* (2010) and MDA (MacDonald, Dettwiler and Associates), Canada and Pinnacle Technology.

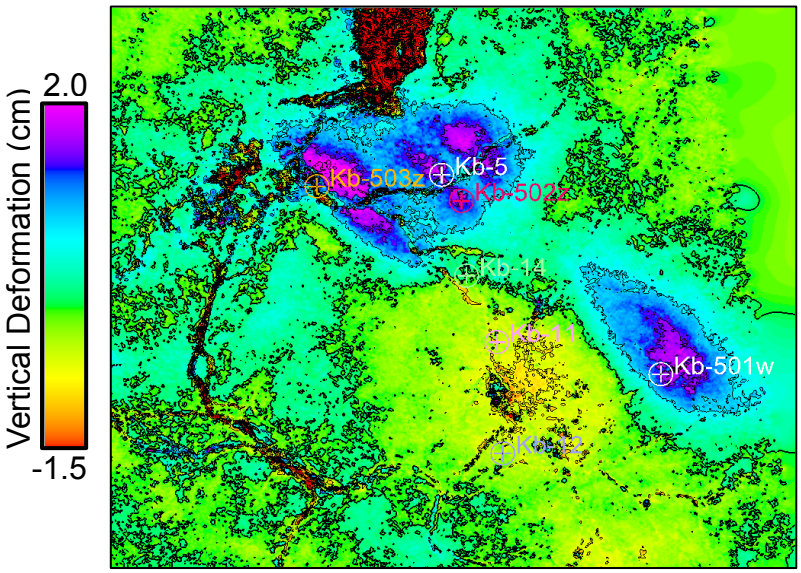


Figure 4.10: Janurary 20, 2012 Surface deformation detected over the CO_2 injection and production wells using PSInSAR (Courtesy of the In Salah Gas Joint Industry Project).

The InSAR monitoring and data processing at In Salah went through three stages during the CO_2 injection period as:

ENVISAT 2003-2009 monitoring campaign - During the period 2003-2009 only an ENVISAT descending dataset was available for monitoring. For this period of time only the component of displacement along the line of sight of the ENVISAT satellite was able to be measured.

X-Band 2009-2012 monitoring campaign - During the period 2009-2012 X-band SAR scenes from both ascending and descending geometries were acquired. By combining these data both vertical and East-West components of the displacement vector were estimated.

Envisat and X-Band joint analysis - In order to retrieve an InSAR time series spanning the 2003-2012 period, both the vertical and East-West components of

displacement provided by the analysis of X-band data were projected along the line-of-sight of the ENVISAT satellite. A time series of displacement data covering the entire period of displacement data 2003-2012 is available only along the line-of-sight of the satellite.

4.7 *Seismic Surveys*

The 3D seismic surveys acquired over the In Salah field are:

1997 Seismic survey - A pre-injection 3D seismic survey was acquired in 1997, with the aim of imaging the reservoir section. The seismic survey was acquired with conventional land seismic methods. The survey consisted of a shot/receiver spacing of 480 m and a bandwith of 6-70 Hz. The data were reprocessed in 2006 with little improvement in the imaging of the overburden section. Seismic interpretation of the 1997 seismic survey, mapped a fault or delineation intersecting the horizontal leg of KB-502 (Ringrose *et al.*, 2011).

2009 Seismic survey - In 2009 a 3D seismic survey of a much higher quality was acquired in the northern part of the Krechba field, with the aim of improving the imaging of the reservoir-caprock system. The 2009 seismic survey used an improved receiver line spacing of 160 m resulting in a higher fold and an improved bandwith of 6-90 Hz. These lead to a significantly improved imaging of minor faults and lead to an updated structural interpretation of the site (Figure 4.11).

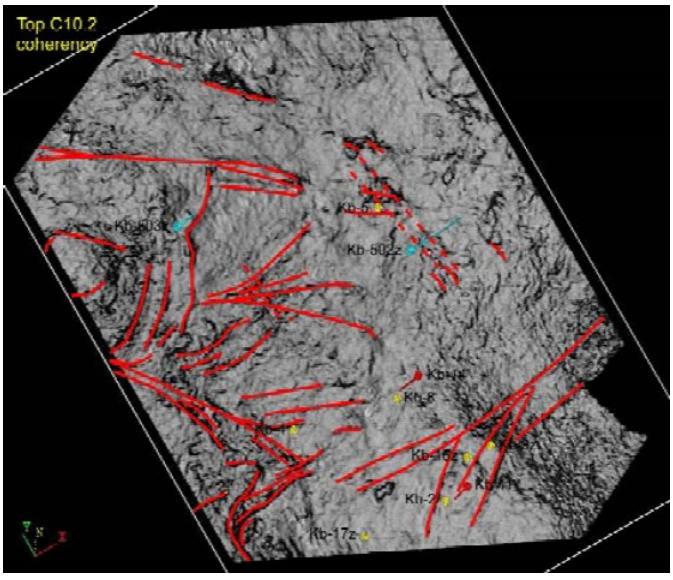


Figure 4.11: Updated fault interpretation from 2009 3D seismic survey (After Ringrose *et al.*, 2011).

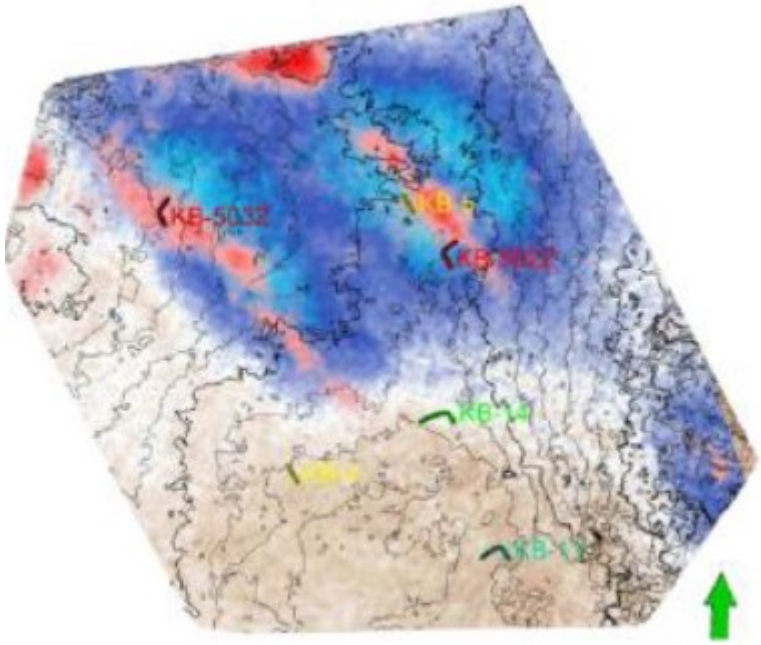


Figure 4.12: Time-lapse seismic time-shifts (red) superimposed on the InSAR surface uplift (blue) at injection wells KB-502 and KB-503 (Courtesy of M. Nickel, Schlumberger Stavanger Research, Norway).

Time-lapse seismic analysis - Using the 1997 baseline survey and the 2009 repeat survey on the northern segment of the field, covering injection wells KB-502 and KB-503 only, a time-lapse analysis was performed by Schlumberger. Their analysis revealed seismic anomalies in the form of time-shifts above injectors KB-502 and KB-503. Figure 4.12 shows the time-lapse seismic time-shifts superimposed on the InSAR data showing a strong correlation. In should be noted, however, that the results are subject to significant uncertainty due to repeatability issues between the base-line and repeat seismic survey.

4.8 *Microseismic monitoring*

Microseismic recording at the In Salah site is limited. The recordings came from a single geophone string in a shallow well (KB-506). Of the 48 three-component downhole geophones only one geophone was oriented correctly and provided reliable data (Oye *et al.*, 2013). The microseismic recording started in July 2009, well after injection operations had begun (Eiken *et al.*, 2011). Despite these limitations, microseismic events have been recorded by the single geophone (Oye *et al.*, 2013).

4.9 *Hypotheses for the geomechanical behaviour of the reservoir and caprock system*

In this section the proposed hypothesis to explain the available monitored data at the In Salah site are reviewed. The four plausible hypotheses to explain measured seismic, bottom hole pressure, micro-seismic and surface deformation have been summarised by White *et al.* (2014) as follows:

- Reservoir-only behaviour: The CO_2 and the injection induced excess pressure are contained within the reservoir formation.
- Fault leakge: The reservoir is intersected by vertical faults, providing a permeable migration path.
- Hydrofracture: Injection has created new fracture pathways through tensile opening.
- Pre-existing fractures: Pre-existing fractures are intrinsically permeable or can be reactivated by pressure.

Most of the published literature is focused on injection well KB-502 due to its unusual split two-lobe uplift pattern but analysis presented on the other injection wells are also included.

4.10 *Evidence for reservoir-only pressurisation*

The first hypothesis proposed is that the monitoring data can be explained by the excess pressure and CO_2 being confined to the reservoir interval only. In one of the early attempts to understand the two-lobe uplift pattern at injector KB-502, Vasco *et al.* (2008) performed a linear inversion of the diffusive pressure traveltime estimates from InSAR data. This method makes the assumption that the pressure changes are constrained to the reservoir formation and the underlying mechanism is the iso-volumetric expansion of the grid cells. Their results revealed pressure propagation along two northwest-trending corridors suggesting the existence of two northwest trending high-permeability zones. In other words, it is possible that the observed surface deformation could result from a heterogeneous permeability distribution in the reservoir interval. Figure 4.13 shows the permeability estimates at the reservoir level for KB-502.

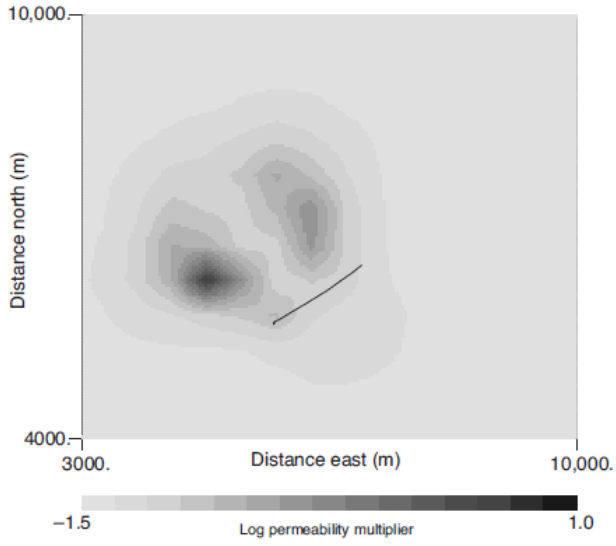


Figure 4.13: Logarithm of permeability estimates at the reservoir interval at injection well KB-502 (After Vasco *et al.*, 2008).

Durucan *et al.* (2011) used the inferred permeability pattern from Vasco *et al.* (2008) in a forward flow modelling study where the permeability pattern could be scaled by a multiplier in order to achieve a better match to the bottom hole pressure data and matched the CO_2 breakthrough at KB-5. Rutqvist *et al.* (2010) coupled a flow model with a geomechanical model and used the InSAR data itself to constrain the modelling. The study concluded that most of the observed surface uplift magnitude could be explained by the pressure-induced, pro-elastic expansion of the reservoir 20 m thick zone. It was stated however that there could potentially be a contribution to surface uplift by the pressurisation of 100 m of the lower caprock. This was done by tuning a uniform matrix permeability value for the reservoir and the caprock but the history-matching process is non-unique. In this study it was assumed that the injection pressures remain below the fracture pressure.

Subsquent work however, provided an altogether different interpretation of the injection process at KB-502. Although, the two-lobe uplift pattern can be explained by the isotropic volumetric expansion of the reservoir, it can also be explained by the tensile opening of a fault/fracture at depth (Figure 4.14) (Davis, 1986).

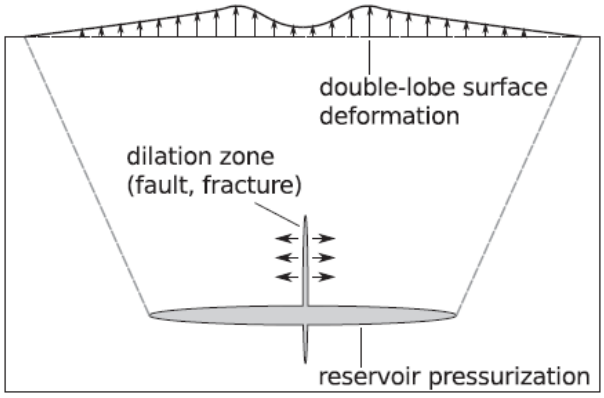


Figure 4.14: Proposed mechanism to explain double-lobe deformation (After White *et al.*, 2014).

Vasco *et al.* (2010) then perfomed a deterministic inversion of InSAR data assuming the mechanism included the tensile opening of a fracture at depth. Although, the geometry of the fracture/fault plane is assumed to be known, the InSAR data was inverted to estimate the aperture changes. The results suggest aperture changes of the order of several cm near the injection well and the fracture/fault plane is assumed not to exceed 40 m above and below the reservoir formation (Figure 4.15). Table 4.1 shows the estimated fault/fracture properties from the inversion.

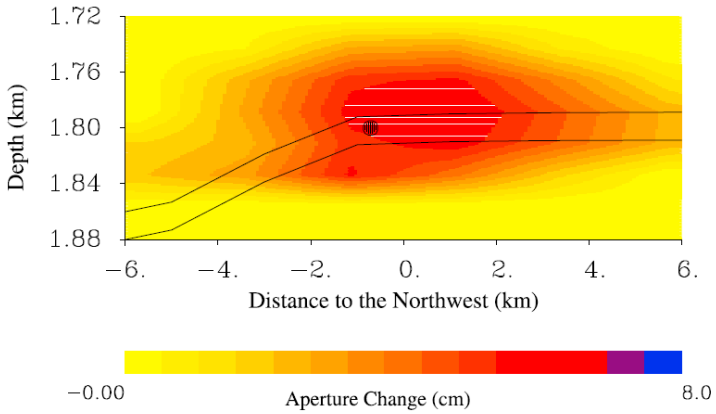


Figure 4.15: The spatial distribution of aperture change over the vertical fault/fracture model at KB-502 from the inversion of surface uplift data (After Vasco *et al.*, 2010).

Again, it was this inverse approach that served as the basis for later forward modelling studies. Based on this work, forward coupled flow-geomechanical studies aimed to reproduce the pressure and surface uplift pattern assuming the tensile opening of a fracture intersecting injection well KB-502.

Table 4.1: Fault/fracture properties derived by Vasco *et al.* (2010).

Azimuth	319
Dip	89
Depth	1800 m
Height	100 m ±80 m
Length	5-7 km

Bissell *et al.* (2011) explicitly modelled the hypothetical fractures from the Vasco *et al.* (2010) inversion at injection well KB-502 and attempt to match the bottom hole pressure and the surface uplift. In order to match the surface uplift a Young's modulus multiplier for the entire subsurface was used. A key insight was the introduction of a fault/fracture zone with dynamic transmissibility at KB-502 by Shi *et al.* (2012). A history match of the bottom hole pressure in terms of the fault/fracture zone dynamic transmissibility was found to be consistent with field observations. Shi *et al.* (2012) interpreted the results as the tensile opening and subsequent growth of the fault/fracture zone.

Rutqvist *et al.* (2011) also based their coupled flow-geomechanical modelling on the previous inversion work. The fracture/fault zone is modelled to have an elastic response to pressure inflation and deflation. However, in order to fit the surface uplift they tune the anisotripic elastic properties of the fault/fracture zone. The coupled flow-geomechanical modelling includes thermal effects to assess the potential for induced seismicity. At the time, it was concluded that the potential for induced microseismicity was low. However the estimate was based on a single value for the maximum horizontal stress which is subject to uncertainty.

The most detailed forward coupled flow-geomechanical modelling study at KB-502 by Rinaldi and Rutqvist (2013) aimed to constrain the vertical extent of the fault/fracture zone by matching both the bottom hole pressure and the transient evolution of the InSAR surface uplift. It should be noted however, that the modelling results are non-unique and model the fault/fracture zone as a single feature with constant flow properties. The fracture growth and the permeability dependence on stress are not considered.

Whereas previous inversion work only used the line-of-sight component of the InSAR data which was approximated as the vertical component of deformation, Rucci *et al*. (2013) combined InSAR data from ascending and descending orbits to estimate both quasi-vertical and quasi-east-west displacements. This provides an additional constraint when fitting a model to the geodetic data (Dieterich and Decker, 1975; Wright et al., 2004). However, the problem is highly non-unique. Nonetheless, a better fit to the data is provided by using both volumetric and aperture changes near the injection wells.

4.11 *Evidence for pre-existing fractures*

Another interpretation is that CO_2 is migrating via pre-existing fracture networks. Iding and Ringrose (2010) presented an extensive fracture characterisation for the In Salah CO_2 storage site. They used available data from Formation Micro-Imager (FMI) and Ultrasonic Borehole Imager (UBI) logs, core samples and mud loss observations:

Core Samples - Core samples from six wells were used to assess the potential of conductive fractures. Several partially cemented fractures proved to be conductive at surface conditions. The fractures are near-vertical and appear to be controlled by the present day stress field. However, it was not attempted to extrapolate the conductivity of fractures at subsurface conditions.

FMI logs - Interpreted image logs from two wells at the reservoir and lower caprock level suggest dominant near-vertical NW-SE fracture orientation. Fracture apertures estimated from the FMI logs range between 10^{-4} to 10^{-3} m. However, these estimates are subject to significant uncertainties as they may be affected by well-bore damage.

Mud-loss data - Mud-loss events during drilling were used to understand the fracture characteristics and estimate fracture apertures. In practice, a mud loss event provides information for the most conductive fracture intersecting the wellbore. Assuming single phase flow in a single fracture an analytical solution was employed to estimate apertures on the order of 10^{-4} m at the reservoir and lower caprock level (Iding and Ringrose, 2010). This is much smaller than the several cm aperture increases from inversion work.

4.11.1 Discrete Fracture Network Modelling

After having integrated all fracture data available Iding and Ringrose (2010) then proceeded to explicity model discrete fracture networks (DFN). In a DFN the fractures are represented explicitly in a three-dimensional grid and estimate the contribution of the discrete fractures to the effective permeability of the fractured medium (Cacas et al., 2001; Oda, 1985). In addition to characterising the fracture networks in the subsurface, Smith *et al.* (2011), for example, developed a methodology to analyse the connectivity of fracture networks prior and post CO_2 injection. A large number of possible fracture distributions are modelled and include shear and tensile failure criteria to include the uncertainties present in the available measurements and the models used. However, these methods do not simulate and couple the flow and geomechanical effects of CO_2 through discrete fractures that can be further conditioned on dynamic data.

Bond *et al.* (2013) used the updated structural interpretation from the 2009 seismic survey and the available fracture data from the In Salah CO_2 storage site to reconstruct the structural history of the site. The top reservoir surface was used as the main structural modelling horizon. The surface was restored to an unfaulted/undeformed state using a geomechanical algorithm. The restored surface was then forward modelled to predict the spatial distribution of strain. The strain predictions where then used as input for a fracture model to predict both fold and fault related fractures. Although many fractures sets may have been created over time, cementation processes can seal conductive fractures over time. A comparison to the InSAR surface uplift patterns suggests it is the fractures that are preferentially aligned with the present day stress field that are conductive and will control the migration of the CO_2.

Cavanagh and Ringrose (2011) presented preliminary results of modelling CO_2 flow an In Salah using high resolution models in order to capture the heterogeneity related with respect to faults and fracture distributions. The high resolution method however has not been coupled with a geomechanical model.

4.12 *Evidence for fault leakage*

Ringrose *et al.* (2011) performed a fault interpretation using 3D seismic data. The interpretation is based on reflector offsets from the 3D seismic volume to identify the main faults. This was combined with the use of seismic attributes such as coherency to identify smaller features (Chopra and Marfurt, 2007). It is clear from the interpretation that the reservoir C20.1 seismic horizon is never fully offset by a fault and the identified faults are all on the limit of seismic resolution. Sub-seismic faults however may be present. The inferred stress regime from the seismic interpretation is a strike-slip stress regime with the vertical stress being the intermediate stress. White *et al.* (2014) summarised the drilling records for KB-502. According to evidence from well cuttings and logging, during the drilling of the horizontal section through C10.2, the well reentered the C10.3 unit. This was interpreted as the presence of an offset fault intersecting the injection well. Injection well KB-502 was subsequently deviated downwards to re-enter the C10.2 formation once again. It should be noted however that the encounter with the interpreted fault does not coincide with the fault interpretation from 3D seismic data. It should also be noted that the latest fault interpretation shows a number of orientations but no preferential alignment with current stress-field estimates.

Early CO_2 breakthrough was observed at the appraisal well KB-5. Based on the interpretation of the 1997 seismic survey a fault connecting injector KB-502 to KB-5 was mapped (Ringrose *et al.*, 2009). The interpreted fault is slightly deviated from the direction of the maximum horizontal stress by ~15^{o}. The fault however was not visible in the higher quality 2009 seismic survey. The fault interpretation is shown in Figure 4.16.

Using analytical solutions for internal displacements in a shear fault in a half-space, (Okada, 1985) such deformations would induce asymmetric uplift pattern at the surface. Given that the current stress regime is interpreted as strike-slip, there is no evidence from InSAR data of lateral shear displacements along a strike-slip fault. The surface uplift expression is in agreement with the theoretical predictions of a tensile source at depth.

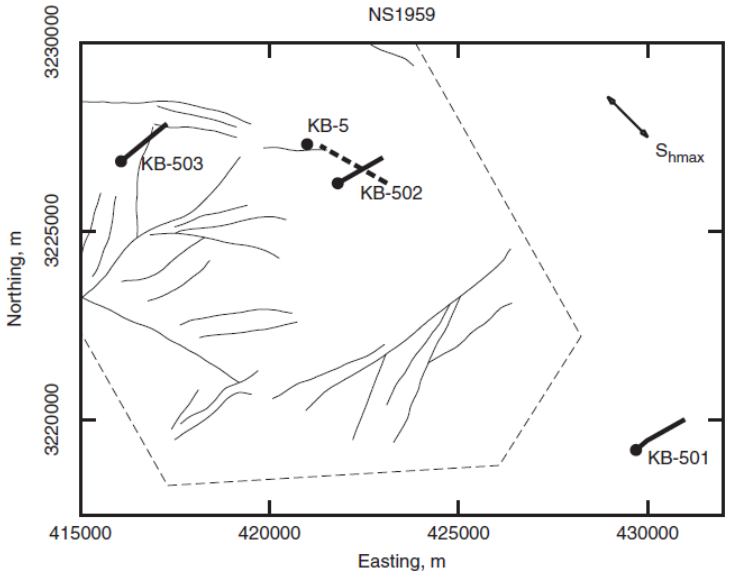


Figure 4.16: Fault interpretation at the reservoir interval (C10.2). The solid lines correspond to the fault interpretation from the 2009 seismic survey. The dashed line is a fault interpreted in the 1997 survey but not visible in the higher quality 2009 survey (After White *et al.*, 2014).

Gemmer *et al.* (2012) used forward 2D plane-strain finite element modelling to calculate the stress and strain resulting from the pore pressure changes associated with CO_2 injection and gas production. A better match to the surface uplift was found by introducing an intersecting fault at the injection wells.

In a forward coupled flow-geomechanical study at KB-502 by Morris *et al.* (2011), conducting and bounding faults were introduced into the model to understand the morphology of the observed surface uplift pattern. They achieve a better agreement with the magnitude and the shape of the uplift pattern by including fluid flow into a vertical extension of the 400 m vertical fault centred on the C10.2 reservoir interval. However, there analysis required assumptions about the overburden and fault geomechanical properties and geometry. In particular the data could be fit just as well with a fluid filled fault entirely above or below the reservoir interval.

4.13 *Evidence for hydro-fracturing*

Another interpretation is that the rise in pressure due to CO_2 injection resulted in the hydro-fracturing of the reservoir and the lower caprock. In order to establish the onset of hydro-fracturing both the pressure and the fracture pressure need to be estimated. Assuming fractures already exist, the tensile opening of the fracture is

initiated when the pressure inside the fracture exceeds the prevailing minimum horizontal stress normal to the fracture.

$$p_f > \sigma_h \tag{4.1}$$

Bissell *et al.* (2011) estimated a fracture pressure of 286 bar using log data and a semi-empirical calculation. Shi *et al.* (2012) published a portion of the leak-off tests and formation integrity tests available. The estimates of the minimum horizontal stress were taken as the fracture pressure. A discontinuity in the minimum horizontal stress profile was observed in the Visean C20 formation above the reservoir. From the higher leak off tests in the lower caprock the fracture pressure was extrapolated to the the reservoir interval to a value of 295 bar. Figure 4.17 shows the minimum horizontal stress profile and its interpolation.

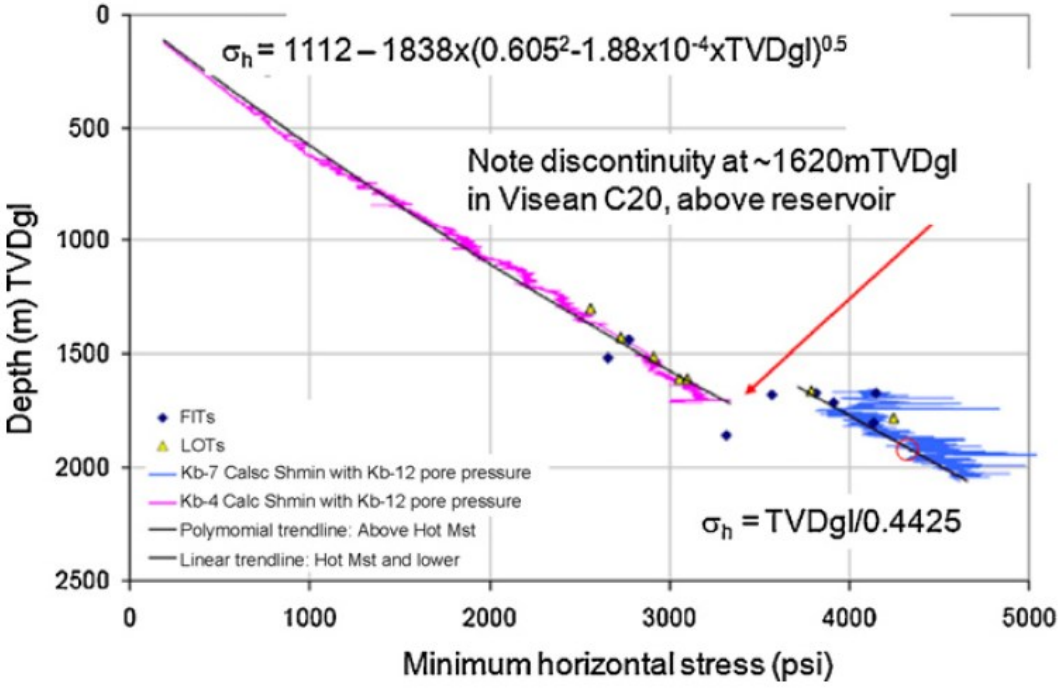


Figure 4.17: Estimated minimum horizontal stress profile. Red circle indicates the interpolated fracture pressure at the top reservoir (After Shi *et al.*, 2012).

White *et al.* (2014) subsequently extended the analysis by Shi *et al.* (2012) and compiled and performed a detailed analysis using all well test data available. These include production wells 9-14 and injection wells KB-501-KB-503. It was emphasised that the most direct measurement of fracture pressure comes from a step-rate test performed at KB-9.

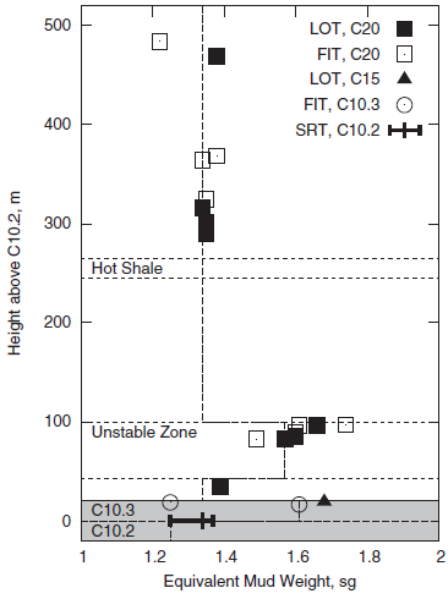


Figure 4.18: Leak-off test (LOT), formation integrity test (FIT), and step-rate test (SRT) data compiled from injection and production wells (After White *et al.*, 2014).

Figure 4.18 shows a compilation of all the well tests available. These include leak off tests (LOT), formation integrity tests (FIT) and a step rate test (SRT). The results are presented in terms of a pressure gradient using the equivalent mud weight (EMW). Hydrostatic conditions correspond to an EMW = 1.0 specific gravity (sg) = 0.1 bar/m. The formation integrity tests represented by hollow symbols signify that the formation could withstand the applied pressure without leak-off. A FIT can therefore not be used for the fracture pressure determination. The filled symbols represent the group of tests in which leak-off occurred. In this context, the fracture pressure refers to pre-existing fractures. In order to estimate the fracture pressure of intact rock a XLOT test would be required.

The data shows a consistent leak-off at EMW = 1.35 sg for the main Visean caprock (C20). A sudden jump is then observed ranging between 1.55 and 1.70 sg. This noticeable jump corresponds to wellbore stability issues encountered during the drilling of the lower caprock (base C20). This unstable zone is interpreted to be a layer of high tectonic stress. The step changes in fracture pressure for different lithologies suggest complex fracture growth should hydro-fracturing occur. At the C10.3 formation only formation integrity tests are available. A leak-off test was also acquired in the mudstone/limestone C.15 unit. At the main reservoir interval, C10.2, leak-off is observed around 1.25 sg.

It was concluded from the available well test observations that the fracture pressure could be exceeded in the sandstone and reservoir units for an EMW between 1.35 to 1.70 sg. At the C10.2 formation this corresponds to a fracture pressure range of 239-301 bar. At the C10.3 formation the estimated fracture pressure range is 237-298 bar. The difference in temperature between the cold CO_2 and the *in situ* reservoir temperature would give rise to thermal stresses. Bissell *et al.* (2011) explicitly take into account the induced thermal stresses and estimate that the cooling of the formation may reduce the fracturing pressure somewhere between 15-50 bars from its initial value. Rutqvist (2012) reached similar results by using an updated shear failure criteria to include the effects of both pore pressure increase and injection-induced cooling by using an expression from Perkins and Gonzalez (1984). Taking into account thermal effects increased the likelihood of shear failure in the near well-bore region.

Based on the fracture pressure estimates from these studies they can then be compared to bottom hole pressure estimates to test whether fracture initiation and propagation has occurred. It must be emphasised that the estimates of the fracture pressure and the estimated bottom hole pressure are subject to uncertainties and no estimate of the errors in the data is given. The only well test where the fracture initiation pressure is exceeded is the step-rate test. Furthermore, the well tests were performed with drilling mud. The behaviour is expected to deviate from injecting super-critical, cold CO_2. The well tests are also only representative in a small region near the wellbore. It should also be noted that some of the well tests previously mentioned were not acquired at the injection wells but from surrounding production wells. Interpolating these values introduces additional uncertainties.

Despite the uncertainties in the estimated fracture pressure for different lithologies and the estimated bottom-hole pressure, it appears that the fracture pressure has been exceeded. At injection well KB-502 a peak bottom hole pressure of 323 bar was estimated by the In Salah Joint Industry Project (Bissell *et al.*, 2011) in March 2006. Rinaldi and Rutqvist (2013) estimated a peak bottom hole pressure of 313 bar. Shi *et al.* (2012) used the most conservative estimate of 293 bar. The differences in estimates is related to the uncertainty in the bottom hole temperature (BHT).

The general observation is that, even for the most conservative estimates of the bottom hole pressure, these are high in comparison for the range of estimated

fracture pressure for the reservoir and lower caprock. A hydrofracture intersecting injection well KB-502 can also explain the timing of the appearance of the two-lobe uplift pattern from InSAR data.

Although it is injection well KB-502 that experienced the highest sustained injection pressure, the estimated bottom hole pressure at the other two injection wells also approaches and exceeds the 300 bar threshold. It is clear that using the estimated BHP and the estimated fracture pressure from all well tests available it can be assessed whether the fracture pressure has been exceeded, i.e. tensile failure has occurred. However, modelling the initiation and growth of the hydrofracture and constraining its geometry still remains a challenge.

Additional evidence supporting the hydro-fracture hypothesis has been provided by microseismic data analysis. Oye *et al.* (2013) correlate the injectivity index with the well head pressures. They found that the injectivity increases when well head pressures exceed ~155 bar (~297 bar BHP). This is within the upper end range of the fracture pressures estimated from the well tests. They associate these two distinct phases with different flow behaviour. Below a well head pressure of ~155 bar, CO_2 flow primarily occurs through the matrix permeability. Above that same well head pressure the CO_2 flows through discrete fractures. They relate the scatter around this trend to growth of fractures and their complex interaction with pre-existing fractures. They were then able to correlate injection rate behaviour with measured microseismic event frequency in the vicinity of injection well KB-502 suggesting the fracture pressures have been temporarily exceeded, resulting in a sudden increase in microseismicity. The observed correlation is between microseismic event frequency and WHP higher than ~155 bar (~297 bar BHP). However, a more extensive microseismic network would be required to resolve event locations.

Despite the mentioned uncertainties, the overall consensus is that the injection pressure is high in comparison with the fracture pressure of both the reservoir and caprock units suggesting injection-induced hydro-fracturing.

4.14 *Summary and Discussions*

The In Salah CO_2 storage site has vastly benefitted from a plethora of monitoring techniques applied at the site. Each monitoring data set on its own is subject to uncertainties and interpretation ambiguities. However, taken together a more

consistent picture begins to emerge. InSAR deformations, seismic anomalies and injection pressure behaviour suggest injection pressures exceeded the fracture pressures for the reservoir and lower caprock units. The evidence is stronger for KB-502, where the timing of the BHP peak correlates with the appearance of the split two-lobe uplift pattern. The creation of hydro-fractures, the re-activation of existing fractures, a combination of both or fluid migration through faults are possible mechanisms to explain the observations at the site.

An interpretation of the structural setting of the storage site provided a framework to understand the interplay between the present-day stress and existing tectonic features and predict the presence of conductive fracture anisotropy.

The compilation of all the well test data such as leak-off tests, formation integrity tests and step-rate tests gave an estimate of the range of possible fracture pressures encountered at depth. The bottom hole pressure estimates can then be used to establish whether fracturing has occurred. This interpretation is strongly correlated with the InSAR surface uplift in particular with the split two-lobe uplift pattern at KB-502, the time-lapse seismic anomalies and micro-seismic observations.

A major challenge however remains incorporating this insight into the coupled flow-geomechanical models and further calibrating our models to the available observations. In order to relate the detected surface uplift to the CO_2 injection process at depth, a well characterised geomechanical and geological model of the reservoir and overburden is required.

All of these studies have emphasised the importance of a well characterised geomechanical model. The geomechanical models must capture the heterogeneity. The variations in the rock mechanical stratification have a significant impact on the surface uplift predictions. The reservoir interval and the overlying tight sandstone formation are characterised by a high stiffness and are in turn overlain by low stiffness overburden shales. Log correlations indicate a significant change in geomechanical properties at the Hercynian Unconformity where the approximately 1 km shale caprock formation begins.

The modelling work utilised can be categorised into forward and inverse modelling. At the In Salah site it has been the inversion of InSAR surface uplift that has set the prevalent interpretation for subsequent forward coupled flow-geomechanical studies.

The inversion work performed to date is based on the assumption that the underlying mechanism for the surface uplift is known whether it be volumetric expansion pressure source or a tensile opening source. Vasco *et al.* (2010) inverts for both types of sources but there is an inherent trade-off between the two. The latest inversion study by Ramirez and Foxall (2014), for example, uses a homogenous geomechanical earth model and does not take into account the more detailed geomechanical models available from forward numerical studies. The most detailed forward coupled flow-geomechanical study to date by Rinaldi and Rutqvist (2013) does not attempt to directly infer flow and geomechanical parameters from InSAR and bottom hole pressure but simply attempts to reproduce the observations based on the currentinterpretation by Shi *et al.* (2012) of the tensile opening and subsequent growth of a fault/fracture zone with a dynamic transmissibility.

Most previous work only make use of a portion of the monitoring data. A framework for integrating monitoring data with detailed models is highly desirable. The remainder of this thesis will present the methodology developed for the integration between the monitoring data and the different modelling tools.

In Chapter 5 a reservoir pressure change inversion scheme is proposed that can use the numerical geomechanical models with variations in the rock mechanical properties. This will aim to close the gap between the simplified geomechanical models used in inverting surface deformation and the better characterised geomechanical models using forward coupled flow geomechanical studies.

To date, most of the literature has focused specifically on the behaviour at injection well KB-502. In Chapter 6 a forward coupled flow-geomechanical study will be performed at injection well KB-503 using insight from InSAR and time-lapse seismic data.

In Chapter 7 inverse and forward modelling are integrated using the EnKF. In an iterative process the predictions from an ensemble of coupled flow-geomechanical simulations can be systematically compared to the available observations and both flow and geomechanical parameters are updated at each time-step. This provides an integrated framework to analyse the performance of the entire CO_2 storage site.

In addition, it is also important to emphasise the CO_2 site selection process. A geological CO_2 storage site beneath a system of multi-layered overburden can be

very beneficial from a storage security perspective. Even in the case of hydro-fracturing or reactivation of a deep fault, such breakdown of the lower caprock units would not compromise the overall storage integrity. At In Salah a 950-m massive caprock provides a robust seal.

Chapter 5 Reservoir Pressure Change Inversion

Advances in satellite and seismic monitoring have made available reliable surface and subsurface deformation data. Inversion of these data sets are now beginning to be used to assess geomechanical behaviour and pressure changes in a reservoir. Past solutions to this inversion problem have relied on analytical approaches like the Geertsma approach assuming a homogeneous earth. In order to integrate a more realistic earth model, this research developed a reservoir pressure change inversion based on transfer functions derived from a numerical geomechanical model. The reservoir pressure change inversion scheme is applied to the In Salah CO_2 storage site using a numerical geomechanical model and a series of InSAR surface uplift data. Using the inversion scheme an estimate of the extent of the pressure plume from CO_2 injection is made at each injection well indicating the preferential flow directions.

5.1 *Review of Inverse Modelling using Overburden Deformation Data*

5.1.1 Analytical Approach

In the literature a number of solutions have been developed to relate overburden deformation to reservoir dynamics. The simplest approach is to assume uniaxial

vertical deformation for the reservoir and the overburden. Assuming linear elasticity, the observed deformation in the overburden is directly proportional to reservoir pressure change or volumetric change. The reservoir pressure change or volumetric change can be estimated by a direct projection vertically downwards into the reservoir and has been used to gain insight into the behaviour of strongly compacting chalks (Guilbot and Brackin, 2002).

A common formulation is the analytical solution for estimating deformation from a disc shaped source with a uniform pressure change throughout the disc (Geertsma, 1973). Segall (1992) later extended this work for general axisymmetric shaped reservoirs.

5.1.2 Semi-Analytical Approach

A more realistic mechanical propagation into the overburden is to use a Green's function representation for a point source of volumetric strain or pressure centered in the reservoir (Geertsma, 1966), commonly referred to as the nucleus of strain. The solution was developed for the limiting case of a homogeneous elastic whole-space or half-space using an analogy from thermo-elasticity (Mindlin and Cheng, 1950). This can be a starting point to determine deformations induced by reservoirs with arbitrary shapes and pressure profiles. This approach requires the nucleus of strain solution to be rescaled and integrated over the entire reservoir formation. As the analytical solution must be numerically integrated over the reservoir volume, this is considered a semi-analytical approach.

An extensive literature is available using this particular formulation. It has been used to understand surface subsidence at the Cerro Prieto geothermal field in Baja California, Mexico from InSAR measurements (Carnel and Fabriol, 1999). Applications also include the Genesis field, Gulf of Mexico where Hodgson *et al.* (2007) used subsurface strain measured from time-lapse seismic to estimate the reservoir pressure change from oil production. These applications however are limited to cases where there is no material property contrast between the reservoir and the overburden. Hodgson (2009) concluded that further investigation was required to develop solutions that account for reservoir/overburden material contrasts and arbitrary subsurface structure.

The analytical approaches for an idealised reservoir shape and the semi-analytical approach for a homogeneous half-space have remained in use as an alternative over numerical approaches. In many cases this is due to the lack of data to characterise a more complex geomechanical model (Kuvshinov, 2007). Numerical methods give more accurate results but at a relatively low speed. This is not just determined by the actual computation time but by the time spent setting up the model and collecting data to adequately characterise the model. It is not only the reservoir but the entire overburden that needs to be characterised.

5.1.3 Numerical Approach

For the more realistic case of layered media, the nucleus of strain solution cannot be found analytically. Garcia *et al.* (2010) developed a method using Weiner filters for relating overburden displacements to reservoir depletion. The method was demonstrated on the Elgin Field, North Sea. Compared to previous methodologies, the method is able to capture structural variations and material contrasts in the subsurface using a small number of numerical geomechanical simulations. Garcia and Macbeth (2013) applied the method to the Ekofisk, Field. In the latter study the Geertsma approach and the Weiner filter approach were compared. The Weiner approach resulted in considerably smaller errors than using the analytical Geertsma solution.

It should be noted that other approaches have been proposed. Fares and Li (1988) developed a plane-layered elastic solution. Chow *et al.* (1991) developed a generalized version of the image source technique. The propagation of the mechanical field may also be obtained by finite differences (Vasco *et al.*, 2000), finite elements (Settari and Mouritis, 1998) or boundary elements (Muntendam-Bos *et al.*, 2008). However, the widespread application of these approaches for the inverse problem has been prevented by their prohibitive computational expense. Some of these methods for example would require a full field simulation of all the potential reservoir sources in order to generate the respective Green's functions.

The Weiner filter approach is a compromise between the analytical solutions for idealised subsurface geometries and the use of a complete numerical simulation. By using a pre-determined number of reservoir pressure sources it provides a far less time-consuming approach than a complete numerical simulation or the use of the

Geertsma approach. It is also able to capture the structural variations and geomechanical material contrasts.

5.1.4 Deterministic vs. Stochastic Inversion

The application of the inversion schemes described above are deterministic and have remained popular due to the computational effort required for a stochastic inversion. Recently, Ramirez and Foxall (2014) used a stochastic inversion to assess the probability that pressure pertubations resulting from CO_2 injection penetrated into the lower caprock seal above the reservoir at one of the injection wells at the In Salah CO_2 storage site. They were able to include multiple deformation modes such as pressure induced volumetric changes and tensile opening. However, they do no make use of the more complex geomechanical models available at the In Salah site and simplify their analysis by the assumption of a homogenous half-space.

5.2 *Green's functions vs. transfer functions*

5.2.1 Linear Filters

Linear digital filters have long been used in geophysical problems. The basic principle underlying a linear filtering process consists in defining a desired and an actual output signal. It is then possible to minimise the difference between the desired and the actual output signal. The solution is the optimum or least squares filter that minimises the difference. This filter is commonly known as the Weiner filter (Wiener, 1964) and is uniquely characterised by its transfer function. The transfer function may simply represent a poorly understood linear relationship between two arbitrary signals. In other cases, the transfer function has a physical meaning. In the case of structures, the transfer function may represent the reciprocal of the mechanical impedance function. In the case of seismic wave propagation it may represent the reciprocal of the acoustic impedance. In electrical circuits, transfer functions are also used to represent any linear process. For the relation between deformation and reservoir pressure change, the transfer functions represent the geomechanical model of the earth.

5.2.2 Green's Function and Transfer Function Comparison

In this section the relationship between the Green's function and the more general transfer functions is presented. A Green's function is the impulse response of a system of differential equations defined on a domain. A Green's function $g(x, x_0)$ of a linear differential operator L^n of n degrees is any solution of the form:

$$\boldsymbol{L^n[g(x, x_0)] = \delta(x - x_0)} \tag{5.1}$$

where L^n represents the equations governing the system and $\delta(x)$ is the Dirac delta function. If the operator is translation invariant then the Green's function can be taken as a convolution operator.

$$\boldsymbol{g(x, x_0) = g(x - x_0)} \tag{5.2}$$

This occurs when the operator L^n has constant coefficients with respect to x. The properties of the Green's function can be exploited to solve differential equations of the form:

$$\boldsymbol{L^n[y(x)] = f(x)} \tag{5.3}$$

where the forcing function $f(x)$ of an arbitrary distribution may be expressed as a sum of localised pulses

$$\boldsymbol{f(x) = \int f(x_0)\delta(x - x_0)dx_0} \tag{5.4}$$

Assuming the Green's function $g(x, x_0)$ can be found for the operator L^n and then multiplying equation 5.1 by $f(x_0)$ and integrating over the variable the following expression is obtained:

$$\boldsymbol{\int L^n[g(x|x_0)]\, f(x_0)dx_0 = \int \delta(x - x_0)\, f(x_0)dx_0 = f(x)} \tag{5.5}$$

which leads to the following relationship

$$\boldsymbol{L^n[y(x)] = \int L^n[g(x|x_0)]\, f(x_0) dx_0} \tag{5.6}$$

By exploiting the linearity of the operator L^n, equation 5.6 can be rewritten as

$$\boldsymbol{L^n[y(x)] = L^n\left[\int g(x|x_0)\, f(x_0) dx_0\right]} \tag{5.7}$$

leading to the following expression:

$$\boldsymbol{y(x) = \int g(x|x_0)\, f(x_0) dx_0} \tag{5.8}$$

Through knowledge of the Green's function and the source term, the function $y(x)$ may be obtained.

Let us now consider a more general scenario governed by the following linear differential equation

$$\boldsymbol{L^n[y(x)] = h(x)} \tag{5.9}$$

subject to the initial conditions $y(0) = y'(0) = 0$ and where $h(x)$ is not restricted to a Dirac delta function. The Laplace transform of the equation leads to

$$\boldsymbol{Y(s) = \frac{1}{P^n(s)} H(s)} \tag{5.10}$$

where $Y(s)$ and $H(s)$ are the Laplace transforms of $y(x)$ and $h(x)$, respectively, and $P^n(s)$ is an nth degree polynomial in s. The solution for $y(x)$ can be readily obtained by applying the inverse Laplace transform. Solving the linear differential equation in this manner would require knowledge of the Laplace transform $H(s)$. For this case, the use of Green's functions could be used to solve the system. Let us now consider the following ratio:

$$\boldsymbol{\frac{Y(s)}{H(s)} = \frac{1}{P^n(s)} = G(s)} \tag{5.11}$$

The ratio depends only on the properties of the system. $G(s)$ is known as the transfer function. It can transfer the input $H(s)$ into the output $Y(s)$ via the product $Y(s) = G(s) \cdot H(s)$.

If the forcing function $h(x)$ is replaced by the dirac delta impulse $\delta(x)$ it is observed that the transfer function $G(s)$, the Laplace transform of $g(x)$, remains unchanged. This can be verified by equation 5.11.

As a consequence, the transfer function of a system can be estimated by imposing a forcing function. The Laplace transform of the response is itself the transfer function. From the convolution theorem

$$\boldsymbol{Y(s) = G(s) \cdot H(s)} \tag{5.12}$$

may be expressed as

$$\boldsymbol{y(x) = g(x) * h(x)} \tag{5.13}$$

The convolution of the impulse response with a particular input gives the response of the system. It is clear that the Green's function is a special case of the transfer function. The forcing function is described by the Dirac delta function. For a more general formulation when no mathematical description of the system exists, the transfer function described by the Weiner filter is of special interest.

The use of the Green's function approach requires finding the Green's function for a particular system L^n in addition to evaluating the integral equation. Solutions of this type have been described in the literature for models with uniform properties. For contrasts in material properties and structural variation the Weiner filter approach provides a more general formulation to approach the problem and will be used to describe systems than cannot be described analytically.

5.3 *A Green's Function Formulation*

In the previous section it was shown how, with knowledge of the Green's functions, a system of linear differential equations can be solved. In this section the Green's function solution developed by Geertsma (1966) for relating deformation to reservoir pressure change is presented. Given an estimate of vertical displacement or strain for

the overburden, the reservoir pressure change can be obtained via a linearised inversion. Segall (1992) shows that the displacement in a poroelastic medium can be given by the distribution of centres of dilation with a magnitude proportional to $\alpha\Delta p(x,t)$. The i^{th} component of the displacement tensor u_i at an observation point x in the subsurface is given by

$$u_i(x,t) = \frac{\alpha}{\mu}\int_v \Delta p(\xi,t)g_i(x,\xi)dV_\xi \tag{5.14}$$

Where α is Biot's coefficient, μ the shear modulus, Δp is the change in pore pressure, $\xi = (\xi_1, \xi_2, \xi_3)$ are the integration coordinates over the volume V and $g_i(x,\xi)$ is the Green's function. The displacement due to the pressure change in the whole reservoir can be calculated by using a superposition of N elements of volume V_k where each element undergoes a constant pressure change Δp_k. The strain is found by differentiating the displacement Green's function.

$$\frac{\delta u_i}{\delta x_j} = \frac{\alpha}{\mu}\sum_{k=1}^{N}\Delta p_k \int_{V_k}\frac{\delta g_i(x,\xi)}{\delta x_j}dV_k \tag{5.15}$$

or in matrix notation

$$\varepsilon_{zz,M} = \sum_{n=1}^{N} G_{n,M}\Delta p_n = \mathbf{G\Delta p} \tag{5.16}$$

where $\mathbf{G}$ is the matrix of coefficients containing the pre-computed Green's function integral describing the strain at a given subsurface observation point due to a unit pressure change in a reservoir volume V. $\varepsilon_{zz,M}$ is the measured vertical strain at the M$^{\text{th}}$ observation point using geodetic techniques like InSAR data or time-lapse seismic, and $\mathbf{\Delta p}$ are the unknown reservoir pressure changes in every element of volume.

The nucleus of strain model (Geertsma, 1966) can be used to provide the displacement field around a volume of pore pressure change Δp in a homogeneous elastic half-space with a traction-free surface. The general approach is to sum the contributions due to the volume elements that make up the reservoir (Vasco *et al.*, 2000). The general expression for displacement at the radial distance r and depth z due to an infinitesimal nucleus of strain located at (0,0,c) is given by

$$u = \frac{C_m}{4\pi}\left[\frac{\vec{S}}{S^3} + \frac{(3-4v)\overrightarrow{S_i}}{S_i^3} - \frac{6z(z+c)\overrightarrow{S_i}}{S_i^5} - \frac{2\vec{k}}{S_i^3}\{(3-4v)(z+c)-z\}\right] \tag{5.17}$$

where $= [r^2 + (z-c)^2]^{1/2}$, $S_i = [r^2 + (z+c)^2]^{1/2}$, $\vec{k}$ is the unit vector in the z direction and C_m is the uniaxial compaction coefficient defined as

$$C_m = \frac{\alpha(1-2\nu)}{2\mu(1-\nu)} \tag{5.18}$$

The vertical derivative of the above expression is the strain in the vertical direction.

$$\boldsymbol{\varepsilon_{zz}} = \frac{\boldsymbol{C_m}}{\boldsymbol{4\pi}}\left[\frac{\mathbf{1}}{\boldsymbol{S^3}} - \frac{\mathbf{3}(\boldsymbol{z}-\boldsymbol{c})^2}{\boldsymbol{S^5}} + \frac{\mathbf{4}\boldsymbol{v}-\mathbf{1}}{\boldsymbol{S_i^3}} + \frac{\mathbf{3}(\boldsymbol{z}+\boldsymbol{c})\big(\mathbf{4}\boldsymbol{v}(\boldsymbol{z}+\boldsymbol{c}) - (\boldsymbol{z}-\mathbf{3}\boldsymbol{c})\big)}{\boldsymbol{S_i^5}} - \mathbf{6}\left\{\frac{(\boldsymbol{z}+\boldsymbol{c})^2}{\boldsymbol{S_i^5}} + \frac{\mathbf{2}\boldsymbol{z}(\boldsymbol{z}+\boldsymbol{c})}{\boldsymbol{S_i^5}} - \frac{\mathbf{5}\boldsymbol{z}(\boldsymbol{z}+\boldsymbol{c})^3}{\boldsymbol{S_i^7}}\right\}\right] \tag{5.19}$$

The geometry to which the above equations are applied is shown in Figure 5.1. The most convenient set of sub-volume for constructing the reservoir is a set of non-overlapping cuboids. This allows the construction of a reservoir of arbitrary shape and pressure profile. The expression for the full displacement field due to a nucleus of strain at an arbitrary locaton can be found in Appendix B.

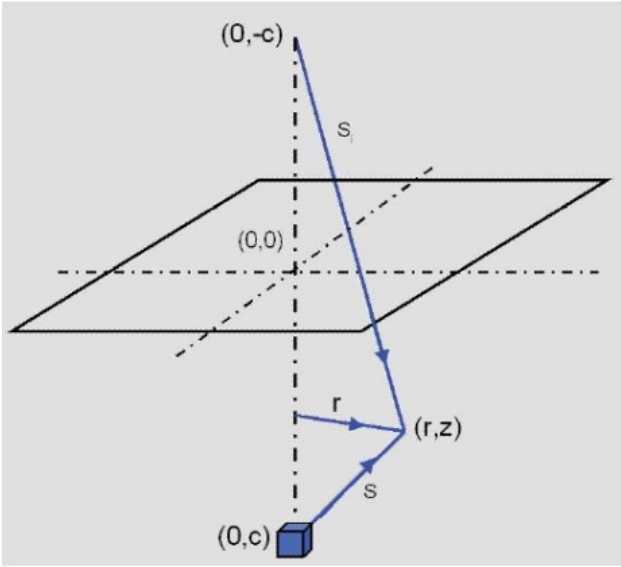


Figure 5.1: Geometry for nucleus of strain model modified from (Hodgson *et al.*, 2007).

5.4 *Resolution*

From the Geertsma solution for a point source or nucleus of strain it is evident that the Green's function is a function of the geometric relationship between the observation and the reservoir. In this section the resolution for different geometrical setups is explored. The resolution for a given geometric configuration can be characterised by the resolution matrix

$$\mathbf{R}=\mathbf{G}^{\dagger}\mathbf{G} \tag{5.20}$$

where $\mathbf{G}^{\dagger}$ is the generalised inverse (Aster *et al.*, 2005).

The relative resolution of different geometrical configurations will be examined by examining the impulse response of the model resolution matrix. A model consisting of a pressure pulse spike multiplied by the resolution matrix would return the original model for a perfect resolution. However, due to the geometric configuration and signal to noise level in the observations the original model cannot be recovered. By assuming noise-free observations and a known geomechanical model the resolution of different geometric configurations can be compared.

5.4.1 Geometrical Setup

A rectangular horizontal reservoir with 8x2 km dimensions and 100 m thickness is located at a depth of 3,000 m. Four different geometric configurations are studied. One horizon is located at the surface and three horizons are located at depths of 2,250 m, 2,500 m and 2,750 m respectively (Figure 5.3). A normalised pressure pulse source is located at the centre of the reservoir (Figure 5.2) and the observations are generated at each overburden horizon. The observation grid is 8x8 km with 100 m spacing. The elastic properties for the homogenous half-space are: Biot's coefficient α=1, Poisson's ratio ν=0.2 and the shear modulus μ=2.5 GPa.

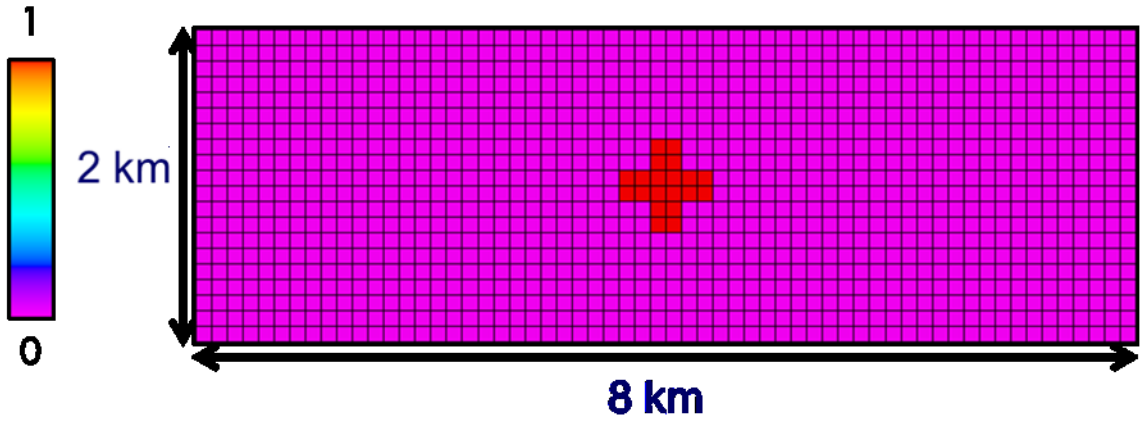


Figure 5.2: Pressure pulse and reservoir geometry used in the resolution test.



Figure 5.3: Geometrical setup for the resolution test.

5.4.2 Resolution Test

Figure 5.4 shows the results of the resolution test. It is clear that the resolution is controlled by the horizon closest to the reservoir. This test highlights the potential advantage of measuring deformation both at the surface and the subsurface. Deformation measured at surface using InSAR or tiltmeters can be acquired at a high temporal rate at a relatively low cost. How well the observations can resolve the pressure front will depend on the geometric configuration as shown in Figure 5.4. Measuring subsurface deformation closer to the reservoir from time-lapse seismic surveys would better resolve the pressure front but cannot be acquired on such a frequent basis as satellite surface deformation and would come at a considerable cost compared to satellite data acquisition.

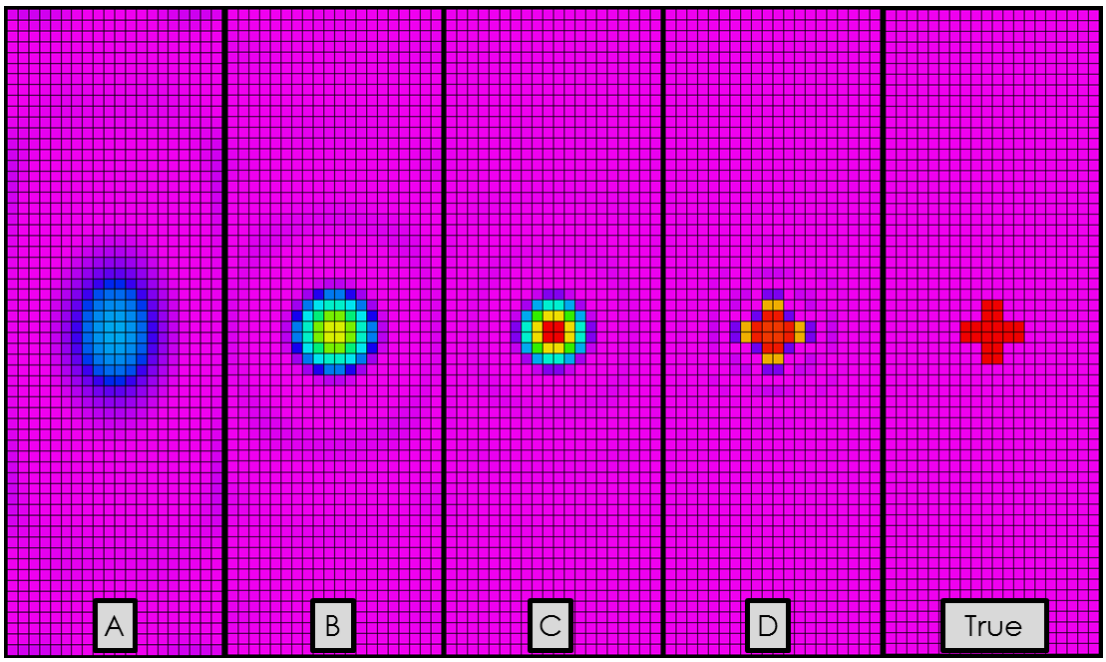


Figure 5.4: Resolution test for different depths. (A) 0 m (B) 2,250 m (C) 2,500 m (D) 2,750 m. The true pressure source solution.

5.4.3 Multi-Component Resolution Test

State-of-the art InSAR surface deformation also allows for both vertical and horizontal components of surface deformation to be measured. In addition to traditional vertical time-shifts, horizontal displacements have also been observed in time-lapse seismic images (Hale *et al.*, 2008). The impact on the resolution of using all three components is therefore explored. The pressure pulse source is used to generate all three components of deformation at the surface. The resolution of inverting any individual component is compared to inverting all three components.

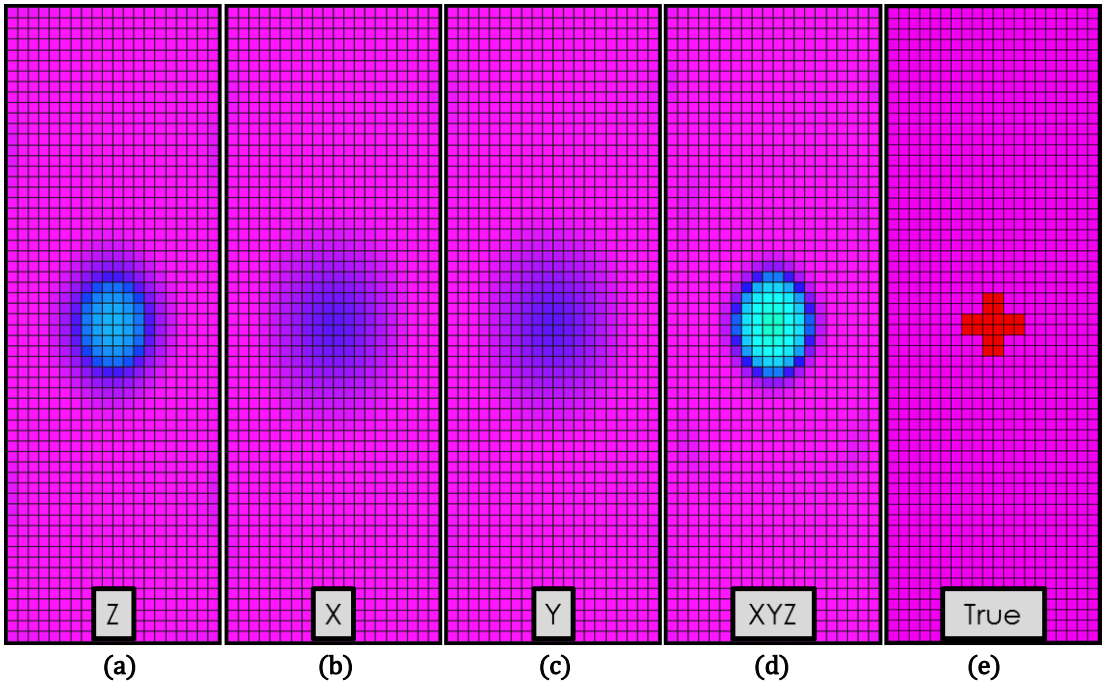


Figure 5.5: Resolution test using multi-component observations, (a) Inversion using Z component, (b) X component, (c) Y component, (d) XYZ component of surface deformation, and (e) the true pressure source solution.

The Z component of the deformation observations has a higher resolution compared to the X or Y component when used on its own (Figure 5.5). However, using all three components simultaneously increases the resolution. This illustrates the potential benefit on the inversion resolution of measuring several components of the deformation tensor.

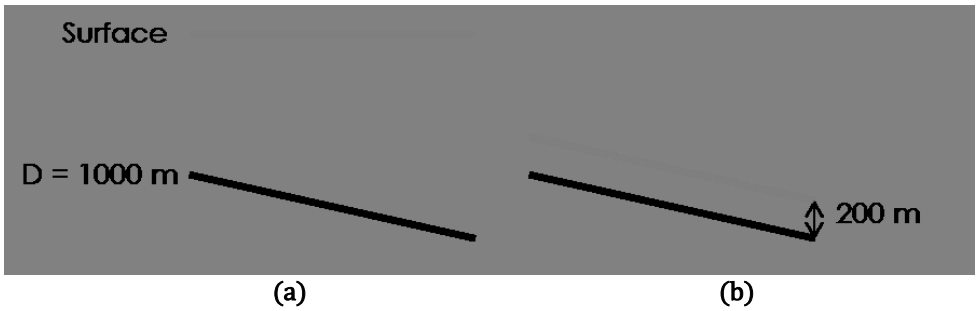


Figure 5.6: Geometric configuration for a dipping reservoir, (a) observations are located at the surface (b) observations are located parallel to the reservoir 200 m above.

5.4.4 Dipping Reservoir Resolution Test

A final geometrical configuration is tested for a dipping reservoir. The reservoir has three pressure pulses applied to it. In the first configuration the observations are located at the surface. In the second configuration the observations are located parallel to the reservoir 200 m above it. Figure 5.6 shows the two geometric configurations.

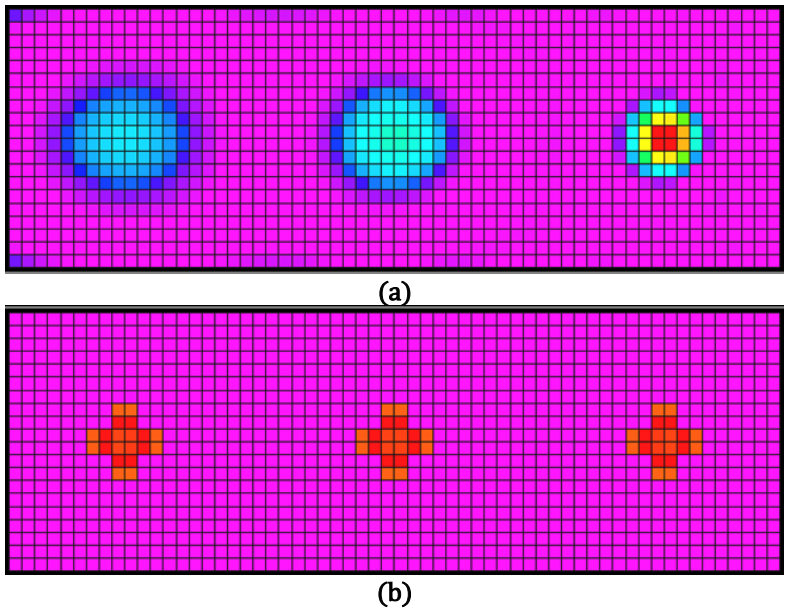


Figure 5.7: Resolution test for a dipping reservoir for two configurations. (a) Observations located at the surface, (b) Observations are located 200 m above the reservoir and parallel to the reservoir dip.

Figure 5.7 shows that, for a dipping reservoir, the resolving power will vary with depth. For a complex reservoir it is certain the pressure front will be better resolved depending on its depth. If the observations are made parallel to the reservoir structure the pressure front is resolved equally well throughout.

5.5 *Regularisation*

A trait common to all inversion problems is the ill-conditioned nature of the problem such as non-uniqueness and stability issues (Aster *et al.*, 2005). Non-uniqueness inevitably arises in inverse modelling both with Green's functions and Wiener filters. There are many a priori constraints and regularization techniques available. Du *et al.* (1994), Hodgson *et al.* (2007) and Vasco *et al.* (2008) faced ill-conditioning when inverting a Green's function and tackled it by using first order Tikhonov regularisation. The use of Weiner filters being an inverse problem is no different and also experience ill conditioning. The stability is addressed by adding a first order Tikhonov regularisation in the objective function. The non-uniqueness inevitably arises in both Green's functions and Weiner filters. This is a characteristic of rank-deficient linear inverse problems. Models that lie in the null space are non-trivial solutions to the forward problem. Therefore any linear combination of these null space solutions can be added to a particular model satisfying the governing equations without affecting the fit to the data.

If a localised pressure source is considered inside a reservoir, the nature of the problem dictates that as the deformation field spreads in the subsurface, the spatial wavelength of the deformation increases. The earth essentially acts as a low pass filter. The parameter controlling the attenuation of the frequency components of the deformation is the depth. As a consequence of the increase in spatial wavelength, the more underdetermined the system will be (Hansen, 1998). For this reason smoothness or inequality constrains are required. As shown by the resolution test, this suggests that to better resolve the features of the reservoir pressure change distribution, deformation measurements closer to the reservoir can potentially capture the lower spatial wavelengths. In general, it can therefore be said that the inverse modelling error will always be larger than the forward modelling case.

5.5.1 The L_2 Norm

If Tikhonov regularisation is considered, the objective function can be written as

$$\boldsymbol{\varphi}(\mathbf{m}) = \|\mathbf{u} - \mathbf{G}\mathbf{m}\|_2^2 + \boldsymbol{\lambda}^2\|\mathbf{L}\mathbf{m}\|_2^2 \tag{5.21}$$

where $\lambda^2$is called the regularisation parameter, the damping parameter or Tikhonov factor (Aster *et al.*, 2005). L is the Tikhonov regularisation matrix. Commonly used matrices for L are the first order derivative and the second order derivative Laplacian operator. In this case it is the model that is smoothed. For the Weiner filter formulation however, the objective function is re-written as

$$\boldsymbol{\varphi}(\mathbf{f}) = \|\mathbf{u} - \mathbf{f} * \mathbf{m}\|_2^2 + \boldsymbol{\lambda}^2\|\mathbf{L}\mathbf{f}\|_2^2 \tag{5.22}$$

In this case it is the filter $f$that is solved for in the least-squares sense. A classic method to decide on the value of the regularisation parameter is the L-curve method. If one plots the model norm $\|\mathbf{u} - \mathbf{f} * \mathbf{m}\|_2^2$ against the smoothness norm $\lambda^2\|\mathbf{L}\mathbf{f}\|_2^2$ on a log scale then a characteristic L-shaped curve is observed. Increasing the value of λ will place greater importance on the smoothness norm and the model misfit becomes greater. If too little smoothing is applied then both the noise and the data will be fit. The optimum value of λ is therefore a trade-off between model smoothness and data fit.

5.6 *Impact of material properties*

It has been established that the resolution of a pressure change inversion is controlled by the geometrical relationship between the pressure source location and the observation. The impact of the uncertainties in material properties are now discussed for both a homogeneous earth model and a layered earth model.

5.6.1 Linear poroelastic halfspace

The material properties in a linear poro-elastic halfspace can be described as a function of three variables:

- Poisson's ratio ν
- Shear modulus μ
- Biot's coefficient α

Poisson's ratio and Biot's coefficient are dimensionless and the shear modulus is in Giga Pascals. The vertical displacement due to a point source in linear poroelastic halfspace can be written as follows:

$$\boldsymbol{u_z = \frac{\alpha(1-2\nu)}{8\pi\mu(1-\nu)} G(x,\xi,\nu)} \tag{5.23}$$

Where $G(x,\xi,\nu)$ is a geometrical term depending on the geometrical relationship between the point source x and observation ξ and it is also dependent on the Poisson's ratio.

It can be seen that the ratio of Biot's coefficient and the shear modulus will only scale the prediction and are independent of the reservoir geometry. This means that, assuming Poisson's ratio is known, the spatial distribution of the vertical displacements will be correct but the magnitude will be underpredicted or overpredicted. The effect of errors in Poisson's ratio is non-linear and is dependent on the reservoir geometry (Hodgson, 2009). The theoretical bounds for Poisson's ratio are $-1 < \nu < 0.5$ for a linear elastic material. In practice however, the value of Poisson's ratio are typically found between between 0.15-0.25 (Fjaer *et al.*, 2008). These errors however might be negligible compared with the assumption of a homogeneous halfspace. Garcia and Macbeth (2013) have shown that the errors arising from assuming a homogenous half-space are significant for both the forward and the inverse problem assuming the true solution is a layered earth.

5.7 *Application to the In Salah CO_2 storage site*

5.7.1 Inversion Setup

In Sections 5.4 and 5.5, the Green's function solution for a homogeneous half-space was presented and used to show the limited resolution of a reservoir pressure change inversion from overburden deformation.

In this section an inversion scheme is used which allows for a more realistic representation of the subsurface. An inversion scheme using a Weiner filter approach with transfer functions as described in Section 3.3 will be applied to the In Salah CO_2 storage site. The dataset available is a series of InSAR surface uplift deformation over three CO_2 injection wells.

A pre-requiste to estimate the transfer functions is a numerical geomechanical model. The numerical geomechanical model may be of arbitrary complexity and

should be built using all the characterisation data available. The numerical geomechancial model used is described in section 5.8.2.

A synthetic pressure source must then be defined at each CO_2 injection well. The design of the synthetic pressure sources and their location are described in Section 5.8.3. The pressure sources and the geomechanical model are then fed to the geomechanical simulator. Using the deformation output from the geomechanical simulator and the known pressure sources the transfer functions can then be estimated.

Having an estimate of the transfer functions they can then be used to invert the measured InSAR surface uplift above each injection well.

5.7.2 Geomechanical Model

The reservoir part of the geomechanical model covers both the gas production field and the CO_2 injection wells at the InSalah CO_2 storage site. Starting with the reservoir grid, the model is embedded in a sideburden and underburden to diminish undesired boundary effects (Figure 5.8). The key geological horizons have been presented in Chapter 4. The shallow aquifer zone consists of three layers. The C20.3+ consists of five layers. The lower caprock C20.1-2 contains four layers. The C10.3 formation contains three layers. The main reservoir C10.2 is modelled as one layer. The extended Devonian underburden contains eight layers. The mechanical behaviour of the model is assumed to be linear and isotropic. The values of the rock elastic properties used are shown in Table 5.1.

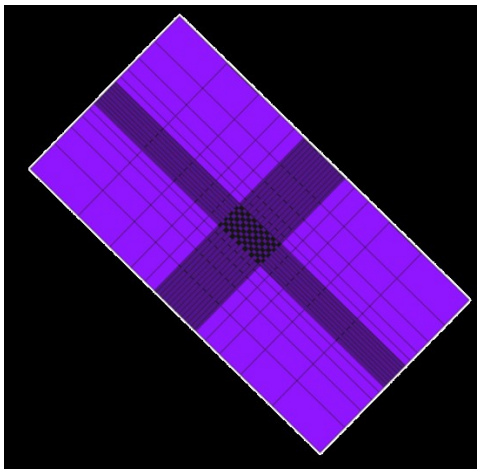


Figure 5.8: Plan view of geomechanical model with lateral dimensions.

Table 5.1: Geomechanical model rock elastic properties (based on data by the In Salah JIP)

	E (GPa)	ν
Shallow Aquifer	3.0	0.25
C20.3+	5.0	0.30
C20.1-2	7.5	0.30
C10.3	20.0	0.25
C10.2	10.0	0.20
Devonian	15.0	0.30

5.7.3 Synthetic Pressure Source Design

The synthetic sources or pulses in this case are pressure changes that consist of a 10 bar peak that decays to zero in the neighbouring cells in order to ensure a smooth pulse and a correspondingly well behaved surface deformation impulse-response. Figure 5.9 shows a representation of a synthetic pressure source. Synthetic pressure sources have been placed at all three CO_2 injection wells. Figure 5.10 shows the pressure source location for injection wells KB-501, KB-502 and KB-503. This pressure distribution is then fed into the geomechanical simulator to obtain the associated impulse-response overburden deformation. It is important to note that the pressure source is confined to the reservoir interval.

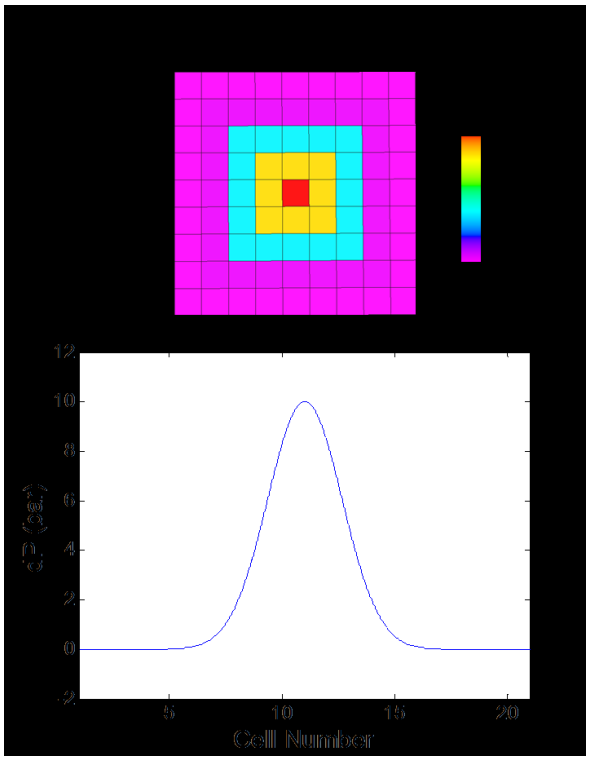


Figure 5.9: Synthetic source used to simulate the system's impulse-response. The source consists of a 10 bar peak that decays exponentially.

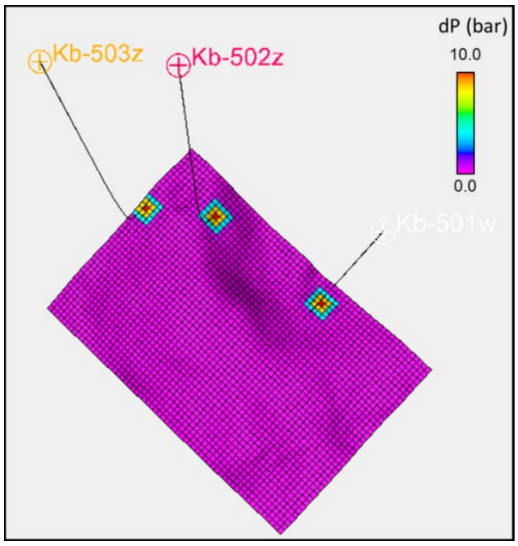


Figure 5.10: Pressure source location for injection wells KB-501, KB-502 and KB-503.

5.7.4 Transfer function computation

The pressure source distributions are then fed into the geomechanical simulator to obtain the associated overburden displacements or impulse response. Figures 5.11, 5.12 and 5.13 show the resulting overburden displacements for each of the injection wells.

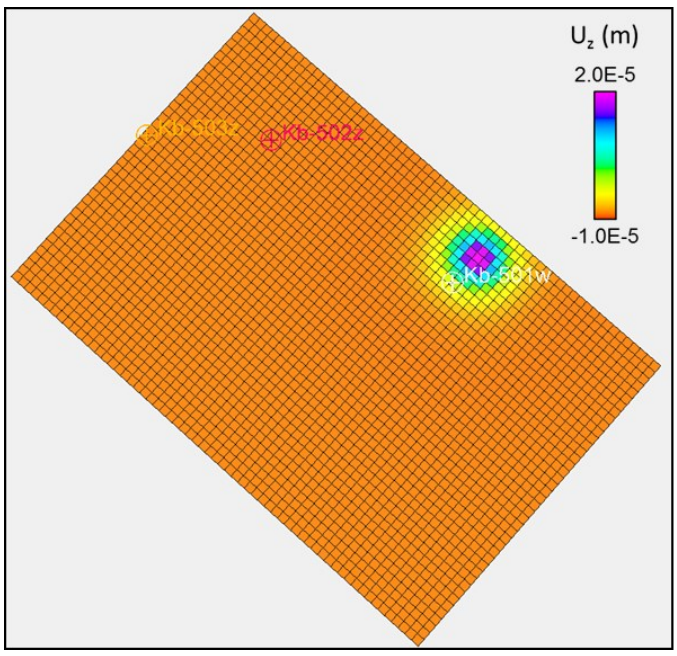


Figure 5.11: Simulated deformation for injection well KB-501.

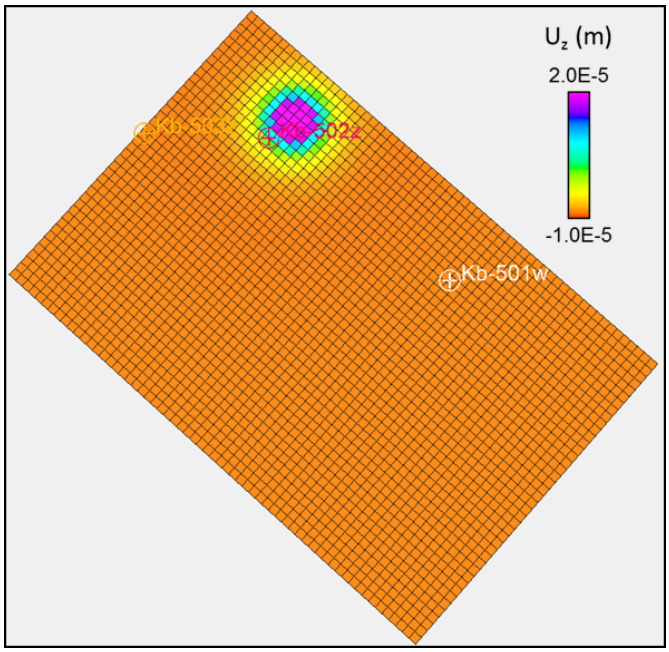


Figure 5.12: Simulated surface deformation for injection well KB-502.

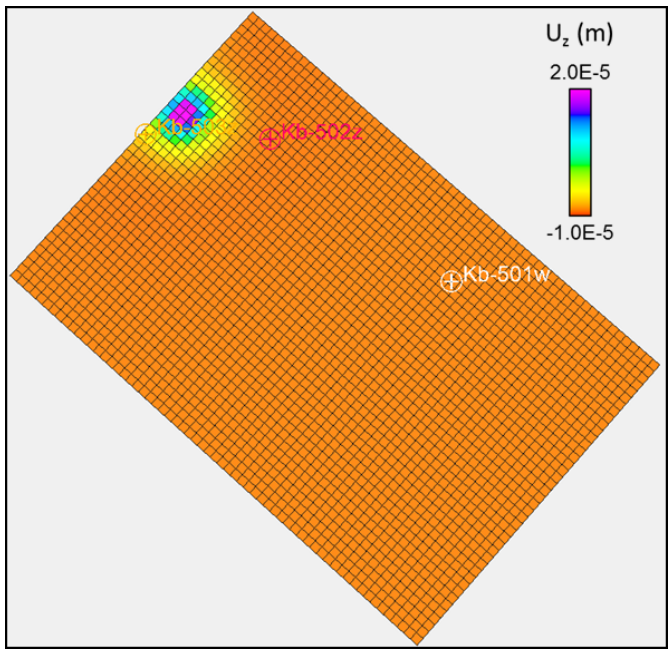


Figure 5.13: Simulated surface deformation for injection well KB-503.

Before performing deconvolution the pressure source signal should be padded with zeros by the same number of samples in order to ensure the deconvolution of the entire signal. The set of transfer functions for the pressure-impulse and the overburden deformation response are then estimated using Weiner deconvolution.

5.7.5 Results

One of the conditions for the Weiner deconvolution approach is that the deformation data have the same sampling as the pressure grid. For this purpose the InSAR data has been upscaled to match the model grid. The InSAR data is spatially sampled at approximately 5 m. The data was then re-sampled or upscaled using the arithmetic mean to a spatial sampling of approximately 200 m consistent with the numerical model grid. Figure 5.14 shows a time-series of the upscaled InSAR deformation data at eight different dates.

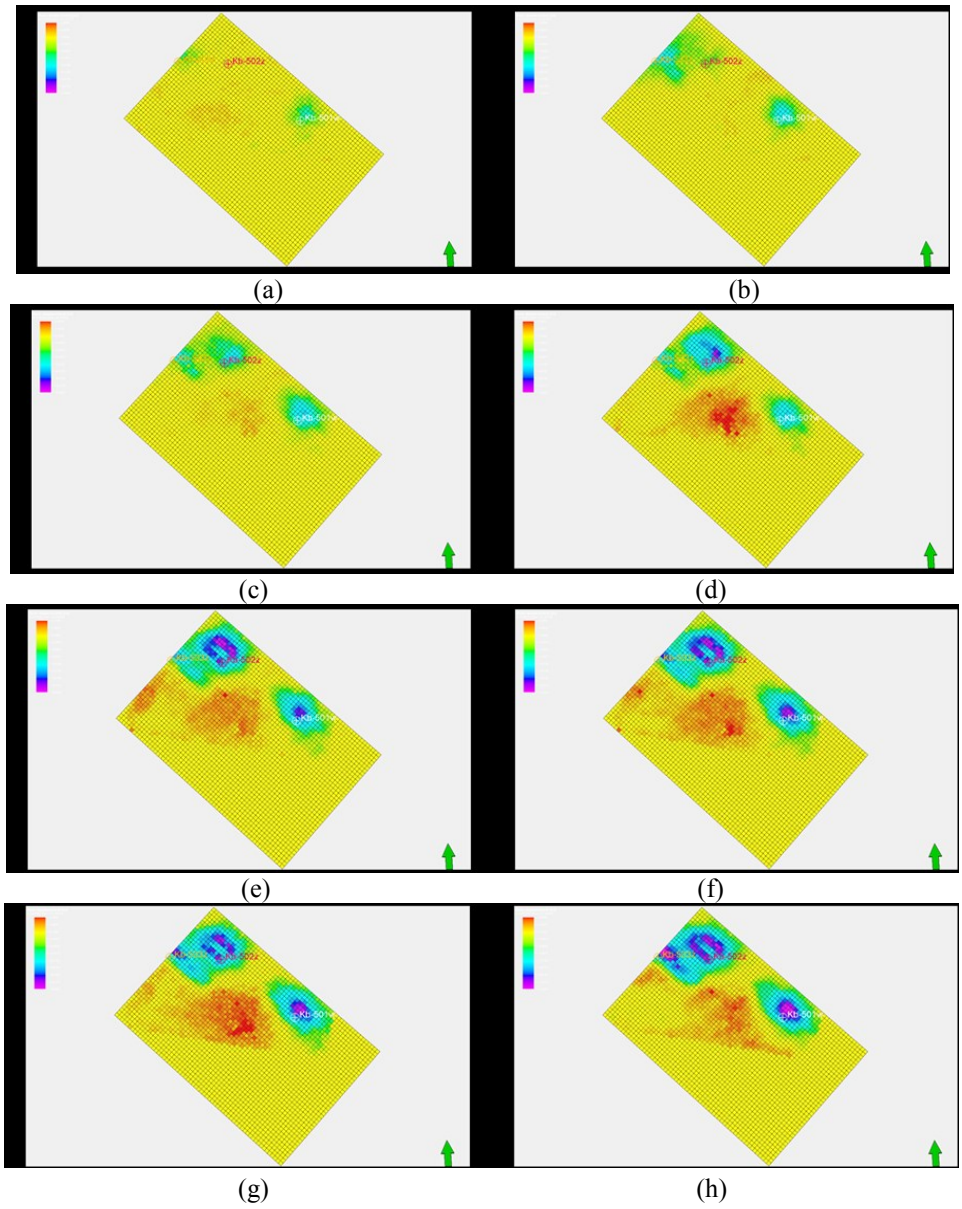


Figure 5.14: InSAR data upscaled to model resolution, (a) February 26, 2005, (b) March 18, 2006, (c) December 23, 2006 (d) January 12, 2008, (e) December 27, 2008, (f) May 16, 2009, (g) February 20, 2010, (h) May 6, 2010.

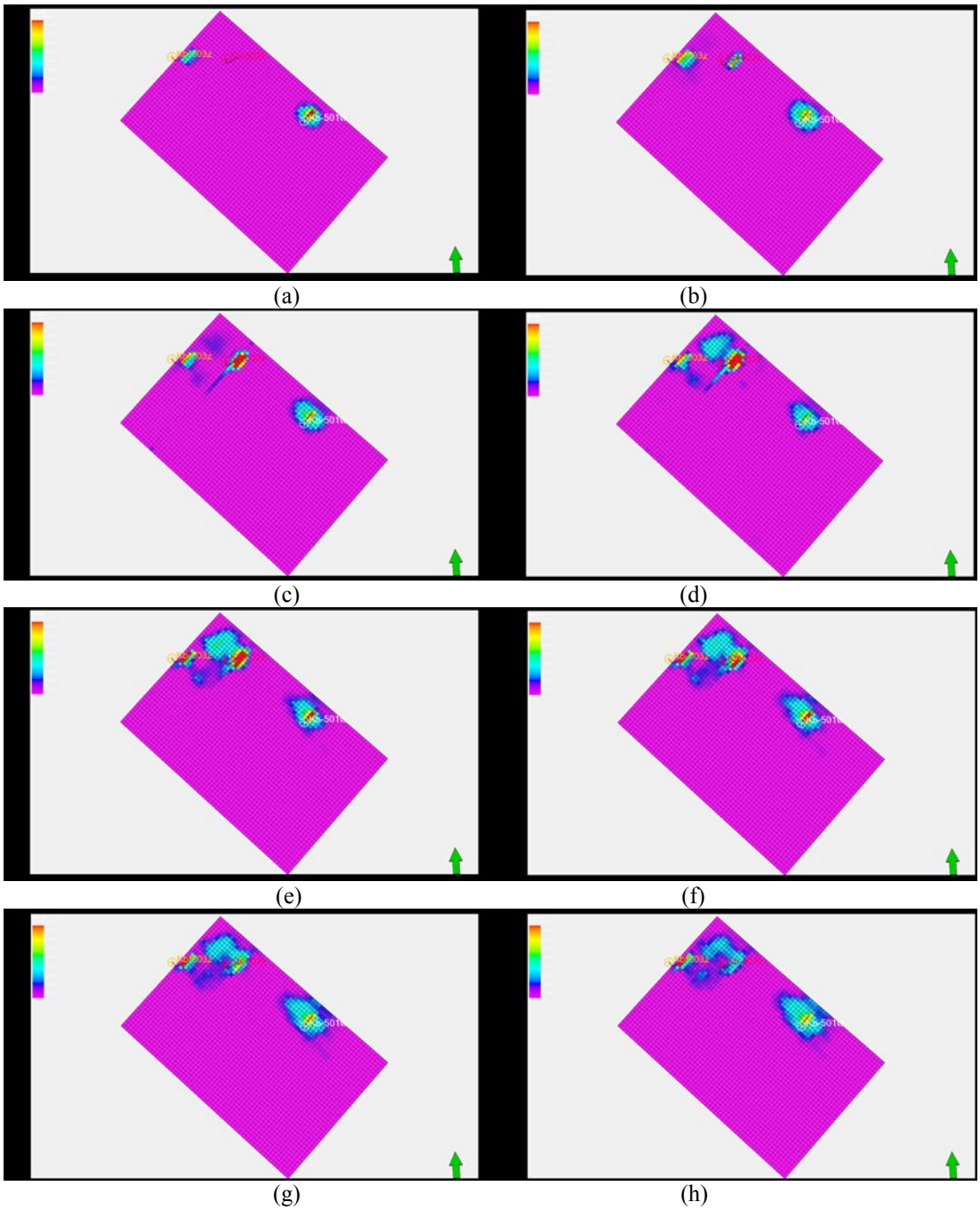


Figure 5.15: Reservoir pressure change inversion using InSAR deformation data, (a) February 26, 2005, (b) March 18, 2006, (c) December 23, 2006 (d) January 12, 2008, (e) December 27, 2008, (f) May 16, 2009, (g) February 20, 2010, (h) May 6, 2010.

The corresponding time-series of reservoir pressure change estimated from the InSAR observations are shown in Figure 5.15 for the same eight dates. As explained earlier, due to limits on the resolution of the inversion, the mapped pressure front will be under-predicted in magnitude and smoothed. The results are therefore a conservative estimate of the extent of the pressure change front.

The reservoir pressure change inversion time-series displayed in Figure 5.15 shows how at the initial stage of injection, the pressure front expands faster at injection well KB-501 while the pressure front is more localised around injection wells KB-502 and KB-503. The results suggest a pressure build up at injection well KB-502 and KB-503 followed by a sudden pressure release in the NW-SE axis. The pressure front is observed to diminish in magnitude and extend at KB-502 once the well is shut-in. The pressure front continues to expand at KB-501 in the NW-SE direction with no indication of there being a sudden pressure release. In summary:

- The mapped pressure front at injection well KB-501 begins to spread symmetrically in the initial injection stages. There is a clear anisotropy observed in the pressure front towards the NW-SE direction. The pressure front is slightly more elongated towards the NW of the injection well. The maximum extension of the pressure front in the preferential direction axis is approximately 6.5 km and 3.7 km in the minor axis.
- The pressure front at KB-502 is initially highly localised along the injection well. Unlike the other injection wells, the pressure front migrates almost entirely to the NW. If the pressure front is approximated to an ellipse, it major axis extends aproximately 4 km in the NW-SE direction and the minor axis extends 2.6 km in the NE-SW direction.
- At injection well KB-503, the pressure front appears to propagate preferentially to the SE of the injection well. The maximum extension of the pressure front to the SE from the injection well is approximately 4 km and with a width of 1.4 km. The initial localised pressure front and its subsequent expansion to the SE suggest some pressure build up occurred before extending.

5.8 *Summary and Discussions*

In this chapter a series of InSAR surface deformation data have been inverted for reservoir pressure changes. The method used is computationally fast and straightforward to implement. Given the uncertainties inherent in the inversion, they are used to gain a qualitative understanding of the subsurface CO_2 pressure front. An important insight gained is that the results suggest pressure build up at KB-502 and KB-503 followed by a sudden pressure release. The evolution of the pressure front at KB-501 expands in a much more consistent manner throughout injection. The

behaviour of the injection well will be explored in more detail in the next chapter using forward coupled-flow geomechanical modelling. Given the limited resolution from surface deformation measurements, the extent of the inverted reservoir pressure change should be taken as the maximum extent assuming the pressure changes are confined to reservoir interval.

An important assumption of the method used is that the reservoir pressure changes are constrained to a single unit reservoir interval. Although this may be a good approximation for relatively thin reservoir formations, more complex multi-layer reservoir systems will require the mapping of the pressure distribution into different reservoir units. The approach used in this thesis consists of a single input and a single output channel where one contains the reservoir pressure changes and the other contains the deformation at a given horizon. The natural extension of this would be to develop a multi-channel approach (Treitel, 1970) where the relation between multiple inputs and outputs can be described. In such a manner, multiple deformation measurements at differents depths could be inverted into multiple reservoir units and overlying caprock formations. Such an approach would be desirable for CO_2 storage monitoring.

Another important assumption is that the deformation mode is driven by pressure driven isotropic volume change. Other deformation modes include tensile opening, shear displacement and shear-induced dilation. Including different deformation modes of different strength and size at different depths will increase the non-uniqueness as more solutions exist to explain the surface deformation pattern.

In this application a single geomechanical model was used to estimate the transfer functions. The model itself is subject to uncertainties and the inversion scheme should be extended to included stochastic variations in the geomechanical model. This however would considerably increase the computational cost. Nonetheless, it is an advantage over previous techniques which assume a homogeneous earth.

A major challenge for inverting deformation measurements is the trade-off between pressure changes within layers at different depths due to the inherent non-uniqueness of the problem. Nonetheless, the large scale features of the pressure front at depth can still be captured. Additional data like reliable time-lapse seismic time strains could also help constrain the approach. If the the measurements are of a sufficient quality they would increase the resolution of the inversion.

Although some insight has been gained through this approach it can be improved by including the following:

- Subsurface estimates of displacement/strain to improve resolution
- Uncertainty in the geomechanical model
- Mapping vertical pressure components

The first can be acquired through high repeatability time-lapse seismic surveys. Sufficient computational power would allow the second to be achieved via a stochastic inversion. The third remains particularly challenging but it is the author's view that multi-channel filters should be further researched for this application.

Chapter 6 Coupled Flow-Geomechanical Simulation of CO_2 Injection at the In Salah Storage Site

Building on previous work on flow and geomechanical simulations at the InSalah CO_2 storage site, a coupled flow-geomechanical simulation study has been carried out to better understand the flow behaviour around one of the injectors (KB-503). In order to further improve the match of the injection pressure at KB-503 that is consistent with the InSAR surface uplift data, an in-depth analysis of the InSAR surface uplift pattern and its temporal evolution was first carried out in conjunction with a preliminary time-lapse seismic analysis carried out by Michael Nickel of Schlumberger Stavanger Research within the context of EU funded research project CO_2ReMoVe. The picture emerging is that preferential flow paths (along the NW-SE maximum stress direction) appear to have been created, as a result of fluctuations in the injection rate from September 2005 onwards, which led to the pressurisation of the reservoir rock away from the immediate vicinity of the wellbore as reflected by elongated surface uplift pattern around KB-503. A plausible explanation is that CO_2 injection has caused hydraulic stimulation of pre-existing fractures/faults in the area. Based upon this understanding, a much improved match of the BHP pressure for KB-503 was achieved by incorporating a fractured zone with dynamic transmissibility into the reservoir model based on InSAR surface uplift observations.

6.1 *Previous model mismatch at injection well KB-503*

Shi *et al.* (2013) used a two-step approach to assess the performance of the three CO_2 injection wells at In Salah. In the first step, the flow model is calibrated on bottom hole pressure data. Once the flow model model is calibrated it is then coupled with a geomechanical simulator to compare the predicted surface uplift to the observed InSAR surface uplift. It was reported that, unlike for injection well KB-502, the estimated bottomhole pressure for KB-501 and KB-503 could largely be history-matched by tuning the matrix permeability alone around the injection wells. Shi *et al.* (2013) then used coupled flow-geomechanical modelling to match the measured surface uplift evolution over the two wells.

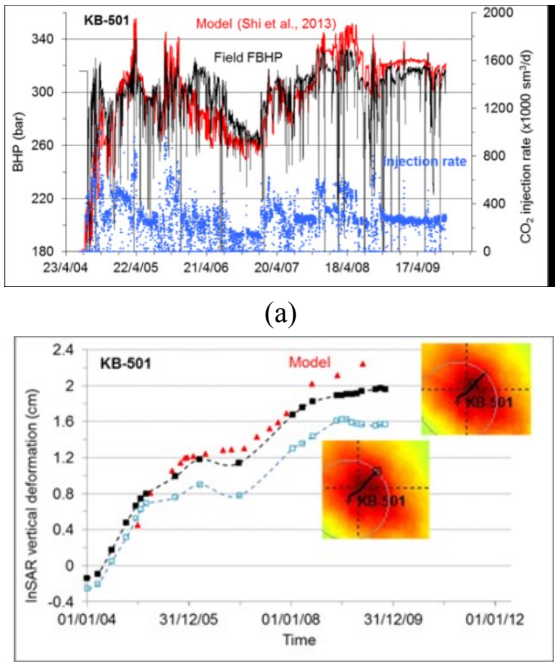
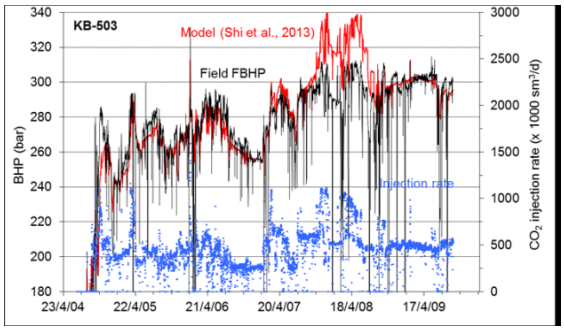
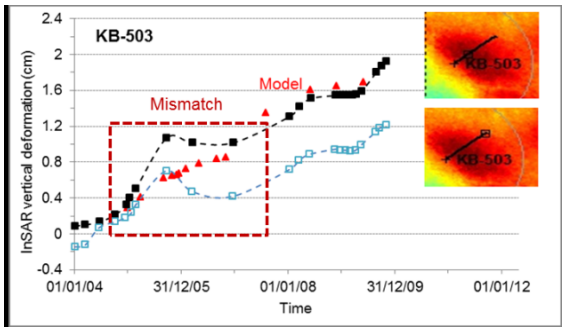


Figure 6.1: (a) Previous history match of the CO_2 injection pressure at KB-501. (b) InSAR surface uplift time series (Courtesy of the In Salah Gas Joint Industry Project) and the previous model predictions. The two curves (with different offsets) correspond to two marked locations (centre and the toe) along the borehole (after Shi *et al.*, 2013).

The model performance was mixed: a satisfactory overall match of the observed surface uplift was obtained at KB-501 (Figure 6.1); however the observed surface uplift trend at KB-503 could not be reproduced. In Figure 6.2, the mismatch between the modelled and the measured surface uplift at KB-503 is highlighted and will be the focus of further discussion in this chapter.



(a)



(b)

Figure 6.2: (a) Previous history match of the CO_2 injection pressure at KB-503. (b) InSAR surface uplift time series (Courtesy of the In Salah Gas Joint Industry Project) and the previous model predictions. The two curves (with different offsets) correspond to two marked locations (centre and the toe) along the borehole (after Shi *et al.*, 2013).

The mismatch suggests that there is still margin for an improved understanding of the flow and pressure behaviour at injection well KB-503. The bottom hole pressure and the surface uplift history-match only cover the injection period from 2004 to 2009. There is an overall agreeable match with the bottom hole pressure in trend. Concerning the pressure magnitude, at the beginning of 2008 the model overpredicted the pressure response. For the surface uplift, the mismatch is greatest during the initial years of injection. The modelling effort failed to capture the rapid rise in surface uplift but later caught up with the correct trend in the later stages of the injection period.

6.2 *Modelling Approach*

The approach used by Shi *et al.* (2013) consisted of first calibrating the flow model on the bottom hole pressure. The calibrated flow-model was then coupled with a geomechanical simulator to predict the geomechanical response at the ground surface. In this chapter this approach is modified and extended. Coupled flow-geomechanical modelling continues to be used as the main tool to make predictions

of the injection pressure and the ground deformation at surface. However, an additional data source in the form of time-lapse seismic data is introduced into the analysis. A joint analysis of the InSAR surface uplift and time-lapse seismic data is first made to gain insight into the CO_2 injection process. The insight gained from interpreting these observations is then used to guide the coupled flow-geomechanical modelling effort in order to improve the match to the estimated bottom hole pressure and the observed ground suface uplift.

6.3 *Analysis of InSAR surface uplift at In Salah*

6.3.1 CO_2 injection rates and cumulative injection

In this section a detailed analysis of the InSAR surface uplift pattern and its temporal evolution at injection well KB-503 is made. The CO_2 injection rate history and the cumulative CO_2 injection at well KB-503 are shown in Figure 6.3. The complex injection history shows fluctuations in the CO_2 injection rate with many associated peaks. Throughout the entire injection period from 2004 to 2011 approximately 1.75 million metric tons of CO_2 were stored at KB-503.

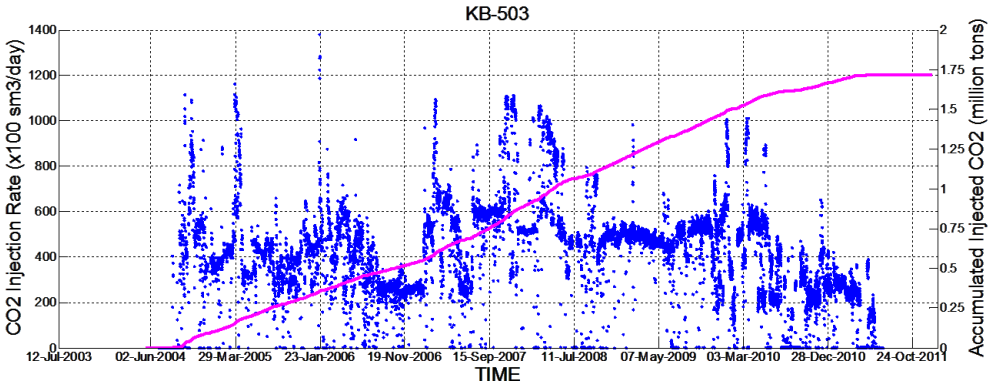
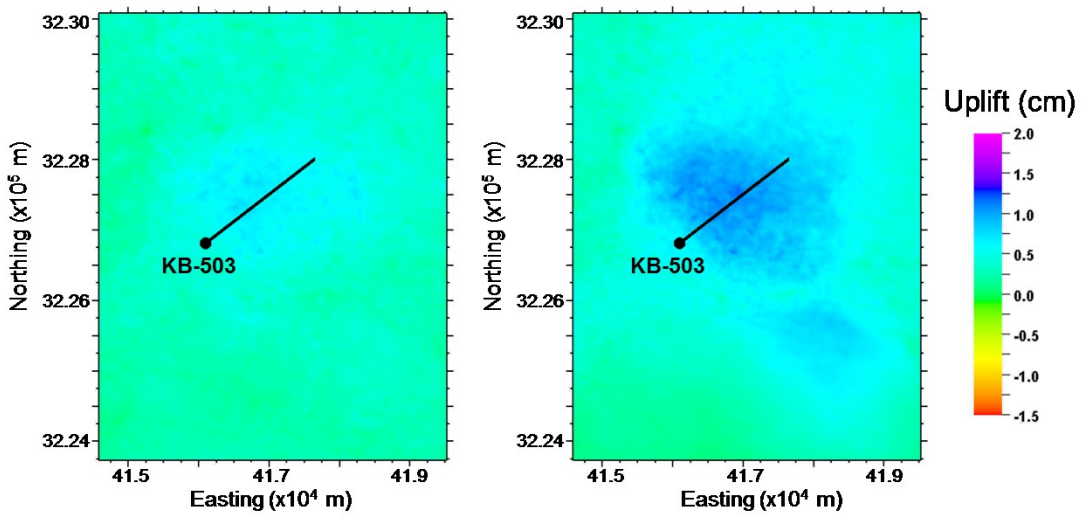


Figure 6.3: CO_2 injection rate and cumulative injected CO_2 at injection well KB-503.

6.3.2 Understanding the deformation pattern

Before attempting any flow and geomechanical modelling, the InSAR surface uplift will be analysed and interpreted. Emphasis is made of the initial years of CO_2 injection where previous studies show that the mismatch between surface uplift predictions and observations is greatest.



(a) (b)

Figure 6.4: InSAR surface uplift at KB503. (a) Single uplift lobe suggesting well pressurisation (February 2005); (b) South-East uplift lobe elongation suggesting pressure propagation along a fault/fracture zone (September 2005). (Courtesy of the In Salah Gas Joint Industry Project).

The overall surface deformation pattern at KB-503 was one of surface heave around the vicinity of the injection well followed by an elongation towards the South-East (Figure 6.4). From the start of injection in 2004 to the appearance of the deformation elongation towards the South-East in September 2005 a rapid rise in surface uplift was observed up to a peak of approximately 1 cm. From September 2005 onwards the deformation pattern expanded from its initial local pattern to a predominantly South-Easterly direction. After the local deformation peak observed in September 2005 the temporal evolution shows a decrease in the rate of deformation followed by a more gradual rise in surface uplift relative to the initial 2004-2005 injection period (Figure 6.2).

The rapid surface uplift rate during the initial 2004-2005 period corresponds to the pressurisation of the reservoir rock in the immediate vicinity of the wellbore as a possible explanation for the local spatial pattern of the deformation at surface and the associated rapid rise in surface uplift. The subsequent period from September 2005 onwards corresponds to possible tensile opening associated with the hydraulic stimulation of pre-existing fractures/faults at depth. The initial pressurisation around the vicinity of the wellbore was then able to propagate along an enhanced permeability migration path related to the fracture/fault zone, resulting in the observed decrease in surface uplift rate followed by its gradual rise. The InSAR data

being well sampled in time allows an estimate of the timing of the hydraulic stimulation of the fracture/fault zone in response to CO_2 injection.

6.3.3 InSAR multi-point analysis

The surface deformation at five different points at KB-503 have been analysed. The location of the points is shown in Figure 6.5. Figure 6.6 shows the temporal evolution of the surface deformation at KB-503 at the five different points.

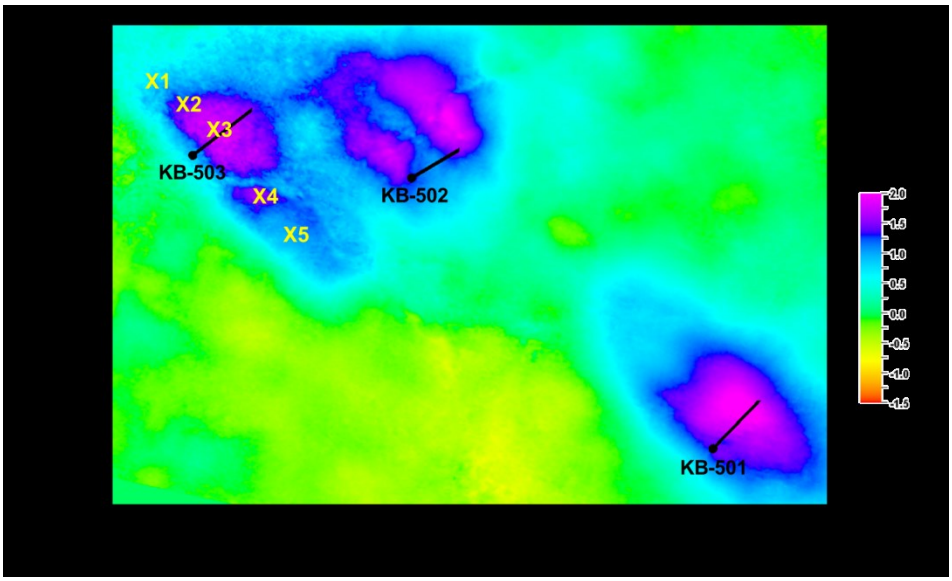


Figure 6.5: Location of five different points at injection well KB-503 for the InSAR surface uplift time series analysis (Courtesy of the In Salah Gas Joint Industry Project).

Point X3 is located directly over the injection well with points X1 and X2 to the North-West and points X4 and X5 to the South-East. Despite being farther away from the injector than X1 and X2, points X5 and X4 show a larger amount of surface deformation respectively, highlighting the preferential South-East migration path. The injection period for the first couple of years corresponding to the rapid rise in surface uplift was subject to high fluctuations in the injection rate (Figure 6.3). This effect is more pronounced at points X2 and X4 in the immediate vicinity of the injection well at X3. After this initial phase the rate of surface uplift at X4 and X5 overtakes that observed at X2 and X1 respectively, consistent with the interpretation of the creation of an enhanced migration pathway to the South-East through the hydraulic stimulation of a fracture/fault zone.

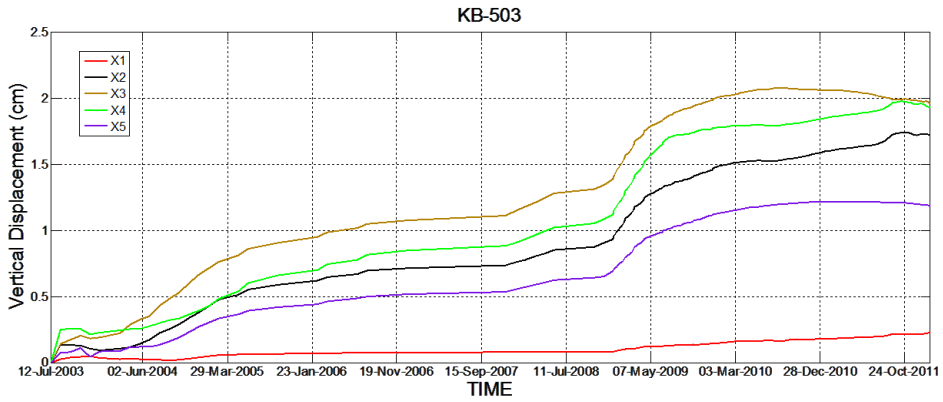


Figure 6.6: InSAR surface uplift at five different locations.

6.3.4 Hydraulic stimulation timing and geometry

From an analysis of both the spatial pattern and the transient evolution of the surface uplift, the timing of the hydraulic stimulation and its geometrical characteristics due to CO_2 injection can be interpreted.

The timing of the hydraulic stimulation has been interpreted on two features of the InSAR surface uplift. The first feature is the transition of a localised pattern of surface heave to an elongated pattern towards the South-East. The second feature is the decrease in the rate of surface uplift observed from the transient evolution of the surface uplift. Based on these two features it has been interpreted that hydraulic fracturing potentially occurred after approximately two years of sustained CO_2 injection.

Some general features about an existing fault or fracture network at depth have also been interpreted. It is evident from the surface deformation pattern that the preferential flow direction is along the NW-SE axis. By comparing the strength of the transient evolution of the surface uplift along the axis of the preferential flow direction, it is observed that the magnitude of the surface deformation is greater to the South-East of the injection well compared to points diametrically opposed to the North-West. This characteristic of the surface deformation is related to heterogeneity at the reservoir level. A uniform permeability field would have resulted in a suface deformation of equal strength to either side of the injection well. A structural feature at depth and its response to CO_2 injection however could control the flow and pressure behaviour and explain the observations. The direction of the structural

feature is well constrained and, at this point, it can be established that it extends predominantly to the South-East of the injection well.

6.4 *Insight from time-lapse seismic*

As discussed above, an interpretation of the InSAR surface uplift at injection well KB-503 suggested the creation of a preferential flow-path after approximately two years of CO_2 injection. In this section a similar analysis is performed using time-lapse seismic data. In section 6.5.1 several geomechanical models in use for the interpretation of time-lapse seismic time-shifts are described in detail. The data quality and repeatability issues with the time-lapse seismic surveys at In Salah are then discussed. The limitations of using other seismic attributes other than time-lapse seismic time-shifts at In Salah are also considered. Finally, an interpretation of the time-lapse seismic time-shifts is made and compared with the InSAR data interpretation made in the previous section.

6.4.1 Geomechanical basis for time-lapse seismic time-shifts

Time-lapse seismic time-shift technology has a geomechanical basis. As a reservoir deforms, stress will change and reorient itself in the reservoir as well as in the overburden, sideburden and underburden. As the reservoir is physically connected to the surrounding rock, there will also be deformation in these rocks. These resulting stress changes will induce velocity changes that will in turn affect the travel time of both up-going and down-going seismic waves. Laboratory experiments on cores have demonstrated that changes in the stress state of a rock will cause the acoustic velocity to change, showing that velocities initially increase rapidly at low effective stresses but this increase will plateau at high stresses resulting in a non-linear relationship. Holt *et al.* (2005) explains that several sources of non-linearity can be distinguished: changes in porosity with stress, the existence of sharp grain contacts and the presence of cracks and fractures. Both macroscopic models based on continuum mechanics (Prioul *et al.*, 2004) and microscopic models (Sayers and Kachanov, 1995) have been proposed to understand the velocity dependence on stress and strain.

The time-shift anomaly is therefore interpreted as the cumulative effect of both changes in layer thicknesses and seismic velocity changes due to a stress transfer to

the overburden. The time-lapse seismic time-shifts can then be used to map the zone that has potentially undergone geomechanical changes at the reservoir level. If the *in situ* conditions are adequate a well-repeated seismic survey can measure time-shifts of the order of several milliseconds.

6.4.2 The R Factor

The physical interpretation of the time-lapse seismic time-shift anomaly can be understood using a simple model proposed by Hatchell and Bourne (2005). In the case of normal incidence P-waves, it has been proposed that fractional changes in velocity are proportional to fractional changes in vertical path length where the constant of proportionality is referred to as the R-factor.

$$\frac{\boldsymbol{dv}}{\boldsymbol{v}} = -\boldsymbol{R}\boldsymbol{\varepsilon}_{\boldsymbol{zz}} \tag{6.1}$$

From this relationship, the fractional change in traveltime can be expressed as

$$\frac{dt}{t} = (1 + R)\varepsilon_{zz} \tag{6.2}$$

where R denotes the ratio between the vertical velocity change and the vertical strain at a given depth. The total time-shift the P-wave travel time would experience between the surface and any given number of geological layers can be written as

$$\Delta\boldsymbol{t} = \int_{\boldsymbol{0}}^{\boldsymbol{z}} (\boldsymbol{1} + \boldsymbol{R})\frac{\boldsymbol{\varepsilon}_{\boldsymbol{zz}}}{\boldsymbol{v}}\boldsymbol{dz} \tag{6.3}$$

In other words, the time-shifts estimated at the reservoir level are the cumulative effect of both vertical strain in the overburden and the associated velocity changes. This has the advantage of being a robust indicator of geomechanical effects as they are effectively integrated along the raypath but the disadvantage of not being able to highlight the regions of most dramatic change.

The empirical and pragmatic approach of relating velocity changes to vertical strain via a single parameter has appeared to be extremely effective at explaining seismic time-shift anomalies and is widely used to study geomechanical effects in the overburden (Staples *et al.*, 2007; Tura *et al.*, 2005).

6.4.3 The U Factor

An equivalent model is to cast the velocity changes in terms of stress changes

$$\Delta \boldsymbol{v} = \boldsymbol{U}\Delta\boldsymbol{\sigma} \tag{6.4}$$

where the constant of proportionality is referred to as the U-factor. In practice this model is seldom used as the U-factor covers a much wider range of values than the R-factor (Schutjens, 2005). Assuming linear elasticity the fractional change in travel-time can be expressed as

$$\frac{\Delta t}{t} = \frac{(1+R)}{E}(\Delta\sigma_{zz} - \nu(\Delta\sigma_{xx} - \Delta\sigma_{yy})) \tag{6.5}$$

Under this stress formulation, the Young's modulus E and Poisson's ration ν are now required in addition to knowledge of the triaxial stress state.

6.4.4 Offset dependence

It should be noted that the models described in the previous sections are only suitable for zero-offset seismic data. In general however, velocity changes will be lithology dependent and tri-axial stress changes may lead to stress induced velocity anisotropy. Modelling of offset-dependent time-shifts has shown a strong dependence on the deviatoric stress (Fuck *et al.*, 2011). Injection induced stress changes are typically tri-axial. Stress can decrease in one direction and increase in the other. To understand geomechanical failure knowledge of the tri-axial stress state is crucial. Since triaxial stress changes cause anisotropic velocity changes, this in turn leads to a detectable time-lapse signal (Herwanger and Horne, 2009). Although still an immature technology, offset dependent time-lapse time-shift measurements can potentially characterise tri-axial stress changes.

6.4.5 Time-Strain

In addition to time-shifts, time-strains are of great interest as an indicator of geomechanical changes. Time-strains are the vertical derivatives of time-shifts. A time-lapse seismic time-shift is an integrated measurement. Assuming a vertical ray path, the time-shift at a specific point is the accumulation of travel time differences

due to all the layers above it. In order to locate geomechancial effects, the integrated measurement is differentiated to give the fractional change in travel time at a determined location. By analogy with physical strain the fractional change in travel-time is referred to as the time-strain. The time-strain is related to the physical strain and the fractional change in seismic velocity via the equation:

$$\frac{dt}{t} = \frac{dz}{z} - \frac{dv}{v} \tag{6.6}$$

In practice it is the time-shifts that are first estimated from the time-lapse seismic data. Methods for time-shift estimation are available in the literature (Hale, 2009; Hall, 2006). These in turn can be differentiated to estimate the interval time-strain. Assuming the R-factor is known for the subsurface lithology, an estimate of the subsurface strain can be made from the derived time-strains. Time-strains can potentially be interpreted more directly than time-shifts. However, the differentiation involved in estimating the time-strains will increase the noise levels in the data. Consequently, time-shifts are a more robust measurement as they are an integrated measurement.

6.4.6 Data quality and repeatability

So far the generalised behaviour of a time-lapse time-shift signal has been described. However, the ability to use these time-shifts for CO_2 storage management will rely on the ability to to accurately measure them. It is now widely accepted that subtle time-lapse time-shifts (1 ms) can be detected around geomechanically active reservoirs. Such subtle measurements however were not always possible due to the presence of noise. The sources of noise have been reduced by dedicated time-lapse seismic acquisition and processing. The first significant change in data quality came from using parallel seismic processing. Processing errors were significantly reduced by parallel processing of the base and monitor seismic survey. The second improvement in data quality has come from the acquisition efforts to repeat source and receiver positions as accurately as possible.

The use of legacy data was the norm in the early days of time-lapse seismic surveys. The baseline seismic data was acquired and designed for other purposes other than monitoring such as exploration or development seismic surveys. The legacy surveys

would often have different acquisition and processing parameters from the monitor surveys. This would result in significant differences between the seismic surveys unrelated to the dynamic changes in the subsurface. It is now the norm however, that time-lapse seismic surveys are designed and acquired for the purpose of reservoir management.

6.4.7 Processing

Time-lapse seismic data sets were acquired in 1997 and 2009 at the Krechba field at InSalah. The baseline seismic survey acquired in 1997 is a legacy-survey covering the entire field. The 2009 repeat survey extent had to be restricted and only covers the injector wells KB-502 and KB-503. As described previously, legacy data usually has different acquisition and processing parameters. In order to minimise non-repeatability artefacts the 1997 and 2009 survey were co-processed. The shot-receiver grid of the 2009 survey was decimated to match that of the 1997 survey. Nickel (2013) concluded that despite the parallel processing of the time-lapse seismic data there were differences in amplitude scaling and seismic bandwith. Since the seismic surveys were acquired on land, it is expected to find travel-time differences due to residuals and the statics correction process.

Measures for quantifiying the repeatability have been described in the literature (Kragh and Christie, 2002). The Hercynian unconformity is used as a reference horizon to establish the repeatability of the time-lapse seismic since no fluid changes are expected at this depth. Therefore the estimated amplitude changes are a direct indicator of the survey non-repeatability. In the reservoir region, hower, injection fluid effects are expected to occur.

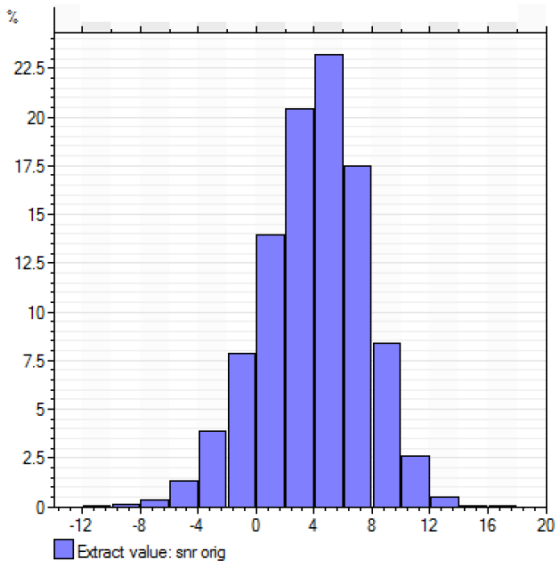


Figure 6.7: Histogram of the time-lapse signal to noise ratio (SNR) extracted along the Hercynian unconformity (Courtesy of M. Nickel, Schlumberger Stavanger Research, Norway).

The repeatability indicator shows that the signal to noise ratio is distributed around 4 dB (Figure 6.7). Nickel (2013) used a cross-equalisation method to improve the signal to noise ratio to an average of 6.5 (Figure 6.8). Despite this improvement the seismic data is still considerably affected by noise and subject to uncertainty.

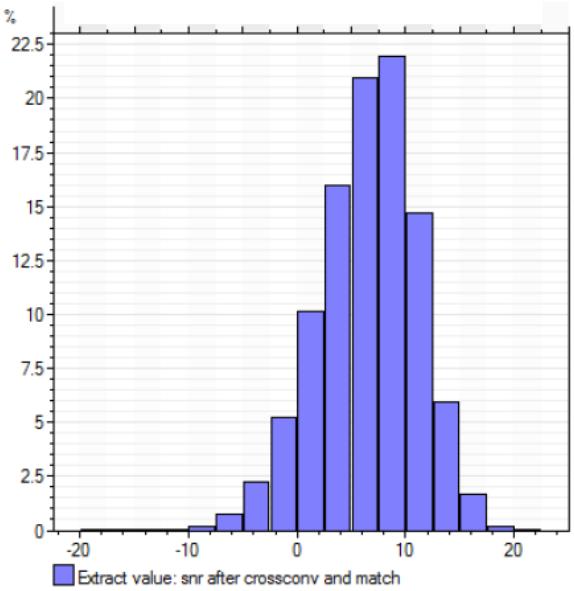


Figure 6.8: Histogram of the time-lapse signal to noise ratio (SNR) extracted along the Hercynian Unconformity after cross-equalisation (Courtesy of M. Nickel, Schlumberger Stavanger Research, Norway).

This is a measure of the noise floor. Consequently, to have a detectable dynamic change due to CO_2 injection, the induced change in the seismic signal must be higher than the estimated noise floor.

Until now geomechanical changes in the form of time-lapse seismic time-shifts have been described. In addition to this kinematic component there is also an amplitude component due to pressure and saturation changes at the reservoir level. At this point the question can be asked, if the ultimate goal is to demonstrate the safe storage of CO_2, why not map the CO_2 saturation and pressure changes directly in the reservoir region from the amplitude component (Landrø, 2001)? The ability of this monitoring technique to successfully image the CO_2 plume is site-specific and is highly dependant on the petro-physical properties. Feasability studies have shown that given the depth and thus the temperature and pressure regime for the injected CO_2 and the given petrophysical properties, the amplitude component of the time-lapse signal will be weak in addition to being below the noise floor (Nickel, 2013).

For these reasons, it is the time-lapse seismic time-shift that is considered the most robust attribute and will be subsequently used in combination with InSAR data to understand the flow and pressure behaviour from CO_2 injection.

6.4.8 Time-lapse Seismic Interpretation

Using a preliminary analysis of the time-shift data during the CO_2ReMoVe project, Nickel (2013) observed a time-lapse seismic time-shift anomaly at wells KB-502 and KB-503. The extent of the time-shift anomaly relative to the wells is shown in Figure 6.9 for illustrative purposes. The vertical zero-offset component has been used to map the time-shifts. The estimated time-shifts are on the order of 3 milliseconds. The time-shifts are mapped along the NW-SE direction consistent with InSAR observations. The time-shifts are also observed to extend towards the South-East of the injection well KB-503 in agreement with the previous InSAR analysis in Section 6.4. At injection KB-502 the time-shifts extend predominantly to the North-West, also consistent with InSAR data

No attempt has been made to construct a stress/strain-dependent velocity model to forward model the time-shifts. The time-shifts are used as a qualitative indicator of the reservoir region that has undergone geomechanical deformation between 1997 and 2009. They support and provide confidence in the emerging interpretation from

InSAR data. They also provide a measure of the lateral extent of the structural feature at depth that has been affected by the CO_2 injection process.

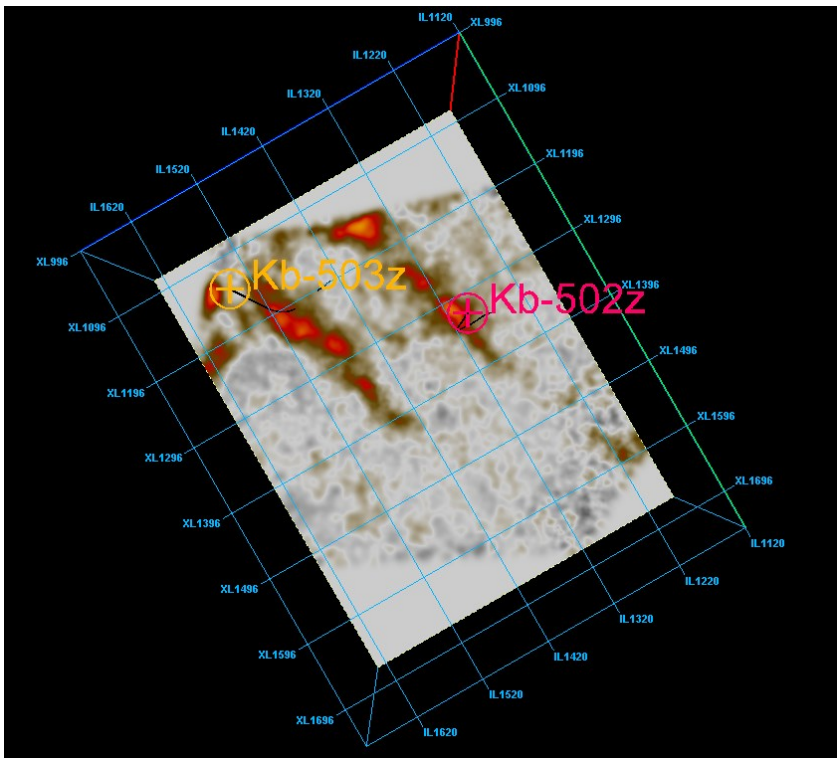


Figure 6.9: A preliminary analysis of the time-lapse seismic time-shifts between 1997 and 2009 for illustrative purposes (Courtesy of M. Nickel, Schlumberger Stavanger Research, Norway).

6.4.9 Mapping the fault/fracture zone

The structural feature is interpreted to be a fault/fracture zone. A mapping of the horizontal length of the structural feature exceeds 3 kilometres. As with the observed InSAR surface uplift, the time-shift anomaly suggests a structural feature controls the evolution of the CO_2 fluid and pressure front. A similar feature is also observed at injection well KB-502 aligned in the NW-SE direction and also consistent with InSAR surface uplift. The strong correlation between the time-lapse seismic time-shift signal and the InSAR surface deformation helps support and build confidence towards the current interpretation.

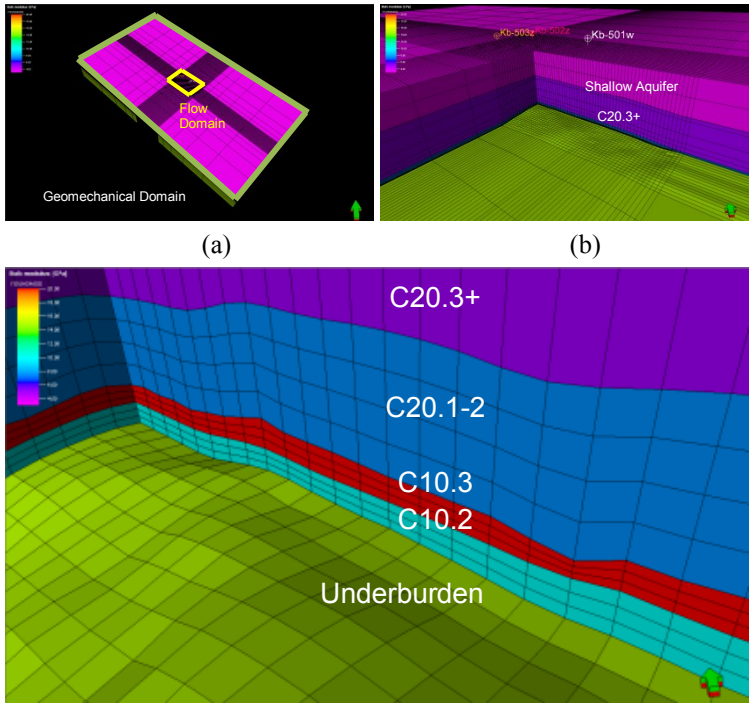
6.5 *Numerical Modelling*

6.5.1 Model Description

In this section the flow model and the geomechanical model to be used are described. A one-way coupling approach between the flow modelling code ECLIPSE and the geomechanical code VISAGE was chosen in order to assess the geomechanical changes associated with CO_2 injection. In a one-way coupling approach the reservoir model is exported from ECLIPSE to VISAGE and embedded into a larger geomechanical model with sideburden and underburden added to minimize boundary effects. The static model based on data provided by the In Salah Gas Joint Industry Project is summarised in Table 6.1.

Table 6.1: Flow properties (based on data by the In Salah JIP)

	Mean porosity (std. dev)	Mean k_h, mD	$Log_{10}(k_h)$ (std. dev.)	k_v/k_h
Shallow Aquifer	0.25 (0.2)	1,000	3.0 (0.5)	0.1
C20.3+	0.10 (0.01)	0.001	-3.0 (0.5)	0.1
C20.1-2	0.05 (0.01)	0.1	-1.0 (0.5)	0.1
C10.3	0.01 (0.01)	0.02	-1.7 (0.5)	0.1
C10.2	Numerical grid with stochastically generated permeability and porosity values			



(a) (b)

(c)

Figure 6.10: (a) Flow and geomechanical model domain (b) Overburden layers (c) Reservoir layers.

The model consists of five stratigraphic units and a total of 18 layers. The main storage reservoir C10.2 and the overlying C10.3 formation both consist of three layers each (Figure 6.10). In the flow domain the grid block dimensions are roughly 400 m by 400 m. The geomechanical domain grid size increases with distance from the flow domain

6.5.2 Flow properties

The porosity, permeability and the vertical to horizontal permeability ratio used in the model are shown in Table 6.1. The relative permeabilities and capillary pressures used in the reservoir simulation are shown in Table 6.2. The reservoir simulation is modelled as an open system. The coupled flow-geomechanical simulation was composed of two phases. The initial two-year period is composed of intact layers, followed by the hydraulic stimulation of a fracture/fault zone to account for the observed surface uplift behaviour. Since no prior knowledge of the flow properties of the fracture/fault zone are available they will be estimated directly from BHP and InSAR surface uplift data.

Table 6.2: Gas-water relative permeabilities and capillary pressures used in the reservoir simulations.

Water saturation	Gas relative permeability	Water relative permeability	Capillary pressure (bar)
0.39	1	0	2.44
0.40	0.5935	0	2.39
0.40	0.5805	0	2.34
0.41	0.5543	0	2.25
0.42	0.5281	0	2.16
0.43	0.5020	0	2.06
0.44	0.4760	0	1.97
0.50	0.3513	0.0028	1.65
0.55	0.2404	0.0101	1.43
0.61	0.1485	0.0180	1.27
0.66	0.0788	0.0269	1.15
0.71	0.0318	0.0465	1.04
0.77	0.0137	0.0933	0.93
0.82	0.0093	0.1910	0.82
0.88	0.0087	0.3699	0.70
1	0	1	0

6.5.3 Stress Regime and Geomechanical properties

A rock density of 2,000 kg/m^3 was used to model the lithostatic stress. The initial stress condition is a strike slip regime, where the maximum horizontal stress (NW-SE) exceeds the vertical stress (Ringrose *et al.*, 2011).

For the geomechanical simulation, the side and bottom boundaries are constrained by non-normal displacement boundaries. The surface is modelled by a zero traction boundary.

The set of elastic rock properties defined for the geomechanical model are the Young's Modulus *E* and Poisson's ratio ν of the reservoir and the over/side/under-burden rocks (Table 6.3) based on data provided by the In Salah Gas Joint Industry Project. It has been noted that the variation of rock elastic properties with depth in layered media can have a significant impact on the surface deformation. Vasco *et al.* (2010) have shown that the elastic properties of the lower caprock have a large impact on the surface uplift. The elastic properties for the shallow aquifer, the main caprock and the lower caprock (C20.1-3) are subject to considerable uncertainty, whereas those for the tight sandstone layer (C10.3), the main reservoir (C10.2) and the Devonian underburden are estimated from good quality logs (Gemmer *et al.*, 2012). Therefore, in this study, the Young's Modulus for the lower caprock (C20.1-2) was chosen as the history matching parameter for the geomechanical model given its higher uncertainty.

Table 6.3: Geomechanical model rock elastic properties (based on data by the In Salah JIP)

	E (GPa)	ν
Shallow Aquifer	3.0	0.25
C20.3+	5.0	0.30
C20.1-2	2.0	0.30
	(**7.5**)	(this study)
C10.3	20.0	0.25
C10.2	10.0	0.20
Devonian	15.0	0.30

6.5.4 Fault/Fracture zone transmissibility

In practice there are two general approaches for modelling fault/fracture permeability:

- Implicitly, where both the matrix and fault/fracture permeability are modelled in the overall rock permeability and it is assumed that the effect of fault/fractures has been captured as an effective permeability for a geocellular grid block.
- Explicity, where the fault/fracture is represented in the model.

For the explicit case there are then several options for modelling (Nelson, 2011):

- Discrete Fracture Network (DFN) models – the explicit geometry of individual fractures is modelled in a complex network.
- Dual permeability models – the fracture and matrix permeability are explicitly represented. The fracture geometry is represented by a shape factor.
- Dual porosity models – the matrix and fracture porosity is explicitly represented but the permeability is assumed to occur only within the fractures. The fracture geometry is represented by a shape factor.

An implicit approach will be used to model the fault/fracture zone in the reservoir. The introduced fault/fracture zone is implicitly accounted for by employing a technique proposed by van Lingen *et al.* (2001) as implemented in the ECLIPSE 300 compositional simulator. The permeability contribution from the fractures is accounted for by the following relationship:

$$\boldsymbol{k_b = k_m + \frac{n_f k_f w}{a}} \tag{6.7}$$

where k_b is the effective permeability, k_m is the matrix permeability in a grid block, n_f is the number of conductive fractures in the gridblock, w is the fracture aperture, k_f is the fracture absolute permeability and a is the block size. The product $n_f k_f w$ is referred to as the fault/fracture transmissibility, with units mmDarcy. Due to the way the conductive fracture is implemented in the simulator, the fault/fracture zone transmissibility is lumped into the effective permeability of the gridblock. In this manner, a fault/fracture zone can be handled as a single fault/fracture of the same transmissibility. For an ideal fracture, the fracture permeability is given by:

$$\boldsymbol{k_f = \frac{w^2}{12}} \tag{6.8}$$

The fracture transmissibility is therefore $\frac{w^3}{12}$. The permeability updates during the history matching are performed on the fracture transmissibility.

6.5.5 Modelling time frame

Based on the previous interpretation of InSAR and time-lapse seismic data the coupled flow-geomechanical modelling is divided into two-distinct phases. In a one-way coupling scheme between fluid-flow and geomechanics, the effects of stress

changes on permeability are not explicitly taken into account. Permeability changes such as the activation of a fault/fracture zone and its associated timing must therefore be done manually.

In the first phase, the coupled flow-geomechanical modelling is carried out assuming the rock is intact. This period lasts from the start of injection in 2004 to September 2005. In the second phase, CO_2 injection is simulated from September 2005 until the end of injection. During this phase, the fault/fracture zone introduced into the model is assumed to be active.

6.6 *Results*

6.6.1 History Matching and Sensitivity Analysis

Manual history matching was implemented to history-match the coupled flow-geomechanical model using insights gained from bottom hole pressure, InSAR surface uplift and time-lapse seismic time-shifts.

The surface deformation magnitude is strongly coupled to the geomechanical properties of the reservoir, the overburden and the pressure build up. The pressure build up is in turn controlled in large part by the permeability of the reservoir. The current interpretation suggests the hydraulic stimulation of a fault/fracture zone during CO_2 injection. The timing of the hydraulic stimulation is constrained using InSAR data. The geometry of the fault/fracture zone on the other hand is constrained by the time-lapse seismic time-shifts.

Against this backdrop, the Young's modulus of the lower caprock and the transmissibility of the fault/fracture zone are used as the tuning parameters for history matching.

The sensitivity analysis and the history matching of the coupled flow-geomechanical model are divided into two phases based on the current interpretation. The first phase consists of the initial two year period. In this phase the reservoir is composed of intact layers. A sensitivity analysis for the Young's modulus will be made in this initial stage as the fault/fracture zone is not conductive at this stage. Once the Young's modulus has been history matched it is not expected to change over the injection period and is kept fixed for the next phase. In the second phase the

fault/fracture zone is conductive. A sensitivity analysis on the transmibility of the fault fracture zone can then be made and history matched using the available observations.

Figure 6.11 shows the sensitivity analysis for the Young's modulus of the lower caprock. The modelled transient ground deformation is shown for a range of Young's modulus between 7.5 GPa and 20 GPa. As the Young's modulus is decreased the magnitude of the surface uplift increases accordingly. An agreeable match between modelled and measured surface uplift is found for a Young's modulus value of 7.5 GPa. The history matched value is higher than the reference model published by (Gemmer *et al.*, 2012) (2 GPa). At this stage the rock was assumed to be intact with no enchanced permeability due to the presence of fractures, and an agreeable match with the bottom hole pressure was kept.

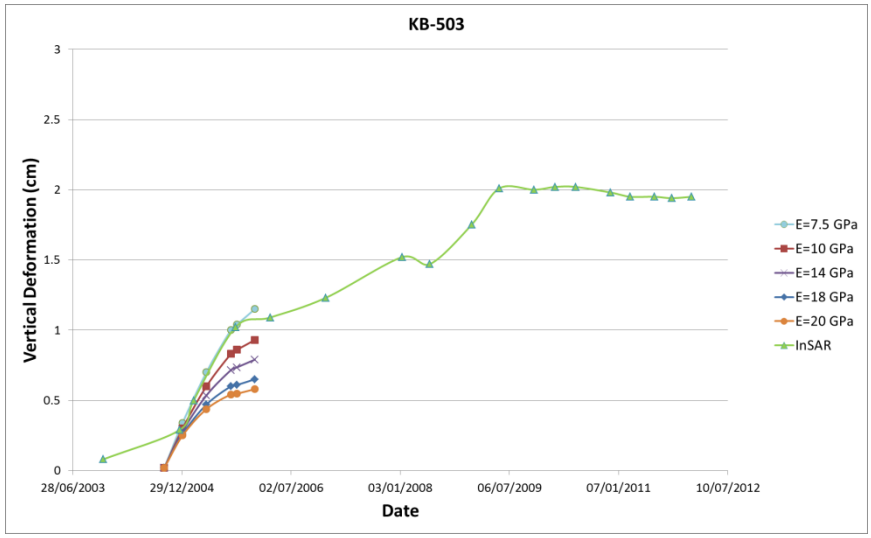


Figure 6.11: Sensitivity analysis for the Young's modulus of the lower caprock.

In the second stage of history matching, the Young's modulus value of 7.5 GPa is kept constant. At this point, the fault/fracture zone is activated.

It should be noted that the transmissibility is assumed to be constant throughout the entire fault/fracture zone. As explained in Chapter 2 the flow rate in a fracture is highly dependent on the stress state and the fracture aperture and roughness. In practice however fracture properties are not easily measured and an equivalent fracture representation must be inferred from dynamic data.

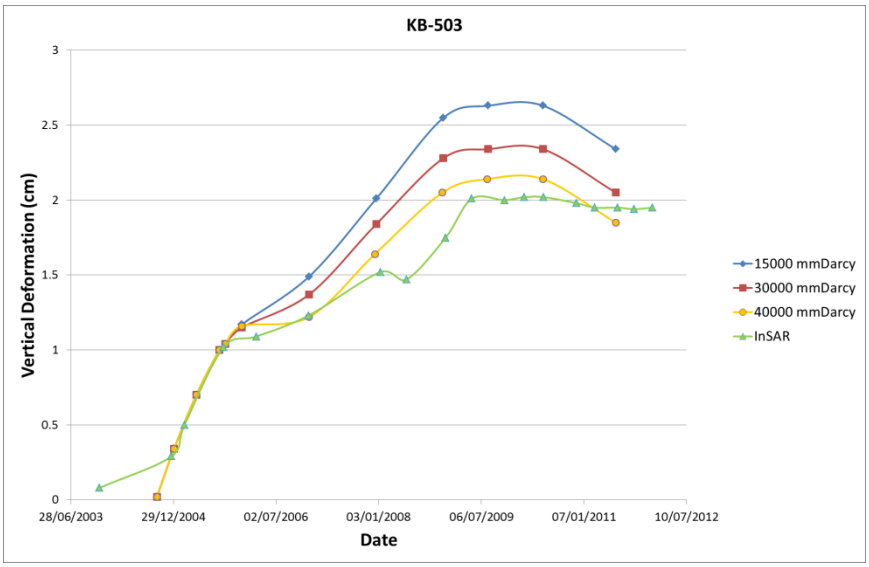


Figure 6.12: Sensitivity analysis for the fault/fracture zone transmissibility.

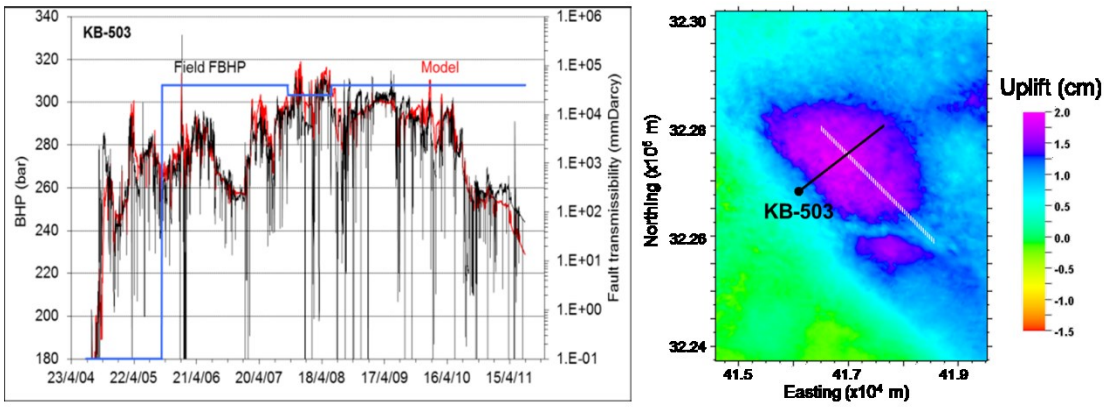
Figure 6.12 shows a sensitivity analysis for the fault/fracture zone transmissibility. As the magnitude of the fault/fracture zone transmssiblity is increased the magnitude of the surface uplift decreases. The same overall trend is observed for all the modelled range of fault/fracture zone transmissibilities. In order to match the observed behaviour the fault/fracture zone transmissibility must be decreased.

Based upon the previous analysis of the InSAR surface uplift and time-lapse seismic time-shift data a fracture zone with a dynamic transmissibility was incorporated into the coupled flow-geomechanical model. The horizontal extent of the fracture/fault zone has been constrained and mapped using seismic data. The fracture/fault zone with dynamic transmissibility introduced is approximately 3 km long and is confined to the main storage formation C10.2 (Figure 6.13). It should be pointed out that there is uncertainty with regards to the vertical extent of this fault/fracture zone as discussed recently by White *et al.* (2014).

6.6.2 BHP History Match

The bottom hole pressure at KB-503 is shown in Figure 6.13 for the entire injection period. After rising to around 260 bar at the start of injection, the field bottom hole pressure then displayed a general upward trend and eventually levelled off at approximately 300 bar towards the end of 2007. Between mid-2009 and 2011, the field BHP displayed an overall decrease reaching approximately 260 bar by the end of injection. The field bottom hole pressure curve was history matched by

introducing a fracture/fault transmissibility of around 40,000 mmDarcy from September 2005 after nearly two years of sustained CO_2 injection. Figure 6.13 shows the bottom hole pressure history-match alongside the dynamic fault transmissibility. The location of the mapped fault/fracture zone superimposed on the InSAR data is also shown. The fracture/fault transmissibility remained conductive at more or less the same level, despite the occasional surge in injection rate for the remainder of the injection operation. The timing of the fracture/fault reactivation is consistent with that from interpreted InSAR surface uplift data.



(a) (b)

Figure 6.13: (a) Improved history matching of the CO_2 injection pressure at KB-503; (b) Modelled fracture/fault zone with dynamic transmissibility.

6.6.3 InSAR History Match

After calibration to the field bottom hole pressure, the reservoir model was imported and embedded into the geomechanical model. An improved match to the observed geomechanical response was obtained. The rapid rise in surface uplift was reproduced for the first two years of injection. Figure 6.14 shows the improved history match to the InSAR surface deformation over the previous history matching effort by Shi *et al.* (2013). In the middle stages of injection, after the inferred hydraulic stimulation of the fracture/fault zone, the coupled flow-geomechanical model slightly overestimates the surface uplift while predicting the correct trend. This overestimation is believed to be a result of the inability of the current single-medium reservoir model to simulate fluid flow in discrete fractures. Instead the entire grid cells are pressurised during CO_2 injection.

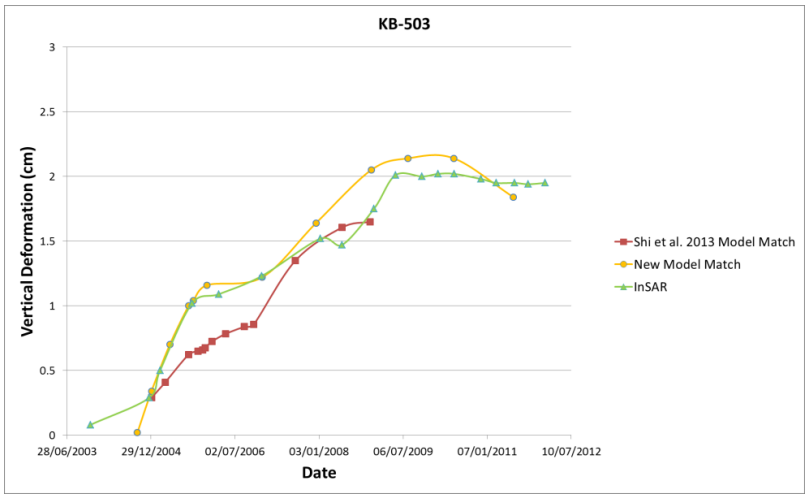


Figure 6.14: InSAR surface uplift time series at the centre of the well and the model predictions at KB-503.

The modelling effort focused on improving the mismatch in the initial stage of injection where two distinct phases of pressure build up and pressure propagation were defined by activating a fault/fracture zone. This has lead to improved predictions in the dynamic behaviour of the reservoir. It is important to note that there is still some mismatch in the later stages of injection. Starting from approximately 2008, the surface deformation is overpredicted but the correct trend is still observed. From 2010 until the end of injection, the modelled surface deformation decreases as the injection rates are reduced. In this final stage, the observed surface deformation remains more or less constant even after the end of injection. After injection stopped in 2011, InSAR data continued to be acquired until 2012. Further investigation of this mismatch would require the explicit modelling of the fault/fracture zone and its growth over time. These differences between the observations and predictions suggest possibilities for simulation model updating and better understanding of the interaction between CO_2 injection and discrete fracture networks and fault zones.

6.6.4 Comparison with other injection wells

It has been proposed that a structural feature controls the dynamic pressure and geomechanical behaviour at injection well KB-503. A similar consensus has been reached at injection well KB-502 where the two-lobed uplift pattern is a clear expression of the tensile opening of a structural feature at depth. In order to explain both the bottom hole pressure and the surface uplift data a fracture intersecting the

injection well must be included in the model. Although a two-lobe uplift pattern has not been observed at KB-503, there is still evidence for the interaction between injection pressure and structural features around the reservoir region. This is visible in both the pattern of surface deformation and its transient evolution. Moreover, a similar time-lapse seismic time-shift signature is observed at both injection wells adding confidence to the interpretation. At injection well KB-501 the interplay between pressure and structural features appears to be lessed pronounced than at the other two injection wells. The repeat seismic survey did not cover injection well KB-501 to see whether a similar time-lapse seismic anomaly can be observed. Nonetheless, the InSAR data suggests preferential flow in the same direction as the other two injection wells but to date the bottom hole pressure and the surface deformation can be matched without having to introduce fault/fracture zones with dynamic transmissibility.

6.7 *Summary and Discussions*

Building on previous coupled flow-geomechanical studies of CO_2 injection at In Salah, an effort has been made to attain an improved understanding of the flow and pressure behaviour at injection well KB-503 over the entire injection period from 2004 to 2011, which is consistent with the bottom hole pressure, InSAR surface uplift and time-lapse seismic data. The deformation data covers the entire period of monitoring from July 2003 to January 2012. A detailed analysis of the InSAR surface uplift pattern was first made suggesting hydraulic stimulation of fractures/faults at depth after almost two years of CO_2 injection. The picture emerging is that preferential flow paths along the NW-SE maximum stress direction appear to have been created, as a result of fluctuations in the injection rate from September 2005 onwards, which led to the pressurisation of the reservoir rock away from the immediate vicinity of the wellbore. A plausible explanation is that CO_2 injection has caused hydraulic stimulation of pre-existing fractures/faults in the area. Time-lapse seismic time-shifts data support this interpretation showing a seismic anomaly in the NW-SE direction. The time-lapse seismic time-shift data was used to map the fault/fracture zone. This insight was then incorporated by introducing the fractured zone with a dynamic transmissibility into the reservoir model. Using forward coupled flow-geomechanical modelling, the injection pressure behaviour

and the geomechanical response at the ground surface has been largely reproduced. The set of flow and geomechanical properties used however do not represent a unique solution to the available observations. Nevertheless, a plausible mechanism has been established to explain the available surface uplift and pressure observations. After nearly two years of sustained CO_2 injection, the reservoir region nearby the injection well was pressurised followed by the hydraulic stimulation of a fault/fracture zone allowing the CO_2 injection-induced pressure increase to propagate towards the South-East.

It should be noted that, in this study, the history matched value for the Young's Modulus for the lower caprock (C20.1-2) at KB-503 is higher than that used by Gemmer *et al.* (2012) (2 GPa) and lower than the history matched value used by Shi *et al.* (2013) (18 GPa) at KB-501, suggesting possible lateral variations in the geomechanical properties.

Here, the hydraulic stimulation of a fracture/fault zone is simulated by substantially increasing its transmissibility enabling the fluid and pressure to propagate. The fault/fracture zone was contained within the reservoir formation, however, there remains considerable uncertainty regarding the vertical extent of this zone, as discussed recently by White *et al.* (2014). Further work is also recommended to overcome modelling limitations in order to explicitly model fracture propagation and the pressurised fractures at depth. The assumption of a spatially uniform transmissibility for the fault/fracture zone must also be overcome. The propagation of the fault/fracture zone is a function of stress and would require the calibration of a coupling function for a stress-dependent permeability.

The joint use of pressure, InSAR surface deformation and time-lapse seismic data coupled with flow-geomechanical deformation has lead to an improved understanding of the pressure behaviour at KB-503. However, it is important to note that, without the use of InSAR and time-lapse seismic data, the presence of a fault/fracture zone intersecting the reservoir may not have been identified. As shown in previous studies the bottom-hole pressure on its own can be history-matched by tunning the matrix permeability in the near wellbore region. The InSAR data being highly sampled in time allowed an estimate to be made of the timing of the reactivation of the fault/fracture zone. The time-lapse seismic time-shifts was utilised

as an indicator of the regions that have undergone geomechanical deformation at the reservoir level and provided a constraint on the fault/fracture zone geometry.

The use of time-lapse seismics to image stress changes inside the earth is still a developing technology. It is nonetheless sensible to consider how this can be further used to detect geomechanical changes during CO_2 injection.

This particular seismic attribute proved to be robust given the repeatability limitations of the time-lapse seismic data set. The base seismic survey is a legacy data set and the acquisition and processing parameters differ than that from the monitoring seismic survey. For future CO_2 storage sites, time-lapse seismic surveys are now routinely dedicated for the purpose of reservoir management, so the the baseline survey acquisition and processing are designed for the purpose of future monitoring.

An alternative approach would be to history-match the measured time lapse seismic time-shifts. Using the predictions from the coupled flow-geomechanical simulations for stress and strain changes in the overburden, the resultant time-shifts are calculated and applied to the seismic data. Based on the residual difference between the time-shifted monitor data and the base seismic data, the flow-geomechanical model would be updated accordingly until arriving at an acceptable match. This however would introduce additional parameters to our models, such as knowledge of the velocity dependence on stress/strain for the overburden rocks and would required the development of coupling tool between the geomechanical simulator and a seismic simulator. This would provide an additional dataset to calibrate flow and geomechanical models to predict CO_2 behaviour.

Chapter 7 Coupled Flow-Geomechanical Performance Assessment using the Ensemble Kalman Filter

This chapter presents the methodology developed for coupled flow-geomechanical CO_2 storage site performance assessment using the ensemble Kalman filter (EnKF). The methodology is applied to the In Salah case study dataset in order to validate the developed technique using field data. The EnKF approach is used to estimate the parameters controlling the performance of the CO_2 storage site by assimilating data from both flow and geomechanical observations. The controlling parameters in this study are the anisotropic permeability at the injection wells, fault/fracture transmissibility and the Young's modulus for the lower caprock. The data sources are the injection wells' flowing bottom-hole pressure (FBHP) and Interferometric Synthetic Aperture Radar (InSAR) surface deformation. The study considers three scenarios. In the first scenario only flow properties are considered and the geomehcanical properties are assumed to known. In the second scenario no lateral variations in the caprock geomechanical properties are considered. In the third scenario lateral variations in the caprock geomechanical properties are introduced. The findings of the third scenario have shown that a model taking into account lateral variations in geomechanical properties provides an improved match to the InSAR surface uplift. Therefore, the developed methodology is shown to be effective

in updating the flow and geomechanical parameters controlling the performance of the CO_2 storage site.

7.1 *EnKF Modelling Implementation*

The EnKF is in principle independent of the reservoir and geomechanical simulator used. Nonetheless, the EnKF code needs a mechanism to communicate with the simulators in use. Specifically, a mechanism is also needed for the reservoir simulator to communicate with the geomechanical simulator in an automated form. In the past chapter the geomechanical simulator VISAGE was implemented in a manual history matching process. In this chapter the geomechanical simulator FLAC^{3D} is used instead given its greater flexibility to manipulate the files containing the model setup. Nevertheless, the same grid used in VISAGE was maintained when modelling in FLAC^{3D}. For the EnKF to work an interface with ECLIPSE and FLAC^{3D} is needed. The sections that are critical for the EnKF to work are the data files where the model parameters and state variables are stored. The EnKF will need to update both the flow and the geomechanical model parameters according to the data assimilation results as it proceeds. At each data assimilation step both ECLIPSE and FLAC^{3D} will need to be stopped and then restarted.

The flow and geomechanical simulators generate restart files at the end of each forward time-step. The EnKF code must therefore to be able to:

- Read the restart files
- Compute the updated model parameters
- Update the restart files with the filtered data

This requires extensive knowledge of the output formats. The interface must read and write the output files from the simulators as well as exchange information between them.

Two key issues are memory management and simulation time. Parallel programming was developed for the flow simulations. This feature however was not extended to the geomechanical simulations due to present licensing limitations. The simulation time is therefore governed by the number of geomechanical simulations.

The forecast step contains the communication with ECLIPSE and FLAC^{3D}. A coupling module is used to take the ECLIPSE output and transfer it to FLAC^{3D}. The

implementation of adding measurment noise has also been included. The available measurements are first read and the measurement perturbation is added using a gaussian random generator. The computation of the model and data covariances and the Kalman gain are computed using standard matrix operations. In order to retrieve the measurements from the model the measurement operator picks out the right variables.

Other functionalities that were developed in the algorithm include:

- Specify upper and lower bounds on parameters
- Use the log value of the parameter if this assumption becomes more appropriate

Appendix A presentas a simple 2D case with a known solution where the EnKF algorithm developed is tested to ensure that the EnKF code and coupling scheme between ECLIPSE 300 and FLAC^{3D} have been successfully developed.

7.2 *The EnKF Setup*

7.2.1 Ensemble definition

Initialising the ensemble Kalman filter is a crucial step of the process. The range of modelled flow and geomechanical parameters is defined as well as the subset of parameters that will be updated by the EnKF. An estimate of the error associated with the available observations must also be defined. The ensemble size defined as the number of coupled flow and geomechanical models to simulate must also be defined by the user. In practice this is usually limited by the amount of computational power available and from the literature (Aanonsen *et al.*, 2012) EnKF runs for a range between 40-100 model runs, which is usual for petroleum engineering applications.

7.2.2 Geostatistical simulation of flow properties

Sequential Gaussian geostatistical simulations of matrix permeability and porosity were generated using core data from six wells and two seismic porosity surfaces that were made available (Nickel, 2013). Figure 7.1 shows the well location where the core data was obtained and the seismic porosity surface for the top reservoir. The seismic data indicates the crest of the reservoir anticline is of a higher porosity than

the flanks of the anticline. As clearly shown in Figure 7.1 significant parts of the reservoir illustrate a very low and near uniform porosity distribution, which would manifest as a noisy near uniform distribution, which are distinctly different than the crest, which exhibits spatial autocorellation. In order to implement this feature correctly in the coupled flow-geomechanical modelling, a cut-off value of 5% was used to define the selection to impose on the seismic data prior to variographic analysis. The porosity map after applying the cut-off value is shown in Figure 7.2.

It is believed that the seismic porosity surfaces should only be trusted in the vicinity of the wells and was used solely to reduce the uncertainty in the variogram parameters. In order to implement the SGS geostatistical algorithm, the porosity and permeability data were transformed to Gaussian frequency distributions using an anamorphosis function that fits the data. The anamorphosis function was also implemented inversely to back transform the results of the SGS algorithm to porosity and permeability values. All geostatistical analysis was carried out using the ISATIS geostatistical software package (Geovariances, 2014).

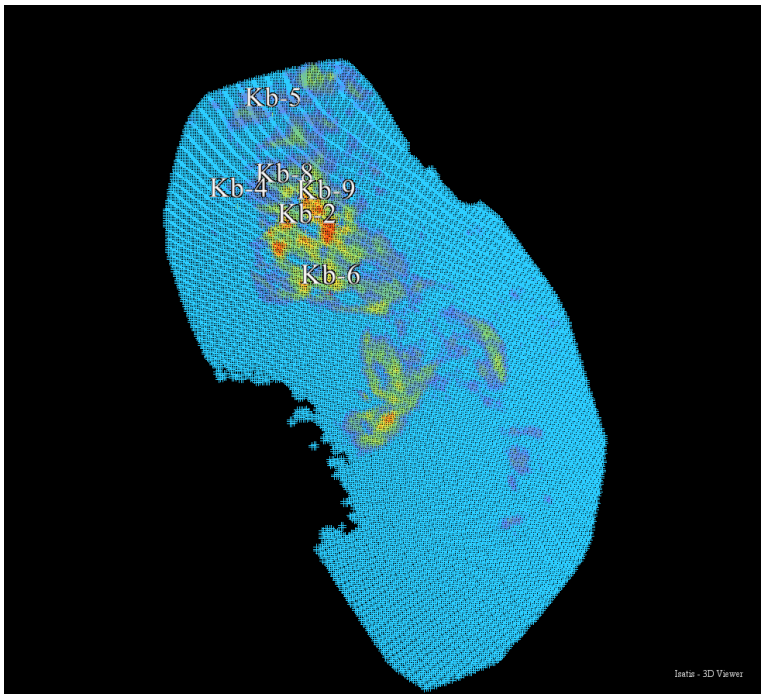


Figure 7.1: Seismic derived porosity surface for top reservoir layer.

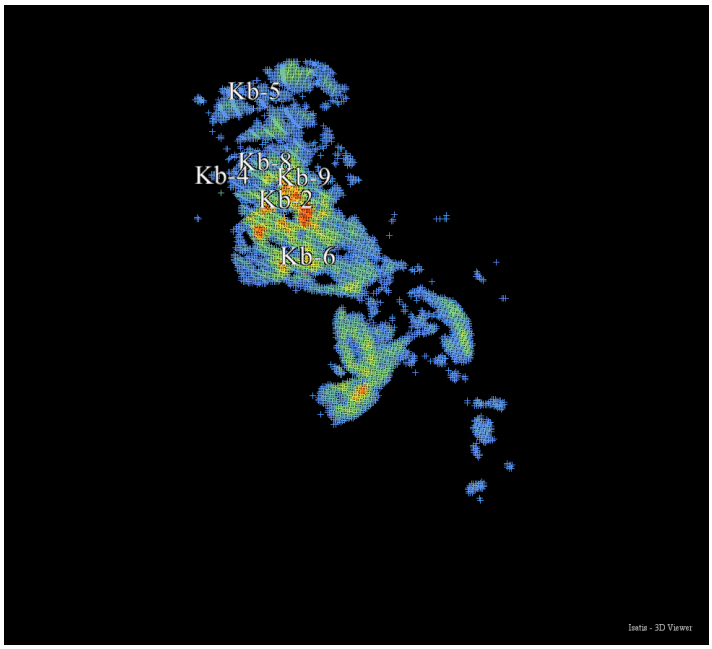


Figure 7.2: Seismic derived porosity surface using a 5% porosity cut-off value.

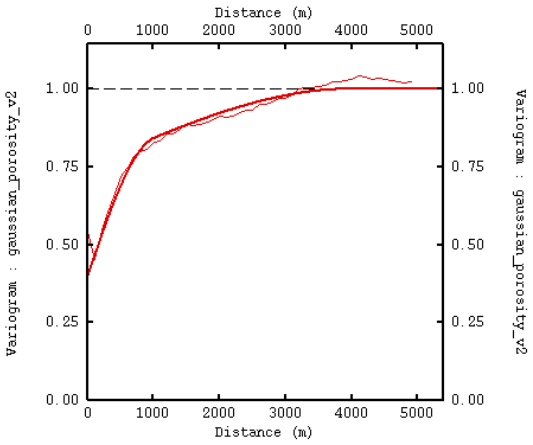


Figure 7.3: Porosity variogram.

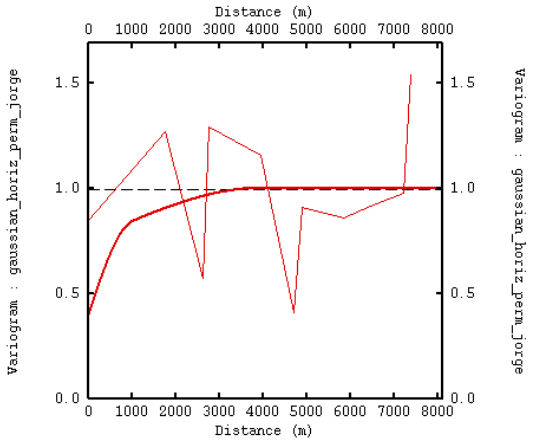


Figure 7.4: Permeability variogram.

The experimental variogram and the fitted model variogram for porosity and permeability are shown in Figures 7.3 and 7.4. The variogram functions chosen to fit the experimental variograms have two spherical spatial components with a range in the region of 2 km, respectively. The nugget component is in the region of 50% of the overall covariance for the experimental and modelled variograms. As expected, the variogram for the porosity has a good structure, as it is driven to a significant extend by reservoir formation lithology, also because it is controlled by the formation depth. In contrast the experimental variogram of permeability (Figure 7.4) appears as a pure nugget effect for the scale of sampling available. Considering permeability variations in the field are correlated to porosity but can have a much smaller correlation range, this is reasonable. In order to choose a realistic variogram function for permeability, the range and proportions of nugget and sill for the two spherical structures fitted to porosity data, were also used for permeability.

Sequential gaussian simulation was then used to generate realisations of the variables conditioned to the seismic data and using the modelled variogram as a constraint. Figure 7.6 and Figure 7.7 show a realistion for the permeability and the porosity fields, respectively. The high porosity and high permeability trend along the crest of the anticline have been preserved with the sequential gaussian simulation algorithm introducing randomness into the 120 realisations generated.

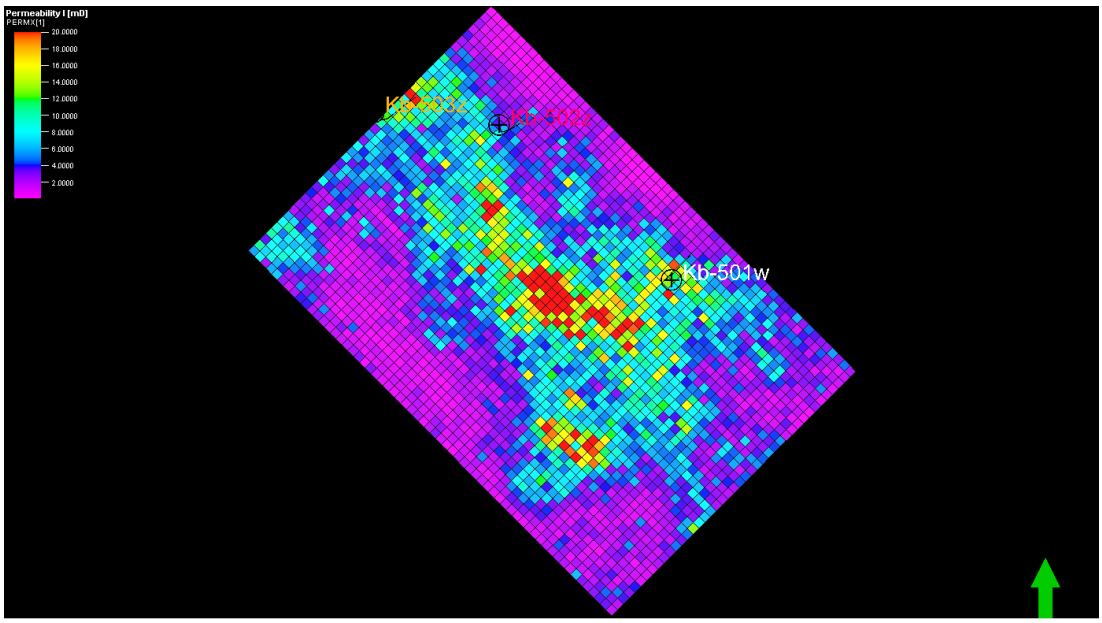


Figure 7.5: Geostatistical simulation of horizontal permeability.

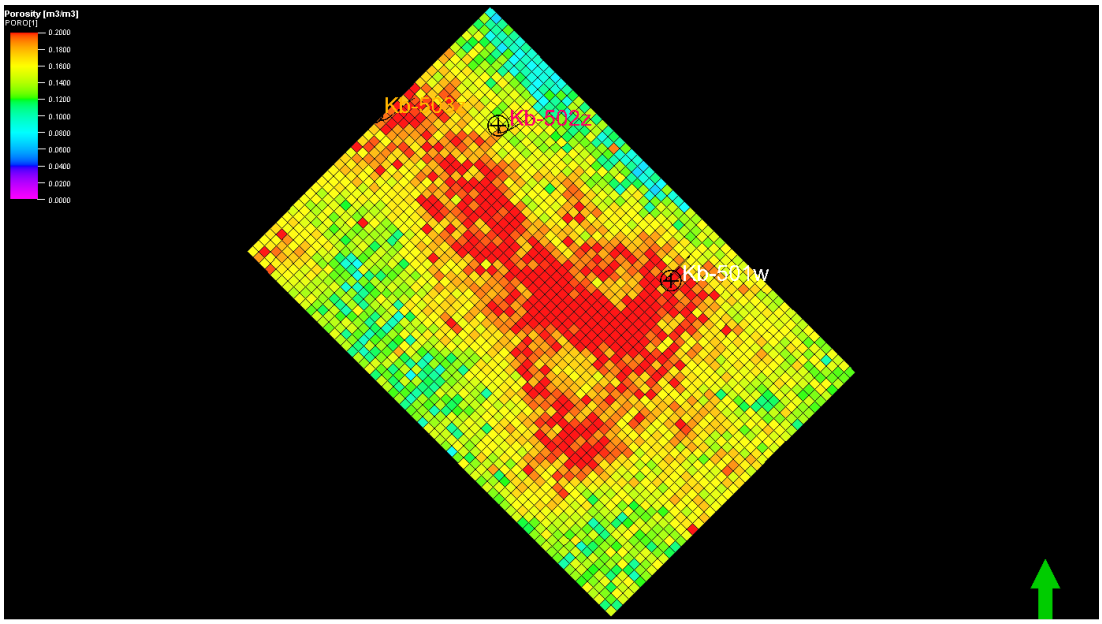


Figure 7.6: Geostatistical simulation of porosity.

7.2.3 Incorporating prior knowledge from InSAR

In the previous section porosity and permeability were attributed using geostatistical techniques using seismic porosity surfaces and core data from several wells. The InSAR data is an invaluable dataset as it contains information not present in the former datasets. In particular, the InSAR data provides information about the preferential flow directions which can be incorportated into the EnKF set up. Anisotropic flow directions are defined on the basis of the InSAR surface deformation patterns. The preferential flow direction is defined in the NW-SE direction with flow perpendicular in the NE-SW defined as the minor flow direction. The defined preferential flow directions are shown in Figure 7.7 superimposed on a map of InSAR data. The preferential flow direction is labelled X and the minor flow direction is labelled Y. The anisotropic permeability multipliers in these two predefined directions can then be used as the tuning parameters by the EnKF algorithm. The EnKF can also be used to update other flow parameters like fault/fracture transmissibility where the fracture orientation is also inferred from InSAR data. For injection well KB-502 the dynamic fault/fracture transmissibility will be the tuning parameter as it is believed to control the performance of the injection well.

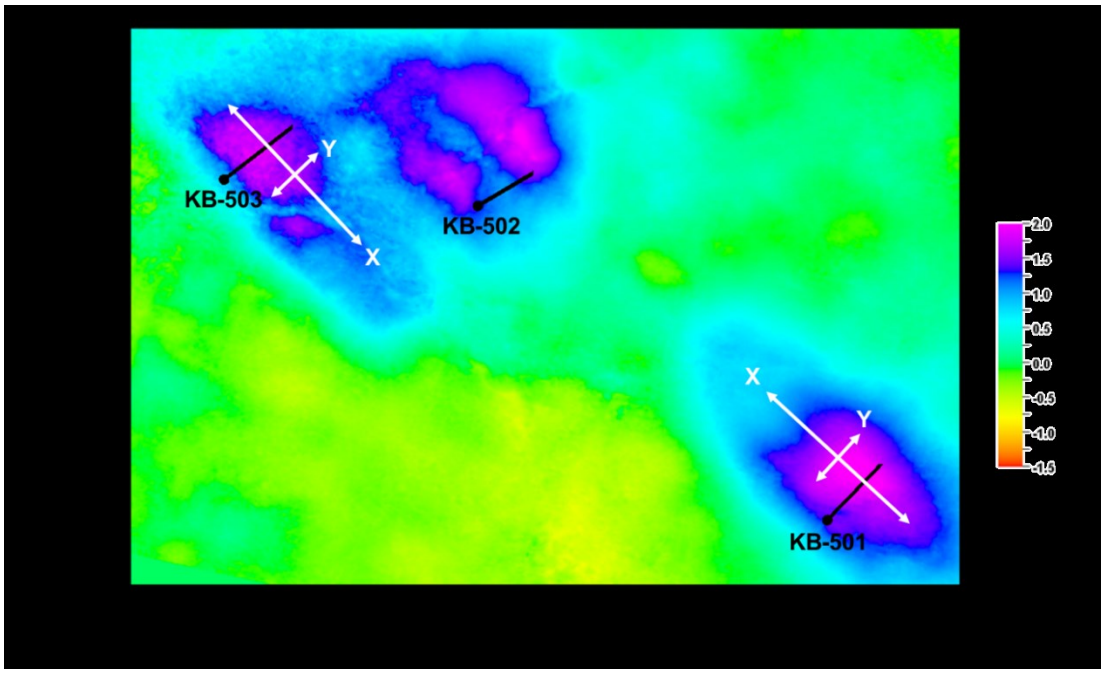


Figure 7.7: InSAR surface uplift map showing preferential flow directions (white arrows). The preferential flow direction is marked by X and the minor flow direction is marked by Y.

7.2.4 Geomechanical properties

As previously described, a layer cake geomechanical model will continue to be used. The EnKF however will focus on the lower caprock geomechanical properties. The Young's modulus will be the updated geomechanical property by the EnKF. Given the degree of uncertainty in caprock properties different cases can be explored. At first geomechanical uncertainty is introduced into the lower caprock but the geomechanical properties remain constant across the lower caprock. Subsequently, this is extended to allow for lateral variations in the lower caprock geomechanical properties. An assumption is made that the geomechanical properties above injection wells KB-502 and KB-503 are similar given there relative proximity. The geomechanical properties are allowed to vary laterally above KB-501 which is further away from the other two injection wells.

7.2.5 Observations

Two data sources are used in the data assimilation process: bottom hole pressure and InSAR surface data deformation. A bottom hole pressure estimate is available on a daily basis whereas the InSAR estimate availability varies over time but overall is more frequently acquired towards the end of the injection process when X-band

technology was used. A gaussian error disbribution with zero mean and 5% error relative to the measurment is assumed for both bottom hole pressure and InSAR surface deformation observations

7.3 *Results*

7.3.1 Scenario 1 - No Geomechanical Uncertainty

This section presents the application of the methodology using the EnKF to the In Salah CO_2 storage site. An ensemble size of 60 coupled flow-geomechanical models is used in this scenario using the fully automated EnKF procedure. There are two modelled cases. In the first case, no data assimilation is performed. In the second case BHP is assimilated on a monthly basis.

Figure 7.8 shows the match to the estimated BHP for all three injection wells compared to the initial case. The ensemble mean is taken as the best estimator and is represented in blue which can then be compared to the observations in red.

In this scenario, the geomechanical model is assumed to be known and only uncertain flow parameters are considered. The fault/fracture transmissibility is the uncertain flow parameter for injection well KB-502. For injection wells KB-501 and KB-503 the anisotropic permeability mulitipliers in the major and minor flow directions are defined as the uncertain flow parameters. The range of fault/fracture transmissibilities and anisotropic multipliers that have been used to initialise the ensemble and are updated at each data assimilation step are shown in Figures 7.9 and 7.10.

It is interesting to note the evolution of the BHP sensitivity to the ensemble parameters for the initial case with no data assimilation. Injection well KB-501 displays a weak BHP sensitivity to the initial parameters and for the second half of injection the BHP is over-predicted. The BHP assimilation has a diminished impact in reducing the uncertainty.

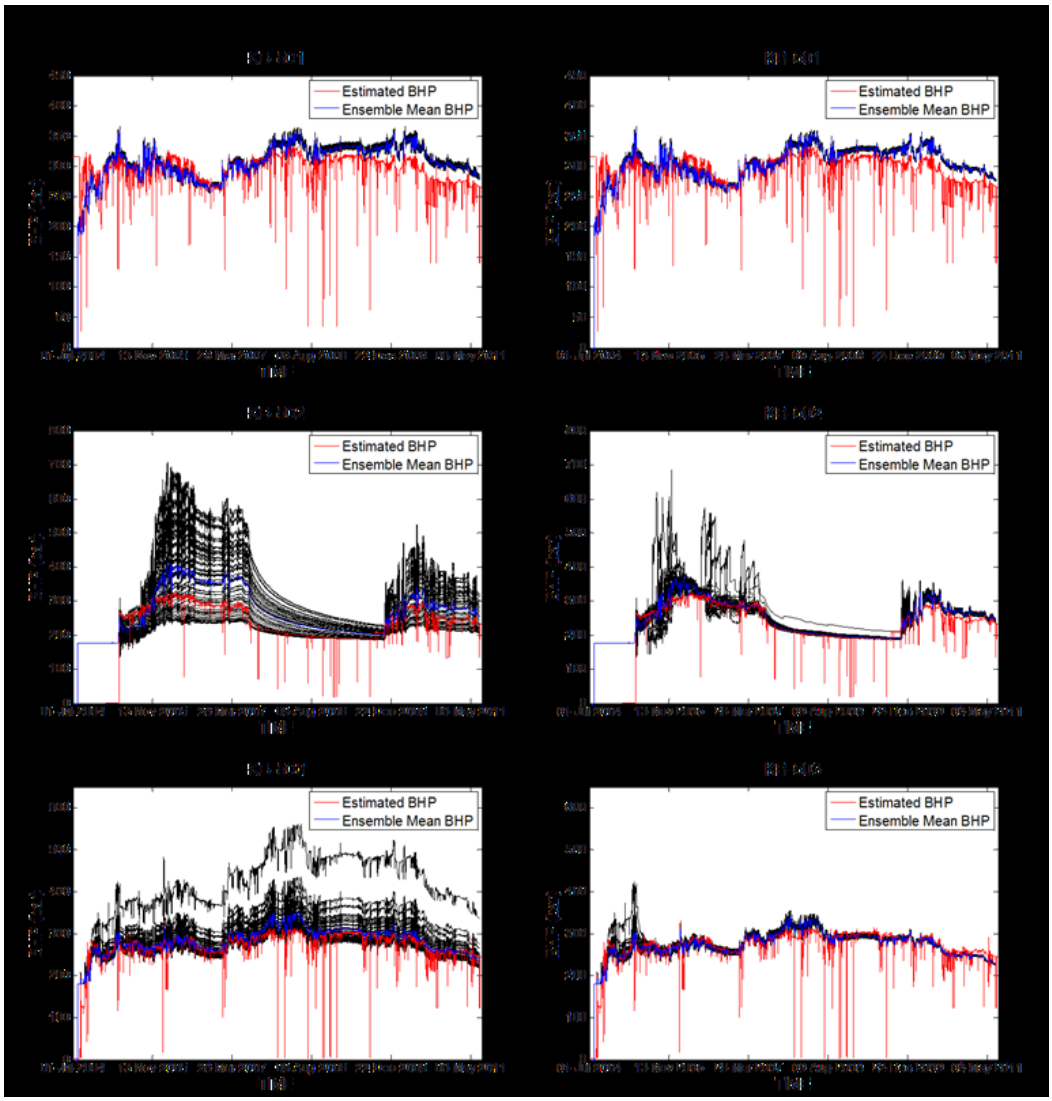


Figure 7.8: Match to estimated BHP data from the initial ensemble and from the updated ensemble using BHP data assimilation for the injection wells KB-501, KB-502 and KB-503.

At injection well KB-502 there is a significant increase in BHP sensitivity to the fault/fracture transmissibility between 2005 and 2007. Afterwards, as expected the sensitivity is gradually reduced throughout the shut-in period between 2007 and 2009. The sensitivity increases once again in the second injection phase starting from the end of 2009 to 2011. BHP assimilation at injection well KB-502 significantly improves the match.

The BHP predictions for injection well KB-503 display a more constant sensitivity throughout the entire CO_2 injection period for the initial parameters. Data assimilation also produces a better match to the estimated BHP. After several BHP

assimilation steps, the uncertainty in the BHP pressure predictions are reduced and there is an overall agreement between the predicted and the estimated BHP.

Figure 7.9 shows the updates for the transmissibility at every data assimilation step. The transmissibility increases considerably starting in November 2005 consistent with the sighting of the two-lobe uplift deformation pattern. The uncertainty increases during the shut in period when injection stopped. Once injection resumes the average transmissibility increases and is tuned by the EnKF, reducing its uncertainty. This is in agreement with previous interpretations and modelling work (Shi *et al.*, 2012) suggesting hydraulic stimulation starting in November 2005.

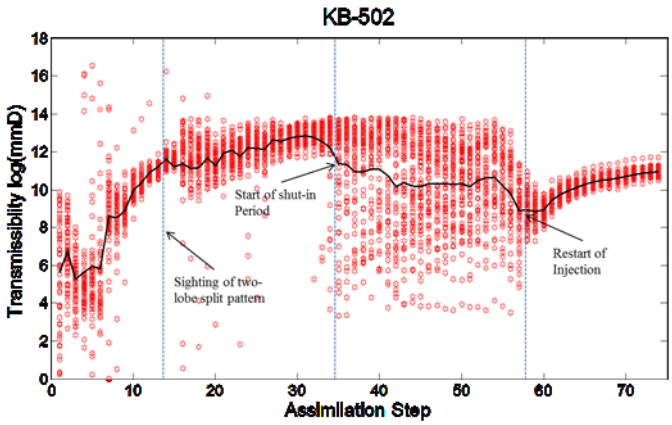


Figure 7.9: Updated ensemble transmissibility for well KB-502.

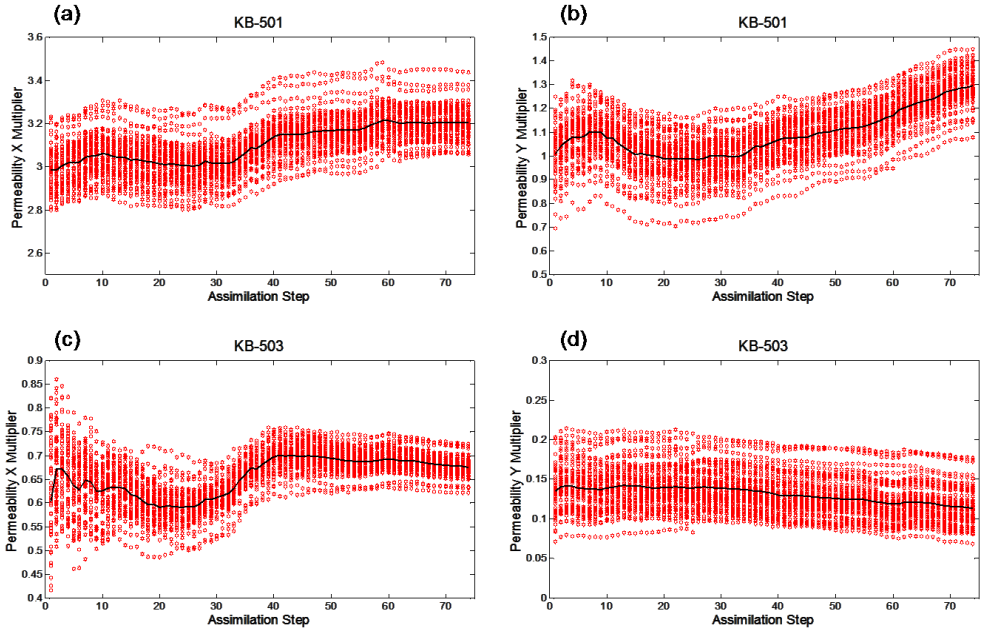


Figure 7.10: Updated ensemble permeability multipliers in the x- and y- direction for injection wells KB-501 and KB-503.

Figure 7.10 shows the updates for the permeability multipliers at every data assimilation step for wells KB-501 and KB-503. The updated anisotropic multipliers for KB-501 suggest an increase in flow over time but the BHP is over-predicted given the weak sensitivity at this injection well. For KB-503, the average anisotropic multipliers for KB-501 in the x-direction is lower for the initial half of the injection period with an increase observed for the second half. The average permeability in the y-direction remains stable. The observed increase in flow over the second half of injection at the site is consistent with CO_2 being diverted to these two wells during the shut-in period at injection well KB-502, increasing the injection rates and enhancing flow.

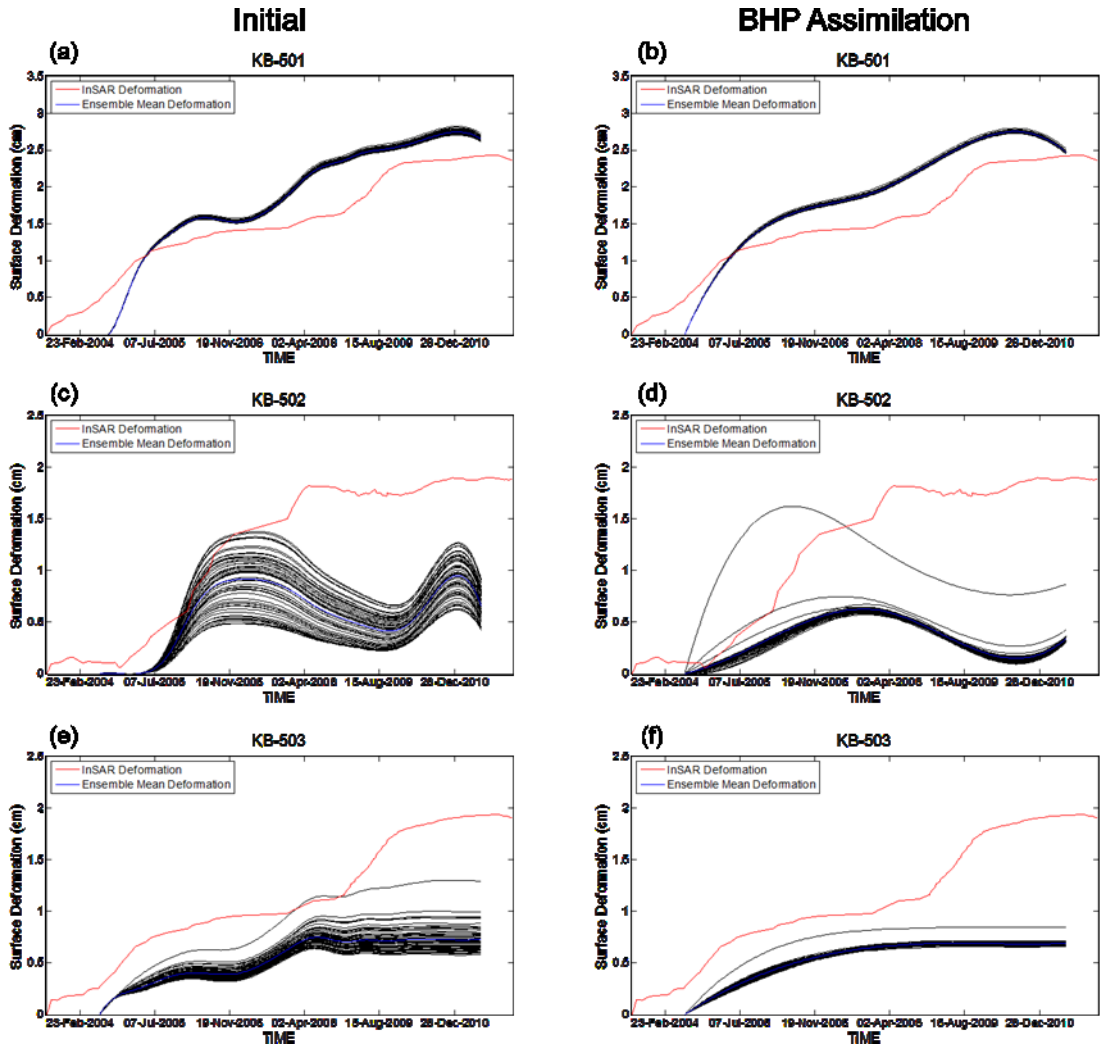


Figure 7.11: Surface deformation predictions from the initial ensemble and from the updated ensemble using BHP data assimilation for injection wells KB-501, KB-502 and KB-503.

Finally, Figure 7.11 shows the predicted surface deformation for the initial ensemble and for the BHP data assimilation case. Injection well KB-501 follows the correct trend but is slightly over-predicted. At injection well KB-502 there is a mismatch starting from the shut-in period, which is visible in the bimodal behaviour of the surface uplift predictions. At injection well KB-503 the deformation is under-predicted with a mismatch in trend at the start of injection and from the start of 2009. Although, the EnKF converged to an agreeable match to the BHP, further model calibration is required to match the observed InSAR surface uplift and will be explored in the next scenarios.

7.3.2 Scenario 2 - Geomechanical Uncertainty

In scenario 2, in addition to the uncertain flow parameters defined in the previous section, uncertain geomechanical properties are introduced in the lower caprock. In scenario 1, only BHP data was assimilated. In this case both BHP and InSAR surface data will be assimilated. Since the number of geomechanical time-steps required has increased an ensemble size of 40 was used due to time management and computational limitations.

Figure 7.12 shows the match to the estimated bottom hole pressure for three cases. In the first case there is no data assimilation. In the second case only BHP data is assimilated. The third case shows the joint assimilation of BHP and InSAR surface deformation data.

At injection well KB-501 a slightly better history match is achieved when assimilating both BHP and InSAR surface deformation data. At injection well KB-502 the ensemble average overestimates the BHP. This effect becomes more pronounced when both BHP and InSAR data are assimilated. Finally, the uncertainty for the BHP predictions at KB-503 appears to be reduced at the same rate when using BHP assimilation or a joint assimilation. The overall trend is for the uncertainty in the BHP predictions to be reduced. However, the ensemble mean is overpredicted at KB-502 while a much better match is observed at KB-501 and KB-503.

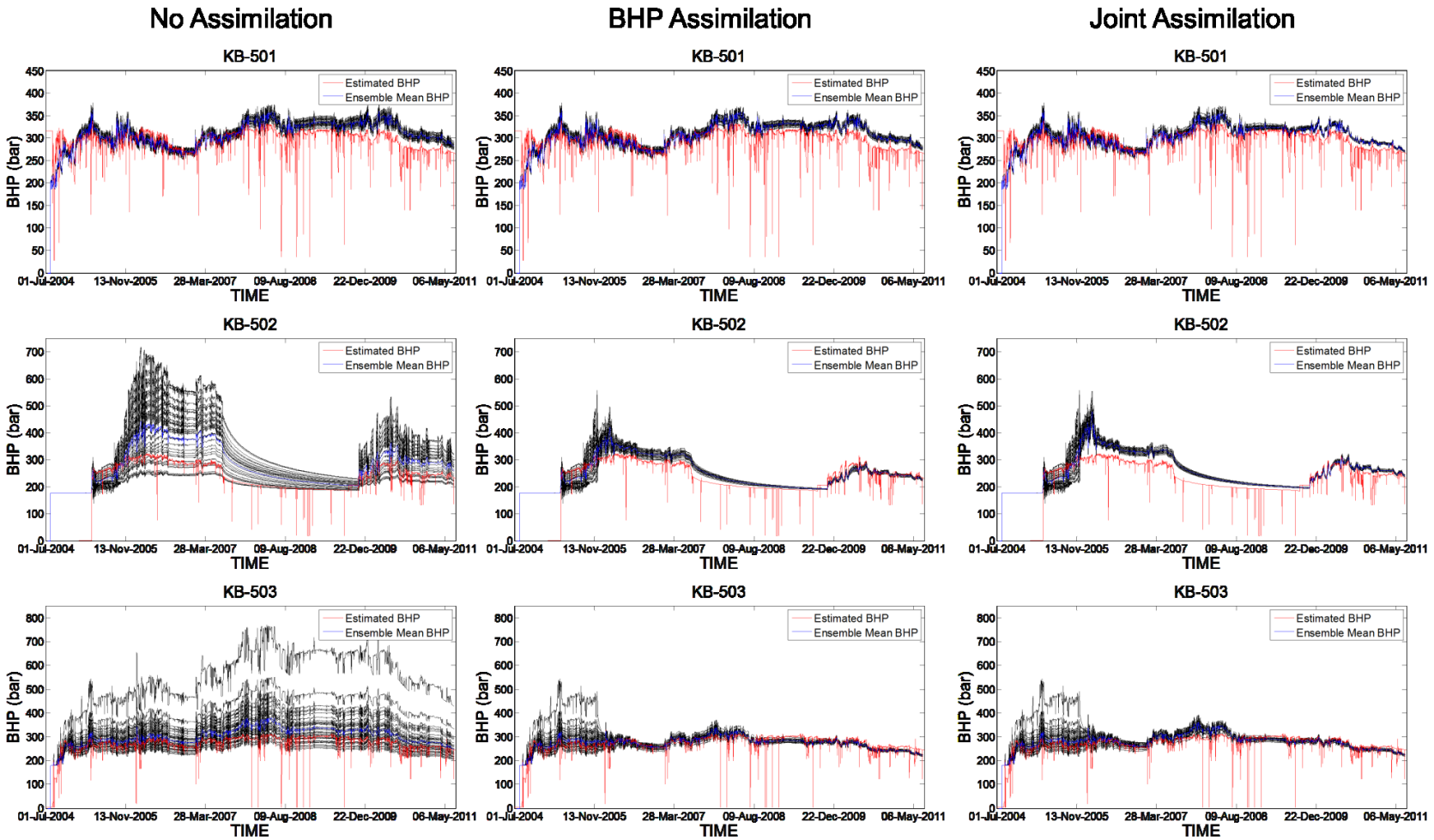


Figure 7.12: Match to estimated BHP data from the updated ensemble using BHP data assimilation and joint BHP and surface deformation data for injection wells KB-501, KB502 and KB-503.

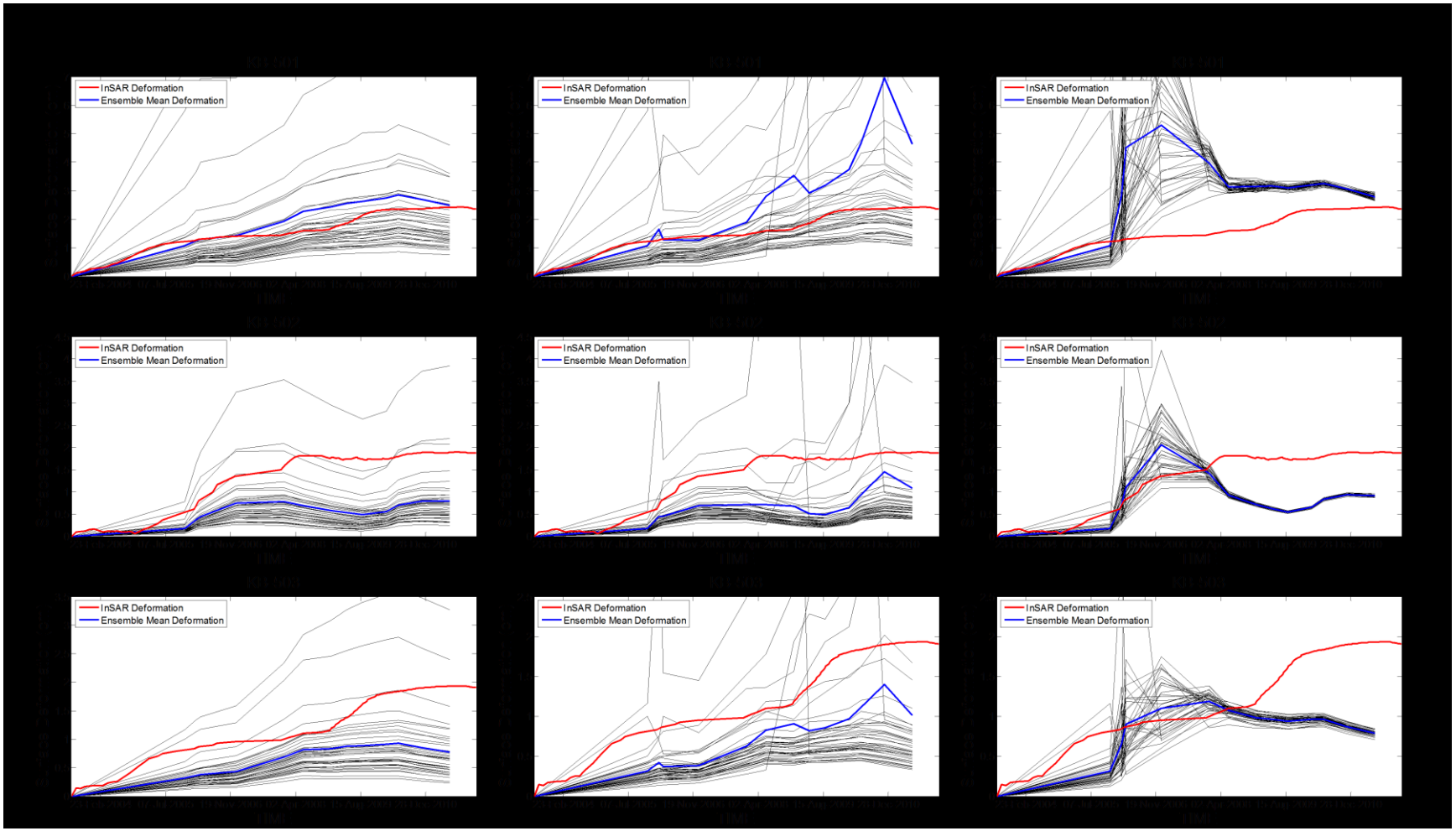


Figure 7.13: Match to estimated InSAR surface deformation data from the updated ensemble using BHP data assimilation and joint BHP and surface deformation data for injection wells KB-501, KB502 and KB-503.

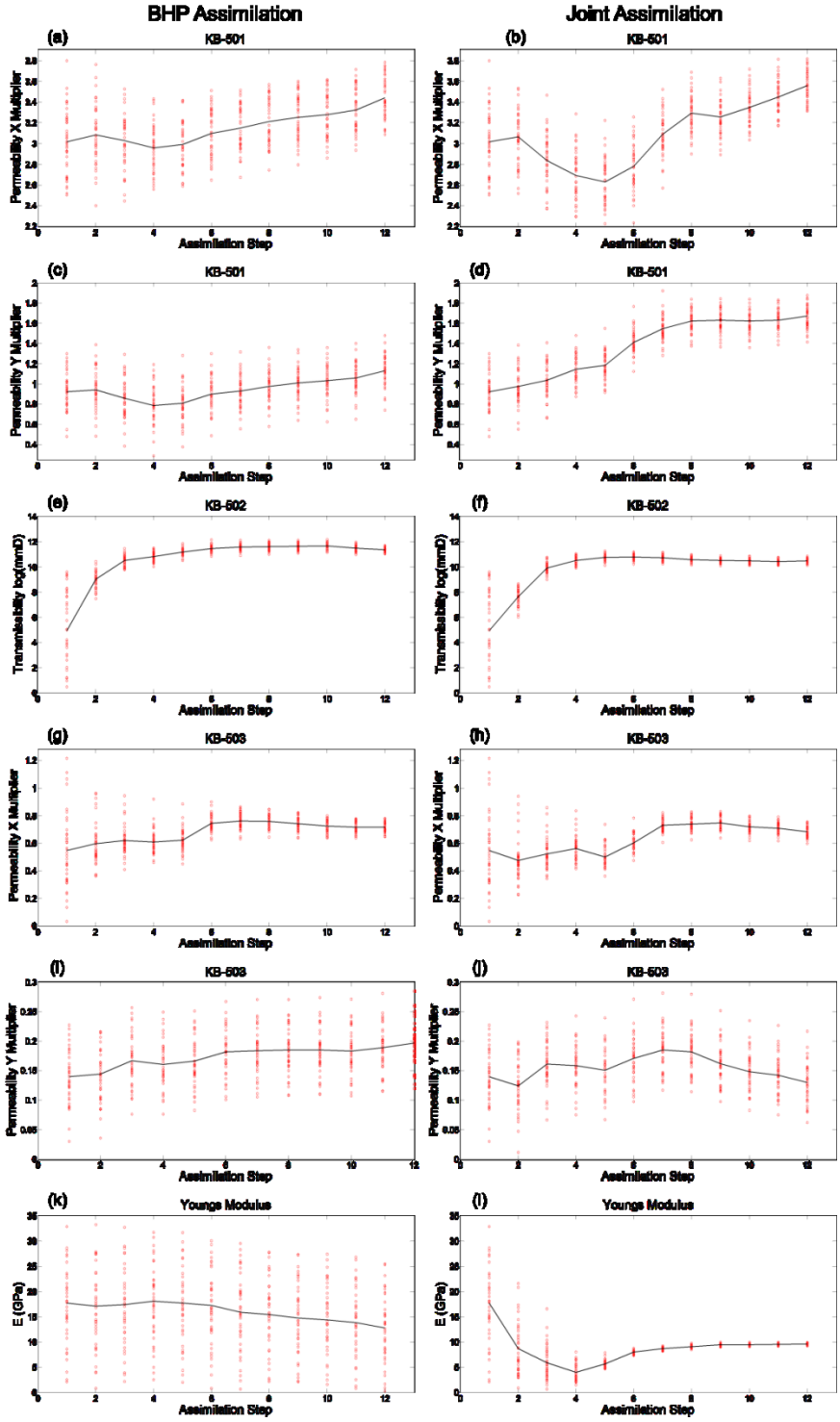


Figure 7.14: Updated flow and geomechanical parameters using BHP data assimilation and joint BHP and surface deformation data; KB-501 (a) Perm. X BHP assimilation (b) Perm. X joint assimilation (c) Perm. Y BHP assimilation (d) Perm. Y joint assimilation; KB-502 (e) Transmissiblity BHP assimilation (f) Transmissibility joint assimilation; KB-503 (g) Perm. X BHP assimilation (h) Perm. X joint assimilation (i) Perm. Y BHP assimilation (j) Perm. Y joint assimilation; (k) Young's Modulus BHP assimilation (l) Young's Modulus joint assimiilation.

Figure 7.13 shows the match to the observed InSAR surface deformation data using no data assimilation, BHP assimilation and joint BHP and surface deformation data assimilation. In the case where only BHP is assimilated the uncertainty in the surface deformation is still significant as the Young's modulus does not have a strong dependence on the bottom hole pressure. It can be seen that the ensemble average overpredicts the surface deformation at injection well KB-501 and underpredicts at KB-502 and KB-503.

Figure 7.14 shows the EnKF updates for the flow and geomechanical parameters. The anisotropic permeability multipliers at KB-501 display an overall increase by the end of injection. In the x-direction of preferential flow there is an observed permeability decrease followed by a steady increase.

The overall pattern follows that of the BHP estimate at the injection well. The permeability in the y-direction remains relatively fixed for the BHP assimilation case. These changes in the preferential flow direction become more pronounced for the joint assimilation case where it is observed that the decrease in the x-direction permeability is compensated by an increase in the y-direction permeability. The transmissibility at injection well KB-502 is highly sensitive to the BHP. After several data assimilation steps most of the variability is lost.

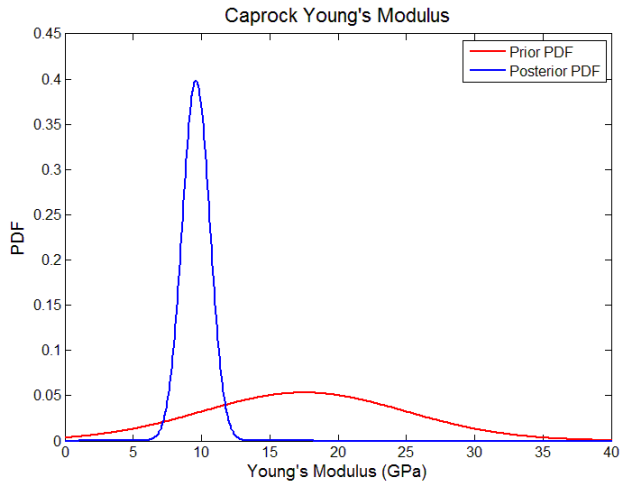


Figure 7.15: Young's modulus prior (red) and posterior (blue) probility density function for the lower caprock.

At injection well KB-503 a similar behaviour is observed in the preferential flow direction for the cases considered. About a 20% increase in permeability is observed

starting from the second half of injection. In the minor flow y-direction, there is a drop in permeability towards the final assimilation steps for the joint case compared to the BHP assimilation case.

The BHP overprediction and the surface uplift underprediction at KB-502 for the joint assimilation case suggests there is a pressure over-compensation at the well due to a low Young's modulus. This is a limitation of the constant Young's modulus used for the entire caprock covering all three wells. The Young's modulus for the caprock is a global parameter for the entire site whereas the flow parameters are local to each injection well.

The use of a layer cake geomechanical model with no lateral variations is unable to explain the available surface deformation patterns. This is in agreement with independent coupled flow-geomechanical simulations performed independently at individual injection wells where different geomechanical parameters have been used to the history-match the surface deformation above the injection wells. Gemmer *et al.*, (2012) used a Young's modulus of 2.0 GPa and Shi *et al.* (2013) used a value of 18.0 GPa. This will be addressed in the next section where a full field geomechanical model which includes lateral variations in the lower caprock geomechanical properties will be used.

7.3.3 Scenario 3 - Lateral Variations in Geomechanical Uncertainty

In the previous section it was concluded that a lateral invariant geomechanical model was insufficient to explain the available surface deformation observations. In this case, lateral variations in geomechanical properties are introduced for the Young's modulus in the lower caprock. The lower caprock has been separated into two zones with different geomechanical properties while maintaining the same grid. Zone 1 includes the injection well KB-501 and zone 2 includes injection wells KB-502 and KB-503. The Young's Modulus is initialised at 17.5 GPa for zone 1 and 7.5 GPa for zone 2.

Figure 7.16 shows the match to the estimated BHP for the initial ensemble, the updated ensemble using BHP data assimilation and using joint BHP and InSAR surface deformation data. The BHP assimilation results are comparable to the previous case.

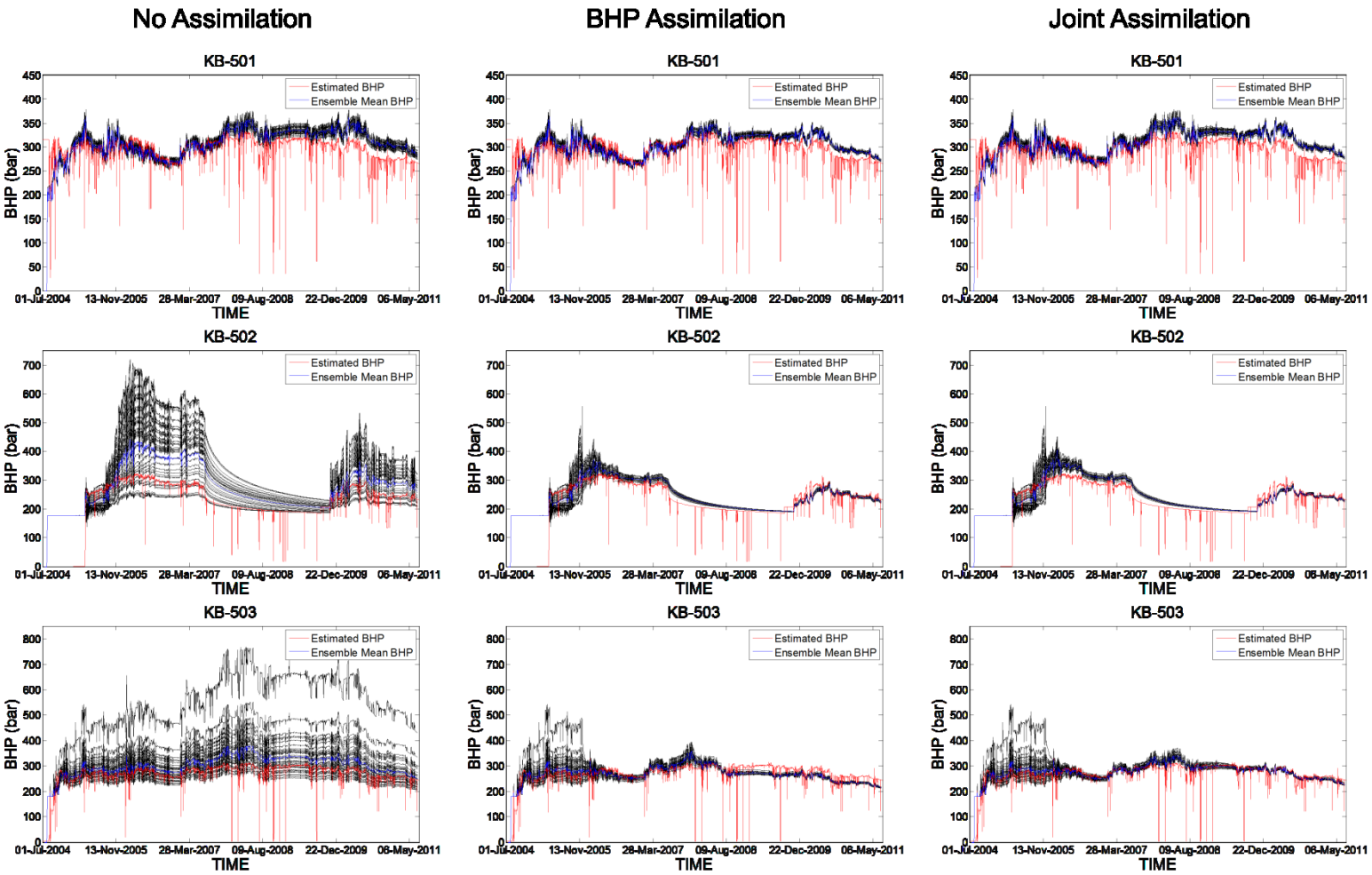


Figure 7.16: Match to estimated BHP data from the initial ensemble and the updated ensemble using BHP data assimilation and joint BHP and surface deformation data for injection wells KB-501, KB-502 and KB-503.

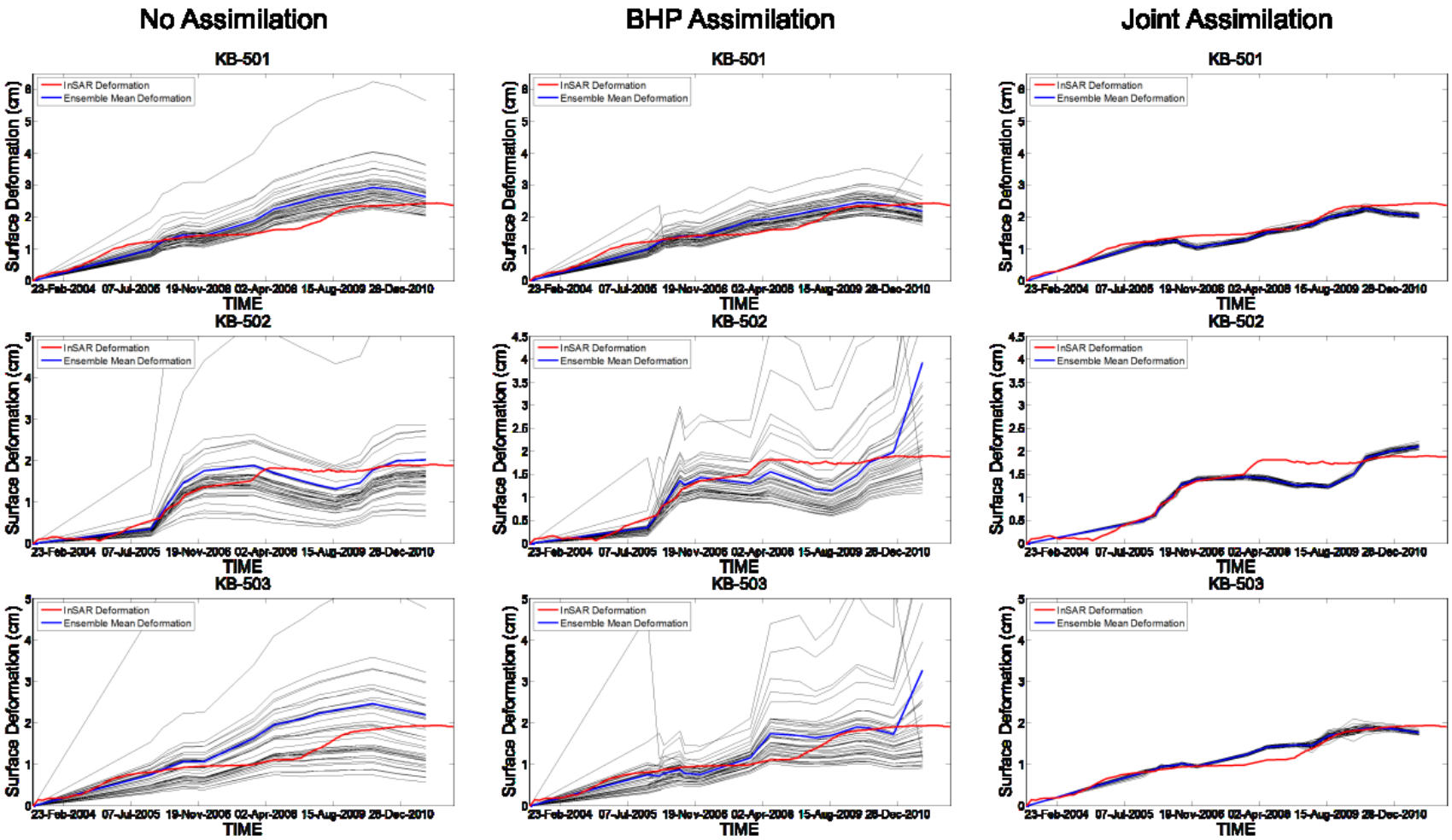


Figure 7.17: Match to estimated InSAR surface deformation data using the initial ensemble and the updated ensemble using BHP data assimilation and joint BHP and surface deformation data for injection wells KB-501, KB-502 and KB-503.

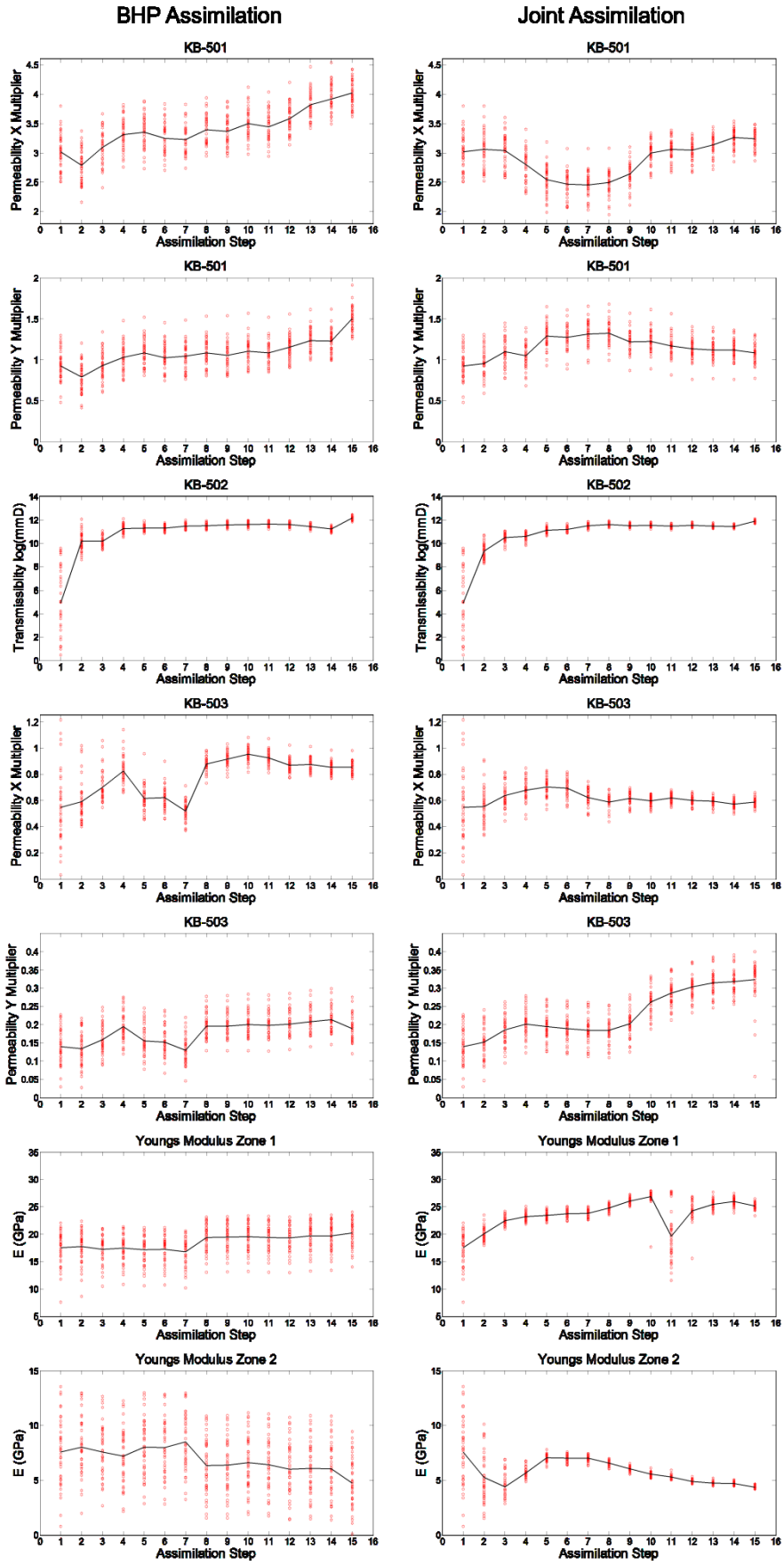


Figure 7.18: Updated flow and geomechanical parameters using BHP data assimilation and joint BHP and surface deformation data.

The flow parameters are updated and the uncertainties in the BHP predictions show a significant reduction.

The joint assimilation results show an improved match for the BHP at KB-502 compared to scenario 2. The effect of the pressure trying to over-compensate for a low Young's modulus has been reduced by relaxing the condition of a laterally continuous caprock.

Figure 7.17 shows a match to the estimated InSAR surface deformation from the EnKF runs for all three assimilation cases. For the BHP assimilation results, the surface deformation has a weaker dependence on the BHP data and the uncertainty in the predictions only show a slight reduction. Once BHP and InSAR data are assimilated an improved match in both trend and magnitude is observed at all three injection wells compared to scenario 2.

Figure 7.18 shows the updated flow and geomechanical parameters. At injection well KB-501 the permeability in the preferential flow direction shows an increase for the BHP assimilation case and a decrease in the joint assimilation case. The permeability in the minor flow y-direction shows a similar behaviour for both cases. The transmissibility at injection well KB-502 loses its variability after a couple of data assimilation steps.

At injection well KB-503 the permeability in the x-direction shows several fluctuations before stabilising around 0.8 for the BHP assimilation case. The permeability in the y-direction similarly displays similar fluctuations. For the joint data assimilation case the permeability in the x-direction retains a similar mean but the uncertainty is reduced.

The Young's modulus for zone 1 corresponds to the Young's modulus for the lower caprock around injection well KB-501. The Young's modulus for zone 2 refers to the lower caprock for injection wells KB-502 and KB-503. The Young's modulus ensemble mean for zone 1 is initialised at 17.5 GPa. The Young's modulus for the lower caprock above injection KB-501 then converges around a value of approximately 22 GPa. At assimilation step 11 the Young's modulus distribution was resampled as some of the updates were outside the defined maximum. In the subsequent data assimilation steps, it converges once again to a value of approximately 22 GPa.

The Young's modulus ensemble mean for zone 2 is initialised at 7.5 GPa. After the joint data assimilation the Young's modulus for the lower caprock above injection wells KB-502 and KB-503 converges around 6.5 GPa.

Figure 7.19 shows the Young's modulus prior and posterior probability density function for zone 1. The uncertainty in the caprock's Young's modulus is reduced after the data assimilation of surface deformation data. The mean prior underpredicted the Young's modulus and is updated to a larger value by the EnKF.

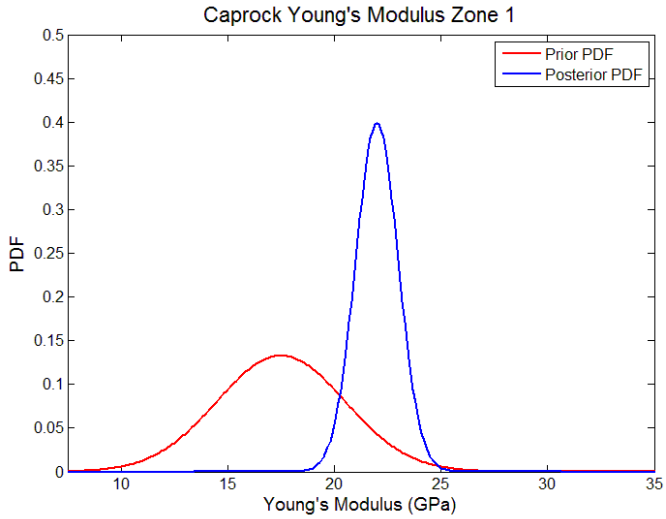


Figure 7.19: Zone 1 Young's modulus prior (red) and posterior (blue) probility density function for the lower caprock.

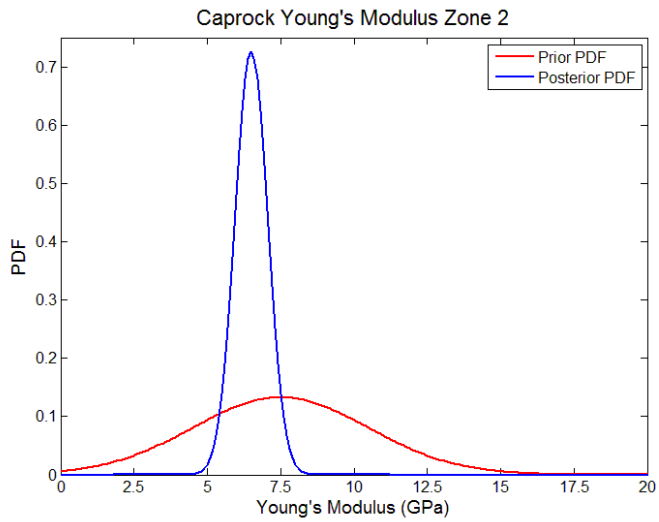


Figure 7.20: Zone 2 Young's modulus prior (red) and posterior (blue) probability density function for the lower caprock.

Figure 7.20 shows the Young's modulus prior and posterior probability density function for zone 2. In zone 2 the uncertainty is also reduced after data assimilation. The mean prior is updated by the EnKF to a lower value.

A model taking into account lateral variations in geomechanical properties provides an improved match to the InSAR surface uplift compared to scenario 2 and the resulting updated geomechanical model should be used for predictions.

7.4 *Limitations of the EnKF*

In a traditional history matching approach, the collection of variables to be estimated consists of the model parameters, for example permeability. As the model parameters are tuned, the state variables such as pressure are then determined from the knowledge of the model parameters using a reservoir simulator that solves the system of governing equations. In essence, the EnKF uses the numerical flow and geomechanical simulators in the forecast step. However, a linearised approximation to the governing flow and geomechanical equations is still used to update the model parameters and the state variables and the update equation is based on gaussian error statistics. This leads to two potential problems with the EnKF. One is unrealistic updates of the model and state variables and the problem of inconsistency or non-conforming behaviour.

For a problem where the statistics do not display Gaussian behaviour, the EnKF has been shown to be problematic. This may lead to unrealistic or non-physical updates of the model parameters and state-variables.

In the EnKF both model and state variables are updated simultaneously. After a given update, if the model parameters do not predict the state variables in a numerical simulation, this is referred to as the problem of inconsistency or non-conformity. An approach to deal with the inconsistency is to re-initialise the numerical flow and geomechanical simulations with the updated model parameters each time a data assimilation step is made. The approach can be summarised in three steps: (1) make the forecast step which propagates the state of the system using reservoir and geomechanical simulators to the current measurement time, (2) the same at which the EnKF update equation is used to correct for the model parameters and (3) re-initialise the flow and geomechancial simulators with the newly updated model parameters and simulate to the current measurement time. It is evident that

this would significantly increase the computational effort required for complex models and in practice can not always be made.

7.5 Summary and Discussions

In this chapter, a methodology using the EnKF for assessing the coupled flow-geomechanical performance of CO_2 storage sites has been demonstrated on the In Salah CO_2 storage site data set. The developed methodology benefits from integrating the flow and geomechanical modelling tools into a single platform. To assist with data-integration, the ECLIPSE and FLAC^{3D} software have been integrated into a single platform where both flow and geomechanical parameters can be updated in addition to the straightforward assimilation of both BHP and surface deformation datasets using the EnKF. The assimilation of BHP and InSAR data using the EnKF provided an effective method for updating the flow and geomechanical model parameters controlling the performance of the CO_2 storage site.

Prior knowledge has been included into the EnKF through several means. Using seismic data and cores from several wells as input data, porosity and permeability values were assigned using geostatistical techniques. The preferential flow directions were inferred using InSAR data to define the anisotropic permeability directions. The geomechanical properties at the reservoir level are well constrained so it was the uncertain caprock properties that were targeted by the EnKF.

The developed methodology has been applied to three scenarios. In the first scenario, only uncertain flow properties were considered with no uncertainty in the geomechanical properties. In the second scenario uncertainty was introduced into the caprock geomechanical properties. A layer cake geomechanical model with no lateral variations was unable to predict the surface deformation magnitude at all three CO_2 injection wells. It was observed that the surface uplift is under-predicted at injection wells KB-502 and KB-503 and over-predicted at KB-501. Based on this result, it was interpreted that local caprock properties at the injection wells should be explored. Lateral variations in the caprock properties were then considered in the third scenario. Injection wells KB-502 and KB-503 were grouped together under a lower caprock with the same Young's modulus. KB-501 was grouped under a lower

caprock with a different Young's modulus. This resulted in an improved match to the surface uplift magnitude.

In this study, fractures are not explicitly modelled. The effect of such is simply taken into account by imposing anistropic flow using multipliers in the maximum and minimum flow direction inferred from InSAR data and previous history-matching studies for KB-501 and KB-503 and adding a transmissibility term to the effective permeability at KB-502. It would be highly desirable to explicitly include the uncertainty in fracture network properties. In future work, the fault/fracture geometries and their specific geomechanical properties should be tested.

An underlying assumption was that the flow parameters are dynamic. The aim was to understand the dynamic reservoir changes in response to CO_2 injection. The well-known problem of inconsistency in the EnKF analysis was not considered and should also be further investigated.

It is clear that despite the rapid developments in the use of satellite InSAR data as a monitoring tool in addition to BHP estimates, a reasonable understanding of the subsurface is required. It has been shown that a layer cake geomechanical model covering all three injection wells cannot explain the available observations. A more complex model with lateral variations had to be introduced to explain the observations. An adequate characterisation and understanding of the structural geological and rock mechanical aspects is critical in order to bring true value from the monitoring data sets.

Chapter 8 Conclusions

This final chapter summarises the work performed and the research achievements throughout this PhD. The results are used to indicate the topics which would warrant further research.

8.1 *Contributions to knowledge*

8.1.1 Reservoir pressure change inversion

An effective technique for mapping reservoir pressure change from surface deformation has been developed. By postulating the problem as a transmitter (reservoir) and a receiver (overburden) configuration, an explicit description of the physical processes that shape the surface deformation signal have been forgone. The advantage of this formulation over other inversion schemes is the straight-forward integration with numerical geomechanical models that can accomodate arbitrary structural complexity and variations in subsurface geomechanical properties. The developed inversion scheme was applied to the In Salah CO_2 storage site where the pressure plume due to CO_2 injection was mapped at three injection wells using a series of InSAR surface uplift measurements and the available numerical geomechanical model.

8.1.2 Understanding flow and pressure behaviour from CO_2 injection

Starting from a previous modelling study where a mismatch between modelled and observed surface uplift was highlighted, an improved understanding of the flow and pressure behaviour at In Salah has been achieved by incorporating insight from InSAR surface deformation and time-lapse seismic data into forward coupled flow-geomechanical modelling. Prior to modelling, the InSAR and time-lapse seismic data were analysed and interpreted. Using this guided modelling approach, the emerging interpretation was the hydraulic stimulation of a fault/fracture zone due to CO_2 injection at well KB-503. The timing of the hydraulic stimulation was inferred from InSAR data and time-lapse seismic time-shifts provided a constraint for mapping the extent of the affected fault/fracture zone at reservoir level. This insight was included into the coupled flow-geomechanical model by introducing a fault/fracture zone with dynamic transmissibility. The transmissibility of the fault/fracture zone was then estimated by history matching the model to BHP and InSAR surface uplift.

8.1.3 Integrated approach using the ensemble Kalman filter

A methodology which integrates coupled flow-geomechanical modelling, InSAR surface deformation, and flowing bottom hole pressure using the ensemble Kalman filter has been developed for the performance assessment of CO_2 storage sites. For this purpose an interface between the flow simulator ECLIPSE 300 and the geomechanical simulator FLAC^{3D} was developed.

Previous work had consisted solely of inverse modelling or forward coupled flow-geomechanical modelling. The methodology developed is an integrated approach to infer properties of the flow-geomechanical model as observations become available and is thus suitable for continuous monitoring of CO_2 storage sites. Prior knowledge of the flow and geomechanical properties can be included in the ensemble initialisation step. The methodology provided an effective method for updating the flow and geomechanical model parameters controlling the performance of a CO_2 storage site.

The developed methodology was validated on the In Salah CO_2 storage field data set. The EnKF was used to update local flow parameters at each CO_2 injection well and caprock geomechanical properties. A key finding is the importance of having an accurate geomechanical model. A layered geomechanical model was overly

simplistic and insufficient to account for the observed surface deformation at all three CO_2 injection wells. This lead to the building of a more complex geomechanical model with local caprock geomechanical properties being introduced above each injection well. This provided an improved match and an updated flow-geomechanical model that conforms to the available observations.

8.1.4 Main Conclusions and Learnings

The key conlusions from this research are summarised below:

- Detailed geomechanical models are required to understand the behaviour of the CO_2 storage complex.
- Detailed site characterisation is required before CO_2 injection
- The EnKF is a suitable methodology for continuous assessment of CO_2 storage process and the updating the flow and geomechanical parameters controlling the performance of the CO_2 storage site.
- Integration between modelling tools and monitoring data is crucial to understand the behaviour of the stored CO_2.

It is clear that site selection and site characterisation will be crucial in order to have a model to relate the observations to and to quantify the uncertainty in model properties. Given the high level of uncertainty in characterising the subsurface, limited monitoring data available and modelling limitations, it is recommended that a CO_2 storage complex be situated below a thick multi-layered overburden. In this way, if the lower portion of the caprock is fractured, the CO_2 will not migrate any further and remain confined to the lower portion of the caprock. It is also recommended that the injection rate be increased gradually and monitored in order to adapt the injection strategy should any geomechanical change be detected in the subsurface.

Adequately characterising the subsurface, however, remains challenging. At the In Salah CO_2 storage site fractures/faults have been critical reservoir features controlling the injection performance of the wells. Characterising fractures is therefore of great interest. The seismic surveys acquired at In Salah show a continuous reflector at the reservoir level showing no detectable fault displacement at the seismic scale. However, it was subseismic fractures/faults that played in key role in the storage site performance.

Although, the effects of faults and fractures on permeability can be understood from dynamic monitoring data sets, it would be highly desirable to characterise the faults and fractures before injection has begun. In the case where a dominant sub-seismic fracture set exists, a seismic signature may be present in the amplitude variation with azimuth (AVAz) (Rüger, 1996). Measuring the AVAz response from a mult-azimuth seismic survey would give a potential indicator of the fracture orientation and intensity as a function of space. This would be highly beneficial for site characterisation. Unlike other seismic attributes the AVAz response is grounded on physical theories. In particular effective medium theories are used to represent idealised fracture sets which are below the seismic resolution. If the AVAz response can be calibrated from log data, and the assumption of a dominant fracture set holds, this would provide a powerful characterisation technique before CO_2 injection begins. In Salah is an ideal site to test this method given the local geology, and this has been proven to be successful at locating areas with high concentrations of oriented fractures in a nearby field in the Tiguentouruine field in South East Algeria (Tod *et al.*, 2007).

Accurate estimates of bottom hole pressure and temperature should be made a priority in future CO_2 storage projects. Estimates of BHP from well head pressure are subject to inherent uncertainties. At InSalah for example BHP estimates varied by more than 30 bar.

The experience at the In Salah site has shown that bottom hole pressure estimates are not sufficient to fully understand the dynamics of a CO_2 storage site. The bi-lobate pattern for example at injection well KB-502 would have been missed without the use of InSAR data. InSAR data and bottom hole pressure are complementary sources of information. Where surface conditions are suited for InSAR monitoring it should be considered simply because it is so cost effective. Although the surface conditions at InSalah were ideal for InSAR monitoring, this most likely will not be the case for other CO_2 storage sites. It has been proposed that in more challenging surface conditions such as highly vegetated areas, pre-existing or purpose built reflectors could be used for ground coverage.

The implementation of the reservoir pressure change inversion scheme and the ensemble Kalman filter would benefit from greater computational efficiency and computational power. The independence of the ensemble members allows the

benefits of parallel programming for the EnKF implementation so that the computational cost is significantly reduced. In this dissertation, the parallelism was only implemented for the flow simulator ECLIPSE 300. Extending this parallelism to the geomechanical simulator would significantly increase the computational speed. The greater computational speed would permit the updating of a larger number of model parameters by increasing the ensemble size and would allow the straightforward testing of different ensemble initialisation setups. In this work the EnKF was used to estimate anisotropic permeability multipliers, fracture/fault transmissibility and geomechanical properties. It can be expanded to include additional parameters of interest such as additional fracture parameters which are difficult to measure directly in practice and caprock sealing properties.

The developed reservoir pressure change inversion scheme is deterministic and would also benefit from greater computation power. This would allow the transition from a deterministic to a stochastic inversion. The latest application of a stochastic inversion at In Salah still makes the limiting assumption of a homogeneous half-space (Ramirez and Foxall, 2014). Increased computational power would allow the integration of a stochastic reservoir pressure change inversion scheme with realistic numerical geomechanical models and uncertain model properties.

8.2 *Recommendations for future research*

The main focus of this PhD research was the integration of InSAR data, flowing bottom hole pressure and coupled flow-geomechanical modelling with the purpose of ensuring the conformity of the actual behaviour of the CO_2 with the modelled behaviour. This was achieved by using the EnKF to integrate all the modelling tools and monitoring data to update the flow and geomechanical parameters controlling the behaviour of the CO_2 storage site.

There is considerable margin for improving the developed methodologies. Recommendations for future research include:

- overcoming fracture and fault modelling limitations
- greater integration with seismic data and modelling tools
- closed loop reservoir management

8.2.1 Two-way coupling between fluid flow and geomechanics

In this thesis a one-way coupling approach between a fluid flow and a geomechanical simulator was used. The effects of the pore pressure increase due to CO_2 injection on rock deformation are taken into account. A two-way coupling approach would also include the effects of rock deformation on porosity, permeability and capillary pressure. The two-way coupling effects were taken into account by manually modifying the reservoir permeability based on interpretations of BHP and InSAR surface deformation data. An explicit two-way coupling approach would require defining coupling functions to take into account these effects.

Predicting the effects of the stress field on fracture flow properties also remains a significant challenge. It has been observed that faults and fractures which are favourably aligned with the present day stress field have a tendency to be more conductive than fractures which are in compression. A more realistic modelling objective is to allow the fracture flow properties to be stress sensitive. A relationship between fracture or fault conductivity and orientation could then be established. This allows the stress field to operate as a control on the fracture flow properties. In practice however, the local stress field in itself is challenging to determine accurately.

In general the coupling functions between permeability and stress are empirical and nonlinear and require calibration against site specific data. The coupling functions would correct the flow properties as a function of stress. To date coupling functions have not been developed and calibrated on the In Salah site but it is an importance exercise to test the model performance of a two-way coupling approach compared to the one-way coupling approach using user modified flow properties through time.

8.2.2 Coupling with a seismic simulator

A significant step would be to couple the flow and geomechanical simulator with a seismic simulator. In this thesis time-lapse seismic time-shifts were used to gain insight into the dynamic behaviour of one of the CO_2 injection wells. InSAR data has the advantage of being highly sampled in time but is limited to deformation at the surface level. Time-lapse seismic time-shifts however contain information about the entire overburden and reservoir. In addition to a flow model and a geomechanical

model, an accurate rock physics model is required to link the time-shifts to geomechanical processes at depth. This would require an even more detailed characterisation of the overburden and reservoir. Time-lapse seismics for the monitoring of geomechanical changes in the subsurface is a promising technology and it is the author's opinion that integration should be further pursued. As it is likely that time-lapse seismics will be deployed at most CO_2 storage sites to monitor fluid substitution effects, the geomechanical effects present in time-lapse seismic data can be readily exploited.

Integrating the flow, geomechanical and seismic modelling tools would have the predictive capabilities to model BHP, stress and deformation changes, velocity changes and the resulting seismic time-shifts all of which can be readily measured at CO_2 storage sites. The model could then be calibrated or history-matched using all the available datasets simultaneously.

Some of the experience and knowledge gained from oil and gas production from high pressure high temperature fields (HPHT) can potentially be transferred to CO_2 storage. Managing HPHT fields have been particulary challenging due to the geomechanical effects of severe pore pressure reduction. Dybvik *et al.* (2009) for example proposed a geomechanical modelling workflow for HPHT fields that integrates flow, geomechanical and seismic modelling that could potentially be adapted for CO_2 storage operations.

8.2.3 Fracture Modelling

Some of the modelling limitations also warrant further research. The explicit modelling of flow through discrete fractures would be desirable. Quantifying the impact of fractures on fluid flow remains challenging due to the complexity and varying nature of fractures. An adequate representation of fractures in grid meshes for fluid flow simulation that capture the correct mathematical description of the physical processes is required.

Methodologies such as that of Smith *et al.* (2011) stochastically model fracture network connectivity between the reservoir and lower caprock taking into account the uncertainties from all the available well measurements. It would be desirable to extend this methodology to include fluid flow through the fractures coupled with geomechanical modelling. This could be included inside the ensemble Kalman filter

framework described and the fracture network geometry could be constrained by conditioning to dynamic data.

In this thesis an implicit method was used to represent fracture and faults. Instead of representing fractures as planes, they are instead treated as a volumetric property of a standard cellular model. Faults are highly complex geological features containing elements acting both as a fluid barrier and conduit. Modelling a fault/fracture zone several kilometres in length as a planar feature with constant permeability which does not take into account important multi-phase flow effects is clearly a simplification. To date this has been the modelled fault/fracture approach used at the InSalah CO_2 storage site.

Faults in reservoirs are sometimes modelled as a single 2D planes. In reality, faults form zones in which many fractures coalesce. Faults are fundamentally volumetric. Representing a fault explicitly as a volume using grid cells within the fault zone and adjacent to the fault zone or a damage zone is rarely used because it may be computationally demanding. Furthermore, these zones most likely have different petrophysical properties.

8.2.4 Closed loop reservoir management

A natural extension of the research developed in this research is a closed-loop methodology. A closed-loop approach consists of two parts: data assimilation and CO_2 injection optimisation. The methodology developed in this PhD covers the data assimilation aspect, adjusting the reservoir flow and geomechanical model parameters to honour injection data and geomechanical observations as they become available. After the data assimilation step, the injection strategy can be optimised on the basis of the ensemble of updated models. The extension of this is to simultaneously optimise CO_2 injection rates with the objectives to maximise the stored amount of CO_2 and to minimise the riske of leakage or spillage out of the storage complex. This objective can be sought while the data-driven physical constraints such as keeping the injection pressure below the fracture pressure are honoured.

Appendices

A.1 Displacement Field around a Nucleus of Strain

A.1.1 Introduction

(*Geertsma*, 1966) developed expressions for the displacement around a nucleus of strain in a poroelastic half-space with a traction free surface. In this section the equations used to calculate all the displacement components are presented.

A.1.2 Displacements

The displacement due to a unit pressure change outside a nucleus of strain at depth $z = c$ and a radial distance $r^2 = (x-a)^2 + (y-b)^2$ from a nucleus of strain located at (a, b, c) is expressed as:

$$\vec{u} = \frac{C_m}{4\pi}\left[\frac{\overrightarrow{R_1}}{R_1^3} + \frac{(3-4v)\overrightarrow{R_2}}{R_2^3} - \frac{6z(z+c)\overrightarrow{R_2}}{R_2^5} - \frac{2\vec{k}}{R_2^3}\{(3-4v)(z+c)-z\}\right] \tag{A.1}$$

where:

$$\boldsymbol{R_1^2} = (\boldsymbol{x}-\boldsymbol{a})^2 + (\boldsymbol{y}-\boldsymbol{b})^2 + (\boldsymbol{z}-\boldsymbol{c})^2 \tag{A.2}$$

$$\boldsymbol{R_2^2 = (x-a)^2 + (y-b)^2 + (z+c)^2} \tag{A.3}$$

$$\boldsymbol{\overrightarrow{R_1} = (x-a)\vec{i} + (y-b)\vec{j} + (z-c)\vec{k}} \tag{A.4}$$

$$\boldsymbol{\overrightarrow{R_2} = (x-a)\vec{i} + (y-b)\vec{j} + (z+c)\vec{k}} \tag{A.5}$$

Where $\vec{i}$, $\vec{j}$, $\vec{k}$ are the unit vectors in the x, y and z directions, respectively. The constant C_m is the uniaxial compressibility coefficient which is given by:

$$C_m = \frac{\alpha(1-2\nu)}{2\mu(1-\nu)} \tag{A.6}$$

where α is the Biot's coefficient, μ is the shear modulus and ν is the poisson's ratio. The individual components of the displacement can then be expressed as:

$$u_x = \frac{C_m}{4\pi}\left[\frac{(x-a)}{R_1^3} + \frac{(3-4\nu)(x-a)}{R_2^3} - \frac{6z(z+c)(x-a)}{R_2^5}\right] \tag{A.7}$$

$$u_y = \frac{C_m}{4\pi}\left[\frac{(y-b)}{R_1^3} + \frac{(3-4\nu)(y-b)}{R_2^3} - \frac{6z(z+c)(y-b)}{R_2^5}\right] \tag{A.8}$$

$$u_z = \frac{C_m}{4\pi}\left[\frac{(z-c)}{R_1^3} + \frac{4\nu(z+c)-(z+3c)}{R_2^3} - \frac{6(z+c)^2}{R_2^5}\right] \tag{A.9}$$

From the individual components of displacement, the strain tensor ε can be computed

$$\varepsilon = \begin{bmatrix} \varepsilon_{xx} & \varepsilon_{xy} & \varepsilon_{xz} \\ \varepsilon_{xy} & \varepsilon_{yy} & \varepsilon_{yz} \\ \varepsilon_{xz} & \varepsilon_{yz} & \varepsilon_{zz} \end{bmatrix} \tag{A.10}$$

where the individual components of the strain tensor are given by the sum of the following derivatives:

$$\varepsilon_{ij} = \frac{1}{2}\left(\frac{\partial u_i}{\partial x_j} + \frac{\partial u_j}{\partial x_i}\right) \tag{A.10}$$

where the subscripts i and j can be the numbers 1, 2, 3 representing the x, y, and z coordinate axis respectively.

B.1 EnKF 2D Example

In order to validate the developed EnKF algorithm is tested on a 2D case study. A synthetic base case where both BHP and surface deformation are assimilated is developed in order to test the effect of the several EnKF options. The only uncertain parameter is the reservoir permeability. All other model parameters are assumed to be known. The effect of assimilating surface deformation and BHP is compared to only assimilating BHP. In the following case, the error distribution is changed. The effect of reducing the ensemble size is analysed. In the final case, permeability and the caprock Young's modulus are the uncertain parameters to be updated.

B.1.1 Model Description

The reservoir is in the x-z cross section. The model extent in the y direction is 152 m. The reservoir interval is 37 m thick. The overburden extends 762 m from the reservoir to the surface. The underburden is 16 m thick. The domain is divided evenly into 30 gridblocks in the x direction. Each gridblock has a length of 152 m. The reservoir interval is divided into 10 layers, each 3.6 m thick. The layers in the overburden and the underburden are modelled by 7.6 m thick layers. The reservoir model is embedded into a larger geomechanical model with sideburdens extending 5 km to the sides. The underburden grid size increases as a geometric series. The

overburden and the underburden rocks are assumed to have very low permeability and porosity. The reservoir porosity is assumed to be 20%. Poisson's ratio is assumed uniform throughout the entire model, being 0.25. The Young's modulus for the reservoir formation is 3.4 GPa and 6.9 GPa for the overburden and underburden.

An injector is located at the centre of the reservoir. The injector is completed throughout the entire reservoir zone. CO_2 injection is assumed at a constant injection rate of 25,000 sm^3/day.

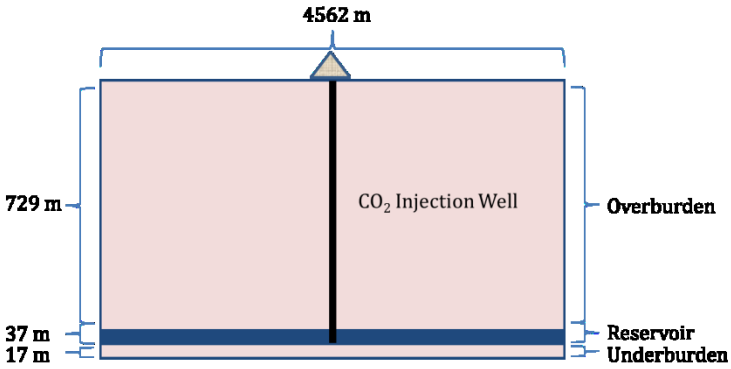


Figure B.1: 2D CO_2 storage site conceptual model.

A closed boundary condition is used for the flow simulation. For the geomechanical simulation, the side and bottom boundaries are constrained by non-normal displacement boundaries. The surface is modelled by a zero traction boundary.

B.1.2 Case 1

In the first case studied the uncertain parameter is the reservoir permeability. An ensemble size of 60 is used. The initial distribrution is described using a Gaussian distribution with a mean of 10 md and a standard deviation of 5 md. The true solution is drawn from the same distribution. The true solution is 11.8 md. The is used to generate synthetic observations for bottom hole pressure and surface deformation. The measurement errors are drawn from a Gaussian distribution with zero mean and 5% standard deviation relative to the measurement. The total numer of observations assimilated are 32. One bottom hole pressure observation and 31 surface deformation observations. Five data assimilation steps are defined throughout the 2400 day injection period. Each time data is assimilated the permeability is updated and re-run from the start of injection up to the next time step.

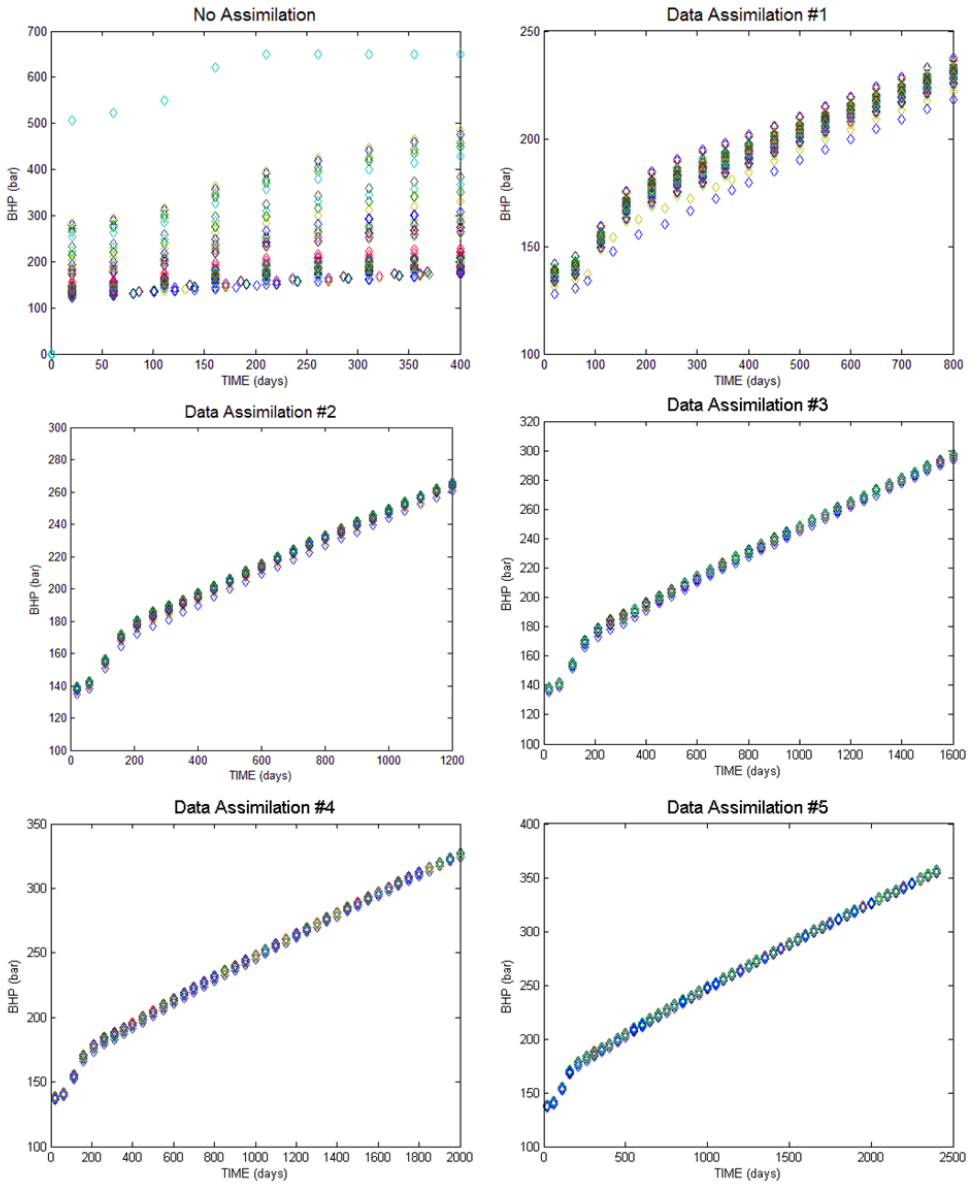


Figure B.2: Case 1: Data assimilation for BHP.

Given the large number of observations the uncertainty in the observations is significantly reduced after two data assimilation steps.

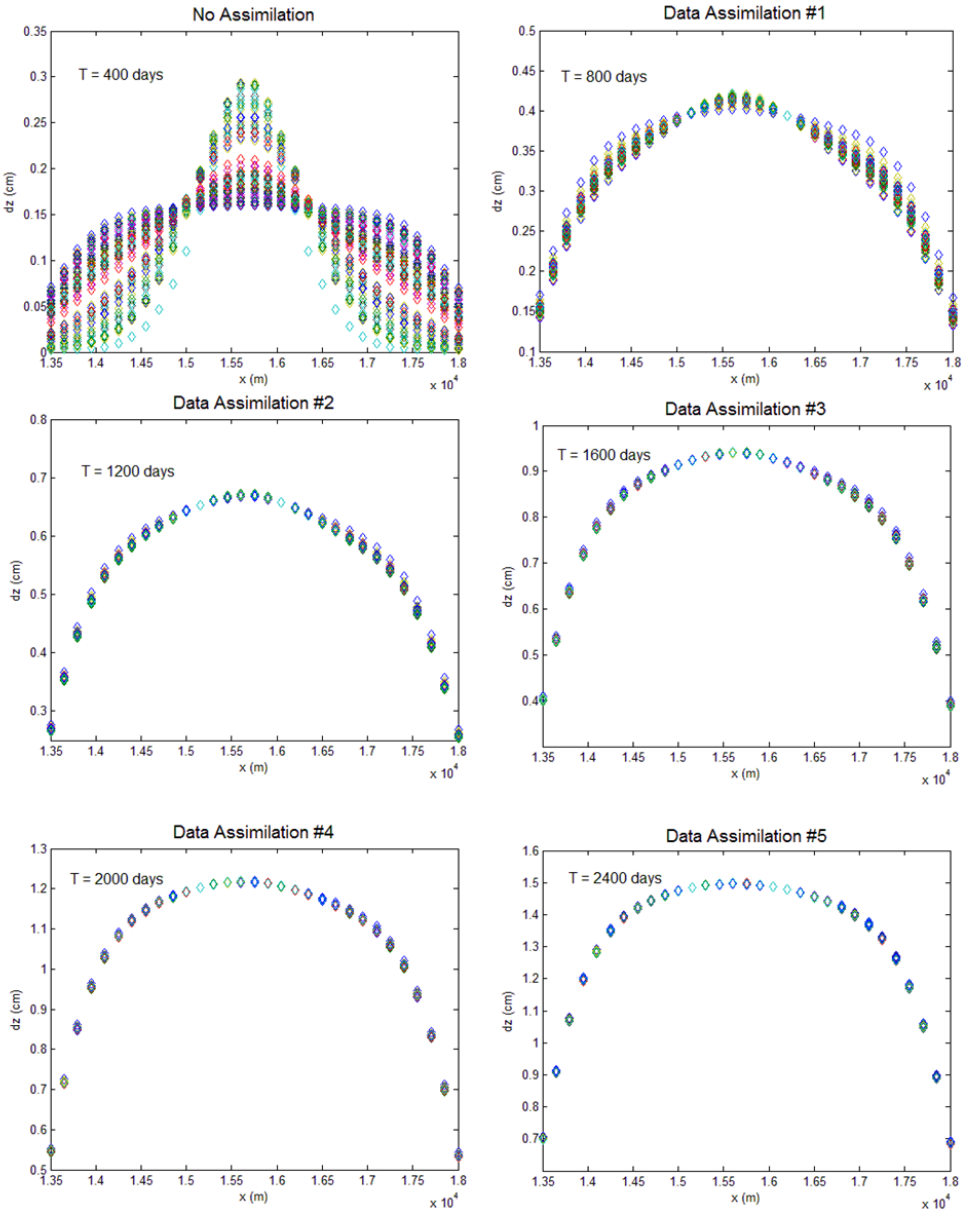


Figure B.3: Case 1: Data assimilation for surface deformation.

B.1.3 Case 2

In the second case study the ensemble is initialised in the same manner as the previous case. The effect of reducing the number of observations is tested. Only bottom hole pressure observations are assimilated. The uncertainty in the bottom hole pressure and surface deformation predictions are reduced compared to the initial case but the rate at which the uncertainty is reduced is reduced given the smaller number of observations.

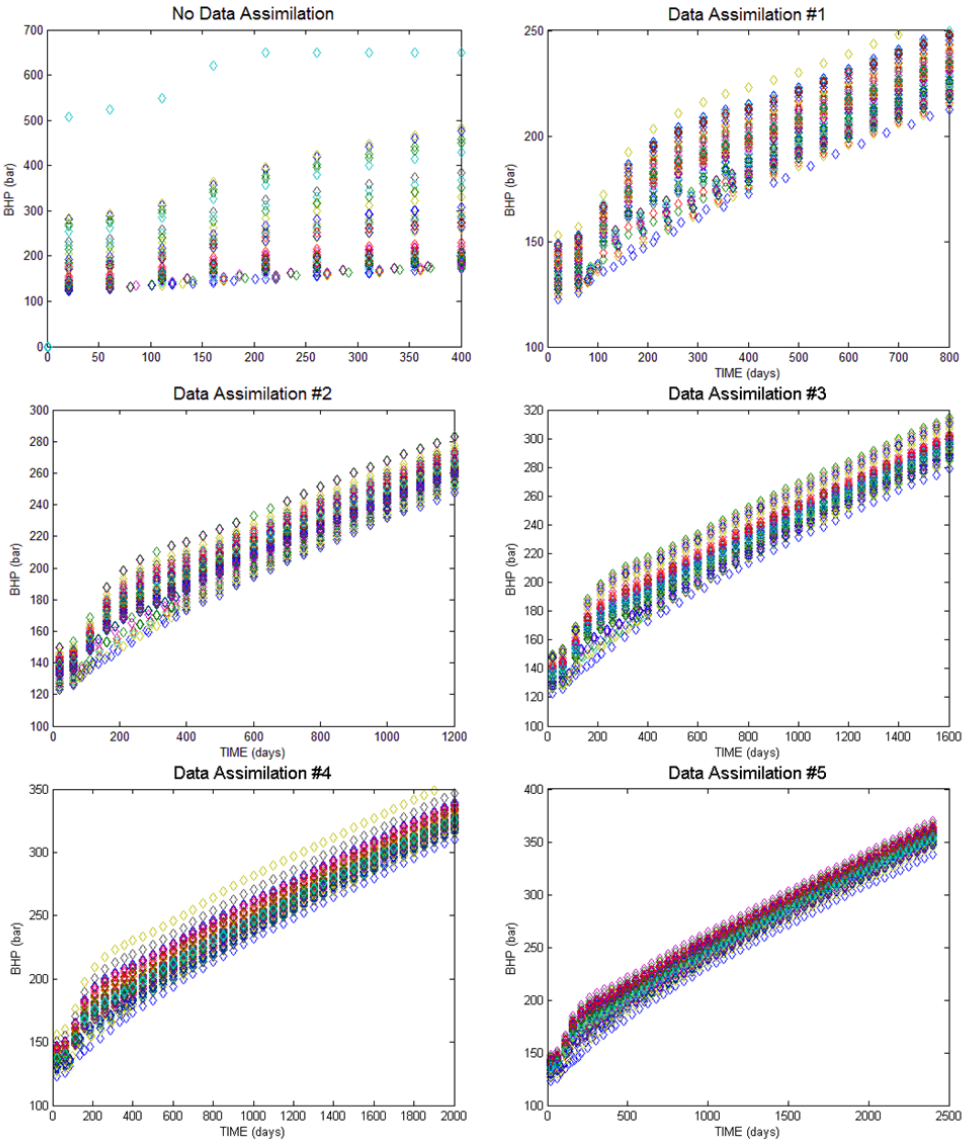


Figure B.4: Case 2: Data assimilation for BHP.

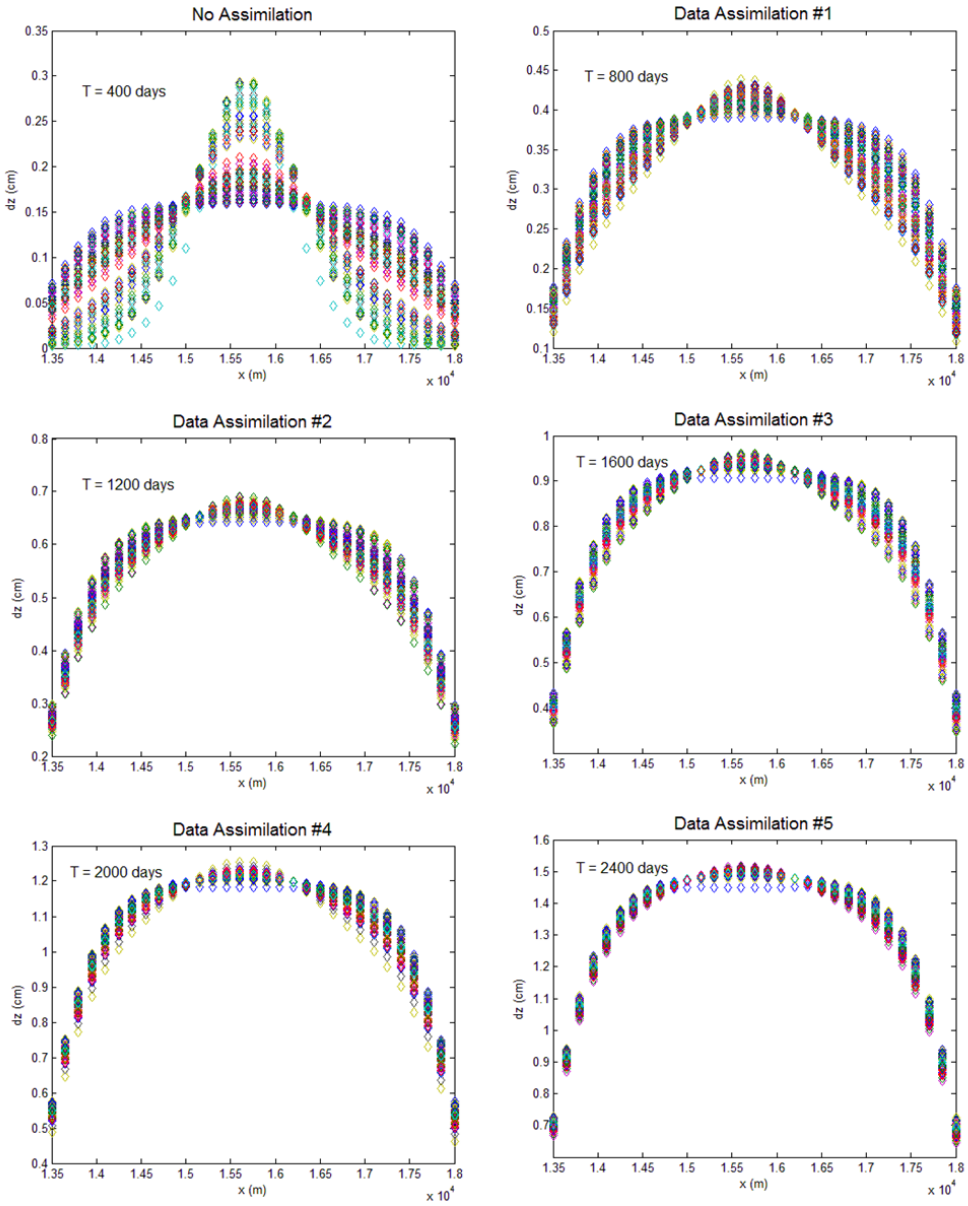


Figure B.5: Case 2: Data assimilation for surface deformation.

B.1.4 Case 3

In the following case the effect of higher observation error is studied. The ensemble setup is identical to case 1. The observation error is 25% relative to the observation magnitude. Both bottom hole pressure and surface deformation is assimilated. It is interesting to note that the EnKF run having more observations with a 25% measurement error outperforms the EnKF run with a single observation with a 5% error.

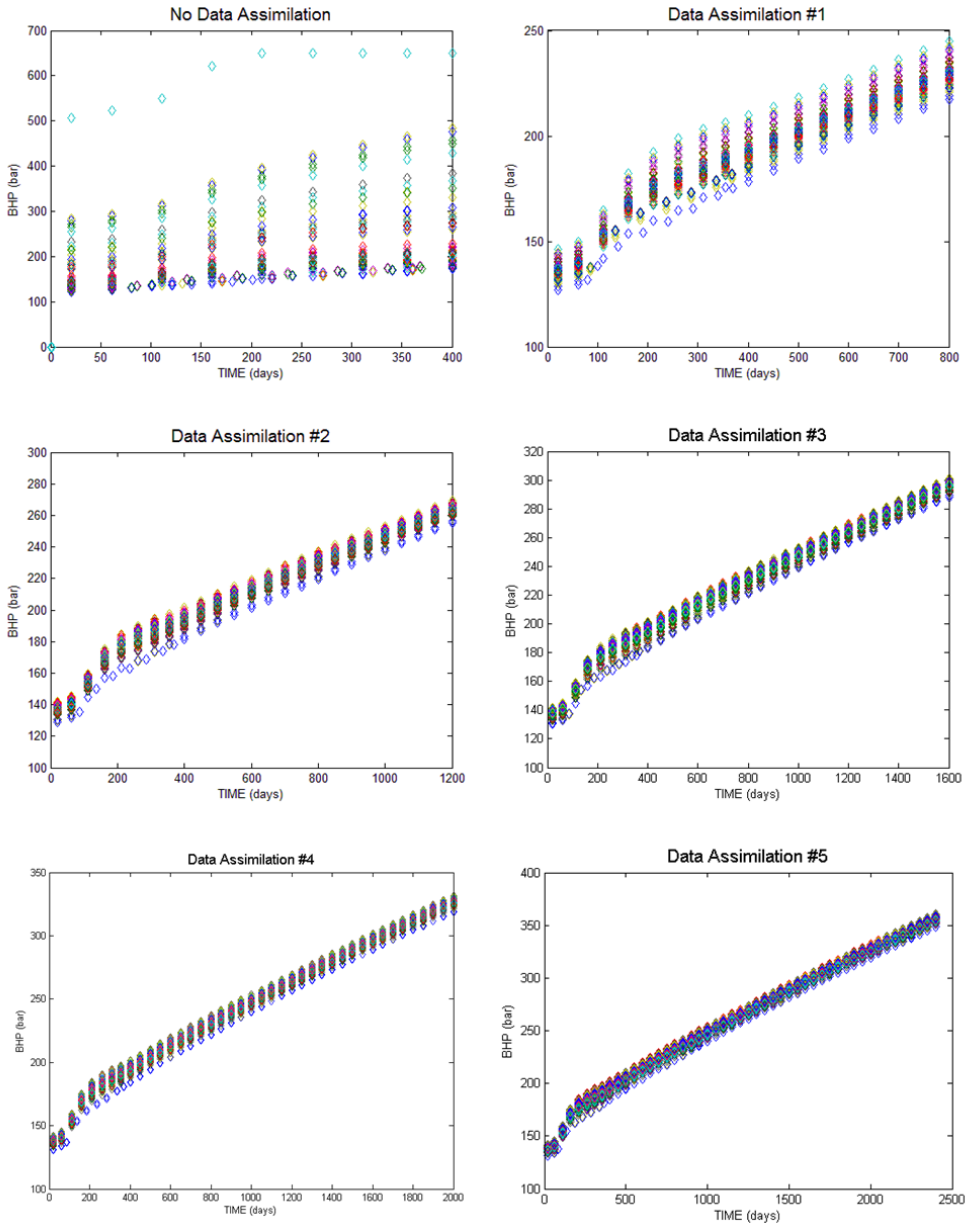


Figure B.6: Case 3: Data assimilation for BHP.

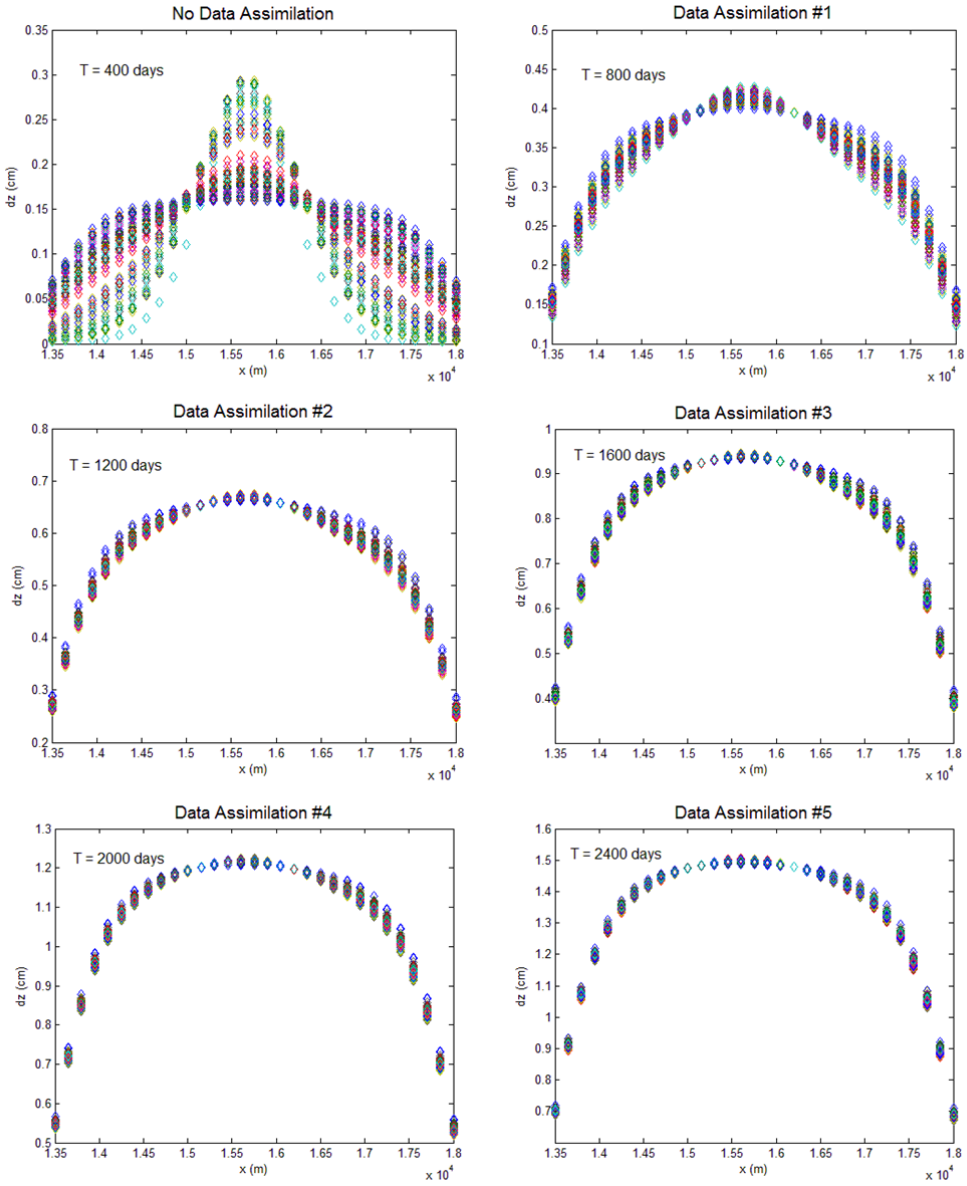


Figure B.7: Case 3: Data assimilation for surface deformation.

B.1.5 Case 4

In this case the the ensemble size is reduced by half. An ensemble size of 30 is used. The other EnKF parameters remain the same as in case 1. Given the smaller ensemble size it quickly loses variability.

B.1.6 Case 5

In this case uncertainty in the geomechanical properties of the caprock is introduced. The uncertainty in the young's modulus of the lower caprock is described by a Gaussian distribution with a mean of 10 GPa and a standard deviation of 6 GPa. The

true young's modulus is taken from a realisation drawn from the distribution. The true modulus for the lower caprock is 4.6 GPa. Synthetic observations are generated using the true values for Young's modulus and reservoir permeability.

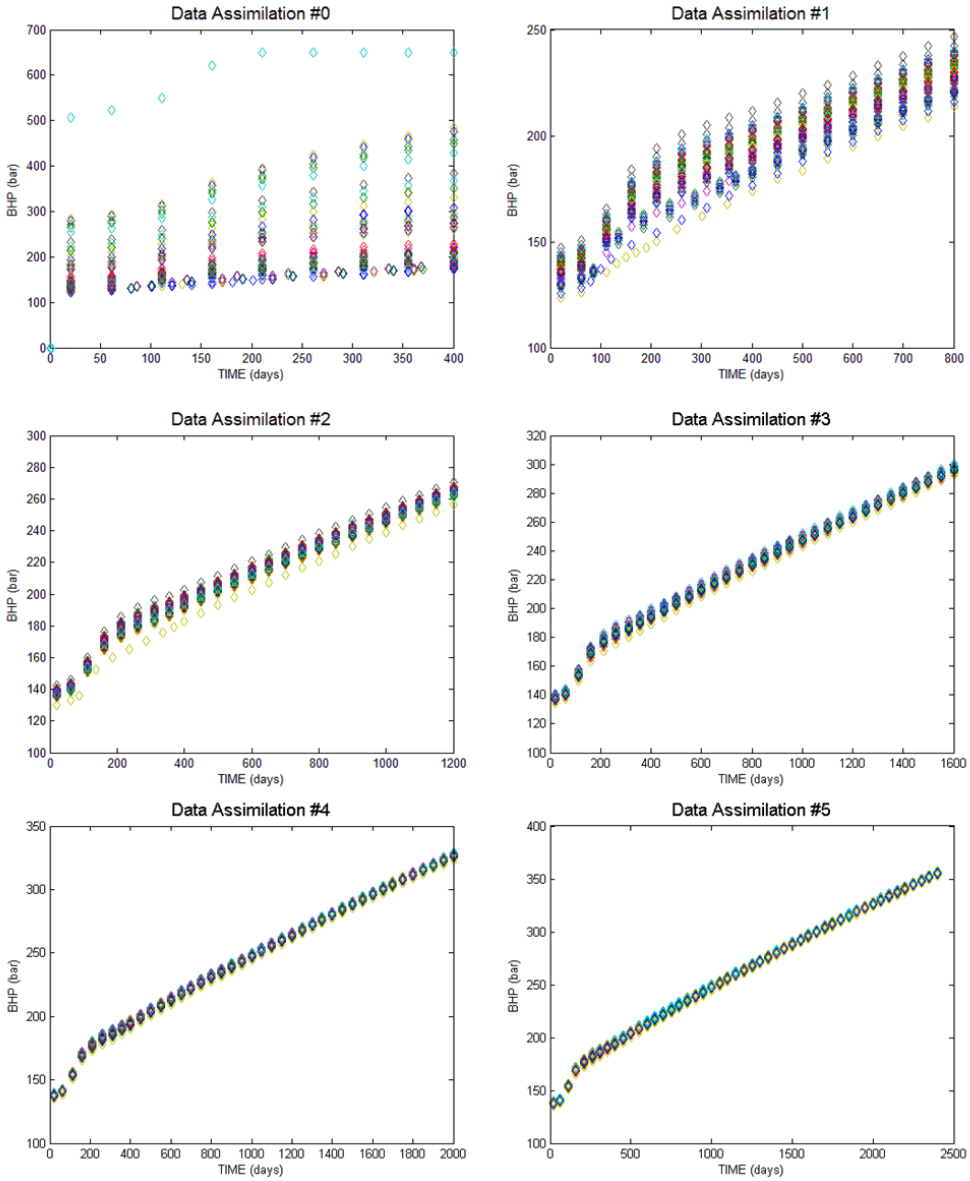


Figure B.8: Case 5: Data assimilation for BHP.

When compared with the initial case where there is no uncertainty in the geomechanical model, the rate at which the uncertainty is reduced is slower. After several data assimilation steps howeve both the flow model and the geomechanical are tuned by the EnKF.

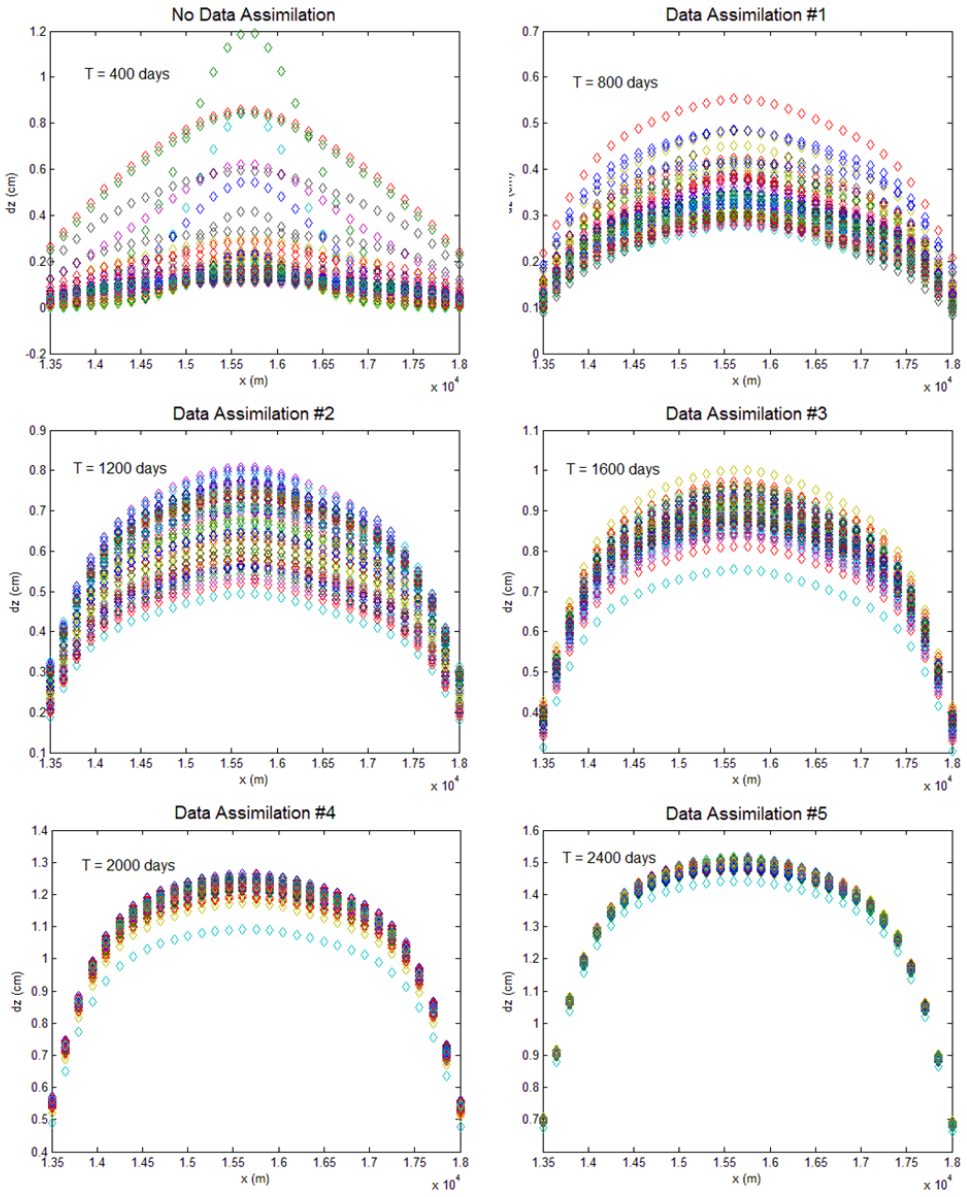


Figure B.9: Case 5: Data assimilation for surface deformation.

B.1.7 Comparison

The uncertainty reduction in the flow parameter is presented in figures B.10 to B.14. In all cases the ensemble mean for permeability has converged to the true solution. The rate at which it converges and the uncertainty associated with it will depend on the number of observations available, the error associated with the observations, the ensemble size and the number of parameters to be updates. The EnKF performs best when both bottom hole pressure and surface deformation are assimilated and the geomechanical model is known. In the cases analysed, the performance is degraded most when only bottom hole pressure is assimilated followed by assimilated both

with an increased error in the observations. Next is the case where the the geomechanical model is not completely known. Reducing the ensemble size leads to quick loss in ensemble variability. Although it converges to the true permeability, losing ensemble variability means further changes in the ensemble will be limited as it based on linear combinations of the available ensemble members. For the final case, the EnKF is successful in updated both the reservoir permeability and the young's modulus for the caprock (Figure B.15).

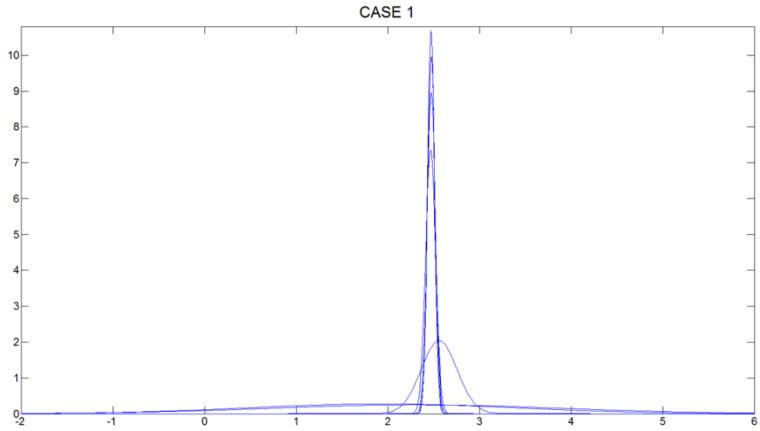


Figure B.10: Permeability pdf for Case 1.

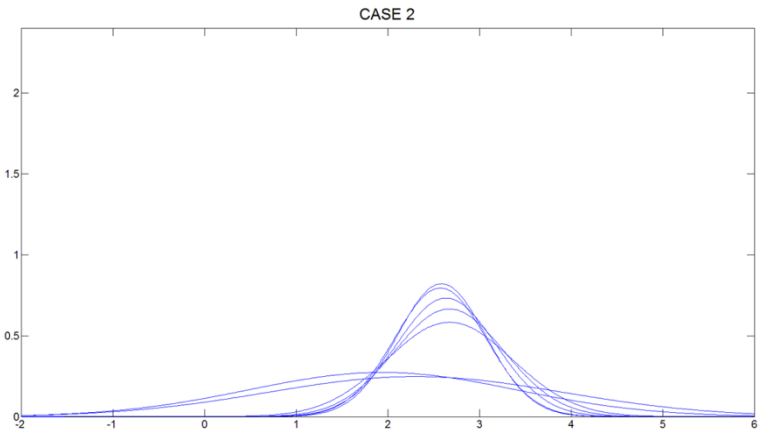


Figure B.11: Permeability pdf for Case 2.

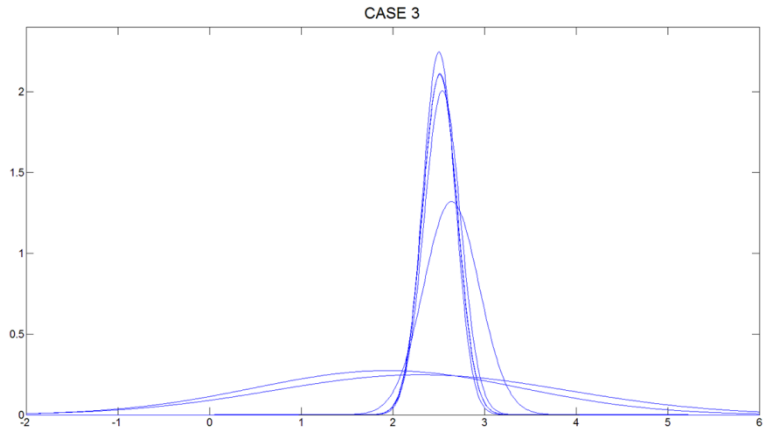


Figure B.12: Permeability pdf for Case 3.

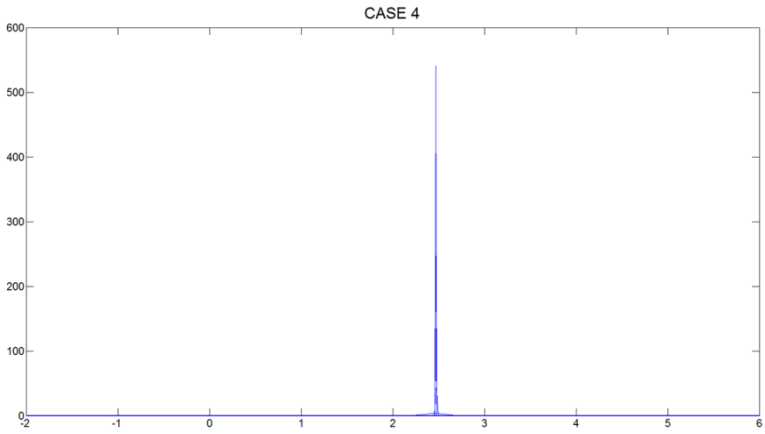


Figure B.13: Permeability pdf for Case 4.

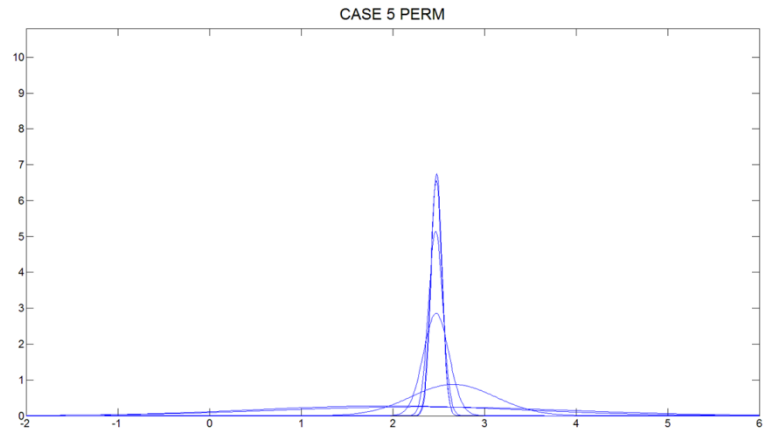


Figure B.14: Permeability pdf for Case 5.

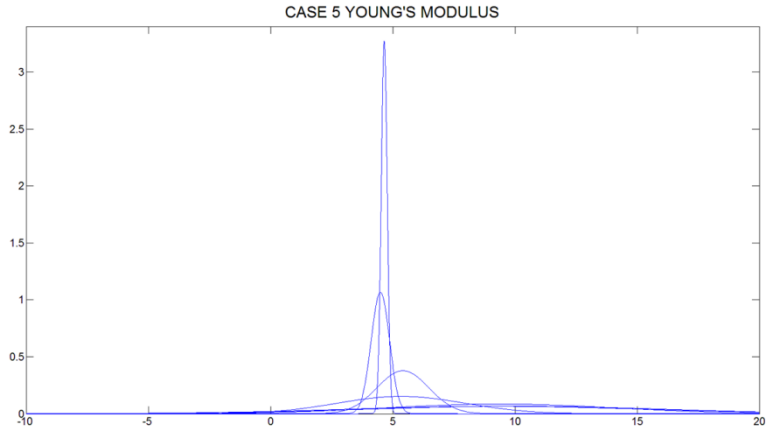


Figure B.15: Young's Modulus pdf for Case 5.

References

Aanonsen, S.I., Naevdal, G., Oliver, D.S., Reynolds, A.C. and Valles,B., 2012. Then Ensemble Kalman Filter in Reservoir Engineering – a Review. *SPE Journal*. pp. 393-412.

Ali, A., Brown, T., Delgado, R., Lee, D., Marsden, R., Prado-Velarde, E., Ramsey, L., Spooner, D., Stone, T. and Stouffer, T., 2003. Watching rocks change – mechanical earth modelling. *Oilfield Review*. pp. 22-39.

Alnes, H., Eiken, O. and Stenvold, T., 2008. Monitoring gas production and CO_2 injection at the Sleipner field using time-lapse gravimetry. *Geophysics*. 73(6), pp. WA155-WA161.

Amadei, B. and Stephansson, O., 1997. *Rock stress and its measurement*. 1st edition, Chapman and Hall, London.

Anderson, E. M., 1951. *The dynamics of faulting and dyke formation with applications to Britain*. Oliver and Boyd, Edinburgh.

Angus, D.A., Kendall, J.-M., Fisher, Q.J., Segura, J.M., Skachkov, S., Crook, A.J.L. and Dutko, M., 2010. Modelling microseismicity of a producing reservoir from coupled fluid-flow and geomechanical simulation. *Geophysical Prospecting*. 58, pp. 901-914.

Armitage, P. J., Faulkner, D. R., Worden, R. H., Aplin, A. C., Butcher, A. R. and Iliffe, J., 2011. Experimental measurement of, and controls on, permeability and permeability anisotropy of caprocks from the CO2 storage project at the Krechba Field, Algeria. *Journal of Geophysical Research*. 116(B12208).

Aster, R. A., Borchers, B. and Thurber, C.H., 2005. *Parameter estimation and inverse problems*. Elsevier Academic Press.

Bachrach, R., Sengupta, M., Salama, A. and Miller, P., 2009. Reconstruction of the layer anisotropic elastic parameters and high-resolution fracture characterization from P-wave data: a case study using seismic inversion and Bayesian rock physics parameter estimation. *Geophysical Prospecting*. 57(2), pp. 253-262.

Bachu, S., 2008. CO_2 storage in geological media: role, means, status and barriers to deployment. *Progress in Energy and Combustion Science*. 34(2), pp. 254-273.

Bachu, S. and Bennion, D.B., 2009. Experimental assessment of brine and/or CO_2 leakage through well cements at reservoir conditions. *International Journal of Greenhouse Gas Control*. 3(4), pp. 494-501.

Barth, A., Reinecher, J. and Heidbach, O., 2008. *Stress derivation from earthquake focal mechanisms*. World Stress Map Project. Available at: http://dc-app3-14.gfz-potsdam.de/pub/guidelines/WSM_analysis_guideline_focal_mechanisms.pdf (Accessed: 07/10/2014).

Barton, C. A., Zoback, M.D. and Moos, D., 1995. Fluid flow along potentially active faults in crystalline rock. *Geology*. 23(8), pp. 683-686.

Bell, J. S., 2003. Practical methods for estimating in situ stresses for borehole stability applications in sedimentary basins. *Journal of Petroleum Science and Engineering*. 38, pp. 111-119.

Benson, S. M., and Cole, D.R., 2008. CO_2 sequestration in deep sedimentary formations. *Elements*. 4(5), pp. 325-331.

Bianco, A., Cominelli, A., Dovera, L. Naevdal, G. and Vallès, B., 2007. History matching and production forecast uncertainty by means of the ensemble Kalman filter: a real field application. EAGE/EUROPEC Conference and Exhibition. London, 11-14 June.

Bickle, M. J., 2009. Geological Carbon Storage. *Nature Geoscience*. 2(12), pp. 815-818.

Bissell, R. C., Vasco, D.W., Atbi, M., Hamdani, M., Okwelegbe, M. and Goldwater M.H., 2011. A full field simulation of the In Salah gas production and CO_2 storage project using a coupled geo-mechanical and thermal fluid flow simulator. *Energy Procedia*. 4(0), pp. 3290-3297.

Bjørnarå, T., Mathias, S., Nordbotten, J. and Park, J., 2014. Fast evaluation of fluid-rock coupling in CO_2 storage. 4th EAGE CO_2 Geological Storage Workshop: Demonstrating storage integrity and building confidence in CCS. Stavanger, Norway.

Bond, C. E., Wightman, R. and Ringrose, P.S, 2013. The influence of fracture anisotropy on CO_2 flow. *Geophysical Research Letters*. 40(7), pp. 1284-1289.

Brown, A. R., 2012. *Interpretation of Three-dimensional Seismic Data*, 7th edition, The American Association of Petroleum Geologists and the Society of Exploration Geophysicists, Tulsa, Oklahoma.

Cacas, M. C., Daniel, J.M. and Letouzey, J., 2001. Nested geological modelling of naturally fractured reservoirs. *Petroleum Geoscience*. 7, pp. S43-S52.

Cairns, G., Jakubowicz, H., Lonergan, L. and Muggeridge, A., 2012. Using time-lapse seismic monitoring to identify trapping mechanisms during CO_2 sequestration. *International Journal of Greenhouse Gas Control*. 11(0), pp. 316-325.

Calvert, R., 2005. *Insights and Methods for 4D Reservoir Monitoring and Characterization*. The Society of Exploration Geophysicists and the European Association of Geoscientists and Engineers, Tulsa, Oklahoma.

Cappa, F. and Rutqvist, J., 2011. Modeling of coupled deformation and permeability evolution during fault reactivation induced by deep underground injection of CO_2. *International Journal of Greenhouse Gas Control*. 5(2), pp. 336-346.

Carles, P., Bachaud, P., Lasseur, E., Berne, P. and Bretonnier, P., 2010. Confining properties of carbonated Dogger caprocks (Parisian basin) for CO_2 storage purpose. *Oil and Gas Science and Technology–Review IFP*. 65(3), pp. 461-472.

Carnec, C. and Fabriol, H., 1999. Monitoring and modeling land subsidence at the Cerro Prieto geothermal field, Baja California, Mexico using SAR interferometry. *Geophysical Research Letters*. 26(9), pp. 1211-1214.

Cavanagh, A. and Ringrose, P., 2011. Simulation of CO_2 distribution at the In Salah storage site using high-resolution field-scale models. *Energy Procedia*. 4(0), pp. 3730-3737.

Chadwick, A., Williams, G., Delepine N., Clochard, V., Labat, K., Sturton, S., Buddensiek, M., Dillen, M., Nickel, M., Lima, A.L., Arts, R., Neele, F. and Rossi, G., 2010. Quantitative analysis of time-lapse seismic monitoring data at the Sleipner CO_2 storage operation. *The Leading Edge*. 29(2), pp. 170-177.

Chadwick, R. A., Williams, G.A., Williams, J.D.O. and Noy, D.J., 2012. Measuring pressure performance of a large saline aquifer during industrial-scale CO_2 injection: The Utsira Sand, Norwegian North Sea. *International Journal of Greenhouse Gas Control*. 10(0), pp. 374-388.

Chang, H., Chen., Y. and Zhang, D., 2010. Data assimilation of coupled fluid flow and geomechanics using the ensemble Kalman filter. *SPE Journal*. pp. 382-394.

Chiaramonte, L., 2008. *Geomechanical Characterization and Reservoir Simulation of a CO_2 Sequestration Project in a Mature Oil Field, Teapot Dome, WY*. Phd Thesis. Stanford University, California.

Chiaramonte, L., White, J. and Trainor-Guitton, W., 2015. Probabilistic geomechanical analysis of compartmentalization at the Snøhvit CO_2 sequestration project. *Jounral of Geophysical Research*. 120(2), pp. 1195-1209.

Chiaramonte, L., Zoback, M., Friedmann, J. and Stamp, V., 2008. Seal integrity and feasibility of CO_2 sequestration in the Teapot Dome EOR pilot: geomechanical site characterization. *Environmental Geology*. 54(8), pp. 1667-1675.

Chopra, S. and Marfurt, K. J.,2007. *Seismic Attributes for Prospect Identification and Reservoir Characterization*. Society of Exploration Geophysics, Tulsa, Oklahoma.

Chow, Y. L., Yang, J.J. and Howard, G.E.,1991. Complex images for electrostatic field computation in multilayered media. *IEEE Transactions on Microwave Theory and Techniques*. 39(7), pp. 1120-1125.

Coward, M. P., and Ries, A.C., 2003. Tectonic development of North African basins. *Geological Society, London, Special Publications*. 207(1), pp. 61-83.

Davis, P. M., 1986. Surface deformation due to inflation of an arbitrarily oriented triaxial ellipsoidal cavity in an elastic half-space. *Journal of Geophysical Research*. 91(B7), pp. 7429-7438.

De Gennaro, S., Onaisi, A., Grandi, A., Ben-Brahim, L. and Neillo, V., 2008. 4D reservoir geomechanics: A case study from the HP/HT reservoirs of the Elgin and Franklin fields. *First Break*. 26(12), pp. 53-59.

Deutsch, C. V., 2002. *Geostatistical Reservoir Modelling*. Oxford University Press, New York.

Dholakia, S. K., Atilla, A., Pollard, D.D., Zoback, M. D., 1998. Fault-controlled hydrocarbon pathways in the Monterey Formation, California. *American Association of Petroleum Geologists Bulletin*. 82, pp. 1551-1574.

Dieterich, J. H., and Decker, R.W., 1975. Finite element modeling of surface deformation associated with volcanism. *Journal of Geophysical Research*. 80(29), pp. 4094-4102.

Du, J. and Olson, J.E., 2001. A poroelastic reservoir model for predicting subsidence and mapping subsurface pressure fronts. *Journal of Petroleum Science and Engineering*. 30(3–4), pp. 181-197.

Du, Y., Segall, P. and Gao, H., 1994. Dislocations in inhomogeneous media via a moduli perturbation approach: general formulation and two-dimensional solutions. *Journal of Geophysical Research*. 99(B7), pp. 13767-13779.

Durucan, S., Shi, J.-Q., Sinayuc, C. and Korre, A., 2011. In Salah CO_2 storage JIP: Carbon dioxide plume extension around KB-502 well–New insights into reservoir behaviour at the In Salah storage site. *Energy Procedia*. 4(0), pp. 3379-3385.

Dybvik, O. P., Gemmer, L., Theune, U. and Østmo, S., 2009. Establishing a geomechanical workflow for time-lapse modelling of an HPHT Field. 71st EAGE Conference and Exhibition, Amsterdam, The Netherlands.

Eiken, O., Ringrose, P., Hermanrud, C., Nazarian, B., Torp, T.A. and Høier, L., 2011. Lessons learned from 14 years of CCS operations: Sleipner, In Salah and Snøhvit. *Energy Procedia*. 4(0), pp. 5541-5548.

Eissa, E. A., and Kazi, A., 1988. Relation between static and dynamic Young's moduli of rocks. *International Journal of Rock Mechanics and Mining Sciences and Geomechanics Abstracts*. 25(6), pp. 479-482.

E.U. Parliament and Council, 2009. Directive 2009/31/EC of the European Parliament and of the Council of 23 April 2009 on the geological storage of carbon dioxide. Off. J. Eur. Union 52, L140/114.

Evans, D. J., 2009. A review of underground fuel storage events and putting risk into perspective with other areas of the energy supply chain. *Geological Society, London, Special Publications*. 313(1), pp. 173-216.

Evensen, G., 1994. Sequential data assimilation with a nonlinear quasi-geostrophic model using Monte Carlo methods to forecast error statistics. *Journal of Geophysical Research*. 99(C5), pp. 10143-10162.

Evensen, G., Hove, J., Meisingset, H.C., Reiso, E., Seim, K.S. and Espelid, S.O., 2007. Using the EnKF for assisted history matching of a North Sea reservoir. SPE Reservoir Simulation Symposium, Houston, 26-28 February.

Fares, N. and Li, V.C., 1988. General image method in a plane-layered elastostatic medium. *Journal of Applied Mechanics*. 55(4), pp. 781-785.

Fjaer, E., Holt, R.M., Horsrud, P., Raaen, A.M. and Risnes, R., 2008. *Petroleum Related Rock Mechanics*. 2nd edition, Elsevier, Amsterdam, The Netherlands.

Fuck, R. F., Tsvankin, I. and Bakulin, A., 2011. Influence of background heterogeneity on traveltime shifts for compacting reservoirs. *Geophysical Prospecting*. 59(1), pp. 78-89.

Garcia, A. and MacBeth, C. ,2013. An estimation method for effective stress changes in a reservoir from 4D seismics data. *Geophysical Prospecting*. 61(4), pp. 803-816.

Garcia, A., Macbeth., C. and Grandi, A. 2010. Time-shift inversion for dynamic reservoir characterization in the Elgin Field. Society of Exploration Geophysicists Annual Meeting, Denver, Colorado.

Geertsma, J., 1966. Problems of Rock Mechanics in Petroleum Engineering. *Proceedings of 1st Congress on International Society of Rock Mechanics*.

Geertsma, J., 1973. Land subsidence above compacting oil and gas reservoirs. *Journal of Petroleum Technology*. 25, pp. 734-744.

Gemmer, L., Olav, H., Iding, M., Leary, S. and Ringrose, P., 2012. Geomechanical response to CO_2 injection at Krechba, In Salah, Algeria. *First Break*. 30, pp. 79-84.

Geovariances, Isatis Technical Reference, version 2014. Avon Cedex, France.

Girard, J.-F., Coppo, N., Rohmer, J., Bourgeois, B., Naudet, V. and Schmidt-Hattenberger, C., 2011. Time-lapse CSEM monitoring of the Ketzin (Germany) CO_2 injection using 2×MAM configuration. *Energy Procedia*. 4(0), pp. 3322-3329.

Gonzalez, R. C. and Wintz, P., 1983. *Digital Image Processing*. Addison-Wesley Publishing Company.

Grechka, V. and Soutter, L., 2005. Simulation of two-phase fluid flow through compactible reservoirs. *Geophysical Prospecting*. 53(6), pp. 829-841.

Grude, S., Landrø, M. and Osdal, B., 2013. Time-lapse pressure–saturation discrimination for CO_2 storage at the Snøhvit field. *International Journal of Greenhouse Gas Control*. 19(0), pp. 369-378.

Gu, Y. and Oliver, D.S., 2005. History matching of the PUNQ-S3 reservoir model using the ensemble Kalman filter. *SPE Journal*. 10(2), pp. 217-224.

Guilbot, J. and Brackin, S., 2002. 4-D constrained depth conversion for reservoir compaction estimation: application to Ekofisk Field. *The Leading Edge*. 21(3), pp. 304-308.

Hale, D., 2009. A method for estimating apparent displacement vectors from time-lapse seismic images. *Geophysics*. 74(5), pp. V99-V107.

Hale, D., Cox, B. and Hatchell, P., 2008. Apparent horizontal displacements in time-lapse seismic images. 78th Annual International Meeting, SEG Expanded Abstracts, pp. 3169-3172.

Hall, S. A., 2006. A methodology for 7D warping and deformation monitoring using time-lapse seismic data. *Geophysics*. 71(4), pp. O21-O31.

Hansen, P., 1998. *Rank-Deficient and Discrete Ill-Posed Problems: Numerical Aspects of Linear Inversion*. Society for Industrial Mathematics.

Hatchell, P. and Bourne, S., 2005. Rocks under strain: strain-induced time-lapse time shifts are observed for depleting reservoirs. *The Leading Edge*. 24(12), pp. 1222-1225.

Haugen, V., Naevdal, G., Natvik, L.-J., Evensen, G., Berg, A.M. and Flornes, K.M., 2008. History matching using the ensemble Kalman filter on a North Sea Field case. *SPE Journal*. 13(4), pp. 383-391

Hawkes, C. D., McLellan., P.J. and Bachu, S., 2005. Geomechanical factors affecting geological storage of CO_2 in depleted oil and gas reservoirs. *Journal of Canadian Petroleum Technology*. 44(10), pp. 52-61.

Herwanger, J. V. and Horne, S.A., 2009. Linking reservoir geomechanics and time-lapse seismics: predicting anisotropic velocity changes and seismic attributes. *Geophysics*. 74(4), pp. W13-W33.

Herwanger, J. V. and Koutsabeloulis, N., 2011. *Seismic Geomechanics: How to Build and Calibrate Geomechanical Models using 3D and 4D Seismic Data*. The European Association of Geoscientists and Engineers, The Netherlands.

Hodgson, N., 2009. *Inversion for reservoir pressure change using overburden strain measurements determined from 4D seismic*. PhD Thesis. Heriot-Watt University, Edinburgh.

Hodgson, N., MacBeth, C., Duranti, L., Rickett, J. and Nihei, K., 2007. Inverting for reservoir pressure change using time-lapse time strain: application to Genesis Field, Gulf of Mexico. *The Leading Edge*. 26(5), pp.649-652.

Holt, R., Nes, O.-M. and Fjaer, E., 2005. In-situ stress dependence of wave velocities in reservoir and overburden rocks. *The Leading Edge*. 24(12), pp. 1268-1274.

Hossain, M. M., Rahman, M.K. and Rahman S.S, 2000. Hydraulic fracture initiation and propagation: roles of wellbore trajectory, perforation and stress regimes. *Journal of Petroleum Science and Engineering*. 27(3–4), pp. 129-149.

Houtekamer, P. L., Mitchell, H.L., Pellerin, G., Buehner, M. Charron, M., Spacek, L. and Hansen, B., 2005. Atmospheric data assimilation with an ensemble Kalman filter: results with real Observations. *Monthly Weather Review*. 133(3), pp. 604-620.

Huffman A. and Bowers, G. L., 2002. *Pressure regimes in sedimentary basins and their prediction: AAPG Memoir 76*. The American Association of Petroleum Geologists, Tulsa, Oklahoma.

Iding, M. and Ringrose, P., 2010. Evaluating the impact of fractures on the performance of the In Salah CO_2 storage site. *International Journal of Greenhouse Gas Control*. 4(2), pp. 242-248.

IPCC (Intergovernmental Panel on Climate Change), 2005. Metz, B., Davidson O., de Coninck, H.C., Loos, M. and Meyer, L.A. (editors). *Special Report on Carbon Dioxide Capture and Storage*. Cambridge University Press, Cambridge.

Isaaks, E.H. and Srivastava, R.M., 1989. *An Introduction to Applied Geostatistics*. Oxford University Press, New York.

Itasca, 2012. *FLAC^{3D} - fast Lagrangian analysis of continua*. Itasca Consulting Group Inc.

Jaeger, J. C., Cook, N.G.W. and Zimmerman, R.W., 2007. *Fundamentals of Rock Mechanics*. 4th edition. Blackwell Publishing, Malden, Massachusetts.

Kalman, R. E., 1960. A new approach to linear filtering and prediction problems. *Transactions of the ASME - Journal of Basic Engineering*. 82 (Series D), pp. 35-45.

Konstantinovskaya, E., Rutqvist, J. and Malo, M., 2014. CO_2 storage and potential fault instability in the St. Lawrence Lowlands sedimentary basin (Quebec, Canada): insights from coupled reservoir-geomechanical modelling. *International Journal of Greenhouse Gas Control*. 22(0), pp. 88-110.

Kragh, E., and Christie, P., 2002. Seismic repeatability, normalized rms, and predictability. *The Leading Edge*. 21(7), pp. 640-647.

Kuvshinov, B.N., 2007. Analytical Geomechanical Models – Insightful, Fast, Cheap. *Offshore*. 67(4), pp. 140-142.

Landrø, M., 2001. Discrimination between pressure and fluid saturation changes from time-lapse seismic data. *Geophysics*. 66(3), pp. 836-844.

Lüth, S., 2011. Time-lapse seismic surface and down-hole measurements for monitoring CO_2 storage in the CO_2 SINK project (Ketzin, Germany). *Energy Procedia*. 4, pp. 3435-3442.

Mathias, S. A., Hardisty, P.E., Trudell, M.R. and Zimmerman, R.W., 2009. Screening and selection of sites for CO_2 sequestration based on pressure buildup. *International Journal of Greenhouse Gas Control*. 3(5), pp. 577-585.

Mathieson, A., Midgley, J., Dodds, K., Wright, I., Ringrose, P. and Saoul, N., 2010. CO_2 sequestration monitoring and verification technologies applied at Krechba, Algeria. *The Leading Edge*. 29(2), pp. 216-222.

Michael, K., Golab, A., Shulakova, V., Ennis-King, J., Allinson, G., Sharma, S. and Aiken, T., 2010. Geological storage of CO_2 in saline aquifers—A review of the experience from existing storage operations. *International Journal of Greenhouse Gas Control*. 4(4), pp. 659-667.

Mindlin, R. D., and Cheng, D.H., 1950. Thermoelastic stress in the semi-infinite solid. *Journal of Applied Physics*. 21(9), pp. 931-933.

Moos, D. and Zoback, M.D., 1990. Utilization of observations of well bore failure to constrain the orientation and magnitude of crustal stresses: application to continental deep sea drilling project and ocean drilling program boreholes. *Journal of Geophysical Research*. 95, pp. 9305-9325.

Morris, J. P., Hao, Y., Foxall, W. and McNab, W., 2011. A study of injection-induced mechanical deformation at the In Salah CO_2 storage project. *International Journal of Greenhouse Gas Control*. 5(2), pp. 270-280.

Muntendam-Bos, A. G., Kroon, I.C. and Fokker, P.A., 2008. Time-dependent inversion of surface subsidence due to dynamic reservoir compaction. *Mathematical Geoscience*. 40(2), pp. 159-177.

Naevdal, G., Johnsen, L.M., Aanonsen, S.I and Vefring, E.H., 2005. Reservoir monitoring and continuous model updating using ensemble Kalman filter. *SPE Journal*. 10(1), pp. 66-74.

Nakamura, K., 1977. Volcanoes as possible indicators of tectonic stress orientation—principle and proposal. *Journal of Volcanology and Geothermal Research*. 2(1), pp. 1-16.

Nelson, R. A., 2001. *Geological Analysis of Naturally Fractured Reservoirs*. Butterworth-Heinemann, Boston.

Nickel, M., 2013. Personal Communications, August 2013.

Nicol, A., Carne, R., Gerstenberger, M. and Christophersen, A., 2011. Induced seismicity and its implications for CO_2 storage risk. *Energy Procedia*. 4(0), pp. 3699-3706.

Nooner, S. L., Eiken, O., Hermanrud, C., Sasagawa, G.S., Stenvold, T. and Zumberge, M.A., 2007. Constraints on the in situ density of CO_2 within the Utsira formation from time-lapse seafloor gravity measurements. *International Journal of Greenhouse Gas Control*. 1(2), pp. 198-214.

Oda, M., 1985. Permeability tensor for discontinuous rock masses. *Géotechnique*. 35(4), pp. 486-495.

Okada, Y., 1985. Surface deformation due to shear and tensile faults in a half-space. *Bulletin of the Seismological Society of America*. 75(4), pp. 1135-1154.

Oliver, D. S., Reynolds, A.C. and Liu, N., 2008. *Inverse Theory for Petroleum Reservoir Characterization and History Matching*. Cambridge University Press, Cambridge.

Onishi, K., Ueyama, T., Matsuoka, T., Nobuoka, D., Saito, H., Azuma, H. and Xue, Z., 2009. Application of crosswell seismic tomography using difference analysis with data normalization to monitor CO_2 flooding in an aquifer. *International Journal of Greenhouse Gas Control*. 3(3), pp. 311-321.

Onuma, T. and Ohkawa, S., 2009. Detection of surface deformation related with CO_2 injection by DInSAR at In Salah, Algeria. *Energy Procedia*. 1(1), pp. 2177-2184.

Orlic, B., 2009. Some geomechanical aspects of geological CO_2 sequestration. *KSCE Journal of Civil Engineering*. 13(4), pp. 225-232.

Ouellet, A., Bérard, T., Desroches, J., Frykman, P., Welsh, P., Minton, J., Pamukcu, Y., Hurter, S. and Schmidt-Hattenberger, C., 2011. Reservoir geomechanics for assessing containment in CO_2 storage: a case study at Ketzin, Germany. *Energy Procedia*. 4(0), pp. 3298-3305.

Oye, V., Aker, E., Daley, T.M., Kühn, D., Bohloli, B. and Korneev, V., 2013. Microseismic monitoring and interpretation of injection data from the In Salah CO_2 storage site (Krechba), Algeria. *Energy Procedia*. 37(0), pp. 4191-4198.

Perkins, T. K. and Gonzalez, J.A., 1984. Changes in earth stresses around a wellbore caused by radially symmetrical pressure and temperature gradients. *Society of Petroleum Engineers Journal*. 24(2), 129-140.

Pollard, D. D. and Atilla, A., 1988. Progress in understanding jointing over the past century. *Geological Society of America Bulletin*. 100, 1181-1204.

Preisig, M. and Prévost, J.H., 2011. Coupled multi-phase thermo-poromechanical effects. Case study: CO_2 injection at In Salah, Algeria. *International Journal of Greenhouse Gas Control*. 5(4), pp. 1055-1064.

Prioul, R. B., Bakulin, A. and Bakulin, V. 2004. Nonlinear rock physics model for estimation of 3D subsurface stress in anisotropic formations: Theory and laboratory verification. *Geophysics*. 69(2), pp. 415-425.

Preuss, K. 2005. Numerical studies of fluid leakage from a geologic disposal reservoir for CO_2 show self-limiting feedback between fluid flow and heat transfer. *Geophysical Research Letters*. 32(14), L14404.

Qi, R., LaForce, T.C. and Blunt, M.J., 2009. Design of carbon dioxide storage in aquifers. *International Journal of Greenhouse Gas Control*. 3(2), pp. 195-205.

Ramirez, A. and Foxall, W., 2014. Stochastic inversion of InSAR data to assess the probability of pressure penetration into the lower caprock at In Salah. *International Journal of Greenhouse Gas Control*. 27(0), pp. 42-58.

Redlich, O. and Kwong, J.N.S., 1949. On the Thermodynamics of Solutions. V. An Equation of State. Fugacities of Gaseous Solutions. *Chemical Reviews*. 44(1), pp. 233-244.

Reeves, S. Geological Sequestration of CO_2 in Deep, Unmineable Coalbeds: An Integrated Research and Commercial-Scale Field Demonstration Project. Paper SPE 71749 presented at the 2001 SPE Annual Technical Conference and Exhibition, New Orleans, 30 September – 3 October.

Reeves, S., Taillefert, A., Pekot, L. and Clarkson, C., 2003. The Allison Unit CO2 – ECBM Pilot: A Reservoir Modeling Study. Topical Report, U.S. Department of Energy, DE-FC26-0NT40924.

Reinecker, J., Stephansson., O. and Zang, A., 2008. Stress analysis from overcoring data. World Stress Map Project. Available at: http://dc-app3-14.gfz-potsdam.de/pub/guidelines/WSM_analysis_guideline_overcoring.pdf (Accessed: 07/10/2014).

Rezmer-Cooper, I., Bratton, T. and Krabbe, H., 2000. The use of resistivity-at-the-bit images and annular pressure while drilling in preventing drilling problems. SPE-55225-MS, pp. 1-13.

Rice, J. R. and Cleary, M.P., 1976. Some basic stress diffusion solutions for fluid-saturated elastic porous media with compressible constituents. *Reviews of Geophysics*. 14(2), pp. 227-241.

Rinaldi, A. P. and Rutqvist, J., 2013. Modeling of deep fracture zone opening and transient ground surface uplift at KB-502 CO_2 injection well, In Salah, Algeria. *International Journal of Greenhouse Gas Control*. 12(0), pp. 155-167.

Ringrose, P., Atbi, M., Mason, D., Espinassous, M., Myhrer, O., Iding, M., Mathieson, A. and Wright, I., 2009. Plume development around well KB-502 at the In Salah CO_2 storage site. *First Break*. 27, pp. 85-89.

Ringrose, P. S., Roberts, D.M., Gibson-Poole, C.M., Bond, C., Wightman, R., Taylor, M., Raikes, S., Iding, M. and Østmo, S., 2011. Characterisation of the Krechba CO_2 storage site: Critical elements controlling injection performance. *Energy Procedia*. 4(0), pp. 4672-4679.

Rocca, F., Rucci, A., Ferretti, A. and Bohane, A., 2013. Advanced InSAR interferometry for reservoir monitoring. *First Break*. 31(5), pp. 77-85.

Rucci, A., Vasco, D.W. and Novali, F., 2013. Monitoring the geologic storage of carbon dioxide using multicomponent SAR interferometry. *Geophysical Journal International*. 193(1), pp. 197-208.

Rüger, A., 1996. Variation of P wave reflectivity with offset and azimuth in anisotropic media. 66th International Annual Meeting, SEG Expanded Abstracts, pp. 1810-1813.

Rutqvist, J., 2002. A study of caprock hydromechanical changes associated with CO_2-injection into a brine formation. *Environmental Geology*. 42(2), pp. 296-305.

Rutqvist, J., 2012. The geomechanics of CO_2 storage in deep sedimentary formations. *Geotechnical and Geological Engineering*. 30(3), pp. 525-551.

Rutqvist, J., Birkholzer, J.T. and Tsang, C.-F., 2008. Coupled reservoir–geomechanical analysis of the potential for tensile and shear failure associated with CO_2 injection in multilayered reservoir–caprock systems. *International Journal of Rock Mechanics and Mining Sciences*. 45(2), pp. 132-143.

Rutqvist, J., Vasco, D.W. and Myer, L., 2010. Coupled reservoir-geomechanical analysis of CO_2 injection and ground deformations at In Salah, Algeria. *International Journal of Greenhouse Gas Control*. 4(2), pp. 225-230.

Rutqvist, J., Liu, H.-H., Vasco, D.W., Pan, L., Kappler, K. and Majer, E., 2011. Coupled non-isothermal, multiphase fluid flow, and geomechanical modeling of ground surface deformations and potential for induced micro-seismicity at the In Salah CO_2 storage operation. *Energy Procedia*. 4(0), pp. 3542-3549.

Samier, P., Onaisi, A. and de Gennaro, S., 2008. A practical iterative scheme for coupling geomechanics with reservoir simulation. *SPE Journal*. 11(5), pp. 892-901.

Samier, P., Onaisi., A. and Fontaine, G., 2006. Comparisons of uncoupled and various coupling techniques for practical field examples. *SPE Journal*. 11(1), pp. 89-102.

Sato, K., Mito, S., Horie, T., Ohkuma, H., Saito, H., Watanabe, J. and Yoshimura, T., 2011. Monitoring and simulation studies for assessing macro- and meso-scale migration of CO_2 sequestered in an onshore aquifer: Experiences from the Nagaoka pilot site, Japan. *International Journal of Greenhouse Gas Control*. 5(1), pp. 125-137.

Sayers, C. M. and Kachanov, M., 1995. Microcrack-induced elastic wave anisotropy of brittle rocks. *Journal of Geophysical Research*. 100(B3), pp. 4149-4156.

SchlumbergerGeoQuest, 2010. ECLIPSE reservoir simulator, Technical description, Houston, Texas.

Schön, J., 2004. *Physical Properties of Rocks: Fundamentals and Principles of Petrophysics*. Elsevier, Pergamon Press.

Schutjens, P. M., 2005. Reservoir Monitoring with Seismic Timeshifts: Geomechanical Modeling for its Application in Stacked Pay. *Proceedings of the International Petroleum Technology Conference*, Doha, Qatar, 21- 23 November.

Segall, P., 1985. Stress and subsidence resulting from subsurface fluid withdrawal in the epicentral region of the 1983 Coalinga earthquake. *Journal of Geophysical Research*. 90(B8), pp. 6801-6816.

Segall, P., 1992. Induced stresses due to fluid extraction from axisymmetric reservoirs. *Pure and Applied Geophysics*. 139(3), pp. 535-560.

Settari, A. and Mouritis, F.M., 1998. A coupled reservoir and geomechanical simulation system. *SPE Journal*. 3(3), pp. 219-226.

Shi, J.-Q., Xue, Z. and Durucan, S., 2007. Seismic monitoring and modelling of supercritical CO_2 injection into a water-saturated sandstone: Interpretation of P-wave velocity data. *International Journal of Greenhouse Gas Control*. 1(4), pp. 473-480.

Shi, J.-Q., Sinayuc, C., Durucan, S. and Korre, A., 2012. Assessment of carbon dioxide plume behaviour within the storage reservoir and the lower caprock around the KB-502 injection well at In Salah. *International Journal of Greenhouse Gas Control*. 7(0), pp. 115-126.

Shi, J.-Q., Smith, J., Durucan, S. and Korre, A., 2013. A coupled reservoir simulation-geomechanical modelling study of the CO_2 injection-induced ground surface uplift observed at Krechba, In Salah. *Energy Procedia*. 37, pp. 3719-3726.

Skjervheim, J.-A., Evensen, G., Aanonsen, S.I. and Johansen, T.A., 2007. Incorporating 4D seismic data in reservoir simulation models using ensemble Kalman filter. *SPE Journal*. 12(3), pp. 282-292.

Smart, B. G. D., Somerville, J.M., Jin, M. and Koutsabeloulis, N.C., 2003. Reservoir characterization for the management of stress-sensitivity. *Geological Society, London, Special Publications*. 209(1), pp. 145-153.

Smith, J., Durucan, S., Korre, A. and Shi, J.-Q., 2011. Carbon dioxide storage risk assessment: Analysis of caprock fracture network connectivity. *International Journal of Greenhouse Gas Control*. 5(2), pp. 226-240.

Soltanzadeh, H. and Hawkes, C.D., 2009. Assessing fault reactivation tendency within and surrounding porous reservoirs during fluid production or injection. *International Journal of Rock Mechanics and Mining Sciences*. 46(1), pp. 1-7.

Spycher, N. and Pruess, K., 2005. CO_2-H_2O mixtures in the geological sequestration of CO_2. II. Partitioning in chloride brines at 12–100°C and up to 600 bar. *Geochimica et Cosmochimica Acta*. 69(13), pp. 3309-3320.

Staples, R. Ita, J., Burrell, R. and Nash, R., 2007. Monitoring pressure depletion and improving geomechanical models of the Shearwater Field using 4D seismic. *The Leading Edge*. 26(5), pp. 636-642.

Stephenne, K. Start up of the world's first commercial post-combustion coal fired CCS project: Contribution of Shell Cansolv to SaskPower boundary dam ICCS Project, Presented at the 12th International Conference of Greenhouse Gas Control Technologies (GHGT-12), October 5-9 2014, Austin Texas.

Streit, J. E., and Hillis, R.R., 2004. Estimating fault stability and sustainable fluid pressures for underground storage of CO_2 in porous rock. *Energy*. 29(9-10), pp. 1445-1456.

Swarbrick, R. E. and Osborne, M.J., 1998. *Mechanisms that generate abnormal pressures: An overview*. AAPG Memoir. 70, pp. 13-34.

Terzaghi, K., 1923. *Theoretical Soil Mechanics*. Wiley, New York.

Tod, S., Messaoud, H., Taylor, B., Johnston, R. and Allen, T., 2007. Fracture prediction from wide-azimuth land seismic data in SE Algeria. *The Leading Edge*. 26(9), pp. 1154-1160.

Treitel, S., 1970. Principles of Digital Multichannel Filtering. *Geophysics*. 35(5), pp. 785-811.

Tura, A., Barker, T., Cattermole, P., Collins, C., Davis, J., Hatchell, P., Koster, K., Schutjens, P. and Wills, P., 2005. Monitoring primary depletion reservoirs using amplitudes and time shifts from high-repeat seismic surveys. *The Leading Edge*. 24(12), pp. 1214-1221.

van Lingen, P., Sengul, M., Daniel, J.-M. and Cosentino, L., 2001. Single medium simulation of reservoirs with conductive faults and fractures. Paper SPE68165. Presented at SPE Middle East Oil Show, Bahrain.

Vasco, D. W. and Ferretti, A., 2005. On the use of quasi-static deformation to understand reservoir fluid flow. *Geophysics*. 70(4), pp. O13-O27.

Vasco, D. W., Karasaki, K. and Doughty, C., 2000. Using surface deformation to image reservoir dynamics. *Geophysics*. 65(1), pp. 132-147.

Vasco, D. W., Ferretti, A. and Novali, F., 2008. Reservoir monitoring and characterization using satellite geodetic data: Interferometric synthetic aperture radar observations from the Krechba field, Algeria. *Geophysics*. 73(6), pp. WA113-WA122.

Vasco, D. W., Rucci, A., Ferreti, A., Novali, F., Bissell, R.C., Ringrose, P.S., Mathieson, A.S. and Wright, I.W., 2010. Satellite-based measurements of surface deformation reveal fluid flow associated with the geological storage of carbon dioxide. *Geophysical Research Letters*. 37(3), pp. L03303.

Verdon, J.P., Kendall, J.-M. and Maxwell, S.C., 2010a. A comparison of passive seismic monitoring of fracture stimulation from water and CO_2 injection. *Geophysics*. 75(3), pp. MA1-MA7.

Verdon, J.P., Kendall, J.-M., White, D.J., Angus, D.A., Fisher, Q.J. and Urbancic, T., 2010b. Passive seismic monitoring of carbon dioxide storage at Weyburn. *The Leading Edge*. 29(2), pp. 200-206.

Verdon, J. P. and Kendall, J.-M., 2011. Detection of multiple fracture sets using observations of shear-wave splitting in microseismic data. *Geophysical Prospecting*. 59(4), pp. 593-608.

Verdon, J. P., Kendall, J.-M., White, D.J. and Angus, D.A., 2011. Linking microseismic event observations with geomechanical models to minimise the risks of storing CO_2 in geological formations. *Earth and Planetary Science Letters*. 305(1–2), pp. 143-152.

Verdon, J. P., Kendall, J.-M., Stork, A. L., Chadwick, R. A., White, D. J. and Bissell, R.C., 2013. Comparison of geomechanical deformation induced by megatonne-scale CO_2 storage at Sleipner, Weyburn, and In Salah. *Proceedings of the National Academy of Sciences*. 110(30), pp. E2762-E2771.

Vidal-Gilbert, S., Nauroy, J.-F. and Brosse, E., 2009. 3D geomechanical modelling for CO_2 geologic storage in the Dogger carbonates of the Paris Basin. *International Journal of Greenhouse Gas Control*. 3(3), pp. 288-299.

Vidal-Gilbert, S., Tenthorey, E., Dewhurst, D., Ennis-King, J., Van Ruth, P. and Hillis, R., 2010. Geomechanical analysis of the Naylor Field, Otway Basin, Australia: Implications for CO_2 injection and storage. *International Journal of Greenhouse Gas Control*. 4(5), pp. 827-839.

Warren, J.K., 2007, *Evaporites: Sediments, Resources and Hydrocarbons*, Springer.

White, D.J., 2013a. Seismic characterization and time-lapse imaging during seven years of CO_2 flood in the Weyburn field, Saskatchewan, Canada. *International Journal of Greenhouse Gas Control*. 16(0), pp. S78-S94.

White, D. J., 2013b. Toward quantitative CO_2 storage estimates from time-lapse 3D seismic travel times: An example from the IEA GHG Weyburn–Midale CO_2 monitoring and storage project. *International Journal of Greenhouse Gas Control*. 16(0), pp. S95-S102.

White, J. A., Chiaramonte, L., Ezzedine, S., Foxall, W., Hao, Y., Ramirez, A. and McNab, W., 2014. Geomechanical behavior of the reservoir and caprock system at the In Salah CO_2 storage project, *Proceedings of the National Academy of Sciences*. 111(24), pp. 8747-8752.

Wiener, N., 1964. Extrapolation, interpolation and smoothing of stationary time series. The M.I.T Press.

Wilschut, F., Peters, E., Visser, K., Fokker, P.A. and van Hooff, P., 2011. Joint history matching of well data and surface subsidence observations using the ensemble Kalman filter: a field study. *Proceedings SPE Reservoir Simulation Symposium*, Woodlands, Texas, 21-23 Feb.

Wiprut, D., and Zoback, M.D., 2002. Fault reactivation, leakage potential, and hydrocarbon column heights in the northern North Sea. *Norwegian Petroleum Society Special Publication*. 11, pp. 203-219.

Wojtacki, K., Lewandowska, J., Gouze, Ph. and Lipkowski, A., 2014. Numerical computations of rock dissolution and geomechanical effects for CO_2 geological storage. *International Journal for Numerical and Analytical Methods in Geomechanics*.

Wright, I. W., Ringrose, P.S., Mathieson, A.S. and Eiken, O., 2009. An overview of active large-scale CO_2 storage projects. SPE 127096. *Proceedings SPE international conference on CO_2 capture, storage and utilization*, San Diego, California, 2-4 November.

Wright, T. J., Parsons, B.E. and Lu, Z., 2004. Toward mapping surface deformation in three dimensions using InSAR. *Geophysical Research Letters*. 31(1), pp. L01607.

Zoback, M. D., 2010. *Reservoir Geomechanics*, Cambridge University Press.

Zoback, M. D. and Gorelick, S.M., 2012. Earthquake triggering and large-scale geologic storage of carbon dioxide. *Proceedings of the National Academy of Sciences*. 109(26), pp. 10164-10168.

Zoback, M. D., Moos, D., Mastin, L. and Anderson, R.N., 1985. Well bore breakouts and in situ stress. *Journal of Geophysical Research*. 90(B7), pp. 5523-5530.

Zoback, M. L., 1992. First and second order patterns of tectonic stress: The World Stress Map Project. *Journal of Geophysical Research*. 97(11), pp. 11,703-11,728.